Motion-Corrected Simultaneous Cardiac PET-MR Imaging

Munoz, Camila

Awarding institution:
King's College London

Motion-Corrected Simultaneous Cardiac PET-MR Imaging

Camila Muñoz Escobar

Supervised by:
Dr Claudia Prieto
Professor Andrew Reader

Thesis submitted to King's College London in fulfilment
of the degree Doctor of Philosophy

September 2018

Abstract

Simultaneous cardiac positron emission tomography and magnetic resonance (PET-MR) imaging is a promising non-invasive hybrid technique for comprehensive assessment of cardiovascular disease in a single examination. However, image degradation due to respiratory and cardiac motion during data acquisition remains a major challenge that has hindered the adoption of PET-MR in the clinical setting.

State-of-the-art PET-MR technical developments have focused on using MR information for improving PET image quality. However, this significantly increases the overall examination time, since diagnostic MR images need to be acquired after the PET-MR scan. Furthermore, this approach leads to misaligned PET and MR images that are difficult to interpret together.

In this thesis a novel framework for truly simultaneous motion-corrected cardiac PET-MR has been developed. This was achieved by designing an MR acquisition sequence that allowed the measurement of physiological respiratory and cardiac motion while producing coronary MR angiography (CMRA) images, and a reconstruction scheme that included this motion information to produce co-registered motion-corrected cardiac PET and CMRA images from a single efficient examination with short and predictable scan time.

This general framework was implemented for three applications. First, a scheme that enables respiratory motion-corrected PET-CMRA was developed. The scheme was validated in healthy subjects, oncology patients and patients with cardiac disease, enabling assessment of myocardial viability by PET and visualisation of coronary artery anatomy by CMRA. The second application extended this scheme to include both cardiac and respiratory motion-correction of PET and CMRA data. In this approach, left ventricular function can also be measured by MR, potentially allowing for a comprehensive assessment of coronary artery disease from a single scan of $\sim$12 minutes. Finally, the proposed scheme was extended to perform water-fat CMRA imaging, enabling the simultaneous visualisation of coronary anatomy and cardiac fat, and estimation of respiratory-resolved attenuation correction maps to further improve the quantification of the cardiac PET images.

Acknowledgements

I am very grateful to my supervisor, Claudia Prieto, for her excellent guidance and encouragement throughout my PhD and to René Botnar, for his invaluable advice and optimism when the results didn't look nice at all. I would also like to thank Andrew Reader for his critical view of my work, which allowed me to improve. The work developed in this dissertation would not have been possible without the continuous support and expertise of Radhouene Neji.

I would like to thank Sami Jeljeli and James Stirling for their patience and willingness to find time for my short-notice experiments in the scanner. Special thanks to Karl Kunze and Stephan Nekolla for their enthusiasm and good feedback about my research. They provided a key insight about the ideas we were developing.

I am grateful for having met so many amazing people at KCL during my PhD. Thanks to Gastao, Giulia, Teresa, Isabel R, Thomas, Giovanna, Olivier, Imran, Karina, Bego, Dr. Dregely, Giorgia, Elisa, Niccolo, Aurelien, to name a few, for all the good times together both in London and at conferences, and also thanks for all the hours of volunteering for my experiments.

I'd like to thank Chris and Patrick for their friendship and all the fun times, you're really cool people. Thank you Dan for the nice conversations about science, life and everything else.

I owe much to Marcelo Andía, who convinced me to come to London in the first place, and whose love for research in biomedical sciences continues to inspire me.

Agradezco el apoyo y el amor fundamental de mi Mamá, Nicolás, Felipe y la Nena. Gracias por llenarme de cariño desde la distancia y hacerme parte de su día a día. A mis amigos Johana, Jan, Fernando, Toño, Kaipi y Víctor, muchas gracias por estar conectados desde lugares remotos y a horarios aleatorios. Es una manera de tenerlos cerca. A Renatito todo mi agradecimiento por la amistad de años, las largas caminatas y los mejores cafés en Londres.

Estoy muy agradecida de Pancho por cuidarme y alentarme siempre a ser una mejor persona. Finally, my deepest gratitude to Sam, the best companion, for all of his love and patience and for always being there for me.

This PhD was funded by the King's College London & Imperial College London EPSRC Centre for Doctoral Training in Medical Imaging (EP/L015226/1).

Contents

List of Abbreviations

1D	One-dimensional
2D	Two-dimensional
3D	Three-dimensional
AAR	Area at risk
ACD	Annihilation coincidence detection
AHA	American Heart Association
AP	Anterior-Posterior
bSSFP	Balanced SSFP
CAD	Coronary artery disease
CG	Conjugate gradient
CMRA	Coronary MR angiography
CNR	Contrast-to-noise ratio
CT	Computed tomography
CTCA	CT coronary angiography
CTO	Chronic total occlusion
CV	Coefficient of variation
CVD	Cardiovascular disease
DCE	Dynamic contrast enhanced

dNAV Diaphragmatic navigator

ECG Electrocardiogram

EDV End diastolic volume

EF Ejection fraction

ESV End systolic volume

FatSat Fat saturation

FDG Fluorodeoxyglucose

FE Frequency encoding

FH Foot-head

FOV Field of view

FWHM Full-width at half-maximum

GMD General matrix description

iNAV Image-based navigator

LAD Left anterior descending artery

LCX Left circumflex artery

LGE Late Gadolinium enhancement

LOR Line of response

LSO Cerium-doped lutetium oxyorthosilicate

LV Left ventricle

MC Motion-corrected (Respiratory motion-corrected in Chapter 5, cardiac and respiratory motion-corrected in Chapter 6)

MCIR Motion-compensated image reconstruction

MIP Maximum intensity projection

MLAA Maximum-likelihood reconstruction of attenuation and activity

MLEM Maximum-likelihood expectation maximisation

MPR Multi-planar reformatting

MR Magnetic resonance

MSE Mean squared error

NMC No motion correction

NMR Nuclear magnetic resonance

OSEM Ordered-subsets expectation maximisation

PCI Percutaneous coronary intervention

PET Positron emission tomography

PE Phase encoding

PSIR Phase-sensitive inversion recovery

RCA Right coronary artery

RespMC Respiratory motion-corrected

RF Radiofrequency

RL Right-left

ROI Region of interest

RTA Reconstruct transform average

RV Right ventricle

SAR Specific absorption rate

SE Slice encoding

SI Superior-inferior

SNR Signal-to-noise ratio

SPECT Single-photon emission CT

SPIR Spectral pre-saturation with inversion recovery

SSFP Steady-state free precession

SUV Standardised uptake value

SV Stroke volume

TC 2D translational motion correction

TC+GMD 2D translational plus 3D non-rigid motion correction

T2-prep T_2 preparation

TE Echo time

TFE Turbo field echo

TR Repetition time

List of Figures

List of Tables

Chapter 1:

Introduction

Cardiovascular disease (CVD) is the leading cause of death worldwide, accounting for 31.5% of the total number of deaths in 2015, according to the Global Burden of Disease Study [1]. Although the age-standardised death rates associated to CVD have decreased by more than 20% during the last three decades thanks to improvements in management of risk factors, and better treatments and therapies, CVD still causes 45.2% of all deaths associated to non-communicable diseases. Amongst all the cardiovascular diseases, coronary artery disease (CAD), also known as coronary heart disease and ischaemic heart disease, has the highest mortality rate and it is overall the most common cause of death globally, producing about 14.8% of the total deaths every year [1]. Moreover, CAD is not only prevalent in high-income countries, but it also affects low- and medium-income countries [2], and its prevention and control is one of the major challenges for healthcare systems worldwide [3].

CAD is caused by the accumulation of calcium, fatty lipids and inflammatory cells within the wall of the coronary arteries, as shown in Figure 1.1. This accumulation will then result in the progressive formation of atherosclerotic plaques in different locations within the coronary tree. Depending on the composition of the atherosclerotic plaque, coronary disease can lead to a steady progressive narrowing of the vessels, chronically reducing the myocardial blood flow supply, and/or can result in total occlusion of the vessels due to the sudden rupture of some of these plaques, causing acute myocardial infarction and in severe cases, sudden death [4]. In the chronic condition, the imbalance between the demand and supply of oxygen-rich blood flow to the myocardium triggers a pathophysiological response known as ischaemic cascade [5]. At the beginning of the cascade, the flow imbalance produces

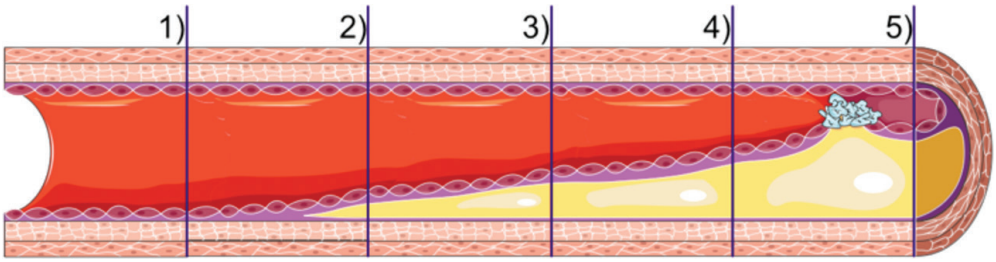

Figure 1.1: Schematic of CAD progression. 1) Healthy vessel. 2) In early stages, initial deposition of plaque occurs without major changes in the vessel lumen and wall. 3-4) Progressive narrowing of the lumen of the artery due to the accumulation of plaque. In these stages, intraplaque haemorrhage may occur within the atherosclerotic plaque, which becomes prone to rupture. 5) Sudden plaque rupture can cause intraluminal thrombosis, and occlude the downstream blood flow in the vessel, which is one of the main manifestations of acute CAD. Reprinted from Ginami G et al. *Technical Advances and Clinical Perspectives in Coronary MR Imaging.* In Cardiovascular Imaging and Image Analysis. Taylor & Francis, 2018 (in press) [6]

a regional hypoperfusion in the myocardium, which in time leads to diastolic and systolic dysfunction. With further progression of the disease, this chronic occlusion of the arteries can lead to angina or heart failure, and an increased risk of acute myocardial infarction.

During the last decades, different medical imaging modalities have been proposed for the diagnosis of CAD through its multiple pathophysiological manifestations by either assessing the presence of vessel narrowing, and more recently the composition of atherosclerotic plaques, or by evaluating the induced changes in regional myocardial perfusion (Figure 1.2). These imaging techniques may allow for early diagnosis of the disease, even before the onset of clinical symptoms, improving prognosis and aiding therapy planning for both stable and acute coronary disease [7].

Invasive X-ray coronary angiography remains the reference modality for imaging of the coronary artery lumen and detection of coronary stenosis. The procedure for X-ray angiography requires catheterisation of the arteries, the use of iodinated contrast agents, and exposes the patient to ionising radiation. Computed tomography (CT) and magnetic resonance (MR) imaging have been proposed as alternative non-invasive diagnostic tools for the detection of stenosis. According to a meta-analysis study including 695 patients [10], the sensitivity of 64-section CT coronary angiography (CTCA) for detecting $> 50\%$ stenosis compared to X-ray angiography was 97% on a patient level, with a specificity of 90% and negative predictive

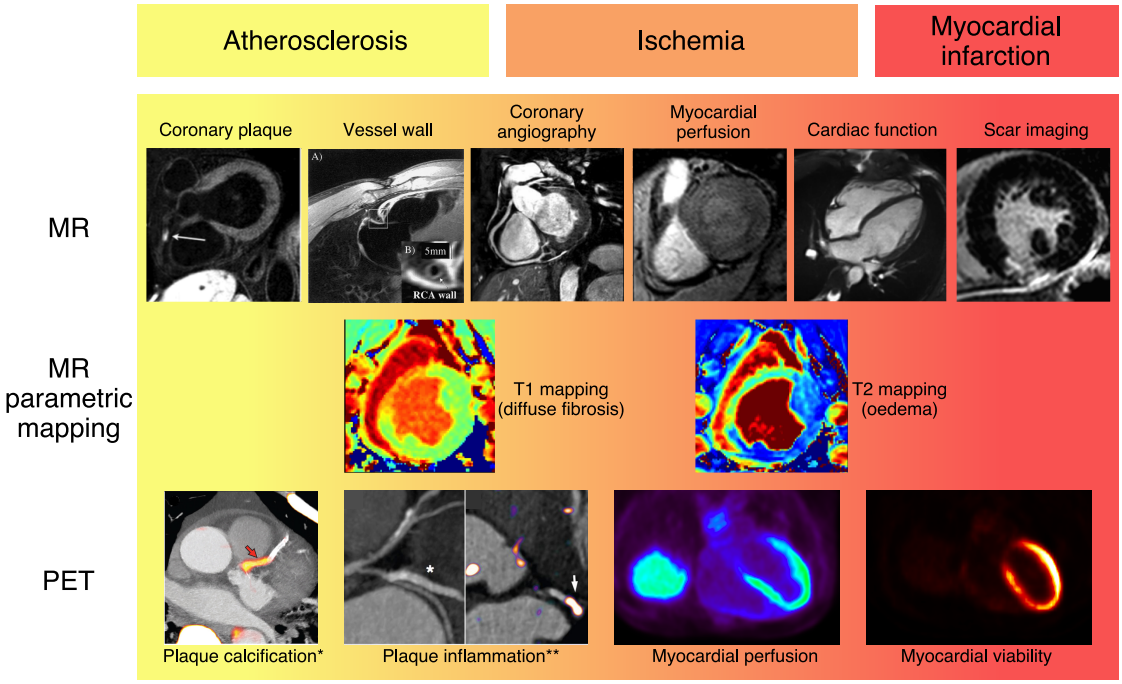

Figure 1.2: Role of PET and MR imaging in the diagnosis and monitoring of CAD progression. Plaque location and composition can be visualised by both PET and MR, while visualisation of the vessel wall integrity is a promising technique in MR. After the onset of ischaemia, both modalities offer great potential for assessing the extent of the hypoperfused areas in the myocardium, while MR allows for visualisation of the coronary lumen and evaluation of cardiac function. After myocardial infarction, MR can be used for scar imaging, while myocardial viability PET can be used for predicting potential functional recovery in the myocardium. Throughout the development of the disease, quantitative MR techniques such as T1 and T2 mapping allow for detection of diffuse fibrosis and oedema in the myocardium, respectively. *Adapted with permission from Joshi N.V. et al. *18F-fluoride positron emission tomography for identification of ruptured and high-risk coronary atherosclerotic plaques: a prospective clinical trial.* The Lancet 2014;383:705–13 [8]. **Adapted with permission from Tarkin J.M. et al. *Detection of Atherosclerotic Inflammation by ^{68}Ga-DOTATATE PET Compared to [^{18}F]FDG PET Imaging.* Journal of the American College of Cardiology 2017;69:1774–1791 [9].

value of 96%. Although CTCA has the advantage of being a non-invasive procedure, it results in an average radiation dose of 16 mSv (range of 5 to 32 mSv) to the patient [11]. On the contrary, MR is a radiation-free imaging modality, which also allows visualisation of the coronary arteries using a variety of techniques collectively referred to as coronary magnetic resonance angiography (CMRA). The reported sensitivity of CMRA compared to X-ray angiography in a meta-analysis study from 2004 including 607 patients was 88% with a specificity of 56% on a patient level [12]. New technical developments have significantly improved CMRA performance, particularly when performed in 3 T scanners, achieving a sensitivity of 93% and specificity of 83% compared to X-ray angiography according to a more recent study [13]. Furthermore, MR allows the performance of several tests that can be used for a comprehensive assessment of cardiovascular disease, including assessment of cardiac function and regional myocardial wall motion, presence and size of infarcted areas, myocardial oedema, and more recently, parametric tissue mapping techniques that enable a quantitative analysis of tissue changes throughout disease progression [14]. Nonetheless, several technical challenges remain open problems in cardiac MR imaging. In particular for coronary artery imaging, the small diameter and tortuous path of the vessels result in requirements of volumetric coverage and high spatial resolution that are challenging to attain within a reasonable scan time. Data acquisition in cardiac MR is in general slower than physiological motion, so mechanisms for compensating the effect of the motion are fundamental for obtaining good quality images. Furthermore, in order to obtain a good depiction of the vessels, robust techniques that allow suppression of the signal arising from tissues surrounding the coronary arteries are required.

CAD can be also diagnosed by assessing myocardial perfusion and viability: while the extent and severity of myocardial perfusion defects can be used for risk stratification of CAD patients [15], the presence of viable myocardium can be used to guide therapy decision making, as it has been shown to predict potential functional recovery in patients with chronic disease after revascularisation therapy [16]. Although several imaging modalities have been proposed for both perfusion and viability myocardial imaging, the most well-established methods are single-photon emission CT (SPECT) and positron emission tomography (PET) [14]. While con-

ventional SPECT is widely available and less expensive than PET, it has several technical disadvantages compared to the latter, including lower sensitivity, lower spatial resolution and less suitability for absolute quantification. The recent development of high-speed dedicated cardiac SPECT cameras, such as D-SPECT [17] or Discovery NM530c [18], has alleviated some of these pitfalls, offering a 5 to 10-fold increase in sensitivity and some gains in spatial resolution [19]. Such improvements have enabled a reduction in scan time, and therefore, decreased cost and improved patient comfort compared to conventional SPECT. However, absolute quantification remains a challenge due to the difficulty of performing accurate attenuation correction. Furthermore, sensitivity of 3D PET remains an order of magnitude higher than dedicated SPECT systems [20]. Therefore, PET has been established the reference modality for the assessment of myocardial perfusion [21], with a reported sensitivity and specificity of 93% and 92% respectively for the diagnosis of CAD, according to a meta study including 791 patients [22].

Despite being the reference modality, the accuracy of the quantitative assessment of myocardial perfusion and viability is limited by the low spatial resolution of cardiac PET images, compared to other imaging modalities such as MRI. Even though modern clinical PET scanners can achieve a spatial resolution of up to 4 mm full-width at half-maximum (FWHM), in practice this resolution can not be achieved in cardiac PET imaging due to the extensive motion of the heart during data acquisition. Both the cardiac- and respiratory- induced motion can degrade image quality, compromising the detectability of small myocardial lesions due to image blurring. Moreover, quantitative PET imaging requires a number of data corrections. One of the most relevant of such data corrections is the so-called attenuation correction, which accounts for the effect of varying tissue densities in the resultant measured data. In cardiac PET imaging, motion-induced mismatches between the emission data and the attenuation maps can lead to inaccurate PET images and potentially to erroneous diagnosis, such as the detection of false myocardial perfusion defects [23].

The recent development of hybrid PET-MR systems has opened new possibilities for a comprehensive non-invasive assessment of cardiovascular disease, by enabling the simultaneous acquisition of complementary anatomical and functional information in a single scan session [24]. In particular for CAD, PET-MR systems offer great

potential for simultaneous assessment of myocardial integrity (perfusion or viability) by PET and coronary lumen integrity by CMRA in a single examination. However, image degradation due to cardiac and respiratory motion during data acquisition in both modalities remains a major challenge.

Conventionally, the effect of cardiac and respiratory motion in both CMRA and PET imaging has been mitigated by using techniques that sort the acquired data into near motion-free frames representing different positions within the cardiac and respiratory cycles. External electrocardiogram (ECG) devices are widely used in clinical settings to synchronise the data acquisition with the cardiac cycle, so that data acquired over multiple cardiac cycles can be sorted into frames representing different cardiac phases (e.g. systole or diastole), typically using the R-wave as a reference. Similarly, the effect of respiratory motion can be reduced by aggregating data acquired at similar respiratory positions over multiple breathing cycles. Surrogate signals that are strongly correlated with the respiratory motion of the heart, such as the motion of the chest wall or the position of the diaphragm, can be used for sorting the data into respiratory phases (e.g. end-inspiration or end-expiration). These techniques, widely known as gating techniques, can be used to acquire data (or accept data for image reconstruction) only when both the respiratory and cardiac signals are within a predefined phase, typically end-expiration and mid-diastole respectively, rejecting all the other data being acquired. The main drawback of gating approaches is that long acquisition times are required in order to acquire enough data in this acceptance window, i.e. with enough signal-to-noise ratio (SNR) for PET and enough samples for a desired spatial resolution and coverage for MR.

Alternatively, the problem of cardiac and respiratory motion can be addressed by obtaining information about the motion from all the acquired data and then using it to produce motion-compensated images with improved image quality in a shorter acquisition time. Although several motion compensation approaches have been developed over the last decades separately for both PET and MR imaging, the introduction of hybrid PET-MR scanners has allowed the development of novel techniques to alleviate the problem of motion simultaneously for both modalities.

In the context of cardiac PET-MR imaging, most of the research efforts about motion compensation have focused on improving PET image quality by acquiring

MR images with high spatial resolution and superior soft-tissue contrast simultaneously with PET, so that motion information obtained from such MR images can be used to correct the PET data [25]. Although this approach has been shown to positively impact PET image quality and quantification, in general the simultaneously acquired MR data is being used only for motion estimation, limiting their use for diagnosis purposes.

Therefore, whereas clinical application of simultaneous cardiac PET-MR imaging for the diagnosis of CAD and other cardiovascular conditions would benefit from the complementarity between the functional and morphological diagnostic information provided by both modalities, in practice, state-of-the art approaches acquire diagnostic information from each modality sequentially, leading to long acquisition times and misaligned diagnostic PET and MR images.

In this thesis, a novel framework for truly simultaneous motion-compensated cardiac PET-MR imaging is proposed, enabling visualisation of the coronary arteries by CMRA and assessment of myocardial integrity by PET from a single examination. An efficient and robust acquisition and reconstruction methodology was developed so that the complex non-rigid deformation of the heart due to cardiac and respiratory motion is estimated from MR images and used to correct both the CMRA and PET datasets to the same position. This approach is highly efficient since nearly all acquired data is used for image reconstruction (100% scan efficiency), resulting in shorter scan time than conventional gated acquisitions. Additionally, this framework enables the acquisition of diagnostic MR and PET images simultaneously, significantly reducing the total exam time compared to techniques that perform diagnostic MR acquisitions after the PET acquisition, without sacrificing image quality.

The organisation of the rest of this document is described below. **Chapter 2** gives a brief description of the human heart, focusing on the coronary arteries and left ventricular anatomy and function. **Chapter 3** gives an overview of cardiac PET-MR imaging, describing the techniques traditionally used for acquisition of CMRA and cardiac PET as well as conventional image reconstruction and motion compensation techniques for each imaging modality. A brief discussion about state-of-the-art approaches for cardiac PET-MR imaging, including research developments for motion correction in PET-MR and clinical applications is also included.

Chapter 4 describes the proposed approach for respiratory motion-corrected CMRA-PET, including results from an initial validation of the motion correction framework in healthy subjects and a proof-of-concept study in oncology patients. A first clinical validation of this approach is described in **Chapter 5**, where the framework is used for the simultaneous visualisation of coronary integrity by CMRA and myocardial viability by ^{18}F-FDG PET in patients with documented chronic total occlusion of the coronary arteries.

Chapter 6 extends the framework presented in Chapter 4 to include cardiac motion compensation, based on a dual-phase CMRA acquisition. This framework allows visualisation of the coronary anatomy, estimation of left ventricular function and cardiac and respiratory motion-corrected PET to be obtained from a single examination. Results from a first study testing this approach in a small cohort of healthy subjects and cardiac patients are also presented and discussed here.

Chapter 7 adapts the respiratory motion-corrected approach presented in Chapter 4 for simultaneous water/fat CMRA imaging. The water/fat CMRA approach allows for an improved contrast between the coronary arteries and surrounding epicardial fat in the water CMRA image, and provides an additional image that contains useful diagnostic information about the distribution of cardiac fat. Furthermore, as it provides good-quality water/fat anatomical images throughout the respiratory cycle, this approach potentially allows for an improved attenuation correction of simultaneously acquired cardiac PET data. Preliminary results obtained from a validation study in a cohort of healthy subjects are discussed in this Chapter.

A brief discussion about the contributions and findings of this thesis are included in **Chapter 8**, which also presents some final remarks including areas of future work.

The work presented in this thesis resulted in several publications. An extended version of the discussion about motion correction for cardiac PET-MR (Chapter 3, Section 3.5) was published as a review paper in PET Clinics [26]. Some of the results presented in Chapters 4 and 6 have been published as peer-reviewed articles appearing in Magnetic Resonance in Medicine [27, 28], while the study in Chapter 5 has been published in EJNMMI [29]. Finally, the work presented in Chapter 7 has been accepted for publication in Magnetic Resonance in Medicine (in press).

Chapter 2:
The Human Heart

The heart is a muscular organ located in the thoracic cavity, whose main function is to pump blood through the arteries, veins and capillaries throughout the rest of the body, in order to carry oxygen and nutrients required for metabolic activity of the cells and assist in the removal of carbon dioxide and metabolic waste products. As any other muscular tissue, the heart muscle (or myocardium) requires a reliable and steady supply of oxygenated blood. This oxygen supply is delivered by the coronary arteries, which together with the coronary veins form the extensive and complex system of coronary circulation. As described in Chapter 1, when the coronary circulation is impaired or interrupted, the pumping function of the heart is compromised, with a sustained oxygen deprivation resulting in the death of myocardial cells.

This Chapter provides a brief description of cardiac anatomy and function, focusing on the coronary arteries and left ventricular function. Additionally, a brief characterisation of the physiological motion of the heart is included, and some standard techniques for the visualisation of cardiac structures of interest for this thesis are described.

2.1 Cardiac Anatomy and Function

The human heart consists of four chambers: two upper chambers, called atria, whose purpose is to receive blood and push it towards the two lower chambers, called ventricles, whose function is to pump blood out of the heart towards the lungs or the rest of the body. In the heart circulation, depicted in Figure 2.1a, the deoxygenated blood coming from the body is collected in the right atrium, and

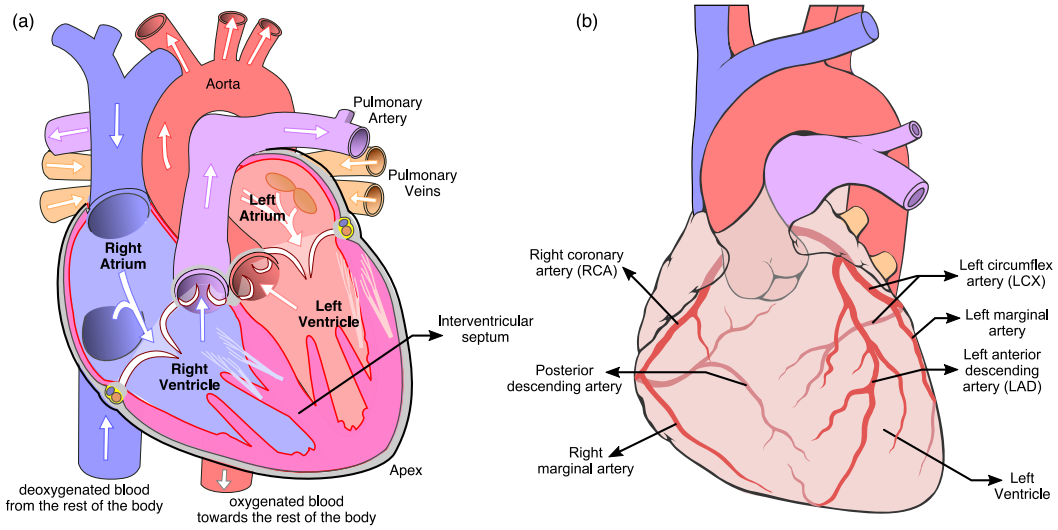

Figure 2.1: Anatomy of the heart. (a) Four chambers of the heart and major vessels in the heart circulation system. Adapted from [30]. (b) Coronary arteries and main branches. During most of their course, the coronary arteries are embedded in epicardial fat (not depicted in the figure). Adapted from [31].

pumped into the lungs by the right ventricle through the pulmonary arteries. Then, the oxygenated blood returns to the left atrium through the pulmonary veins, and it is pumped towards the rest of the body by the left ventricle via the aorta.

The coronary arteries are small vessels (typically around 3 to 5 mm diameter in the proximal segments and 1 to 2 mm in the distal section) that provide oxygenated blood to the myocardium and other cardiac structures. They arise from the base of the aorta and follow a tortuous path covering the heart, as depicted in Figure 2.1b, and are embedded in epicardial adipose tissue during most of their course. While the right coronary artery (RCA) distributes blood to the right atrium and portions of both ventricles, the left coronary artery distributes blood to the left atrium, left ventricle and the interventricular septum through its two main branches, the left anterior descending (LAD) and left circumflex (LCX) arteries. The coronary arteries give rise to several smaller branches that interconnect with each other in order to provide a reliable blood supply to the myocardium, even in cases of partial blockage of some of the branches.

In order to pump blood towards the rest of the body, the muscular cells of the myocardium contract 50 to 80 times per minute in a healthy adult in rest state, triggered by an electrical signal that travels from the atria down to the ventricles. The sequence of mechanical events regulated by the electrical activity of the myocardium

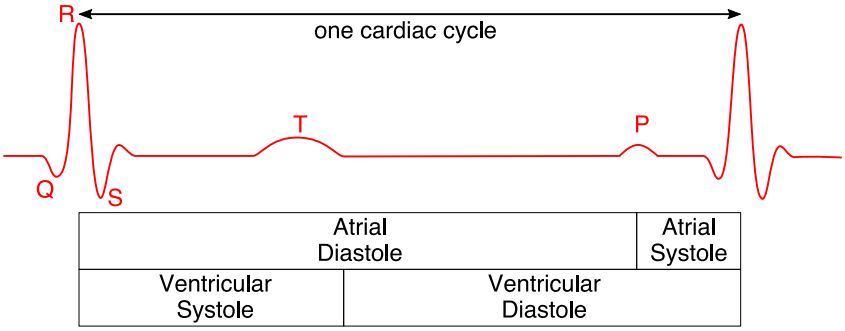

Figure 2.2: Schematic ECG signal during one cardiac cycle. The beginning of the ventricular systole is given by the R wave, while ventricular diastole is produced between the end of the T wave and beginning of the next QRS complex.

in one heartbeat is known as the cardiac cycle, and it comprises the contracting phase that pumps blood to the body, known as systole, and the relaxation and refilling of the ventricles, known as diastole. The electrical activity of the heart can be detected by placing electrodes on the chest to produce an electrocardiogram (ECG) as shown in Figure 2.2. The QRS complex represents the electrical depolarisation of the ventricles as the electrical impulse travels through the myocardium, which indicates the beginning of the systolic phase. The T wave represents the repolarisation of the ventricles, and marks the beginning of the diastolic phase of the cycle. The length of the cardiac cycle can be measured by detecting consecutive R waves, typically known as the RR interval.

The pumping efficiency and the volume of blood pumped by the ventricles are relevant clinical measures of how well the heart is meeting the demand of oxygenated blood from the rest of the body. One such functional measurement is the cardiac output, defined as the average volume of blood pumped by the heart per unit time. The cardiac output is typically computed by multiplying the heart rate (usually in beats per minute) and the stroke volume (SV), defined as the volume of blood pumped by each of the ventricles in one cardiac cycle. The SV can be obtained by subtracting the end systolic volume (ESV) from the end diastolic volume (EDV), obtained from ECG-synchronised images acquired with a variety of imaging modalities or by invasive procedures involving cardiac catheterisation. A conventional measurement of the pumping efficiency of the heart is the ejection fraction (EF), which represents the fraction of blood that is pumped by the ventricle in each con-

traction. The EF is computed by dividing the SV by the EDV, and it is usually expressed as a percentage. Equation 2.1 shows the formulas for computing these two functional indices. In a healthy adult, the SV ranges from 55 to 100 ml, while the EF ranges from 55 to 70%.

$$\mathrm{SV} = \mathrm{EDV} - \mathrm{ESV} \tag{2.1a}$$

$$\mathrm{EF} = \frac{\mathrm{EDV} - \mathrm{ESV}}{\mathrm{EDV}} \times 100\% \tag{2.1b}$$

2.2 Physiological Motion of Cardiac Structures

The heart is continually moving due to the cardiac and respiratory cycles. In MR and PET imaging, such motion can induce blurring and artefacts in the images, compromising their diagnostic quality. This section describes the main characteristics of the cardiac and respiratory-induced motion of the heart, focusing on the coronary arteries and the left ventricle.

2.2.1 Cardiac-Induced Motion

The heart moves periodically due to the contraction and relaxation of the atria and ventricles. The frequency of such motion is given by the heart rate, which ranges from 50 to 80 beats per minute in healthy adults, but can vary significantly more in patients with cardiovascular disease. While the duration of the ventricular systolic phase is approximately constant (around 400 ms) among a wide range of heart rates, the length of ventricular diastole varies greatly, with a typical duration between 200 and 800 ms.

In order to estimate more accurately the duration of each of these cardiac phases for a given heart rate, linear models have been proposed for adult healthy subjects and patients with congestive heart failure [32, 33], with linear coefficients shown in Table 2.1. However, the applicability of such models is limited in younger and elderly patients, or patients with other cardiovascular conditions [34, 35].

Throughout the cardiac cycle, there is not an exact correspondence between the

	a (ms)	b (ms·bpm^{-1})	Reference
Male	541	2.2	[33]
	546	2.1	[32]
Female	540	2.0	[33]
	549	2.0	[32]

Table 2.1: Linear coefficients proposed in the literature for defining the length of ventricular systole as a function of the heart rate, so that systole $= a - b \times$ heart rate.

motion of the left ventricle and the motion of the coronary arteries. Although there are periods of minimal motion in both systolic and diastolic cardiac phases for both the left ventricle and each of the coronary arteries, the duration of such periods varies greatly between structures.

The movement of the left ventricle between diastole and systole is the product of three components: 1) inwards radial contraction, 2) longitudinal shortening and 3) twisting of the apex in relation to the base [36]. According to a review study using MR imaging for estimating the amplitude of each component of the motion in the left ventricle myocardium [37], the radial contraction ranges from 4.4 ± 1.0 mm in the apex of the left ventricle to 5.4 ± 1.0 mm in the base, while the length of the base-to-apex longitudinal contraction is 11.2 ± 2.2 mm, with most of the motion resulting from the base of the ventricle and the apex remaining nearly stationary. Finally, the twisting movement consists of a basal clockwise rotation of $4.4 \pm 0.4°$ and an apical counter-clockwise rotation of $10.0 \pm 2.3°$.

Different imaging techniques have been used to measure the cardiac-induced motion of the coronary arteries both in free breathing and breath-holding conditions. In [38], a study on 25 healthy subjects where MR images were acquired under free breathing conditions showed that there are two periods of minimal motion of the coronary arteries: a first one of ∼50 ms duration at end-systole, and a longer one around mid-diastole. This study also showed that the mid-diastolic quiescent period for the RCA is shorter and starts later than for the LAD artery, as summarised in Table 2.2. This is consistent with the findings presented in [39], where CT images were used to measure the motion of the RCA, LAD and LCX arteries in a cohort of 70 patients. In this study, it was shown that in patients with heart rates below 80 beats per minute, the coronary arteries have two motion-free periods, the first of them corresponding to end-systole (40%–50% of the RR interval), and the second

	RCA	LAD
Onset	$69 \pm 11\%$	$66 \pm 10\%$
Duration	$17 \pm 9\%$	$25 \pm 10\%$

Table 2.2: Onset and duration of the mid-diastolic quiescent period for the RCA and LAD as a percentage of the RR interval. Data from [38].

	RL	AP	SI
LAD	6.8 ± 1.7 mm	7.9 ± 1.5 mm	6.8 ± 1.9 mm
LCX	9.3 ± 2.1 mm	12.7 ± 2.3 mm	10.5 ± 1.3 mm
RCA	9.0 ± 1.7 mm	10.6 ± 1.7 mm	11.3 ± 2.8 mm

Table 2.3: Maximum displacements of the RCA, LAD and LCX arteries during the cardiac cycle in the right-left (RL), anterior-posterior (AP) and superior-inferior (SI) directions. Data from [40].

one in mid-diastole (60%–80% of the RR interval). In patients with higher heart rates, only the end-systolic rest period was observed.

The maximum displacement of each coronary artery during the cardiac cycle was measured in [40] for a cohort of 8 healthy subjects using MR images acquired under breath-hold conditions. Table 2.3 summarises the findings of this study, where it can be observed that the amplitude of the motion of the RCA and LCX is larger than the LAD in all directions.

2.2.2 Respiratory-Induced Motion

Breathing also induces motion of the heart, due to movement of both the diaphragm and the chest wall. From these two sources, a dominant superior-inferior (SI) translation of the heart is produced, ranging from 10.5 ± 4.8 mm for the root of the RCA (i.e. the point where the RCA arises from the aorta) to 18.1 ± 9.1 mm for the inferior margin of the heart for an average diaphragm motion of 19.7 ± 11.9 mm, according to a well-known study in healthy subjects [41]. This study used MR images acquired under breath-hold conditions at seven different respiratory positions throughout the breathing cycle.

In addition, this study found a linear relationship between the movement of the different cardiac structures and the motion of the diaphragm. In particular, a factor of 0.6 was found to correlate the SI displacement of the diaphragm and the

displacement of the root of the RCA and LAD. It is worth noting that in [41], the amplitude of SI motion was found to differ across the heart, with superior regions of the heart experiencing about 40% less SI displacement compared to inferior regions. Therefore, the height of the heart is reduced during the respiratory cycle as the diaphragm moves upwards.

Furthermore, additional studies have shown that during free breathing there are hysteretic loops in some subjects, so the relation between the motion of the heart and the motion of the diaphragm follows different paths for expiration and inspiration [42]. Thus, a given diaphragm position might correspond to different heart positions for these different phases of the respiratory cycle. The extent of the hysteresis effect is strongly subject dependant, as shown in Figure 2.3 for four representative healthy subjects.

Displacements in the SI direction are not the only component of the respiratory-induced motion of the cardiac structures. Smaller displacements have been observed in the anterior-posterior (AP) and right-left (RL) directions, with 4.3 ± 3.7 mm and 2.0 ± 2.1 mm displacement on average, respectively, using MR images acquired in a cohort of 8 healthy subjects and 10 patients with cardiovascular disease [43]. Furthermore, in agreement with [41], several studies have shown that the motion of the heart due to the breathing cycle, and in particular that of the coronary arteries, is not purely translational but a complex deformation. This motion has been modelled as an affine transformation, and more generally, as a non-rigid deformation [43–45].

It is worth noting that due to time restrictions in MR image acquisition, some of these early studies measured the motion using images acquired during breath-holds at different respiratory positions. Studies using other imaging modalities, such as X-ray angiography, have shown much smaller average displacements of the coronary arteries during normal tidal breathing, with average translation in the SI, AP and RL directions of 4.9 ± 1.9 mm, 1.3 ± 1.8 mm and 0.4 ± 2.0 mm, respectively, in a cohort of 10 patients with cardiovascular disease [46].

Compared to cardiac-induced motion, the respiratory-induced motion of the heart has more inter-subject variability. A healthy adult in rest state breathes at a rate of 12–20 times per minute, with an inspiration length ranging 1–2 seconds, and a slightly longer expiration period of 2–3 seconds. There are quiescent periods

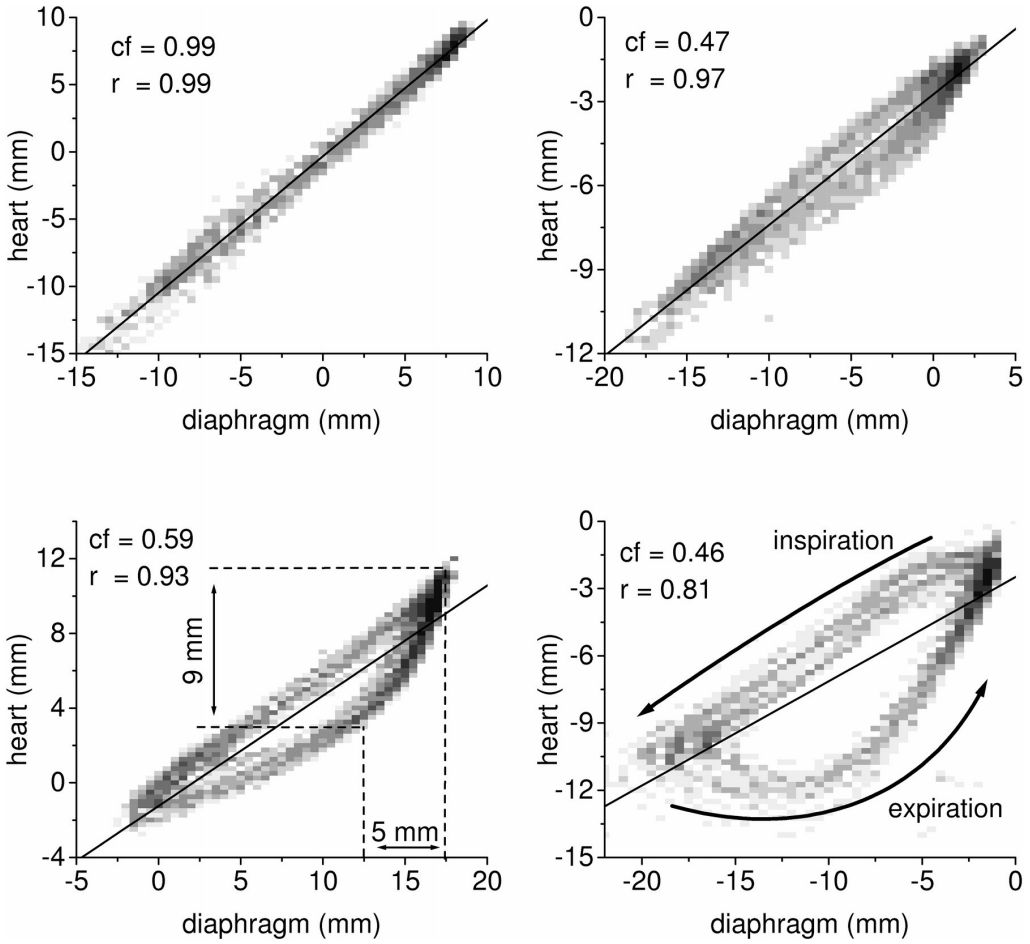

Figure 2.3: Histograms of SI respiratory-induced motion of the heart versus that of the diaphragm in four healthy subjects. Darker squares indicate a higher occurrence of the measurement; and straight lines correspond to linear fits to the data (cf = correction factor, r = correlation coefficient). Reprinted with permission from Nehrke K., et al. *Free-breathing cardiac MR imaging: Study of implications of respiratory motion—Initial results.* Radiology 2001;220:810-815 [42].

within each of these respiratory phases. According to a study in healthy subjects, the quiescent phase at end-expiration was observed to have a length of 1.1 ± 1.6 seconds, while a shorter quiescent period at end-inspiration of 0.4 ± 0.2 seconds was observed, with an average respiratory period of 4.3 ± 1.1 seconds [47].

2.3 Visualising Cardiac Structures

As described in Chapter 1, different non-invasive imaging modalities have been used for visualisation of the integrity of the coronary arteries and the left ventricle myocardium. Due to the extensive differences in the cardiac anatomy and orientation between subjects, but also due to the intrinsic characteristics of each imaging tech-

nique, the resulting images greatly differ from each other. In order to prevent such variability from hindering intra- and inter-modality comparisons, several approaches have been introduced for standardising the visualisation of the coronary arteries and the left ventricle myocardium. Conventional approaches for depicting both cardiac structures are briefly described in this section.

2.3.1 Visualising the Coronary Arteries

The coronary arteries follow a tortuous path, as depicted in Figure 2.1b. Although multi-planar reformatting (MPR) and maximum intensity projections (MIPs) techniques have been used for improving visualisation and quantitative analysis of the coronary arteries [48], these techniques assume that the vessel of interest is contained in a thick plane. Therefore, these approaches only allow for the visualisation of a segment of an individual vessel in one image. Furthermore, they do not allow for a direct comparison of image quality between different imaging techniques.

Alternatively, approaches that use curved reformatting of the coronary arteries have been proposed in the literature, which enable the simultaneous visualisation of two or three vessels, covering from the proximal to the distal segments. In particular, for MR angiography, a widely used tool for visualisation of the coronary arteries and objective image quality assessment is the 'Soap Bubble' software [49]. This software is extensively used throughout this thesis, so its main features are described here.

The 'Soap Bubble' approach assumes that the coronary tree is contained in a smooth surface resembling a bubble, as shown in Figure 2.4. Once this smooth surface is defined, a 2D image that depicts the whole coronary anatomy can be created by projecting this smooth surface onto a plane.

Initially, the user manually selects a collection of points P_i in each of the vessels of interest (depicted in red in Figure 2.4), that define a convex surface D'. Then, the software creates a parallel projection in a direction normal to the surface at each selected point. In this way, more than one vessel can be visualised in a single image as shown in Figure 2.5a. It is worth noting that in this planar image, the distance between voxels is not constant. Therefore, metrics such as vessel length, sharpness or diameter are performed directly in the 3D volume, using the points selected by the user. Figure 2.5b shows an example of the points selected by the user for a

representative coronary MR angiography, indicated by yellow crosses. The software includes tools for measuring the length of each vessel (Figure 2.5c) and the average vessel sharpness, calculated from an edge image (Figure 2.5d) obtained by applying the first-order derivative to the input image.

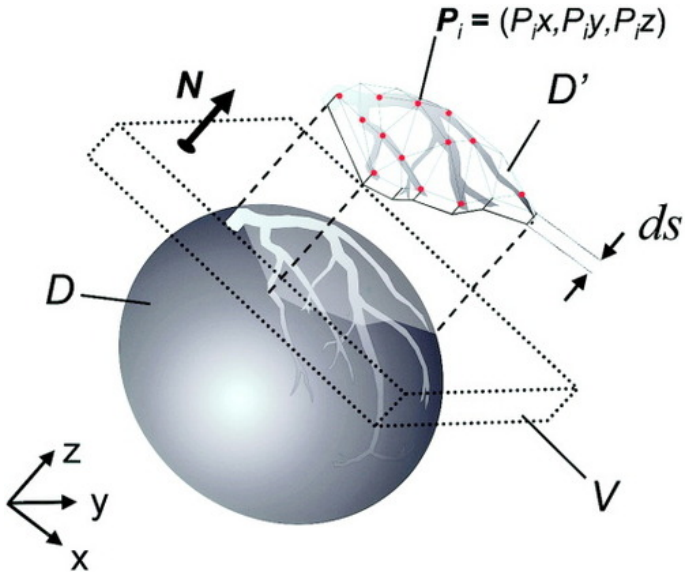

Figure 2.4: Curved reformatting using the 'Soap Bubble' software tool. The MR angiography image is acquired in a Cartesian grid (x, y, z) within a volume V. The user selects a series of points P_i that can be used to define a smooth surface D'. By creating a MIP parallel to this surface, a planar coronary reformatting can be obtained. Reprinted with permission from Etienne A., et al. *"Soap-Bubble" visualization and quantitative analysis of 3D coronary magnetic resonance angiograms.* Magnetic Resonance in Medicine 2002;48:658–66 [49].

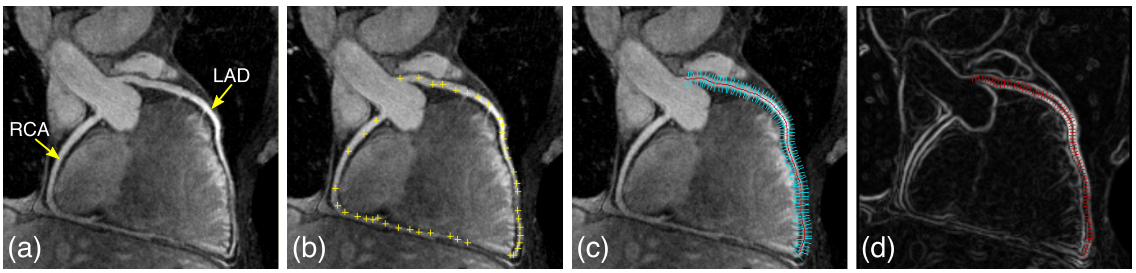

Figure 2.5: Planar reformatting example from 'Soap Bubble'. (a) The curved reformatting enables the visualisation of both the right (RCA) and left (LAD) coronary arteries. (b) User-selected points (yellow crosses) produce the reformatted image. (c) Measurement of the length of the vessel (LAD) by tracking the central line (in red). (d) Vessel sharpness is measured in a collection of profiles (in red) perpendicular to the central line of the vessel.

2.3.2 Visualising the Left Ventricle

The American Heart Association (AHA) proposed a standardized segmentation and nomenclature for left ventricular myocardial imaging that has been widely adopted in the clinical practice [50]. In this approach, three orthogonal planes oriented with respect to landmarks in the heart are defined. These planes are called 1) vertical long axis, a two-chamber view that depicts the left ventricle and atria; 2) horizontal long axis, a four-chamber view of the heart and 3) short axis slices, where the right and left ventricle are visualised from the base to the apex. Figure 2.6 shows a schematic with such planes, which can be observed for a real cardiac MR scan in Figure 2.7.

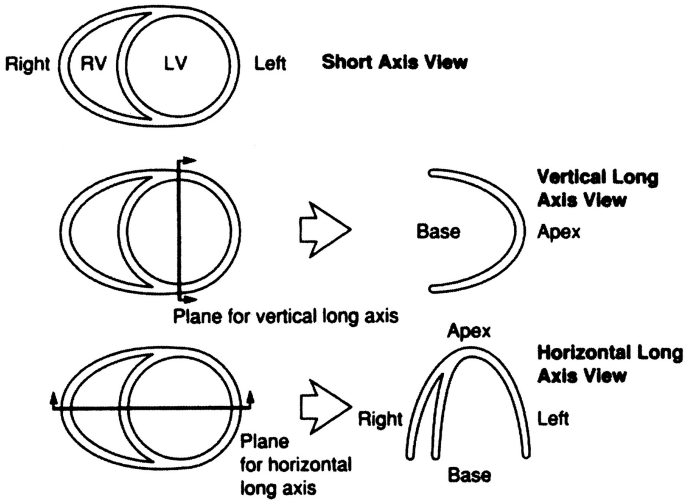

Figure 2.6: Definition of orthogonal cardiac planes for 3D imaging modalities. RV: right ventricle, LV: left ventricle. Reprinted with permission from Cerqueira M.D., et al. *Standardized Myocardial Segmentation and Nomenclature for Tomographic Imaging of the Heart.* Circulation 2002;105:539–542. [50]

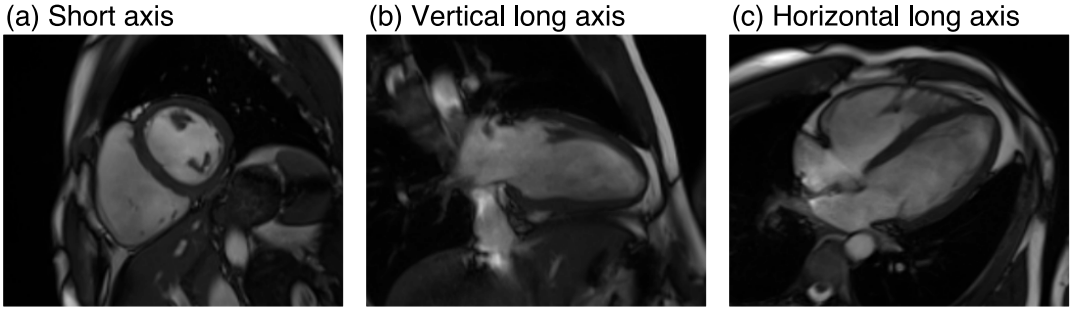

Figure 2.7: Example orthogonal cardiac planes for 3D MR imaging, showing (a) a short axis slice, (b) vertical long axis and (c) horizontal long axis view.

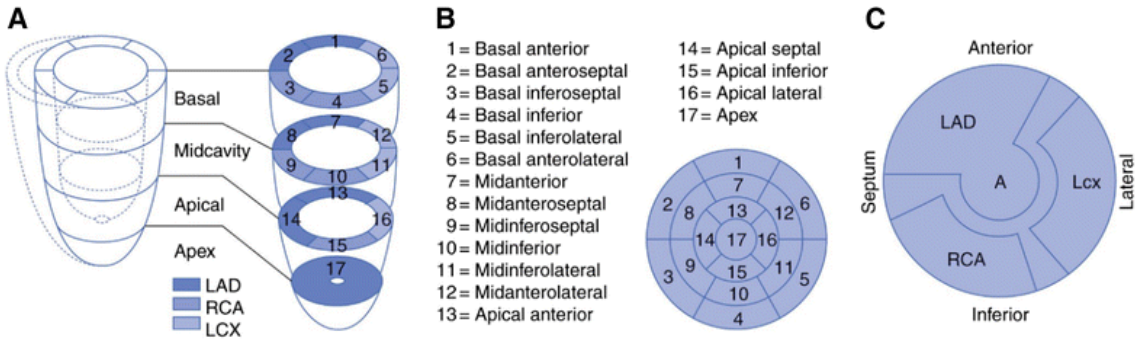

Figure 2.8: Left ventricular myocardial segmentation according to the AHA 17-segment model. (a) The model divides the left ventricle into three short-axis slices: apical, mid-cavity, and basal. The basal and mid-cavity slices are divided into 6 segments, while the apical slice is divided into 4 segments. The apex is added as an additional segment, usually obtained from the vertical long-axis view. (b) Conventional naming for the 17 segments. For perfusion or viability imaging, the segments can be rearranged in polar plots, where the value in each segment is related to the integrity of the myocardium in that specific section. (c) Each segment can be assigned to one or more coronary arteries; however, anatomical variations in the blood supply in different subjects need to be taken into account. Reprinted with permission from Dilsizian V., et al. *ASNC imaging guidelines/SNMMI procedure standard for positron emission tomography (PET) nuclear cardiology procedures.* Journal of Nuclear Cardiology 2016;23:1187–1226 [51].

The short axis view is one of the most widely used planes for acquiring and displaying MR and PET images of the left ventricle myocardium, as it enables the visualisation of the integrity of the myocardial wall and the extent of perfusion or viability defects in both the radial and circumferential directions. The short axis view was therefore proposed as a reference for segmenting the left ventricle myocardium, in the so-called 17-segment AHA model, depicted in Figure 2.8.

This model uses three thick short-axis slices, located at the basal, mid-cavity and apical levels, to represent most of the left ventricle. The basal and mid-cavity slices are divided in 6 segments each, while the apical slice is divided in four segments, as depicted in Figure 2.8a. In order to assess the integrity of the apex, an additional segment is obtained from the vertical long axis view. Although in general each of the segments can be assigned to a particular coronary artery (Figure 2.8c), the guidelines recommend a case-to-case evaluation, as anatomical variations in some subjects do not match the standard scheme [50].

Chapter 3:
Cardiac PET-MR Imaging:
An Overview

This chapter provides an overview of the techniques used for coronary MR angiography (CMRA) and myocardial integrity imaging with PET. The physics of MR and PET imaging are briefly summarised, including details about the data acquisition protocols in both modalities. Standard approaches for motion compensated MR and PET image reconstruction are then described. Finally, techniques that have been recently proposed for MR-based motion compensation and novel clinical applications for cardiac PET-MR imaging are described and discussed.

3.1 Cardiac MR Acquisition

MR is a non-invasive medical imaging modality that uses the nuclear magnetic resonance (NMR) effect to obtain information about the intrinsic physical and chemical properties of an object. According to the NMR effect, when placed in an external static magnetic field, nuclei with a nonzero spin can be excited by applying a radiofrequency (RF) pulse, inducing the emission of a subsequent detectable RF signal after a short period of time. By using spatially variant gradient magnetic fields, this signal can be localised in space, allowing for production of a multi-dimensional image that reflects intrinsic characteristic of the object being scanned, such as nuclear spin density, spin relaxation times, magnetic susceptibility, molecular diffusion and perfusion, and chemical shift. By varying parameters such as the amplitude, shape and timings of the RF pulses and gradients, different contrast between tissues can be

obtained, making MRI a versatile modality that can produce anatomical and functional images with high spatial resolution. This section describes the basic principles of MR data acquisition following the approach proposed by Liang and Lauterbur in [52], and then focuses on pulse sequences for CMRA, including mechanisms used for enhancing tissue contrast and conventional motion compensation approaches.

3.1.1 Fundamentals of MR Imaging

Consider a population of nuclei with an odd number of protons or neutrons. Such nuclei possess an intrinsic angular moment $\vec{J}$, typically called spin, which can be considered analogous to a physical rotation about its axis. The charged and rotating nuclei give rise to an intrinsic magnetic moment $\vec{\mu} = \gamma\vec{J}$, where γ is a nucleus-dependant constant known as the gyromagnetic ratio. According to quantum mechanics, the magnitude of this magnetic moment is given by

$$|\vec{\mu}| = \gamma\hbar\sqrt{I(I+1)} \tag{3.1}$$

where I is the nuclear spin quantum number and $\hbar$ is the reduced Planck constant. Under normal conditions, the direction of $\vec{\mu}$ is random due to thermal motion, resulting in a non-measurable magnetic field, i.e. a zero net magnetic field as illustrated in Figure 3.1a. However, when placed in a magnetic field $\vec{B}_0 = B_0\hat{e}_z$ (where $\hat{e}_x, \hat{e}_y, \hat{e}_z$ correspond to the unitary vectors for a Cartesian coordinate system), each spin will take one of a finite number of orientations in the direction of the magnetic field, so that the z-component of $\vec{\mu}$ becomes quantised into $2I$ levels, according to

$$\mu_z = \hbar\gamma m_I \tag{3.2}$$

where $m_I = -I, -I+1 ... I-1, I$ is the magnetic quantum number. Thus for $I = 1/2$ spin nuclei, such as hydrogen (^{1}H), only two orientations are possible, giving rise to two spin populations, usually called parallel and antiparallel spins (Figure 3.1b). These two populations contain on average a different number of spins, resulting in a net bulk magnetisation in the spin system, which can be derived as described hereafter.

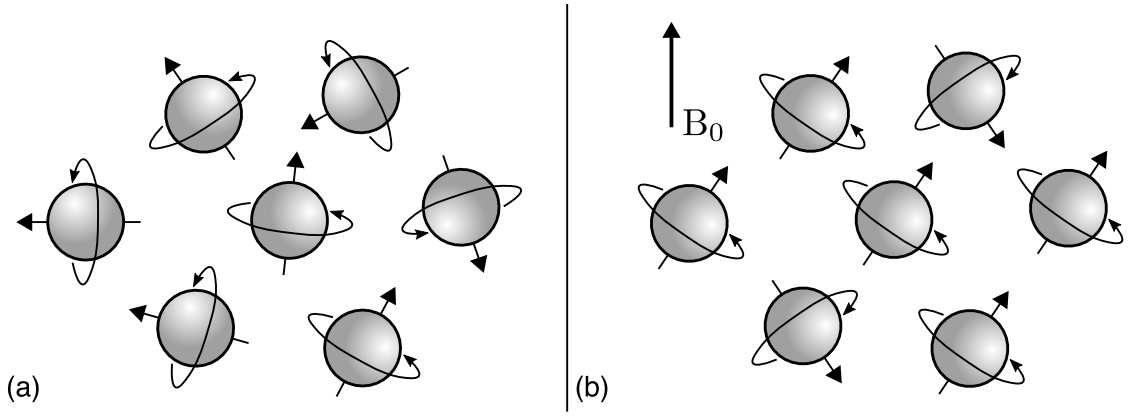

Figure 3.1: Schematic of a $I = 1/2$ spin system. (a) In absence of an external magnetic field, the spins are randomly oriented. (b) In presence of an external magnetic field $\vec{B}_0$, spins will align parallel or antiparallel to the magnetic field.

The ratio between the number of spins in each population depends on the difference between their energy levels and the temperature of the nuclei system, T, and is given by the Boltzmann distribution as follows

$$\frac{N_\uparrow}{N_\downarrow} = \exp\left(\frac{\Delta E}{kT}\right) \tag{3.3}$$

where $N_\uparrow$ and $N_\downarrow$ represent the population of parallel and antiparallel spins, respectively, ΔE is the difference between energy levels and k is the Boltzmann constant. Using that the energy level of each spin is given by

$$E = -\vec{\mu} \cdot \vec{B}_0 \tag{3.4}$$

it follows that $\Delta E = \gamma \hbar B_0$. Thus, the difference between both populations can be approximated as

$$N_\uparrow - N_\downarrow \approx \frac{\gamma \hbar B_0}{2kT} N_S \tag{3.5}$$

where N_S is the total number of spins in the system. For a conventional MR system of $B_0 = 3\,\mathrm{T}$ operating at room temperature, the difference between both populations is approximately 3 ppm.

So far, the z-component of the magnetic moment has been described, but the other two components (x- and y-) have not yet been discussed. Following a classical mechanical approach, when placed in an external magnetic field, magnetic moments

experience a torque equal to the rate of change of their angular moment, therefore

$$\frac{d\vec{\mu}}{dt} = \gamma\vec{\mu} \times B_0\hat{e}_z \tag{3.6}$$

Solving this equation, it can be obtained that

$$\mu_{xy} = \mu_{xy}(0)e^{i\gamma B_0 t} \tag{3.7a}$$

$$\mu_z = \mu_z(0) \tag{3.7b}$$

where $\mu_{xy} = \mu_x + i\mu_y$ represents the transverse component of the magnetic moment in complex notation (corresponding to the transverse magnetic moment vector $\vec{\mu}_{xy} = \mu_x\hat{e}_x + \mu_y\hat{e}_y$) and $\mu_{xy}(0)$ and $\mu_z(0)$ correspond to the initial value of the transverse and longitudinal components of the magnetic moment, respectively. An important implication of this result is that when placed in a static magnetic field, spins will precess about the direction of the magnetic field with an angular frequency $\omega_0 = \gamma B_0$, also known as the Larmor frequency. Moreover, given that spins are initially randomly oriented, the direction of the transverse component of the magnetic moment remains random for each of the spins.

The net bulk magnetisation, $\vec{M}$, can then be obtained by aggregating the magnetic moment of every spin in the system

$$\begin{aligned}\vec{M} &= \sum_{n=1}^{N_S} \vec{\mu}_n \\ &= \sum_{n=1}^{N_S} \mu_{x,n}\hat{e}_x + \sum_{n=1}^{N_S} \mu_{y,n}\hat{e}_y + \sum_{n=1}^{N_S} \mu_{z,n}\hat{e}_z\end{aligned} \tag{3.8}$$

where $\mu_{x,n}$, $\mu_{y,n}$ and $\mu_{z,n}$ are the components in the x-, y- and z-axes respectively of the magnetic moment $\vec{\mu}_n$ corresponding to the nth spin of the system. According to Equation 3.2, $\mu_{z,n} = \pm\frac{1}{2}\gamma\hbar$, depending on whether the spin belongs to the parallel or antiparallel population. Furthermore, given that the orientation of the transverse magnetisation of the magnetic moment remains random,

$\sum_{n=1}^{N_S} \mu_{x,n}\hat{e}_x = \sum_{n=1}^{N_S} \mu_{y,n}\hat{e}_y = 0$. Thus, $\vec{M}$ can be written as

$$\begin{aligned} \vec{M} &= \sum_{n=1}^{N_S} \mu_{z,n}\hat{e}_z \\ &\approx \frac{(\gamma\hbar)^2}{4kT} N_S B_0 \hat{e}_z = M_0 \hat{e}_z \end{aligned} \tag{3.9}$$

The bulk magnetisation is therefore parallel to the external static magnetic field, and its magnitude depends on intrinsic properties of the nuclei system, such as γ and N_S, which makes ^{1}H very attractive as a target for MR, due to its strong gyromagnetic ratio and high natural abundance.

In order to measure this bulk magnetisation, a second magnetic field $\vec{B}_1$ needs to be applied, typically perpendicular to the static magnetic field. Using the same principle of Equation 3.6, the equation of torque for the bulk magnetisation can be written as

$$\frac{d\vec{M}}{dt} = \gamma\vec{M} \times \left(B_0\hat{e}_z + \vec{B}_1\right) \tag{3.10}$$

Consider now a radiofrequency field $\vec{B}_1$, known as the RF excitation field, rotating at the Larmor frequency

$$\vec{B}_1 = B_1(t)\left(\cos(\omega_0 t)\hat{e}_x - \sin(\omega_0 t)\hat{e}_y\right) \tag{3.11}$$

When $\vec{B}_1$ is applied during a short period of time T_p, and given that the initial magnetisation is $\vec{M}_{(t=0)} = M_0\hat{e}_z$, Equation 3.10 can be solved so that the magnetisation of the system is given by

$$\vec{M} = M_0 \sin(\alpha)\sin(\omega_0 t)\hat{e}_x + M_0 \sin(\alpha)\cos(\omega_0 t)\hat{e}_y + M_0\cos(\alpha)\hat{e}_z \tag{3.12}$$

where α is the flip angle, given by

$$\alpha = \gamma \int_0^{T_p} B_1(t)dt \tag{3.13}$$

As can be observed in Equation 3.12, applying a RF magnetic field tips the longitudinal magnetisation toward the transverse plane, and induces an oscillating magnetisation (Figure 3.2a) that can then be detected by means of electromagnetic induction as will be described shortly. The strength of the detected signal depends,

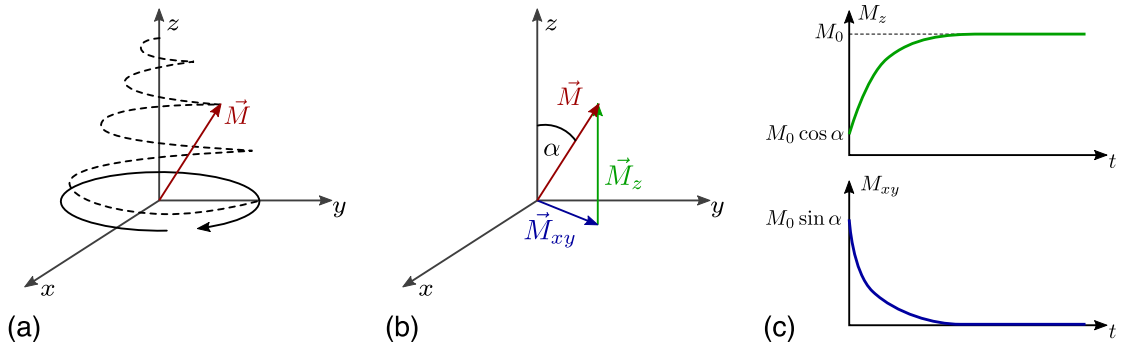

Figure 3.2: Magnetisation evolution when an RF magnetic field pulse is applied. (a-b) The RF field tips the magnetisation towards the transverse plane in an angle α that depends on the shape and duration of the RF pulse. (c) After the RF pulse is switched off the magnetisation returns to the equilibrium, in a process known as relaxation. The longitudinal magnetisation M_z recovers while the transverse magnetisation M_{xy} decays.

among others, on the flip angle used. In particular, for $\alpha = 90°$, the bulk magnetisation is fully tipped to the transverse plane; so that a maximum induced signal is achieved.

After switching off $\vec{B}_1$, the magnetised spin system will return to the initial equilibrium state over time, so that the longitudinal magnetisation recovers while the induced transverse magnetisation disappears. This process is known as relaxation and can be phenomenologically described by the Bloch equation

$$\frac{d\vec{M}}{dt} = \gamma\vec{M} \times \vec{B} - \frac{M_x\hat{e}_x + M_y\hat{e}_y}{T_2} - \frac{(M_z - M_0)\hat{e}_z}{T_1} \tag{3.14}$$

where M_x, M_y and M_z are the components in the x-, y- and z-axes respectively of the magnetisation $\vec{M}$, $\vec{B}$ is the magnetic field being applied, corresponding in this case to $\vec{B}_0$, and T_1 and T_2 correspond to intrinsic properties of the nuclei system that depend on the interactions between the spins and their microenvironment. More precisely, T_1 is the spin-lattice relaxation time, also known as longitudinal relaxation, which reflects the energy exchange between the spins and the static magnetic field. As such, T_1 depends on the value of B_0, with values in the range of 100 to 2000 ms for biological tissues of interest for conventional magnetic field strengths ($B_0 = 1.5$ or 3.0 T). T_2 is the spin-spin relaxation time, also known as transverse relaxation, that reflects the energy exchange of spins with each other. Thus, T_2 times are insensitive

to changes in B_0, with typical values for tissues in the range of 50 to 500 ms.

Solving Equation 3.14, it is possible to obtain that

$$M_{xy}(t) = M_0 \sin(\alpha)\exp(-i\omega_0 t)\exp\left(\frac{-t}{T_2}\right) \tag{3.15a}$$

$$M_z(t) = M_0 \cos(\alpha)\exp\left(\frac{-t}{T_1}\right) + \left(1 - \exp\left(\frac{-t}{T_1}\right)\right) M_0 \tag{3.15b}$$

where $M_{xy}(t) = M_x + iM_y$ corresponds to the transverse magnetisation in complex notation. From Equation 3.15, it can be observed that the longitudinal and transverse relaxations occur at different rates (Figure 3.2c), and that the transverse magnetisation decays rotating around the z-axis.

According to Faraday's law, the voltage $S(t)$ induced by the rotating magnetisation $M_{xy}(t)$ in a nearby receiver coil is equal to the rate of change of the flux through the coil, which in turn is proportional to the rate of change of the magnetisation, so that, assuming that $\omega_0 \gg \frac{1}{T_2}$

$$S(t) \propto \omega_0 \int_v M_0(\vec{r}) \sin(\alpha)\exp(-i\omega_0 t)\exp\left(\frac{-t}{T_2}\right) d\vec{r} \tag{3.16}$$

where v is the volume of magnetisation and $M_0(\vec{r})$ is the equilibrium magnetisation at location $\vec{r}$. Since both ω_0 and $M_0(\vec{r})$ depend linearly on the strength of the static magnetic field B_0, $S(t) \propto B_0^2$, making high magnetic fields attractive for enhancing signal-to-noise ratio (SNR) in MR imaging.

It is worth noting that in Equation 3.16, the integral encompasses the entire volume of magnetisation, so even though the whole magnetisation of the system can now be measured, it is not possible to know its spatial distribution. In order to measure $M_0(\vec{r})$, additional magnetic fields that encode spatial information need to be applied. These fields, commonly known as gradient fields, are parallel to the main magnetic field, but their amplitude changes in space so that they can be written as $(\vec{G}(t) \cdot \vec{r})\hat{e}_z$. Solving Equation 3.14 for a total magnetic field given by $\vec{B} = B_0\hat{e}_z + (\vec{G}(t) \cdot \vec{r})\hat{e}_z$ results in

$$M_{xy}(t) = M_0 \sin(\alpha)\exp\left(\frac{-t}{T_2}\right)\exp\left(-i\vec{r} \cdot \int_0^t \gamma\vec{G}(\tau)d\tau\right) \tag{3.17a}$$

$$M_z(t) = M_0 \cos(\alpha) \exp\left(\frac{-t}{T_1}\right) + \left(1 - \exp\left(\frac{-t}{T_1}\right)\right) M_0 \tag{3.17b}$$

Defining

$$\vec{k}(t) = \frac{\gamma}{2\pi} \int_0^t \vec{G}(\tau) d\tau \tag{3.18}$$

then the induced voltage that can be observed in the receiver coil corresponds to

$$S(\vec{k}(t)) \propto \int_v M_0(\vec{r}) \exp(-i2\pi \vec{k}(t) \cdot \vec{r}) \exp\left(\frac{-t}{T_2}\right) d\vec{r} \tag{3.19}$$

Neglecting the effect of T_2 (by assuming that the acquisition time is in general much shorter than T_2), it can be observed from Equation 3.19 that the relation between the applied gradient fields, the spatial distribution of the magnetisation and the induced signal can be mathematically described by the Fourier transform. Therefore, the MR sampling space, widely known as k-space, contains the Fourier transform of the object that is to be observed, and the problem of estimating $M_0(\vec{r})$ can be solved by collecting an appropriate number of samples of the signal $S(\vec{k})$ and then using an appropriate mathematical mechanism for transforming the acquired k-space data into the image domain. These mechanisms, referred to as MR image reconstruction techniques, will be described in detail in Section 3.3.

As shown in Equation 3.19, the induced signal has to be localised in space in order to produce an MR image, and three gradient fields are typically applied for this purpose. When acquiring transversal two-dimensional images, the first of such gradient fields, known as slice selection gradient, consists of a linear gradient along the z-axis that is applied simultaneously during the RF excitation. The combination of the slice selection gradient and RF excitation produces a linear change in the resonance frequency of the spins in the volume, resulting in a spatially selective excitation where only the spins belonging to a slice of the object will resonate with the RF field (Figure 3.3). The thickness of such slice is given by

$$\Delta z = \frac{BW}{\gamma G_z} \tag{3.20}$$

where BW is the bandwidth of the RF excitation pulse, and G_z is the slope of the slice selection gradient (i.e. the gradient field is given by $\vec{G} = G_z z \hat{e}_z$).

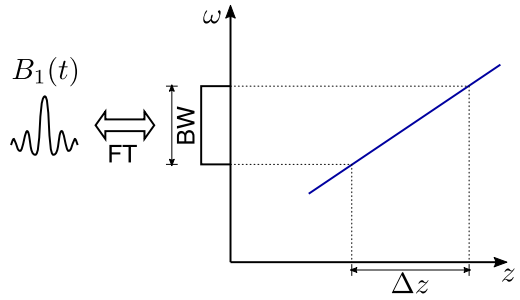

Figure 3.3: Slice selection gradient. When applied simultaneously with an RF excitation pulse $B_1(t)$ of bandwidth BW, the slice selection gradient results in the selective excitation of spins in a slice of thickness Δz.

The second gradient field is known as frequency encoding, and consists of a linear gradient typically varying along the x-axis. This gradient produces a linear change in the resonance frequency of the magnetisation along the x-direction. Therefore, samples acquired at different time points t_n during the application of this gradient correspond to different values of k_x in the MR sampling space, with $k_x(n) = \gamma G_x t_n$ for a gradient field $\vec{G} = G_x x \hat{e}_z$. As the data is acquired while applying this gradient it is also known as readout gradient, and the x-axis is known as the readout direction.

Finally, the third gradient field, known as phase encoding, varies along a direction perpendicular to the readout direction (typically the y-axis), and it is applied prior to data acquisition. After this gradient is switched off, the spins have accumulated a phase that varies linearly with the position of the spins on the y-axis, allowing for encoding the remaining spatial direction in the detected signal. It is worth noting that this description can be generalised for two-dimensional imaging in any orientation. Furthermore, a similar description can be obtained for three-dimensional imaging. In this case, a slice selective gradient is not needed, and instead, two phase encoding gradients are applied: one of them varying along the y-axis and a second one along the z-axis.

Each combination of amplitude, shape and duration of the three gradient fields defines a unique order in which the k-space is sampled, which is commonly known as k-space trajectory. The case described above results in the data being collected line-by-line in a Cartesian grid, and it is one of the most widely used k-space trajectories. However, any arbitrary k-space trajectories is possible by changing the shape of these gradients [53].

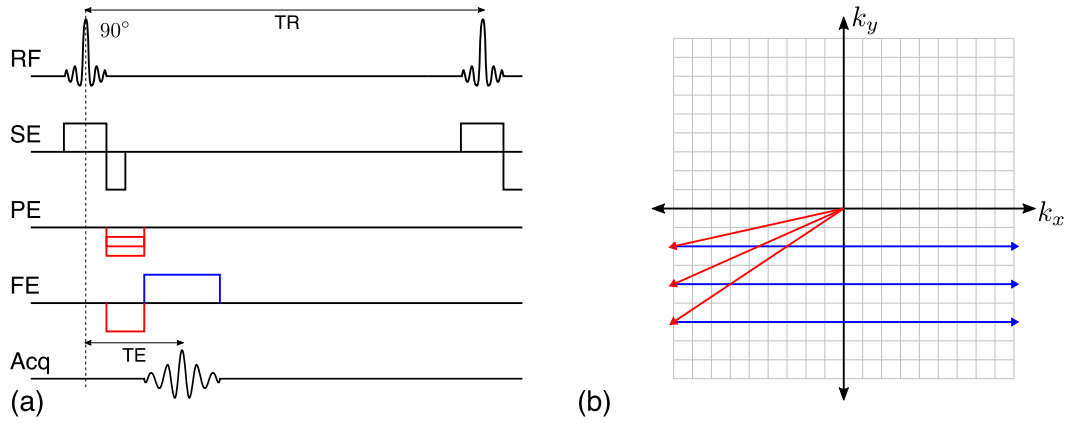

Figure 3.4: (a) Schematic of a generic pulse sequence, showing RF excitation pulses, slice encoding (SE), frequency encoding (FE) and phase encoding (PE) gradients, and the signal acquired (Acq). The repetition time (TR) and echo time (TE) are also indicated. (b) Corresponding k-space trajectory for the pulse sequence shown.

The sequence of RF and gradient fields used to acquire a MR image are collectively known as pulse sequence. By changing parameters in the pulse sequence, such as the shape and duration of the RF excitation pulse, or the timing between the application of RF excitations, gradient fields and data acquisition, the information content of the resulting image will change, producing a contrast that can be based, among others, on the density of ^{1}H, T_1 and T_2 times of the object being scanned or a combination of any of these properties.

Pulse sequences are generally described by schematics similar to the one shown in Figure 3.4a, indicating the flip-angle of the RF excitation pulses, and shape and duration of the gradient fields in the slice encoding (SE), frequency encoding (FE) and phase encoding (PE) directions. Parameters related to the timings of the pulse sequence are also depicted, including the repetition time (TR), corresponding to the time between consecutive RF excitations, and the echo time (TE), corresponding to the time between the RF excitation and the appearance of the peak amplitude of the induced signal, called the echo. As can be seen in Figure 3.4b, the pulse sequence can also be used to describe the k-space trajectory being followed in each particular MR acquisition protocol.

As described above, the MR data are acquired when the peak amplitude of the induced signal is produced. This peak can be induced by using RF pulses and/or by using readout gradients with opposed polarity. Pulse sequences that use RF pulses to induce a signal echo are usually known as spin echo sequences, while

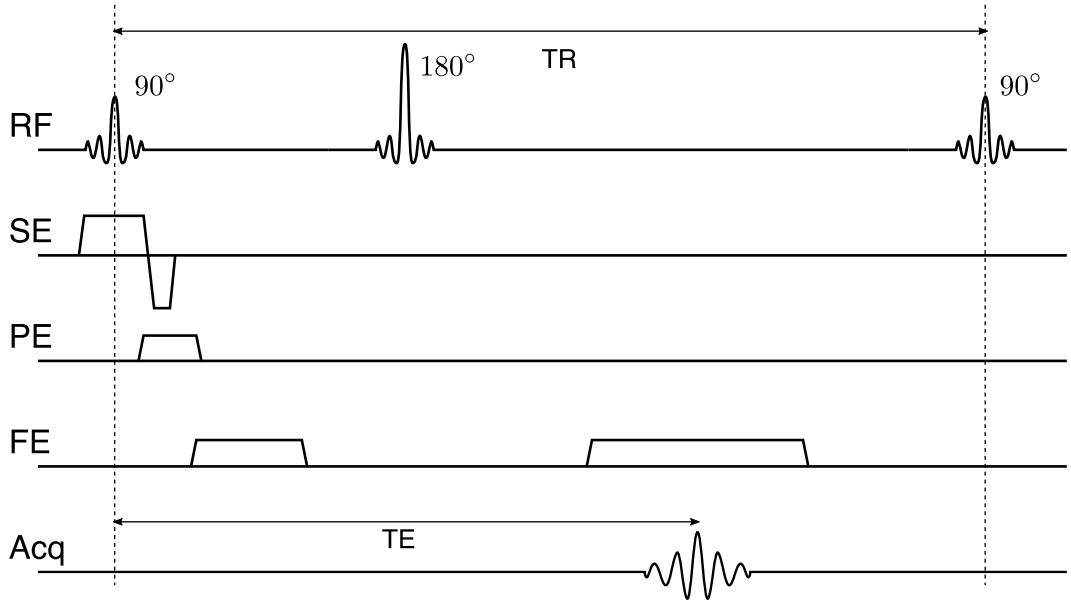

Figure 3.5: Schematic of a spin echo sequence. A 90° RF pulse is used to tip the magnetisation to the transverse plane, and a 180° RF pulse applied after TE/2 is used to induce an echo by refocusing the spins at TE.

sequences that rely only on readout gradients to induce the signal echo are known as gradient echo sequences. Typically, the spin echo sequences use a 90° RF excitation pulse that completely tips the longitudinal magnetisation to the transverse plane. After switching off the RF pulse, the spins start to dephase in the transverse plane according to their T_2 properties. Subsequently, a 180° RF pulse is applied after TE/2, so that the dephasing is reversed and spins get refocused at a time TE. A generic spin echo pulse sequence is depicted in Figure 3.5.

In gradient echo sequences a pre-phasing lobe is used in the readout gradient to produce the signal echo (Figure 3.6). In this case, the RF excitation pulse uses a flip angle $\alpha < 90°$, reducing the time required for the recovery of longitudinal magnetisation and therefore allowing for faster acquisitions. For this reason, gradient echo sequences are one of the most widely used pulse sequences for cardiac imaging.

When TR $\gg T_2$, the transverse magnetisation fully decays between consecutive RF excitations, and the signal induced at the echo time is proportional to parameters intrinsic to the object being scanned and extrinsic acquisition parameters, as shown

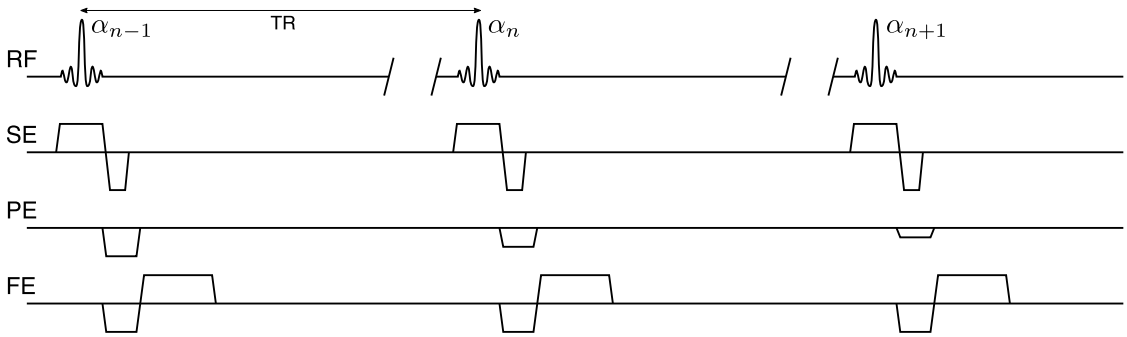

Figure 3.6: Schematic of a gradient echo sequence showing multiple RF excitations. In general TR is long enough for the transverse magnetisation to fully decay between consecutive RF excitations. A pre-phasing lobe is used in the frequency-encoding (FE) gradient to produce a signal echo.

in Equation 3.21.

$$S(\text{TE}) \propto \rho(\vec{r}) \frac{\left(1 - e^{\frac{-\text{TR}}{T_1}}\right)}{\left(1 - \cos(\alpha) e^{\frac{-\text{TR}}{T_1}}\right)} \sin(\alpha) e^{\frac{-\text{TE}}{T_2^*}} \tag{3.21}$$

where $\rho(\vec{r})$ is the density of ^{1}H at location $\vec{r}$, and T_2^* (also known as T_2 star) is a parameter that depends on both the intrinsic parameter T_2 and the local field inhomogeneities ΔB, so that

$$\frac{1}{T_2^*} = \frac{1}{T_2} + \gamma \Delta B \tag{3.22}$$

Note that in general, the parameters T_1, T_2 and ΔB are spatially dependent, so that $T_1 = T_1(\vec{r})$ and so on. This notation has been omitted for simplicity.

MR acquisition time increases linearly with TR. Thus, shorter TRs are desirable in order to accelerate the acquisition and reduce total scan time. However, reducing TR changes the magnetisation relaxation processes. Indeed, when TR $\approx T_2$, the transverse magnetisation M_{xy} does not fully decay between RF excitations, and therefore the induced signal at echo time is influenced by both the residual M_{xy} from previous RF excitations and the new longitudinal magnetisation M_z tipped into the transverse plane. It can be shown that after several repetitions, both M_{xy} and M_z reach a dynamic equilibrium, so that the induced signal reaches a steady state. Alternatively, additional gradient fields can be used to null the residual M_{xy} after data acquisition, using so-called magnetisation spoiling techniques, as shown

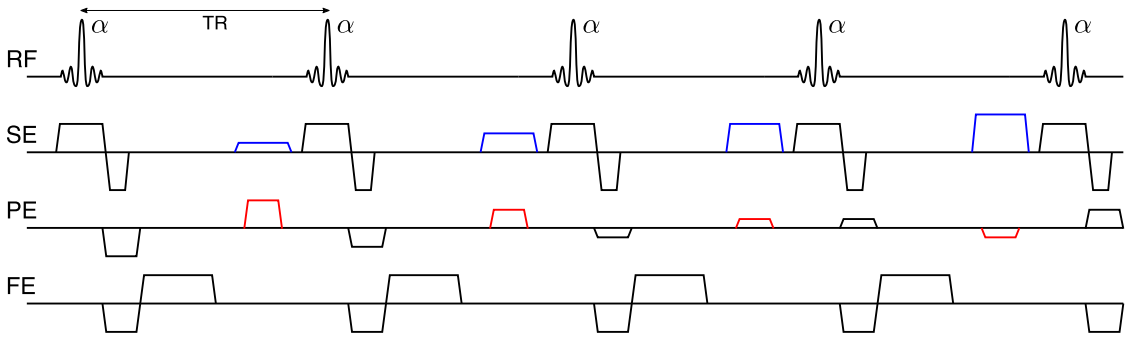

Figure 3.7: Schematic of a spoiled gradient echo sequence showing multiple RF excitations. Additional fields in the slice-encoding (SE) gradient (in blue) spoil the residual transverse magnetisation, allowing for reduced repetition time (TR). Phase-encoding (PE) re-winder gradients (in red), which allow returning to the centre of k-space between consecutive acquisitions, are also shown.

in Figure 3.7. In this case, the induced signal behaves similarly to Equation 3.21, and different image contrasts including T_1, T_2 and proton density weighting can be obtained by appropriately choosing TR, TE and α.

So far we have assumed that all spins within the volume of interest experience the same external static magnetic field B_0 and as a consequence precess at a unique Larmor frequency $\omega_0 = \gamma B_0$. In practice, however, the electrons surrounding nuclei in different molecular structures produce weak local magnetic fields that shield the main field B_0. This effect, known as chemical shift, results in an environment-specific local reduction of the magnetic field, so nuclei that belong to different molecules precess at slightly different frequencies, as described in Equation 3.23.

$$\hat{\omega}_0 = \omega_0(1 - \delta) \tag{3.23}$$

where $\hat{\omega}_0$ is the resonance frequency for a nucleus with a shielding constant δ that reflects its local chemical environment.

A well-known case of chemical shift occurs between water and fat. The most abundant chemical structure in fat is the methylene bridge (-CH_2-), whose protons have a $\delta = 3.35\,\text{ppm}$ compared to protons in water (H_2O), resulting in a difference in the Larmor frequency of 440 Hz at 3 T. Since the spatial position of the MR signal is encoded by the frequency encoding gradient in the readout direction, the difference in the Larmor frequency between the two species will produce a misregistration in the image, as the water and fat signal coming from the same location get

erroneously assigned to different locations. In order to suppress this artefact, a variety of techniques can be used, that either saturate the signal coming from the fat, or excite only the protons in water. Alternatively, the chemical shift effect can be used to produce images that reflect the water and the fat content of an object. Both approaches will be described in the next section in the context of CMRA imaging.

3.1.2 Coronary MR Angiography Imaging

MR has proven to be a robust and reliable technique for cardiovascular imaging, providing detailed information about cardiac anatomy and function and allowing for characterisation of myocardial tissue. As such, it has progressively been incorporated into the guidelines of several cardiology associations worldwide for the diagnosis and management of a variety of cardiovascular pathologies [54, 55]. Cardiovascular MR is mentioned in 78% of the American Heart Association, the American College of Cardiology and the European Society of Cardiology guidelines, with a total of 128 specific recommendations, mainly focused on the diagnosis and management of stable coronary artery disease, hypertrophic cardiomyopathies, aortic disease and congenital heart disease.

For instance, anatomical MR imaging is recommended to show the size, extent, and shape of aortic aneurysms in great-vessel disease, myocardial stress imaging is recommended in scenarios of stable coronary artery disease for evaluating ischaemia and planning myocardial revascularisation therapy, and techniques such as cine MR can be used to study valvular morphology, wall motion abnormalities and cardiac function [56]. More recently, whole-heart CMRA has shown promising results for the accurate depiction of the coronary anatomy, allowing the identification of anomalies and aneurysms in the coronary arteries and non-invasive depiction of stenoses in patients with multi-vessel coronary artery disease, as indicated in [57].

The aim of CMRA is to provide a high-resolution image with sufficient volumetric coverage that allows visualisation of the coronary arteries. The acquisition of such images presents several technical challenges. The complex physiological motion of the heart produces artefacts and blurring of the images, so compensation for respiratory and cardiac motion is fundamental. Additionally, contrast between the coronary blood pool and the surrounding epicardial fat and myocardium needs to be

enhanced in order to properly visualise the arteries. Finally, given the small diameter of the coronary arteries, in the range of 2.8 to 4.2 mm for healthy subjects [58], 3D high-resolution images are required in order to visualise both normal and pathologic vessels, with a spatial resolution typically in the order of 1 mm isotropic [59].

Cardiac Motion in CMRA

The effect of cardiac motion is conventionally minimised in CMRA by synchronising the data acquisition with the cardiac cycle using an external ECG device. Assuming that cardiac motion is periodic, data can be grouped according to their position within the cardiac cycle to produce images with minimal cardiac motion. There are two main approaches for performing this task, as shown in Figure 3.8.

In the first approach (Figure 3.8a), data are acquired only during a short time window within each heartbeat over multiple cardiac cycles, and then combined into a single k-space to produce a 'motion-free' image [60]. The R-wave is used as a reference for triggering the start of the acquisition, so that the data acquisition window coincides with a period of minimal myocardial motion. As described in Chapter 2, this period often corresponds to mid-diastole for adults, with a duration of ∼100 ms, while in paediatric patients or patients with variable heart rates the end-systolic period may be preferable [61–64], which has the disadvantage of being a shorter quiescent period (∼50 ms). In this approach, known as ECG triggered acquisition, two subject-specific parameters are set by the MR operator: the trigger delay and the duration of the acquisition window. Usually, these parameters are visually identified from a high-temporal resolution 2D cine scan performed shortly before the CMRA acquisition [65].

In the second approach, known as "free-running" acquisition (Figure 3.8b), data are continuously acquired during the cardiac cycle. Using the ECG signal as a reference, the data are then retrospectively sorted in a number of cardiac phases, assuming that within each of them there is minimal cardiac motion, so that 'motion-free' images can be reconstructed at each of these phases. The free-running approach is widely used for 2D cine imaging, and it has been demonstrated for whole-heart CMRA in combination with advanced undersampled and motion-compensated reconstruction techniques [66, 67].

Compared to the ECG triggered approach, free-running approaches have the ad-

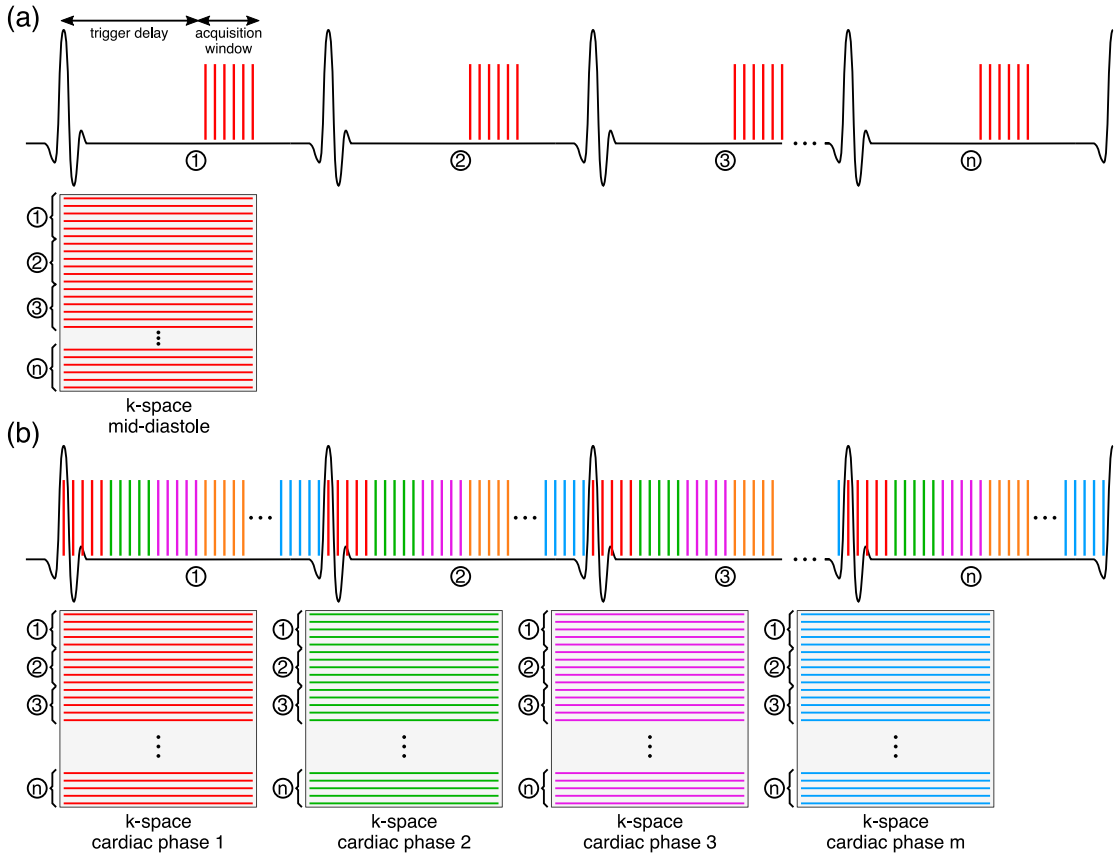

Figure 3.8: Two conventional approaches for minimising cardiac motion in CMRA. (a) ECG-triggered segmented acquisition. In each cardiac cycle a segment of k-space is acquired during a period of minimal motion, typically mid-diastole, so that k-space is filled in a series of n subsequent cardiac cycles. (b) Free-running acquisition. Data are continuously acquired and retrospectively sorted into m cardiac phases, each of them with minimal cardiac motion.

vantage of not needing to prospectively define the length of the acquisition window and trigger delay, reducing operator dependency during data acquisition. Furthermore, the cardiac phase with minimal motion can be found retrospectively, and information from different cardiac phases can be used to obtain clinically relevant parameters, including ventricular function indices, such as stroke volume and ejection fraction. However, since data are acquired continuously, the longitudinal magnetisation does not recover between consecutive excitations, resulting in a loss of SNR in the images. Another disadvantage of free-running approaches is that in order to fill multiple k-spaces, larger amounts of data are required, so total acquisition time tends to be longer than for ECG triggered acquisitions.

Respiratory Motion in CMRA

An approach analogous to ECG triggering can be used for minimising the effect of respiratory motion, by using a signal related to the breathing cycle to combine data acquired at a similar respiratory position during multiple breathing cycles. External devices such as respiratory bellows can be used for respiratory gating, assuming a high correlation between the motion of the heart and the motion of the chest wall. Alternatively, the respiratory cycle can be monitored directly by interleaving one-dimensional (1D) navigator echoes during the MR acquisition.

A navigator echo consists of an image representing a thin column of tissue that can be used to monitor the position of a high-contrast moving structure, such as the liver-lung interface, as shown in Figure 3.9c (in blue). When this interface is within a predefined window, usually placed at end-expiration with a width of 3–5 mm [68], the acquired data is accepted for image reconstruction, as depicted in Figure 3.9d. Otherwise, the data is rejected and reacquired in a later cardiac cycle. The information provided by the navigator echoes can also be used to further reduce motion artefacts by correcting for motion within the acceptance window. This approach, known as gating and tracking, assumes that the motion of the heart due to breathing is predominantly a translation in the superior-inferior (SI) or foot-head (FH) direction, and that this translation is directly proportional to the displacement of the diaphragm [41]. The linear factor that relates the displacement of the diaphragm and the motion of the heart, known as tracking factor, is typically set to 0.6 based on the study by Wang et al. [41].

The navigator echoes can be obtained by either using a spin-echo technique, as originally proposed in [69], where the excitation and refocusing planes are angulated so that the measured signal only arises from the intersection of the two planes (Figure 3.9b), or by applying a spatially selective 2D excitation pulse oriented in the FH direction (so-called pencil-beam navigators) [70, 71] (Figure 3.9a).

Although this approach is widely used in clinical settings due to its robustness, it has several limitations. Firstly, the motion of the heart is not measured directly, but it is inferred from the motion of the diaphragm. The population-based tracking factor of 0.6 is not appropriate for all subjects [44], so techniques that estimate subject-specific tracking factors have been proposed [72, 73]. However, even with

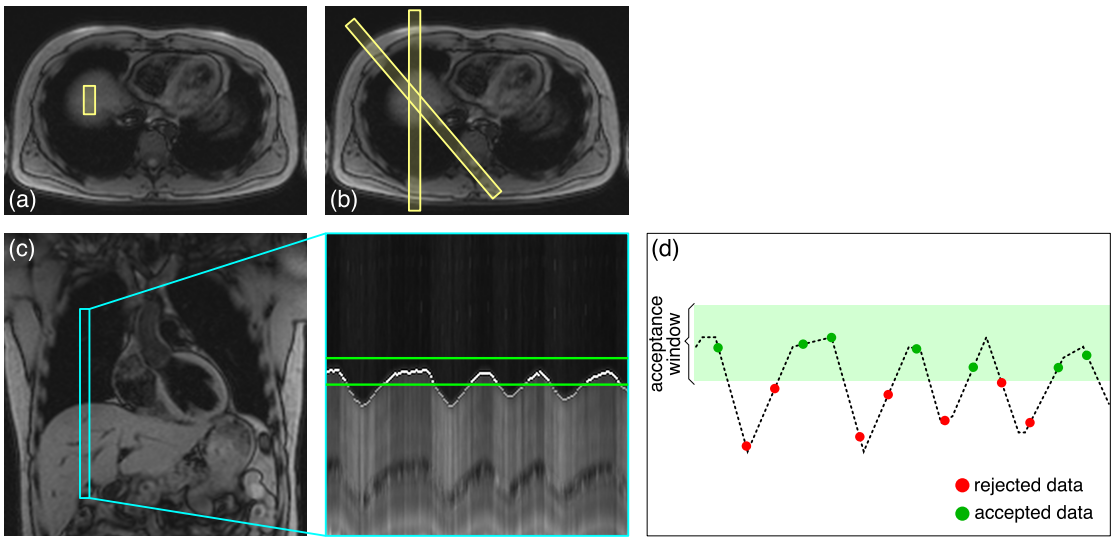

Figure 3.9: Diaphragmatic 1D navigator. An image of a thin column of tissue is acquired at each heartbeat to monitor the respiratory position of the heart; by using either (a) a 'pencil-beam' excitation or (b) two obliquely aligned excitations. (c) The resulting navigator signal can be used to track the lung-liver interface. (d) When the position of this interface is within a predefined acceptance window (in green), the acquired data is accepted (green dots), otherwise, data is rejected (red dots).

subject-specific tracking factors, the 1D navigator approach only accounts for translational motion in the FH direction, and is incapable of including corrections for translational motion in the anterior-posterior (AP) or right-left (RL) directions. Furthermore, this approach does not account for the hysteresis effect described in Section 2.2, as it uses the underlying assumption that a given position of the diaphragm is associated to a unique position of the heart, and it does not consider the complex non-rigid deformations of the heart during the breathing cycle. Finally, the efficiency of the acquisition (i.e. the percentage of acquired data that is accepted for image reconstruction) varies significantly between subjects, typically ranging from 20 to 60%, which leads to increased and unpredictable acquisition times.

Alternatively, self-navigation methods that estimate the respiratory motion of the heart from the acquired data itself have been proposed in the literature. These methods derive a respiratory signal from a repeated acquisition of either the centre of k-space [74] or a central line in k-space [75–77], usually acquired in the FH direction. Compared to diaphragmatic navigator approaches, self-navigation methods have the advantage of removing the need for a correction factor. However, they also perform motion correction in the FH direction only. Furthermore, their ability to estimate

a respiratory signal is impaired by the presence of static tissue, as both the centre of k-space and the central line of k-space are projections of the whole field of view.

In order to address these limitations, respiratory motion compensation techniques that use image-based navigators (iNAVs) have been proposed more recently in the CMRA literature. By acquiring low-resolution 2D [78–81] or 3D images [82–87] instead of the traditional 1D navigator, motion can be directly measured in the heart by tracking a region of interest (ROI). The measured motion can be then used to correct the acquired CMRA data either prospectively or retrospectively, incorporating most of the acquired data for image reconstruction (i.e. they achieve near 100% scan efficiency), which leads to predictable and significantly reduced acquisition times. A detailed description of methods that have been proposed for retrospective motion correction in CMRA using iNAVs can be found in Section 3.3.

Contrast Generation in CMRA

In order to properly visualise the coronary arteries, sufficient contrast between the arterial blood pool and the surrounding epicardial fat and myocardium is required. The contrast between blood pool and myocardium can be enhanced by exploiting the intrinsic properties of the tissues and/or by using exogenous contrast agents. Intravascular contrast agents that reduce the T_1 relaxation time of the blood pool can be used in combination with magnetisation preparation pulses, such as a train of dummy RF pulses [88] or an inversion recovery pulse [89], so that the signal from the myocardium is strongly attenuated or nulled during the acquisition, while the coronary blood pool appears bright.

Alternatively, the difference in the T_2 relaxation time between the arterial blood pool and the surrounding tissues can be used as an endogenous contrast mechanism by including a T_2 preparatory pulse (T2-prep) before the acquisition of imaging data [90, 91]. A T2-prep consists of a 90° RF pulse that flips the longitudinal magnetisation to the transverse plane, an even number of 180° RF refocusing pulses, and a final 90° tip-up pulse (Figure 3.10a). For tissues with long T_2 relaxation times, such as the arterial blood (250 ms), this pulse has minimal effect. But for tissues with short T_2, e.g. the myocardium (50 ms), cardiac venous blood (∼35 ms) or epicardial fat (100 ms), the T2-prep will strongly attenuate the longitudinal magnetisation. Thus, during data acquisition, most of the measured signal is obtained from the

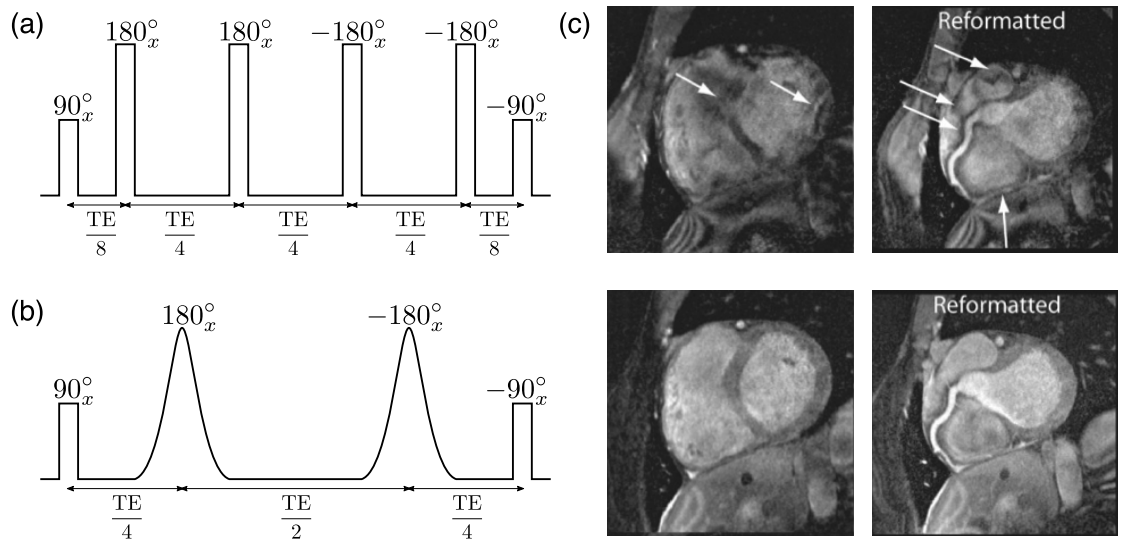

Figure 3.10: Schematic of T2-preparation pulses of duration TE. (a) Conventional non-adiabatic T2-prep (b) Adiabatic T2-prep. (c) Effect of T2-preparation in CMRA at 3 T, non-adiabatic T2-prep shows high sensitivity to field inhomogeneities (top row, arrows) while using an adiabatic T2-prep improves signal homogeneity, reducing image artefacts (bottom row). *CMRA images adapted with permission from Nezafat R., et al. *B1-Insensitive T2 preparation for improved coronary magnetic resonance angiography at 3T*. Magnetic Resonance in Medicine 2006;55:858–864 [92].

arterial blood pool.

The original formulation of the T2-prep module for 3D CMRA at 1.5 T considered four RF refocusing pulses [91], showing promising results in healthy subjects and patients. The tolerance of the T2-prep module to B_0 and B_1 inhomogeneities depends on the number of refocusing pulses used, so at higher magnetic fields a longer train of 180° RF is desirable. However, increasing the number of 180° RF pulses results in an increased energy deposition to the patient (known as the specific absorption rate, SAR) for the T2-prep pulse, which prevents its use at 3 T. Alternatively, adiabatic 180° RF pulses that are intrinsically insensitive to field inhomogeneities can be used, as proposed in [92] (Figure 3.10b). In this study, it was shown that CMRA image quality at 3 T is improved by using two adiabatic 180° RF refocusing pulses instead of the conventional train of four non-adiabatic pulses (Figure 3.10c). Further advances in T2-preparation at 3 T have been recently been proposed in the literature [93], where by using water-selective RF excitation pulses an additional suppression of the fat signal is achieved.

Fat Suppression in CMRA

The coronary arteries are embedded in a layer of epicardial fat for most of their course. Fat has a shorter T_1 relaxation time than the arterial blood, so signal arising from the epicardial fat in T_1-weighted CMRA sequences can obscure the visualisation of the coronary arteries if not adequately suppressed (Figure 3.11). The most common approach for fat suppression in CMRA is based on the use of a spectrally selective RF pulse before data acquisition [91, 94, 95], which relies on the chemical shift and relaxation time differences between water and fat to null or minimise the fat signal. This approach, known as SPIR, selectively saturates the signal arising from protons by applying a frequency selective RF pulse, typically centred in the resonance frequency of the methylene bridge, that partially or completely inverts the fat magnetisation. After applying this inversion RF pulse, the signal arising from the fat will start recovering due to longitudinal relaxation, reaching a null longitudinal magnetisation after a short time. Then, by selecting an appropriate waiting time, CMRA data can be acquired when the fat signal is nulled.

Although this technique has been shown to be robust at 1.5 T, adequately suppressing the fat signal, its intrinsic sensitivity to field inhomogeneities can result in incomplete fat suppression at higher magnetic fields [96]. Shimming techniques that improve field homogeneity in a volume of interest can alleviate this problem, producing good quality images as shown in [97, 98].

Alternatively, the chemical shift between water and fat can be used to separate the two species into images that reflect the water and fat content of each voxel in the image, using so-called water/fat separation methods. The transverse magnetisation

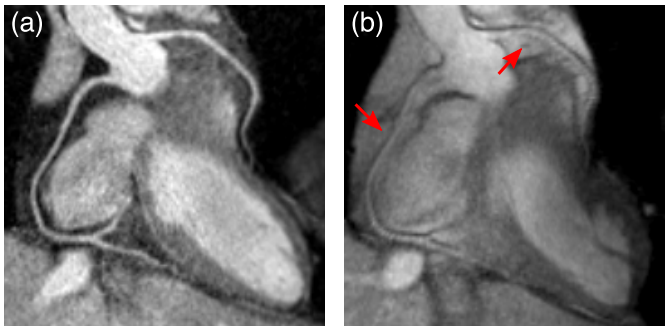

Figure 3.11: Effect of fat suppression on CMRA imaging. (a) Appropriate fat suppression allows for good depiction of the coronary arteries while in (b) incomplete fat suppression (red arrows) obscures the visualisation of the vessels.

in a voxel that contains water and fat can be written as

$$M_{xy}(t) = M_{xy}^{W} + M_{xy}^{F}\exp(i\delta\omega_0 t) \tag{3.24}$$

where M_{xy}^{W} and M_{xy}^{F} correspond to the transverse magnetisation arising from the water and fat protons, respectively. In the original formulation of the water/fat separation approach, proposed by Dixon in 1984 [99], data are acquired at two different times: a first dataset is acquired when $\delta\omega_0 t = 2n\pi$ (in-phase echo) and a second dataset is acquired at $\delta\omega_0 t = (2n+1)\pi$ (out-of-phase echo). By using such times in Equation 3.24, it can be shown that the resulting magnetisation can be written as

$$M_{\mathrm{IP}} = M_{xy}^{W} + M_{xy}^{F} \tag{3.25a}$$

$$M_{\mathrm{OP}} = M_{xy}^{W} - M_{xy}^{F} \tag{3.25b}$$

where M_{IP} and M_{OP} are the in-phase and out-of-phase transverse magnetisation, respectively. From these two acquisitions, it is possible to obtain the signal arising from the fat and water by adding and subtracting the two acquired signals, as shown in Equation 3.26

$$2M_{xy}^{W} = M_{\mathrm{IP}} + M_{\mathrm{OP}} \tag{3.26a}$$

$$2M_{xy}^{F} = M_{\mathrm{IP}} - M_{\mathrm{OP}} \tag{3.26b}$$

This method, known as two-point Dixon, does not take into account the presence of field inhomogeneities, which introduce an additional phase in the acquired data. In order to solve the ambiguity produced by this additional phase, additional echoes can be acquired, using so-called multi-echo or multi-point Dixon approaches [100, 101]. Alternatively, algorithms that estimate the field inhomogeneities from the two-point data itself have been proposed in the literature [102, 103]. Furthermore, methods that do not require exact in-phase and out-of-phase echoes have been proposed [104], allowing for flexible echo times. The water/fat separation approach has been applied to CMRA imaging, and it has been shown to improve image quality at 1.5 T [105] and 3 T [106] compared to conventional spectrally selective fat saturation, increasing SNR of the arterial blood and improving blood-to-fat contrast-to-noise (CNR) ratio in the water images.

Figure 3.12 shows a generic CMRA acquisition sequence, including the most widely used mechanisms for compensating for cardiac and respiratory motion, and for producing enough contrast between arterial blood and surrounding tissues.

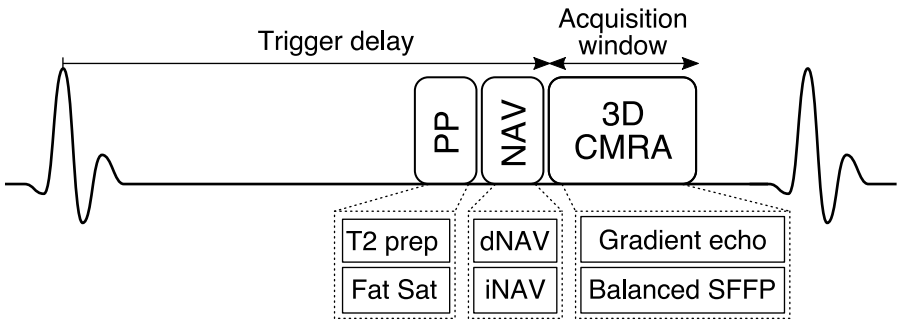

Figure 3.12: Generic ECG-triggered CMRA sequence. Preparation pulses (PP) to improve the contrast between blood and surrounding tissues are applied before data acquisition: T_2 preparation (T2-prep) improves the contrast between blood and myocardium while fat saturation (Fat Sat) minimises the signal arising from epicardial fat. A subject-specific trigger delay and a short acquisition window are used to minimise cardiac motion, while different navigators (NAV) can be used to compensate for respiratory motion, including diaphragmatic navigators (dNAV) or image-based navigators (iNAV). 3D CMRA data are generally acquired with a gradient echo sequence, or with a balanced steady-state free precession (SSFP) sequence, depending on the strength of the magnetic field.

3.2 Cardiac PET Acquisition

PET is a non-invasive imaging technique that allows measurement of the spatial distribution of the concentration of a positron-emitting radiopharmaceutical, administered to a patient via injection or inhalation, in order to provide functional information about a physiological process. Within the body, an emitted positron annihilates with a nearby electron producing two photons travelling in opposite directions, which can be subsequently detected by an array of detectors that constitute the PET scanner. When two photons are simultaneously detected, using so-called coincidence detection mechanisms, it is assumed that they originated from the annihilation of a positron located somewhere along the line between the detectors. By collecting enough such coincidences from sufficient angles around the patient, and using some tomographic image reconstruction technique, the spatial

distribution of the radiopharmaceutical concentration can be estimated, resulting in a multi-dimensional PET image.

Due to the high sensitivity of radiation detectors, PET scanners can detect even nanomolar concentrations of the radiopharmaceutical [107]. Therefore, trace amounts of these compounds, also referred to as radiotracers or simply tracers, are sufficient to produce PET images where the presence or absence of the radiopharmaceutical can be observed without disturbing the biological process being observed. Furthermore, PET systems allow for absolute quantification of the concentration of the radiotracer, providing objective measurements that can be used for accurate monitoring of disease progression or evaluating response to therapy. This section describes the basic principles of PET data acquisition, following the methodology and terminology presented in Cherry et al [107], and then focuses on cardiac PET imaging, including a brief description of the radiopharmaceuticals commonly used for cardiac applications, acquisition protocols and conventional mechanisms used for motion compensation.

3.2.1 Fundamentals of PET Imaging

Consider a positron-emitting radionuclide positioned within a PET scanner, as shown in the schematic in Figure 3.13a. The radionuclide decays by emitting a positron that undergoes mutual annihilation with an ordinary electron from the surrounding atoms, after travelling some distance from the site of emission depending on its energy. This annihilation produces two 511 keV annihilation photons travelling in approximately opposite directions.

These annihilation photons can be detected, typically by using scintillation-based radiation detectors arranged in one or more rings, which register each detected photon as an event. When a pair of such events are recorded within certain coincidence timing window (ranging from 6 to 12 ns for traditional PET systems, to 500 to 600 ps for scanners with time of flight capabilities), it can be assumed that they resulted from the same annihilation, and that the positron that originated them is located somewhere on the line between the detectors. This annihilation coincidence detection (ACD) mechanism constitutes the basis of the PET measurement system. It is worth noting that due to Compton scattering of the annihilation photons within

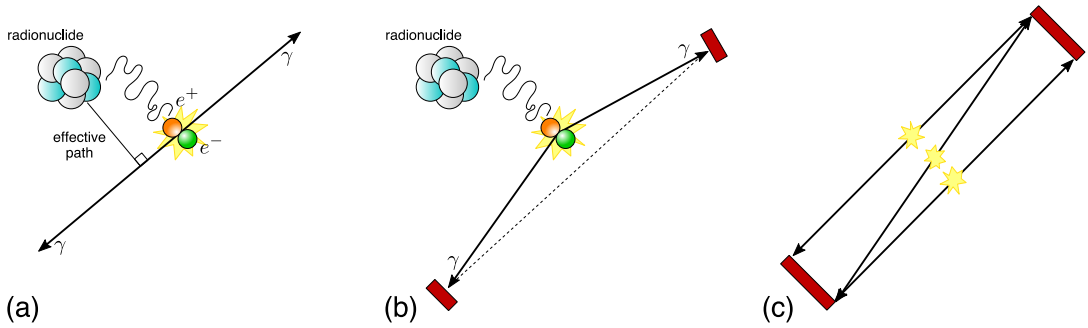

Figure 3.13: (a) A positron-emitting radionuclide decays by emitting a positron (e^+) that annihilates with a neighbouring electron (e^-) after following a tortuous path, producing two annihilation photons (γ) travelling in opposite directions. (b) Residual momentum of the positron before annihilation slightly deflects the annihilation photons, resulting in a noncolinearity effect. (c) The width of the detectors impacts the spatial resolution of the system, as it is not possible to spatially distinguish annihilations within certain distance. Note that in (b,c) the scale of the effects has been exaggerated for illustration purposes.

the detector crystals, the ACD mechanism requires a wide energy window that not only records 511 keV photons but also photons of lower energy. This energy window typically ranges from 400 to 600 keV in conventional PET systems.

The spatial resolution of ACD systems is limited mainly by three factors. The first of them, known as positron range, is related to the distance that positrons travel before annihilation. After emission, the positron will follow a tortuous path before annihilation, as depicted in Figure 3.13a, and the distribution of the effective length of such paths, or effective positron range (i.e. the perpendicular distance between the location of the positron emission and the line formed by the annihilation photons) depends on the energy of the radionuclide involved, the electron density of the medium surrounding the radionuclide, and the presence or absence of a strong static magnetic field. Figure 3.14(a) shows the root-mean-square effective positron range, R_{e^+}, for radionuclides commonly used for in vivo PET imaging as a function of their maximum energy measured in water, while Figure 3.14(b) shows the differences in mean positron range for three of these radiotracers in absence of a surrounding magnetic field and in presence of a 3 T magnetic field, for both water and lung tissue.

It is worth noting that the positron range decreases when the object being scanned is placed in a strong magnetic field (such as the case of clinical 3 T PET-MR systems). This reduction occurs in the plane perpendicular to the static magnetic field of the scanner, resulting in a non-isotropic spatial resolution [108]. However,

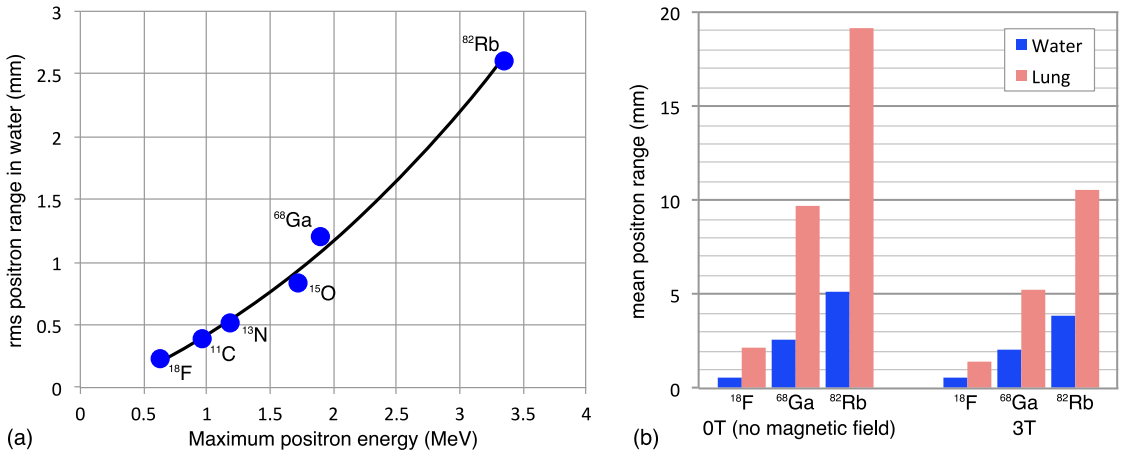

Figure 3.14: (a) Effective root-mean-square (rms) positron range as a function of the positron energy, which ranges from a few hundred microns to a few millimetres. Modified from [107], including data from [110,111]. (b) Mean positron range in both water and lung tissue in absence of a magnetic field and at 3 T. Data from [108].

the effects of this anisotropic positron range are negligible for ^{18}F-based radionuclides compared to the other factors that affect spatial resolution in conventional clinical scanners [109].

The second factor that affects spatial resolution is the noncolinearity of the annihilation photons. Due to a residual momentum of the positron at the end of the path travelled after emission, the resulting annihilation photons get slightly deflected, so that the line connecting the detectors is actually displaced from the location of the annihilation, as illustrated in Figure 3.13b. The noncolinearity effect can be modelled as a point-spread function, whose width increases linearly with the distance between detectors, so that if a distance D separates the detectors, the full-width at half-maximum (FWHM) of this function is given by

$$R_{\text{nonc}} = 0.0022D \tag{3.27}$$

The third factor that plays a role in spatial resolution is the width of the detectors, as shown in Figure 3.13c. For a radionuclide located in the middle of the line that connects two detectors of width d, the contribution of this effect in terms of FWHM is given by

$$R_{\text{size}} = \frac{d}{2} \tag{3.28}$$

Finally, the spatial resolution of the system, R_{sys} can be obtained by combining

the three factors described above, as shown in Equation 3.29. This value represents the FWHM of the overall point-spread function of the detector system.

$$R_{\text{sys}} = \sqrt{R_{e^+}^2 + R_{\text{nonc}}^2 + R_{\text{size}}^2} \tag{3.29}$$

Depending on the configuration of the system, some of the three described factors are negligible compared to others. For instance, in whole-body PET scanners ($D = 60\,\text{cm}$, $d = 4\,\text{mm}$) using ^{18}F based radiotracers; the dominant factor defining the detector system resolution is the detector size, resulting in an overall R_{sys} of $\sim$2.4 mm. It is worth noting that although the effects described here only refer to the intrinsic spatial resolution of the ACD system, the spatial resolution of resulting PET images is affected by additional factors, including the location of the radionuclide within the field of view, the level of activity within the field of view, and the algorithm used for image reconstruction, among others.

The limited spatial resolution of the ACD system is not the only factor that affects PET image quality. So far, it has been assumed that the detected coincidences arise exclusively from the emission of two annihilation photons travelling directly to the detectors, as shown in Figure 3.15a. However, unwanted coincidences may occur when photons from unrelated annihilations are detected within the coincidence timing window, as depicted in Figure 3.15b. These coincidences are known as random coincidences, and their spatial distribution depends on the area of the body being imaged and the radiotracer distribution. For thoracic and abdominal imaging, it is generally assumed that they occur approximately uniformly across the field of view of the scanner. Additionally, one or both annihilation photons may scatter without a significant loss of energy due to Compton scattering, producing an erroneous coincidence detection (Figure 3.15c).

Whereas the rate of random coincidences increases linearly with the duration of the coincidence timing window and with the square of the administered radioactivity, both true and scatter coincidences increase linearly with the activity and are roughly independent of the length of the coincidence timing window. Both random and scatter coincidences raise the background noise, degrading the PET image contrast, so mechanisms to correct for their effect are required to produce accurate quantitative PET images.

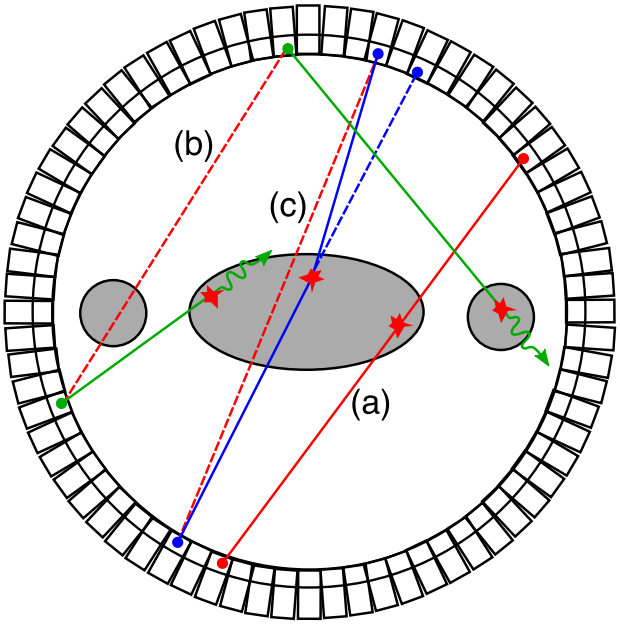

Figure 3.15: Types of coincidence in PET imaging. (a) True coincidences, (b) random coincidences, arising from near simultaneous detection of photons from unrelated annihilations, and (c) scatter coincidences, occurring when one or both photons scatter with minimal loss of energy.

Two methods are conventionally used for estimating random coincidences: the delayed coincidence window and the singles method. In the first method, the ACD mechanism is slightly modified so that the coincidence timing window is delayed by a time much longer than its duration. Such a delay ensures that no true or scatter, but only random coincidences are recorded, and by using the assumption that the rate of random occurrences in the undelayed and delayed coincidence timing window is the same, the rate of random coincidences can be estimated. Alternatively, if knowledge about the rate of single photon detections is available for each detector, the rate of random coincidences for a pair of detectors $r(i, j)$ can be estimated by

$$r(i, j) = 2r_i r_j \Delta T \tag{3.30}$$

where r_i is the rate of single photon detections in detector i and ΔT is the duration of the coincidence timing window.

The rate of scatter coincidences depends on several factors, including the density and geometry of the object being scanned, the density of the photon detector material, the amount of radioactivity administered, and the width of the energy

acquisition window of the PET scanner. Several methods have been proposed to estimate scatter coincidences, including approaches based on using multiple energy acquisition windows and methods that directly simulate the scatter distribution using analytic models or Monte Carlo simulations of the photon-matter interactions. A detailed description of such methods can be found in the comprehensive reviews by Zaidi and colleagues [112, 113].

Considering the described ACD mechanism and neglecting for a moment the random coincidences and scattering effects, the total number of coincidences registered for a particular pair of detectors corresponds to the line integral of the radiotracer distribution along the line defined by the centre of both detectors, L, the so called line of response (LOR). For 2D PET imaging the LORs can be parameterised by their angle θ_L and the distance d_L to the centre of the detector ring, as shown in Figure 3.16. Usually, measured PET data is stored in an array, known as sinogram, where each row represents one projected view of the radiopharmaceutical distribution at an angle θ_L across a range of distances d_L. For 3D PET imaging, each LOR can be described by adding a third parameter that corresponds to the angle of the LOR relative to the long axis of the scanner, so that a set of sinograms parameterised by this angle is obtained. Alternatively, PET raw data can be stored as a list-mode file, where each coincidence is recorded indicating the time of the coincidence event and the corresponding pair of detectors.

Considering the 2D case illustrated in Figure 3.16, the relationship between the radiopharmaceutical distribution $\rho(x, y)$ and the acquired data $m(\theta_L, d_L)$ can be written as

$$m(\theta_L, d_L) = \int\int \delta(x\cos(\theta_L) + y\sin(\theta_L) - d_L)\rho(x, y)dxdy \tag{3.31}$$

It can be observed from Equation 3.31 that when using a purely geometric model for the PET data acquisition, the measured PET data corresponds to the Radon transform of the spatial distribution of the radiotracer concentration. Therefore, the problem of estimating such a distribution could be solved by collecting enough projected views and then using some mathematical transformation for inverting Equation 3.31. These techniques, referred to as PET image reconstruction, will be described in detail in Section 3.4.

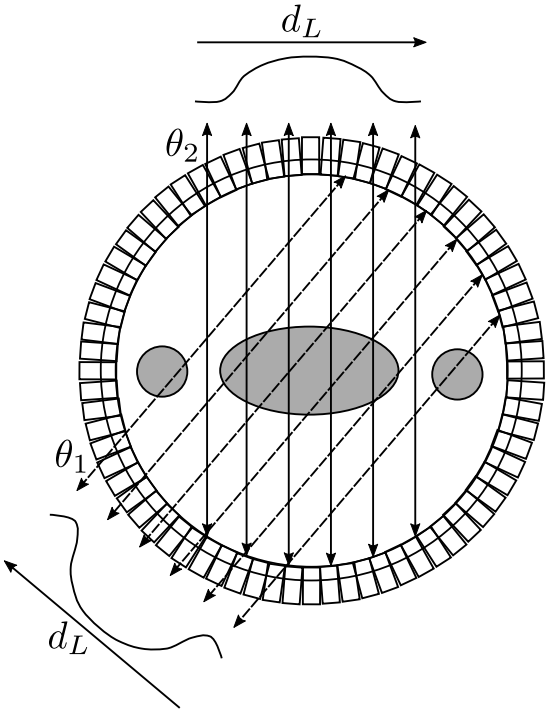

Figure 3.16: Example of lines of response (LORs) for a 2D PET system. Each LOR can be parameterised by the angle θ_L ($L = 1, 2$ in this example) and distance d_L.

It is worth noting that the simple model presented in Equation 3.31 does not account for all the physical effects that characterise the PET acquisition process. For instance, the effect of random and scattered coincidences is not considered. Furthermore, this model assumes that each pair of detectors has an identical sensitivity so that the rate of coincidences only depends on the spatial distribution of the radiotracer. In practice, however, the sensitivity of the individual photon detectors of the PET scanner will affect the number of coincidences registered in each LOR. In order to take this effect into account, a known radiation source can be used, so that the sensitivity of each pair of detectors can be estimated from the corresponding number of coincidences acquired in the phantom scan. This information can be then used to normalise the number of coincidences recorded by each pair of detectors before PET image reconstruction.

Additionally, some of the photons will be absorbed before reaching the detectors, reducing the number of coincidences registered for most of the LORs. The well-known Beer-Lambert law states that the probability that both annihilation photons reach a pair of detectors is given by

$$A(L) = \exp\Big(-\int_L \mu(x)dx\Big) \tag{3.32}$$

where $\mu(x)$ are the linear attenuation coefficients of the tissues in the path L that photons travel in their way to the corresponding detectors.

These attenuation coefficients depend on the objects within the gantry of the scanner, including the subject being scanned, and as such are patient-specific. They are commonly obtained by properly scaling a simultaneously acquired computed tomographic (CT) image for PET-CT systems [114, 115] or can be inferred from anatomical MR images in hybrid PET-MR systems [116].

While CT-based attenuation correction is based on using CT images in Hounsfield units to estimate the density of tissue, and therefore estimate linear attenuation coefficients at 511 keV, MR imaging does not provide a direct measurement of tissue density. Since MR images have a superior tissue contrast, MR-based attenuation correction are typically based on segmenting the acquired MR image into a number of tissue classes, so that known attenuation values are assigned to each class. Although several methods for MR-based attenuation correction have been proposed in the literature in recent years, only a handful of them have been approved by regulatory agencies for routine clinical use. Indeed, commercially available PET-MR systems use either a 3-class (air, soft-tissue and lungs) or a 4-class (air, fat, soft-tissue and lungs) segmentation-based method for creating attenuation maps [117].

Nonetheless, the segmentation-based approach has several limitations. First, in most cases it does not account for bone tissue, introducing bias particularly when imaging areas of the body with abundant presence of bones, such as in brain PET imaging. Second, the assumption that there is a unique attenuation coefficient for each tissue class further limits the accuracy of this approach. For instance, lung tissue has a high variability across different patient populations, within each patient, and even throughout the breathing cycle due to the changes on the air volume within the lungs [118, 119]. Several studies have shown that the use of fixed attenuation values for lung tissue in MR-based attenuation correction results in bias in the quantification of lung lesions [120] and volumes of interest within the lungs [121]. Although the bias induced by assuming a fixed attenuation value of the lung tissue affects the whole PET image, this effect has been shown to be less significant in

cardiac structures. For instance, a recent study focused on cardiac imaging showed no statistically significant differences in average myocardial uptake when comparing PET-CT and PET-MR using MR-based attenuation correction [122]. Finally, additional challenges for MR-based attenuation correction in the context of cardiac PET-MR imaging result from the extensive use of Gadolinium-based contrast agents. Changes of up to 1.3% in linear attenuation coefficients due to varying concentrations of contrast agent have been reported in [123]. Furthermore, if the contrast agent is injected before the acquisition of the MR-based attenuation map, potential errors in the segmentation can be produced due to tissue misclassification arising from T_1 shortening [124].

3.2.2 Cardiac PET Imaging

In cardiac imaging, PET has been established as the reference modality for assessing myocardial integrity through the use of different radiotracers including ^{13}N-NH_3 (^{13}N-ammonia), ^{82}Rb, ^{15}O-H_2O and ^{18}F-fluorodeoxyglucose (^{18}F-FDG). A summary of the main characteristics of these radiotracers is presented in Table 3.1 (modified from [22, 125]). The first three radiotracers are commonly used to quantify myocardial perfusion, as hypoperfused areas may indicate the presence of obstructive coronary artery disease. While both ^{13}N-NH_3 and ^{82}Rb accumulate in the myocardium, ^{15}O-H_2O diffuses freely across cell membranes and capillaries, requiring post processing of the images in order to subtract the signal arising from the blood pool. For this reason, ^{13}N-NH_3 and ^{82}Rb are more commonly used in clinical practice [15]. Furthermore, their relatively short physical half-life allows imaging of myocardial perfusion in both rest and stress during a single scanning session, including a waiting period for full decay of the radiotracer between both scans, with a total duration from 30 to 120 minutes depending on the radiotracer used [22].

As mentioned before, myocardial perfusion PET imaging allows for a highly accurate diagnosis of CAD, with 93% sensitivity and 92% specificity, according to a review of studies including ∼800 patients [22]. However, perfusion imaging does not allow regions of infarcted myocardium to be distinguished from those of hibernating myocardium that have a potentially reversible dysfunction. Given that hibernating myocardium exhibits an active glucose metabolism, ^{18}F-FDG (a glucose analogue)

	Myocardial uptake mechanism	Positron range	Physical half-life	Production	Imaging time (min)
^{13}N-NH_3	Diffusion/ metabolic trapping (perfusion)	0.7 mm	10 min	Cyclotron	10–20
^{82}Rb	Na/K-ATPase (perfusion)	2.6 mm	78 s	Generator	8
^{15}O-H_2O	Free diffusion (perfusion)	1.1 mm	2 min	Cyclotron	5
^{18}F-FDG	Glucose transport (viability)	0.2 mm	110 min	Cyclotron	up to 45

Table 3.1: Characteristics of commonly used radiotracers for cardiac PET imaging.

can be used to distinguish hibernating from infarcted myocardium, highlighting areas that could benefit from revascularisation therapy [126].

The acquisition of ^{18}F-FDG PET images that reflect the glucose uptake in the myocardium is challenging because under normal conditions this muscle derives its energy from a variety of sources [127], leading to a very heterogeneous pattern of radiotracer uptake. Different preparation strategies have been proposed in order to standardise the metabolic conditions for ^{18}F-FDG myocardial viability imaging, enhancing radiotracer uptake and improving image homogeneity. These preparation strategies include instructing the patient to fast for up to 12 hours before examination, use of oral glucose loading for stimulating insulin secretion, hyperinsulinaemic clamping for enhancement of glucose/^{18}F-FDG utilisation, or a combination or them [128, 129].

Alternatively, if the normal physiological glucose metabolism is suppressed, ^{18}F-FDG can be used for imaging inflammatory response in the myocardium, reflecting only the increased glucose uptake by macrophages and other inflammatory cells. This suppression can be achieved by prolonged fasting (more than 12 hours), by prescribing a high-fat low-carbohydrate and protein-permitted diet for approximately 24 hours before examination, by intravenous administration of unfractionated heparin, or a combination of the latter two [51]. Such patient preparation has allowed the use of ^{18}F-FDG for the diagnosis and characterisation of several conditions, including cardiac sarcoidosis [130] and myocarditis [131].

^{82}Rb, ^{13}N-NH_3 and ^{18}F-FDG are the most widely used radiotracers for cardiac PET imaging in clinical practice. However, the flexibility of PET to target specific molecular processes has stimulated the development of novel radiotracers for targeting different mechanisms of cardiovascular disease, as shown in Table 3.2 [132].

Radiotracers		Target	Disease/Condition
^{18}F based	^{18}F-Fluciclatide	$\alpha_V\beta_3$ and $\alpha_V\beta_5$ integrin receptors	Angiogenesis and recovery post myocardial infarction
	^{18}F-flutemetamol, ^{18}F-NaF, ^{18}F-florbetapir, ^{18}F-florbetaben,	Amyloid	Cardiac amyloidosis
	^{18}F-NaF	Micro-calcification	Atherosclerotic plaque and aortic stenosis
	^{18}F-MISO	Tissue hypoxia	Atherosclerotic plaque
	^{18}F-galacto-RGD	Angiogenesis	Atherosclerotic plaque
	^{18}F-choline	Macrophages	Vascular inflammation in atherosclerosis
	^{18}F-flurpiridaz [133]	Myocardial mitochondria	Coronary artery disease
^{11}C based	^{11}C-hydroxyephedrine	Denervation in the myocardium	Ischaemic heart disease and heart failure
	^{11}C-PiB	Amyloid	Cardiac amyloidosis
	^{11}C-PK11195	Translocator protein	Atherosclerotic plaque
	^{11}C-choline	Macrophages	Vascular inflammation in atherosclerosis
Other	^{64}Cu-DOTATATE, ^{68}Ga-DOTATATE	Macrophages	Vascular inflammation in atherosclerosis
	^{68}Ga-NOTA-RGD	Angiogenesis	Atherosclerotic plaque
	^{64}Cu-ATSM [134]	Tissue hypoxia	Myocardial ischaemia

Table 3.2: Novel radiotracers for cardiac PET imaging, modified from [132].

Of particular interest for CAD are the promising results obtained by using ^{18}F-sodium fluoride (^{18}F-NaF) for identifying high-risk and ruptured atherosclerotic plaque [8, 135, 136]. Further studies in larger cohorts of patients are required for assessing the clinical impact of this new radiotracer in terms of improving risk stratification and monitoring of disease progression.

Independently of the radiotracer used, the acquisition of cardiac PET images is much slower than physiological motion, typically 8 min for ^{82}Rb, 20 min for ^{13}N-NH_3 and up to 45 min for ^{18}F-based radiotracers [15, 137]. Therefore, motion compensation techniques are required to reduce image quality degradation due to the effects of cardiac and respiratory motion. Similarly to MR, the most common approach to minimise the effect of cardiac motion in PET is the use of an external ECG device to synchronise the acquisition with the cardiac cycle and sort the acquired data into time frames of 50 to 100 ms, representing different cardiac phases.

For respiratory motion compensation, devices such as respiratory bellows, patients' airflow thermometers and visual tracking systems, can be used to obtain a surrogate signal for respiratory gating [138]. By using a dual-gating approach, i.e. sorting the data according to both the cardiac and respiratory position where it was acquired, a set of nearly motion-free datasets can be obtained. However, since only a fraction of the total detected counts is used for image reconstruction, the SNR of each of these datasets is highly reduced. In static PET imaging, a sufficient number of detected counts can be obtained in each motion-free dataset by increasing the acquisition time. However, for dynamic PET studies this approach is not suitable; since the aim of such studies is to obtain temporal information about the radiopharmaceutical distribution, increasing the total acquisition time would not improve the SNR of the individual gated datasets.

Alternatively, when information about the motion during the acquisition is available, such information can be used to correct the acquired PET data retrospectively by incorporating the motion in the image reconstruction process, as will be described in Section 3.4. The cardiac and respiratory motion information can be obtained from the PET data itself, when the radiotracer distribution provides sufficient information, or from simultaneously acquired MR anatomical images in hybrid PET-MR systems.

3.3 MR Image Reconstruction

MR image reconstruction refers to the mechanisms used for obtaining an image that reflects the spatial distribution of the magnetisation and/or tissue properties from the induced signal that constitutes the measured MR data. This section describes conventional MR image reconstruction algorithms, first describing reconstruction as an inverse problem, and then focusing on widely used algorithms for fully sampled, undersampled and motion-corrected reconstruction.

As described in Section 3.1, MR data is measured in the spatial frequency domain, which is related to the spatial distribution of the magnetisation $M_0(\vec{r})$ by the Fourier transform as follows

$$\begin{aligned} S(\vec{k}) &= \int_v M_0(\vec{r}) \exp(-i2\pi\vec{k}\cdot\vec{r}) d\vec{r} \\ &= \mathfrak{F}\{M_0(\vec{r})\} \end{aligned} \tag{3.33}$$

where $S(\vec{k})$ represents the signal measured in k-space and $\mathfrak{F}\{\cdot\}$ represents the Fourier transform. Although Equation 3.33 provides a continuous description of MR data acquisition, in practice, MR systems acquire a discretised and quantised signal, resulting in a finite number of discrete samples of k-space being acquired. The sampling process can be written as a multiplication of Equation 3.33 by a train of Dirac delta functions, as shown in Equation 3.34a, where $\vec{k}_n$ is the discrete frequency space position where the nth sample of k-space was acquired and $\vec{\Delta}_k$ is the spacing between samples. Using the convolution theorem, it can be shown that sampling in k-space results in replicating the image periodically, with each replica separated by $1/\vec{\Delta}_k$ as shown in Equation 3.34b. In order to avoid overlapping replicas that would distort the reconstructed image, a given sampling density in k-space imposes a limit on the size of the object being imaged. Conversely, for a finite image of width $\vec{r}_w$, it results in a maximum spacing between samples in k-space of $\vec{\Delta}_k = 1/\vec{r}_w$.

$$S(\vec{k}_n) = S(\vec{k}) \sum_{n=-\infty}^{\infty} \delta(\vec{k} - n\vec{\Delta}_k) \tag{3.34a}$$

$$M_0(\vec{r}_n) = \frac{1}{\vec{\Delta}_k} \sum_{n=-\infty}^{\infty} M_0\left(\vec{r} - \frac{n}{\vec{\Delta}_k}\right) \tag{3.34b}$$

The effect of acquiring a finite number of samples N_s in each dimension of k-space can be written as a multiplication in k-space by a box function of width $N_s\vec{\Delta}_k$, which results in a convolution of the image with a sinc function, as shown in Equation 3.35.

$$S^{\sqcap}(\vec{k}_n) = S(\vec{k}_n)\sqcap\left(\frac{\vec{k}}{N_s\vec{\Delta}_k}\right) \tag{3.35a}$$

$$M_0^{\sqcap}(\vec{r}_n) = \frac{1}{\vec{\Delta}_k}\sum_{n=-\infty}^{\infty} M_0\left(\vec{r} - \frac{n}{\vec{\Delta}_k}\right) * N_s\vec{\Delta}_k \,\mathrm{sinc}(N_s\vec{\Delta}_k\vec{r}) \tag{3.35b}$$

From Equation 3.35 it can be observed that, given a fixed $\vec{\Delta}_k$, limiting the number of acquired samples limits the spatial resolution of the image, as the image of a point source will be spread according to the width of the sinc function. The spatial resolution of the image is thus given by $\vec{\Delta}_r = 1/N_s\vec{\Delta}_k$. A further effect of the limited sampling in k-space is the so-called Gibbs ringing artefact, which appears as an oscillating over- and undershoot in areas of the image with sharp transitions due to the convolution with a sinc function.

The described relations between k-space and image space are both instances of the Nyquist's sampling theorem, where the extension of k-space (i.e. the maximum frequency sampled) defines the resolution of the reconstructed image, and the density of samples in frequency space defines the extension of the image. Thus, for a desired field of view (FOV) and image resolution, a defined number of samples with a specific spacing are to be acquired, as depicted in Figure 3.17

When all of the required samples are acquired, the k-space is said to be fully sampled, and image reconstruction can be performed by using the inverse discrete Fourier transform. An underlying assumption when obtaining an image using this method is that the object being scanned can be approximated by a discrete representation, as follows

$$M_0(\vec{r}) = \sum_{j=1}^{J} x_j\phi_j(\vec{r}) \tag{3.36}$$

where $\phi_j(\vec{r})$ are a collection of non-overlapping basis functions, most commonly voxels, and x_j is the value in the jth voxel, namely the intensity value that in MR can be represented in general as a complex number.

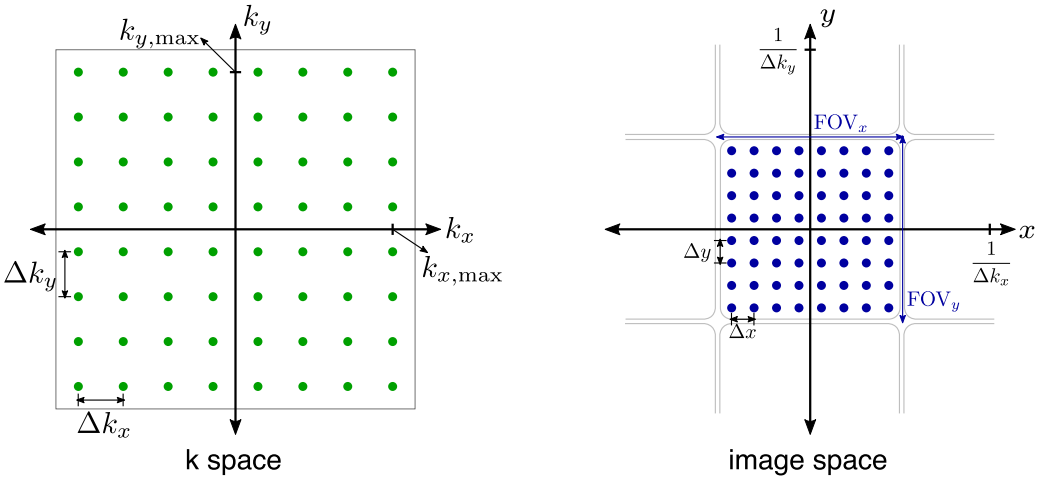

$$\Delta x \approx \frac{1}{2k_{x,\max}} \quad \Delta y \approx \frac{1}{2k_{y,\max}} \qquad \mathrm{FOV}_x \approx \frac{1}{\Delta k_x} \quad \mathrm{FOV}_y \approx \frac{1}{\Delta k_y}$$

Figure 3.17: Relationship between the extension and resolution in k-space and image space. The spacing between the samples acquired in k-space defines the extension of the field of view (FOV) in the image space, while the extension of k-space defines the resolution in image space.

Thus, Equation 3.33 can be re-written as a matrix vector product, as shown in Equation 3.37, where $\mathbf{k}$ represents the sampled k-space, $\mathbf{F}$ is the discrete Fourier transform operator, and $\mathbf{x}$ is a J-dimensional vector containing the voxel intensities of the discretely sampled image. Using this representation, the MR acquisition model can be written as a system of linear equations, and therefore, MR image reconstruction can be studied as a linear inverse problem.

$$\mathbf{k} = \mathbf{F}\mathbf{x} \tag{3.37}$$

In general, any mathematical problem can be classified as being correctly posed or incorrectly posed, and this will have implications on how difficult it is to solve such a problem. According to Hadamard [139], a problem is said to be correctly or well-posed when it meets the following three requirements

1. A solution exists
2. The solution is unique
3. The solution is stable

In the context of MR imaging, the first condition is generally true, because the data is acquired from a real object. However, noisy measurements can lead to

inconsistencies in Equation 3.37. This issue can be solved by reformulating MR image reconstruction as a minimisation problem

$$\mathbf{x}_{\mathrm{LS}} = \arg\min_{\mathbf{x}} \|\mathbf{F}\mathbf{x} - \mathbf{k}\|_2^2 \tag{3.38}$$

where $\mathbf{x}_{\mathrm{LS}}$ is the least squares solution. This minimisation has a closed form solution given by

$$\mathbf{x}_{\mathrm{LS}} = (\mathbf{F}^{\mathrm{H}}\mathbf{F})^{-1}\mathbf{F}^{\mathrm{H}}\mathbf{k} \tag{3.39}$$

where $(\cdot)^{\mathrm{H}}$ denotes the Hermitian transpose of a matrix.

The second of Hadamard's conditions is rarely met in MR imaging. As described above, the discrete sampling in k-space results in replicas of the object in image space. Therefore, there are multiple images that will produce the same data measurements. Similarly, given the characteristics of the Fourier transform, small perturbations in the measured k-space, result in errors across the whole reconstructed image, particularly in low SNR cases. Therefore, the third condition is also usually unmet, so that in general MR image reconstruction is an ill-posed problem.

In order to improve the posedness of the MR reconstruction problem, prior knowledge or prior assumptions about the object being imaged can be incorporated into the minimisation problem described in Equation 3.38. This approach is widely known as regularisation, and it has been successfully used in MR image reconstruction in a variety of contexts, particularly for highly undersampled acquisitions. Some of the most widely used assumptions for regularised MR image reconstruction are that images have minimum energy, which can be expressed as the L2 norm of the image, or that the images are sparse in some domain, which can be expressed as the L1 norm of the transformed image. Both of these approaches result in more stable solutions than the un-regularised problem, however, they require finding an appropriate balance between how well the reconstructed image matches the acquired data (known as data consistency) and how well the image meets the defined assumption. Since regularisation methods were not used in this thesis, they are not described in further detail here, but relevant applications to cardiac MR imaging can be found in [140–144].

It is worth noting that for the fully sampled case under normal SNR conditions, the solution in Equation 3.38 provides a good estimate of the acquired MR image. However, the inversion of the matrix $\mathbf{F}^{\mathrm{H}}\mathbf{F}$ in Equation 3.39 is computationally expensive. Alternatively, iterative methods to find $\mathbf{x}_{\mathrm{LS}}$ can be used. One such method is the well-known conjugate gradient (CG) approach [145], that will be briefly described here.

Considering a general linear problem

$$\mathbf{Q}\mathbf{x} = \mathbf{b} \tag{3.40}$$

with $\mathbf{Q} \in \mathbb{R}^{n \times n}$ a positive definite matrix. The CG method will converge to $\mathbf{x}_{\mathrm{LS}}$ in a finite number of steps by successively minimising the residual $\mathbf{r} = \mathbf{b} - \mathbf{Q}\mathbf{x}$ along an optimal set of directions $\mathbf{p}$. At each iteration, the algorithm moves towards $\mathbf{x}_{\mathrm{LS}}$ along a new direction, orthogonal to all previous search directions. The steps required for performing CG after (it) iterations are summarised in Equation 3.41

$$\lambda_{(\mathrm{it})} = \frac{\mathbf{r}_{(\mathrm{it})}^{\mathrm{T}}\mathbf{r}_{(\mathrm{it})}}{\mathbf{p}_{(\mathrm{it})}^{\mathrm{T}}\mathbf{Q}\mathbf{p}_{(\mathrm{it})}} \tag{3.41a}$$

$$\mathbf{x}_{(\mathrm{it}+1)} = \mathbf{x}_{(\mathrm{it})} + \lambda_{(\mathrm{it})}\mathbf{p}_{(\mathrm{it})} \tag{3.41b}$$

$$\mathbf{r}_{(\mathrm{it}+1)} = \mathbf{r}_{(\mathrm{it})} - \lambda_{(\mathrm{it})}\mathbf{Q}\mathbf{p}_{(\mathrm{it})} \tag{3.41c}$$

$$\mathbf{p}_{(\mathrm{it}+1)} = \mathbf{r}_{(\mathrm{it}+1)} + \frac{\mathbf{r}_{(\mathrm{it}+1)}^{\mathrm{T}}\mathbf{r}_{(\mathrm{it}+1)}}{\mathbf{r}_{(\mathrm{it})}^{\mathrm{T}}\mathbf{r}_{(\mathrm{it})}}\mathbf{p}_{(\mathrm{it})} \tag{3.41d}$$

It is worth noting that the CG algorithm can use any arbitrary initial guess for $\mathbf{x}_{(0)}$. Therefore, in general, the first residual and direction for minimisation, $\mathbf{r}_{(0)}$ and $\mathbf{p}_{(0)}$ respectively, can be written as

$$\mathbf{r}_{(0)} = \mathbf{b} - \mathbf{Q}\mathbf{x}_{(0)} \tag{3.42a}$$

$$\mathbf{p}_{(0)} = \mathbf{r}_{(0)} \tag{3.42b}$$

In the context of MR image reconstruction, the CG algorithm is generally stopped when the norm of the residual is less than a certain threshold or after a pre-defined number of iterations.

3.3.1 Iterative SENSE for Undersampled MR Reconstruction

Despite its potential to produce high-resolution images, MR performance is limited by acquisition time, as a limited number of k-space samples can be acquired within a reasonable scan time. In order to overcome this limitation, undersampled acquisition schemes and specialised reconstruction techniques have been proposed to reduce scan time without degrading image quality or to improve image resolution without significantly increasing acquisition time.

Techniques such as SMASH [146], SENSE [147] and GRAPPA [148] pioneered the field of parallel imaging undersampled MR reconstruction, by using spatial information obtained from the sensitivity of multiple receiver coils to partially recover samples not acquired in k-space. The basic concept behind the SENSE method is depicted in Figure 3.18, where information from the sensitivity of the receiver coils, known as coil sensitivity maps, is used to unfold aliased images acquired with a regular undersampling pattern, i.e. an MR acquisition scheme where k-space lines are skipped at regular intervals.

The SENSE approach can be generalised to other undersampling schemes, in a method known as iterative SENSE. The iterative SENSE method, originally proposed in [150], is discussed here in more detail as it is used for MR image reconstruction throughout this thesis. The acquisition model described by Equation 3.37 assumes a unique receiver coil with a uniform sensitivity over all the acquired field of view. In practice, multiple receiver coils with spatially dependant sensitivities detect the MR signal, thus, for a system with N_C receiver coils (also called channels), N_C measurements of k-space are acquired simultaneously. Each of them can be described as

$$\mathbf{k}_n = \mathbf{F}\mathbf{C}_n\mathbf{x} \;\; \forall n = 1...N_C \tag{3.43}$$

Knowledge about the coil sensitivities $\mathbf{C}_n$ can be obtained by acquiring additional MR measurements with a so-called body coil and information from images reconstructed for each channel [147], or estimating them from the MR data itself [151,152]. Once knowledge about the coil sensitivities is available, images reconstructed separately for each channel can be combined by weighting them appropriately, maximising the signal to noise ratio of the resulting combined image [153]. Alternatively, as

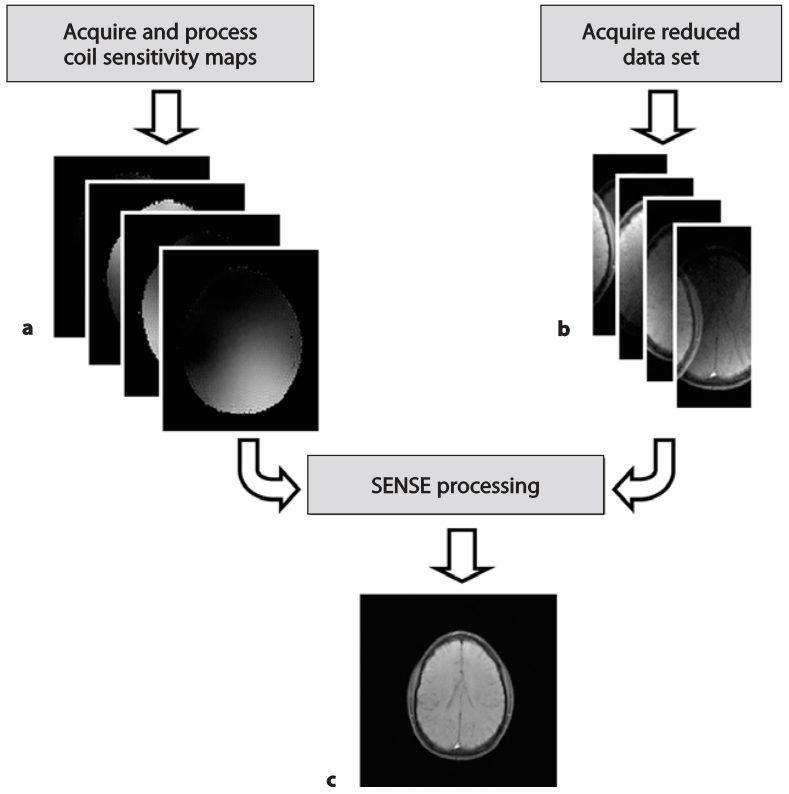

Figure 3.18: SENSE reconstruction method for undersampled MR imaging. Undersampled data are acquired, resulting in aliased images with a reduced field of view (b). By using information from acquired coil sensitivity maps (a), an unfolded image with full field of view can be obtained (c). Reprinted from Griswold M.A. *Basic Reconstruction Algorithms for Parallel Imaging.* In: Schoenberg S.O., Dietrich O., and Reiser M.F., editors. Parallel Imaging in Clinical MR Applications. Springer Berlin Heidelberg 2007 [149].

proposed in the iterative SENSE method, the additional information provided by the multiple coils can be used to reduce the required number of samples. By applying a sampling mask $\mathbf{S}$ that defines which samples of k-space are to be acquired, the MR acquisition can be modelled as

$$\mathbf{k} = \mathbf{SFCx} \tag{3.44}$$

where $\mathbf{k}$ is now a vector that contains the N_C undersampled k-spaces concatenated, and similarly $\mathbf{C}$ contains the corresponding sensitivities for the N_C receiver coils. Although in some cases direct inversion of Equation 3.44 can be used to compute an estimated image $\mathbf{x}$, this is even more computationally expensive than in the single coil case, with a number of operations on the order of N^6 for reconstructing a $N \times N$ 2D image [150]. Alternatively, $\mathbf{x}$ can be iteratively estimated by using the

CG method described above. In order to apply the CG method, Equation 3.44 has to be rewritten as

$$(\mathbf{Q}^{\mathrm{H}}\mathbf{E}^{\mathrm{H}}\mathbf{D}\mathbf{E}\mathbf{Q})\mathbf{x}' = \mathbf{k}' \tag{3.45}$$

with $\mathbf{x}' = \mathbf{Q}^{\mathrm{H}}\mathbf{x}$, $\mathbf{k}' = \mathbf{Q}^{\mathrm{H}}\mathbf{E}^{\mathrm{H}}\mathbf{D}\mathbf{k}$. $\mathbf{E} = \mathbf{SFC}$ is known as the encoding matrix, and includes the coil sensitivities, the Fourier operator and the sampling mask used, $\mathbf{Q}$ is a matrix compensating for the coil sensitivities and $\mathbf{D}$ takes into account the inhomogeneous sampling density in k-space.

3.3.2 Motion-Compensated MR Reconstruction

The iterative SENSE method, as well as the MR acquisition model presented so far, assumes that the object being scanned remains static during the acquisition. In practice, for many MR applications such as cardiac imaging, physiological motion occurs during data acquisition. Respiratory and cardiac motion during MR acquisition results in image artefacts whose effect depends on the region of k-space being sampled. For example, if motion occurs when the outer region of k-space is being sampled (i.e. when sampling higher spatial frequencies), the artefacts will appear as blurred edges of the moving object, and the severity of the artefact will depend on the amplitude of the motion. On the other hand, if motion occurs during the acquisition of the central region of k-space, the whole image is affected, and in extreme cases this could result in ghosting and severe image degradation.

As described in Section 3.1, effects of motion can be minimised in CMRA imaging by acquiring data only in a predefined cardiac and respiratory phase. Alternatively, if knowledge about the motion that occurs during the MR data acquisition is available, its effect can be compensated for during image reconstruction.

Depending on the nature of the motion, there are different approaches that can be used for motion correction in MR reconstruction. For instance, if the motion can be represented by a translation of the object, so that the moved image can be written as

$$\mathbf{x}_b(\vec{r}) = \mathbf{x}(\vec{r} - \Delta\vec{r}_b) \tag{3.46}$$

where $\mathbf{x}$ is the object in a reference position and $\Delta\vec{r}_b$ is the translation vector that moves the object from the reference position to a motion state b, then by using

the definition of the Fourier transform it can be shown that the sampled k-space at motion space b, $\mathbf{k}_b$, is related to the Fourier transform of the object at the reference position, $\mathbf{k}$, by

$$\mathbf{k}_b = \mathbf{S}_b \mathbf{k} \exp(-2\pi i \vec{u} \Delta \vec{r}_b) \tag{3.47}$$

where $\vec{u}$ contains the spatial frequency coordinates of the sampled point in k-space, and $\mathbf{S}_b$ is a sampling matrix containing the information of which samples were acquired at each motion state b. From Equation 3.47 it can be observed that it is possible to correct each motion state to the reference position by applying an appropriate linear phase shift. Then, by aggregating all of the motion states together, a motion-corrected k-space, $\mathbf{k}_{\text{mc}}$, can be obtained as follows

$$\mathbf{k}_{\text{mc}} = \sum_b \mathbf{k}_b \exp(2\pi i \vec{u} \Delta \vec{r}_b) \tag{3.48}$$

Therefore, the motion-corrected reconstruction problem can be reformulated as

$$\mathbf{k}_{\text{mc}} = \left(\sum_b \mathbf{S}_b \right) \mathbf{FCx} = \mathbf{SFCx} \tag{3.49}$$

It is worth noting that once the phase corrections in k-space have been applied, solving Equation 3.49 does not require knowledge about the motion, and any conventional reconstruction technique, such as the CG iterative SENSE technique described above, can be used to estimate the motion-corrected image.

A similar formulation can be used for correcting rotation, shearing and scaling in k-space, allowing for this k-space motion correction technique to compensate for 3D affine motion. This approach has been successfully applied to free-breathing CMRA for respiratory motion compensation, where 2D and 3D iNAVs acquired at each heartbeat have been used to estimate translational or affine motion and correct each segment of k-space acquired, in a beat-to-beat fashion [78, 80, 83, 154]. In this approach, each heartbeat is in principle considered as a different motion state, so the total number of motion parameters to estimate scales linearly with the total number of heartbeats and subsequently, with the length of the acquisition.

Other approaches have used 1D diaphragmatic navigators [155] or self-navigation [156] for sorting the data into a number of respiratory bins, and estimating affine motion from images reconstructed at each respiratory position. These approaches

apply the motion correction in a bin-to-bin fashion, reducing the total number of motion states to ∼3 to 6. However, depending on the size of the respiratory bins, this approach can result in residual intra-bin motion, that can affect the estimation of the motion parameters and the subsequent correction. More recently, approaches based on 2D iNAVs for a combined beat-to-beat 2D translational motion correction with bin-to-bin 3D affine motion correction have been proposed for CMRA [157].

The k-space correction approach is limited to a motion model where the entire object contained in the field of view is affected by a unique affine transformation. In practice, however, different tissues and organs move differently during MR data acquisition. In particular for 3D CMRA, there are some regions of the image that remain mostly static during the acquisition, such as the spine, arms and subcutaneous fat; and different organs, such as the stomach, the liver and the heart, are affected differently by the expansion and contraction of the lungs during the breathing cycle. Therefore, applying a global k-space correction using motion parameters estimated by tracking the heart will induce ghosting and artefacts arising from an erroneous correction of the surrounding organs and tissues.

This issue can be alleviated by using a more general motion model, where each voxel in the field of view is allowed to move freely between different motion states. This motion model then allows for local arbitrary deformations of any magnitude and orientation, including for some regions to remain static (i.e. without any motion). Such motion model, known as non-rigid motion, does not have an equivalent description in k-space, and therefore it cannot be corrected using the approach described above.

Alternatively, non-rigid motion can be included directly in the image acquisition model, as described by Batchelor et al. [158], using a General Matrix Description (GMD) formulation. This approach assumes: 1) that k-space data are acquired in a number of shots, 2) that the motion within each shot is negligible, and 3) that information about the motion of the object relative to a reference position is known for each shot. Using these assumptions, the static MR acquisition model presented in Equation 3.44 can be extended including the effect of the motion, as shown in Equation 3.50

$$\mathbf{k}_c = \sum_b \mathbf{S}_b \mathbf{F} \mathbf{C} \mathbf{U}_b \mathbf{x} \tag{3.50}$$

where $\mathbf{k}_c$ represents the motion-corrupted acquired data, $\mathbf{S}_b$ represents the sampling mask containing the shots acquired in motion state b, and $\mathbf{U}_b$ is a motion operator that transforms the object in the reference position to the motion state b. A motion-corrected image $\mathbf{x}_{\mathrm{MC}}$ can then be directly estimated by solving

$$\mathbf{x}_{\mathrm{MC}} = \arg\min_{\mathbf{x}} \|\mathbf{E}\mathbf{x} - \mathbf{k}_c\|_2^2 \tag{3.51}$$

where the encoding matrix $\mathbf{E}$ now includes motion information, i.e.

$$\mathbf{E} = \sum_b \mathbf{S}_b \mathbf{F} \mathbf{C} \mathbf{U}_b \tag{3.52}$$

Using a formulation similar to Equation 3.45, Equation 3.51 can be solved with the previously described conjugate gradient approach. The GMD approach has been successfully applied to ECG-triggered CMRA imaging in a conventional 1.5 T MR system [159], and that work constitutes the starting point for the MR reconstruction approach used in this thesis.

3.4 PET Image Reconstruction

PET image reconstruction refers to the mechanisms used for obtaining an image that reflects the spatial distribution of the radiotracer concentration from the measured projections that constitutes the measured PET data. This section describes conventional PET image reconstruction algorithms, including a brief description of the PET acquisition model, and then focusing on iterative reconstruction and options for motion compensated PET image reconstruction.

Considering the measurement model presented in Equation 3.31 as starting point, and using a discrete object approximation for the radiotracer spatial distribution similar to the one presented in Equation 3.36, the acquisition model can be written as a matrix-vector product

$$\mathbf{m} = \mathbf{P}\boldsymbol{\rho} \tag{3.53}$$

where the matrix $\mathbf{P}$, usually called the system matrix, contains in each of its elements $p_{i,j}$ information about the contribution of positrons emitted at the spatial location j to the LOR i, $\mathbf{m}$ is a column vector of length I that contains the total number of

coincidences detected for each LOR, and $\boldsymbol{\rho}$ is a vector of length J that represents a discretised version of the spatial distribution of the radiopharmaceutical, also known as the emission map. This model is widely known as forward projection or the forward model.

This simple model can be extended to include the physical processes that occur during PET acquisition as described in Section 3.2. For instance, a diagonal matrix $\mathbf{N}$, known as the normalisation matrix, can be included in the forward model in order to account for the variations in the sensitivity of the individual photon detectors of the PET scanner. Similarly, the effect of attenuation coefficients in each LOR can be arranged in a diagonal matrix $\mathbf{A}$ to be included in the model. Finally, as described in Section 3.2, background coincidences may occur due to scattering of one or both annihilation photons or due to random detection of photons from unrelated positron annihilations. These effects can be accounted for in the measurement model by including an additive term $\mathbf{b}$. Including all these effects, a more complete and realistic forward model can be obtained (Equation 3.54).

$$\mathbf{m} = \mathbf{NAP}\boldsymbol{\rho} + \mathbf{b} \tag{3.54}$$

The image reconstruction problem consists then in estimating $\boldsymbol{\rho}$ given $\mathbf{m}$ and knowledge of the physical model ($\mathbf{N}$, $\mathbf{A}$, $\mathbf{P}$, $\mathbf{b}$). Similarly to Equation 3.39, a straightforward method to do this is to use an analytical reconstruction approach so that

$$\hat{\boldsymbol{\rho}} = (\mathbf{P}^{\mathrm{T}}\mathbf{P})^{-1}\mathbf{P}^{\mathrm{T}}(\mathbf{NA})^{-1}(\mathbf{m} - \mathbf{b}) \tag{3.55}$$

It is worth noting that the matrix $\mathbf{P}$ is not necessarily square, as the number of image voxels J is in general smaller than the number of measurements I for 3D PET imaging, and thus a direct inversion of the system matrix is not possible. Moreover, given that for modern PET systems both I and J are in the order of 1×10^4 to 1×10^6, the inversion of $(\mathbf{P}^{\mathrm{T}}\mathbf{P})$ is computationally expensive, and in most cases not possible, as the system matrix $\mathbf{P}$ is rarely full rank. Finally, this reconstruction approach might produce physically unrealistic negative values in the radiopharmaceutical distribution due to the subtraction of estimated background coincidences in regions of low or null radioactivity.

Alternatively, statistical iterative PET reconstruction can be performed by modelling the acquisition process using Equation 3.54 and using a series of forward-projection ($\mathbf{P}$) and back-projection ($\mathbf{P}^{\mathrm{T}}$) operations that result in a reliable and realistic estimate of $\boldsymbol{\rho}$.

3.4.1 Statistical PET Reconstruction

The nature of PET data acquisition, based on counting inherently random occurrences of positron annihilations, results in randomness in the measured data, which can be statistically modelled as a collection of conditionally independent random Poisson processes. The conditional probability of observing m_i coincidences in sinogram bin i is therefore Poisson distributed with expectation q_i

$$P(m_i|q_i) = \frac{q_i^{m_i} \exp(-q_i)}{m_i!} \tag{3.56}$$

Considering that every q_i is a function of the radiotracer distribution $\boldsymbol{\rho}$, as shown in the forward model in Equation 3.54, the likelihood of $\boldsymbol{\rho}$ given the set of measurements $\mathbf{m}$ can be written as

$$O(\boldsymbol{\rho}|\mathbf{m}) = \prod_{i=1}^{I} \frac{q_i(\boldsymbol{\rho})^{m_i} \exp(-q_i(\boldsymbol{\rho}))}{m_i!} \tag{3.57}$$

A reasonable choice for estimating $\boldsymbol{\rho}$ in this context is to maximise $O(\boldsymbol{\rho}|\mathbf{m})$, i.e. to estimate the most likely radiotracer spatial distribution given the acquired projections. In order to make the function easier to maximise, the log-likelihood can be used instead; since $\ln(\cdot)$ is a monotonically increasing function, any estimate that maximises $\ln(O(\boldsymbol{\rho}|\mathbf{m}))$ will maximise $O(\boldsymbol{\rho}|\mathbf{m})$. Thus, the maximum-likelihood estimator for $\boldsymbol{\rho}$ can be written as

$$\boldsymbol{\rho}_{\mathrm{ML}} = \arg\max_{\boldsymbol{\rho}} \sum_{i=1}^{I} (m_i \ln(q_i(\boldsymbol{\rho})) - q_i(\boldsymbol{\rho})) \tag{3.58}$$

Equation 3.58 does not have an analytical solution. Instead, iterative methods that seek to converge to the maximum likelihood estimate have been commonly used in the PET reconstruction literature. The most widely known of such methods is the maximum-likelihood expectation-maximisation (MLEM) algorithm, first pro-

posed by Shepp and Vardi [160], that converges to $\boldsymbol{\rho}$ after a relatively large number of iterations of a two-step algorithm. In the first step, the forward model of the acquisition (Equation 3.54) is applied to the current estimate of the radiopharmaceutical distribution, and the estimated projections are compared with the measured projections by taking the ratio. In the second step, this ratio is back-projected and used to update the estimation of the activity distribution. The update equation of the MLEM algorithm can be written as

$$\boldsymbol{\rho}^{(\mathrm{it}+1)} = \frac{\boldsymbol{\rho}^{(\mathrm{it})}}{(\mathbf{NAP})^{\mathrm{T}}\mathbf{1}_I}(\mathbf{NAP})^{\mathrm{T}}\frac{\mathbf{m}}{\mathbf{NAP}\boldsymbol{\rho}^{(\mathrm{it})} + \mathbf{b}} \tag{3.59}$$

where $\boldsymbol{\rho}^{(\mathrm{it})}$ is a column vector that contains the PET voxel values at iteration (it) and $\mathbf{1}_I$ is a column vector of ones of length I. All vector multiplications and divisions are taken element-by-element.

This algorithm requires an initial estimation of the radiotracer distribution. Most conventionally a blank image is used to initialise the algorithm (i.e. $\boldsymbol{\rho}^{(0)} = \mathbf{1}_J$). The multiplicative nature of the update equation of the MLEM algorithm implies that it is not possible to produce negative or zero voxel values, resulting in a bias in high-noise low-activity regions.

As mentioned above, the MLEM algorithm requires a relative large number of iterations to produce a good image, which has prevented its widespread use in clinical settings. In order to alleviate this problem, an accelerated version of the MLEM algorithm, called ordered-subsets expectation-maximisation (OSEM) is typically used instead [161]. The OSEM algorithm groups the acquired projections into a number of subsets, and applies the MLEM algorithm to each subset in turns, using the estimated activity distribution obtained with one of the subsets as starting point for the next one. As the system matrix for each of the subsets is smaller, the forward and back-projection process for updating the activity estimation is faster than in traditional MLEM. OSEM is nowadays the most widely used PET reconstruction algorithm in clinical systems [162].

3.4.2 Motion Compensation in PET

The PET acquisition model described so far assumes that the object being scanned remains static during the whole acquisition. In cardiac PET imaging, however, physiological (cardiac and respiratory) motion occurs during the scan, resulting in image quality degradation if the motion is not compensated for. A moving emission map will produce image blurring around the moving organs, due to the assignment of coincidences from moving tissues to the wrong LORs. Furthermore, motion can produce mismatches between the moving emission map and the static attenuation map, which is conventionally acquired during a breath-hold, inducing artificial voids or enhancements in the PET signal. These artefacts are particularly severe in regions of abrupt change in the attenuation values, such as the heart-lung boundaries. Indeed, some studies have shown that motion-induced emission-attenuation mismatches can appear as false myocardial perfusion defects [163].

Although such artefacts can be minimised by rejecting data acquired outside a pre-defined respiratory and cardiac phase, as described in Section 3.2, this approach reduces the amount of data available for PET image reconstruction, increasing image noise. Alternatively, if motion information throughout the PET acquisition is available, e.g. it can be estimated from the PET data itself, or from simultaneously acquired CT or MR data, two different approaches can be used to compensate for motion in PET images: reconstruct transform average (RTA) and motion-compensated image reconstruction (MCIR).

In RTA approaches, also known as reconstruct register average (RRA) or post reconstruction registration (PRR) [164], the acquired data is first binned into a number of near motion-free datasets that are to be reconstructed independently, using any standard algorithm, most typically OSEM.

In order to avoid mismatches between emission and attenuation maps, an attenuation map $\mathbf{A}_b$ is created for each motion-free dataset, by using the motion information to transform the attenuation map acquired at the reference position to the corresponding motion state b. Thus, omitting the subsets notation for simplicity, each bin is reconstructed according to

$$\boldsymbol{\rho}_b^{(\mathrm{it}+1)} = \frac{\boldsymbol{\rho}_b^{(\mathrm{it})}}{(\mathbf{N}\mathbf{A}_b\mathbf{P})^{\mathrm{T}}\mathbf{1}_I}(\mathbf{N}\mathbf{A}_b\mathbf{P})^{\mathrm{T}}\frac{\mathbf{m}_b}{\mathbf{N}\mathbf{A}_b\mathbf{P}\boldsymbol{\rho}_b^{(\mathrm{it})} + \mathbf{b}} \tag{3.60}$$

where $\boldsymbol{\rho}_b^{(\mathrm{it})}$ is the vector representation for the PET image at motion state b after (it) iterations of the reconstruction algorithm, and $\mathbf{m}_b$ is a vector that contains the fraction of the data acquired in motion state b. In this model, background coincidences are assumed to vary slowly compared to changes in the activity distribution $\boldsymbol{\rho}$, so the effect of motion on them is typically neglected.

Once all frames have been reconstructed, they are transformed back to a reference frame using inverse motion operators, and ultimately aggregated so that one motion compensated image is obtained using all measured data, as depicted in Figure 3.19. The reference frame for cardiac PET imaging is usually end-expiration and end-diastole. Instead of using a simple average, an alternative approach has been recently proposed in [165], where images are weighted before being combined according to the estimated intra-frame motion amplitude. Thus, better quality images acquired at quiescent phases of the cardiac and respiratory cycles have more influence in the final motion compensated image.

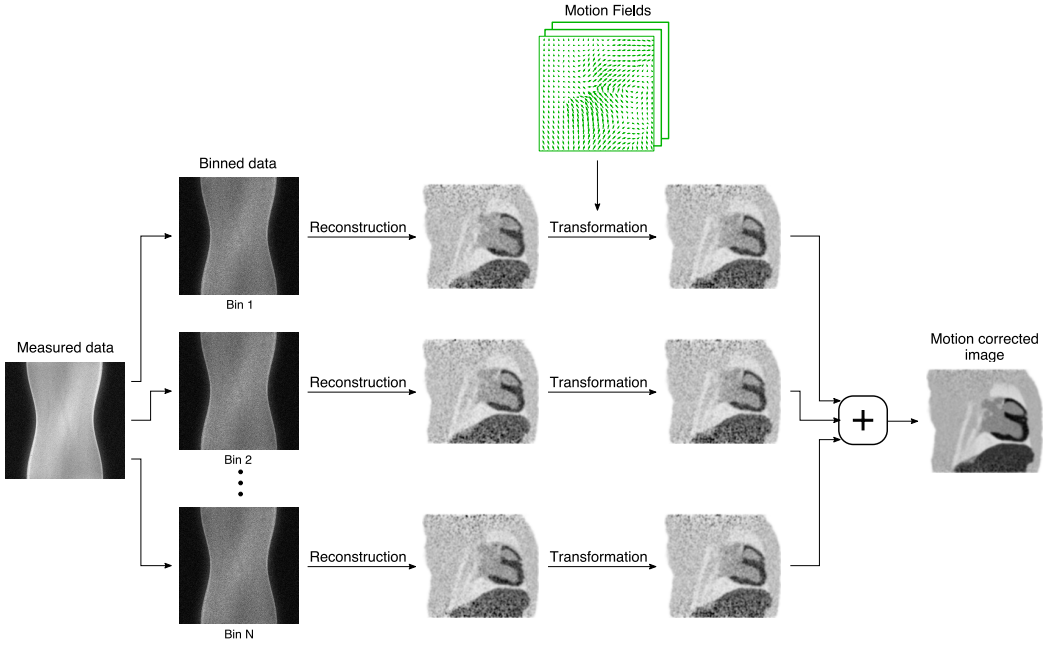

Figure 3.19: Reconstruct Transform Average (RTA) approach for motion compensated PET imaging. Acquired data is binned into near motion-free datasets that are independently reconstructed. These reconstructed images are transformed to a reference frame using inverse motion operators, and aggregated to produce the motion-corrected PET image.

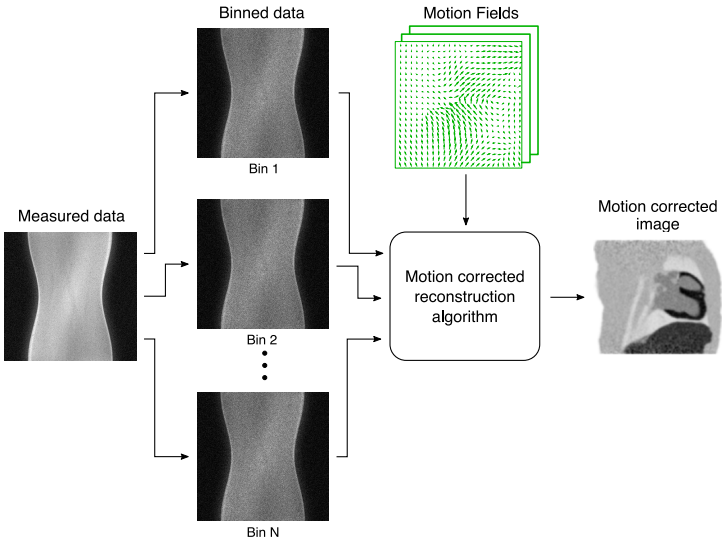

Figure 3.20: Motion Compensated Image Reconstruction (MCIR) approach for PET imaging. Acquired data is binned into near motion-free datasets and information about the motion between such frames is included in an iterative reconstruction algorithm, directly resulting in a motion-corrected PET image.

In MCIR approaches [166], the motion information is incorporated as an additional term in the forward projection model, so that a motion-corrected image is directly obtained by modelling the motion during the image reconstruction process. Theoretically, if continuous motion information is available throughout the PET acquisition, PET data could be corrected in a coincidence-by-coincidence fashion, by incorporating the transformation between the current position and a reference position into the forward model of any iterative reconstruction algorithm.

This approach would lead to increased and impractical reconstruction times, so in practice PET data is also binned into near motion-free frames in MCIR approaches and the motion information is also used in a frame-to-frame fashion (Figure 3.20). For instance, the MLEM algorithm can be modified to include motion as part of the forward model, as shown in Equation 3.61 [167].

$$\boldsymbol{\rho}^{(\mathrm{it}+1)} = \frac{\boldsymbol{\rho}^{(\mathrm{it})}}{\sum_b (\mathbf{N}\mathbf{A}_b\mathbf{P}\mathbf{U}_b)^{\mathrm{T}}\mathbf{1}_I} \sum_b (\mathbf{N}\mathbf{A}_b\mathbf{P}\mathbf{U}_b)^{\mathrm{T}} \frac{\mathbf{m}_b}{\mathbf{N}\mathbf{A}_b\mathbf{P}\mathbf{U}_b\boldsymbol{\rho}^{(\mathrm{it})} + \mathbf{b}} \tag{3.61}$$

where $\boldsymbol{U}_b$ is a motion operator that transforms an image at the reference position to a motion state b and $\mathbf{A}_b$ is a diagonal matrix containing the effect of the attenuation at position b. In this case, $\boldsymbol{\rho}$ corresponds to the motion-corrected image reconstructed at the reference position. Also in this case the background coincidences are assumed

to vary slowly compared to the activity distribution, so the effect of motion on them is neglected.

The performance of the RTA and MCIR approaches for motion compensation has been compared in a number of abdominal and thoracic simulation studies, including respiratory motion only. A study based on pseudo-PET images simulated from healthy volunteer abdominal and thoracic MR data [168] concluded that RTA and MCIR reconstructions result in comparable global measures of similarity compared with a motion-free reference, but RTA produces greater resolution loss than MCIR.

Additional studies [169,170] have shown that MCIR achieves better contrast and smaller bias in low-activity regions compared to RTA at the expense of reduced SNR in the final motion compensated image. These studies also showed that MCIR has a smaller mean squared error (MSE) only for a small number of OSEM iterations (i.e. 1–2). As the number of iterations increases, RTA has significantly less MSE than MCIR, suggesting that MCIR may provide better overall performance only when SNR is high. For low SNR cases, MCIR can be applied in conjunction with regularisation methods to control noise levels. For instance, a regularised MCIR based on a maximum *a posteriori* one-step-late algorithm with median-root-prior has been proposed in [171]. This study concluded that regularised MCIR achieves less bias and MSE, and similar contrast and SNR compared to regularised RTA.

3.5 Cardiac PET-MR: State-of-the-Art

Since the development of simultaneous PET-MR scanners, cardiovascular imaging has been proposed as one of the clinical applications that could benefit the most from this new technology. The complementary anatomical and functional information offered by both imaging modalities, and the ability to simultaneously produce high-resolution MR images with superior tissue contrast and quantitative PET images has shown promise for improving the diagnosis of different cardiac conditions from a single scan session. This section describes some of the clinical applications that have been proposed for cardiac PET-MR imaging, and briefly reviews the state-of-the art techniques for motion correction in the context of cardiac PET-MR.

3.5.1 Clinical Applications

The recently published joint statement by the European Society of Cardiovascular Radiology (ESCR) and the European Association of Nuclear Medicine (EANM) suggests that including hybrid PET-MR examinations in the routine clinical practice could enhance the diagnosis and aid decisions in the management of a variety of cardiac conditions, including stable coronary artery disease, acute coronary syndrome, ischaemic cardiomyopathies and cardiac inflammation [24]. The potential of PET-MR for each of these applications is briefly discussed hereafter.

As mentioned before, PET has been established as the reference modality for myocardial perfusion imaging, allowing for an accurate diagnosis of obstructive CAD through the assessment of myocardial perfusion defects. Recent studies using simultaneous PET-MR scanners have shown a good correspondence between myocardial perfusion quantified by PET and by dynamic contrast enhanced (DCE) MRI imaging [172]; however, the capabilities of the PET-MR system in this study were mostly used to provide a gold-standard for cross validation between imaging modalities. A different approach for perfusion imaging is proposed in [173], where MR images are used for MR-based cardiac motion correction of simultaneously acquired ^{18}F-Flurpiridaz (a novel perfusion radiotracer), showing improvements in image quality in a pre-clinical study.

In the context of CAD, the feasibility of imaging atherosclerotic plaque by ^{18}F-NaF using a PET-MR system has been recently demonstrated in a cohort of 12 patients with either documented CAD or documented risk factors for developing the disease [174]. This approach, in combination with simultaneously acquired MR anatomical images that provide information about the plaque location and integrity of the artery lumen, in addition to novel MR sequences that allow for characterisation of intraplaque haemorrhage [175,176], could potentially allow for a comprehensive non-invasive assessment of vulnerable plaque.

A more conventional approach for PET-MR in CAD has been the use of ^{18}F-FDG in combination with conventional late Gadolinium enhancement (LGE) imaging by MR. Whereas LGE allows detection of both transmural and non-transmural scar in the myocardium, ^{18}F-FDG allows identification of areas of viable myocardium. By

combining both modalities, an improved stratification of patients that could benefit from revascularisation therapy can be achieved [177]. The simultaneous ^{18}F-FDG PET–LGE MRI imaging approach has been also demonstrated in patients after acute myocardial infarction [178–180]. In [178], good correlation was found between the area of reduced ^{18}F-FDG uptake (defined as $> 40\%$ reduction compared to the remote myocardium) and the area-at-risk (AAR) as estimated by delineating the endocardial surface area, although ^{18}F-FDG overestimated the size of the AAR. Similarly, in [179] a very good correlation was found between the size of AAR as defined by a reduction of $> 50\%$ in ^{18}F-FDG uptake and as defined by delineation in MR T2-mapping. In both studies, the AAR estimated by reduced ^{18}F-FDG uptake was larger than the infarct size delineated in the LGE images, suggesting that reduced ^{18}F-FDG uptake can accurately estimate myocardial viability early after infarct. Furthermore, the presence of viable myocardium as estimated by residual ^{18}F-FDG uptake was shown to predict segmental wall motion recovery in follow-up examinations [179, 180].

Finally, the simultaneous ^{18}F-FDG PET–LGE MRI approach has been used to improve the differential diagnosis in myocardial inflammation. Recent clinical experience has been reported in [181], including cases of myocarditis, congestive heart failure and cardiac sarcoidosis. In particular, the latter has received a lot of attention in the cardiac PET-MR community, as early reports suggest that the complementary information obtained by PET and MR improves the diagnostic accuracy of cardiac sarcoidosis compared to using each modality alone [182–184]. Therefore, cardiac PET-MR could potentially become the reference modality for a non-invasive tool for the detection and monitoring of cardiac involvement in patients with known or suspected sarcoidosis.

3.5.2 Motion Correction for Cardiac PET-MR

As mentioned in Chapter 1, simultaneous PET-MR systems have made possible the use of MR-measured motion fields to correct the motion-degraded PET data using either of the techniques for motion-compensated PET imaging described in Section 3.4.2. In the early days of MR-based PET motion compensation, several simulation studies showed improved lesion detectability and reduced noise levels in motion

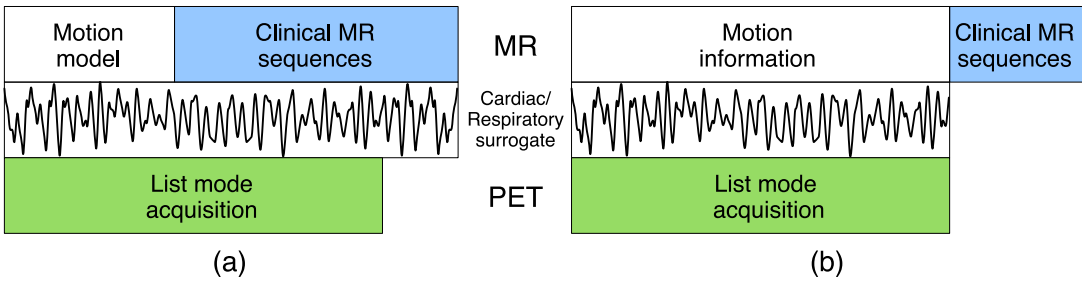

Figure 3.21: Conventional approaches for MR-based motion correction of PET data in PET-MR imaging. (a) Pre-calibrated motion models estimate a motion model before or during the first part of the PET-MR examination. (b) Simultaneous motion models estimate motion information by using MR images acquired throughout the whole PET data acquisition.

compensated images compared to gated images, in addition to reduced blurring and improved contrast compared with uncorrected images for a variety of cardiac [167, 185] and abdominal and thoracic [168,169,171,186–189] applications. Phantom [190–193] and preliminary patient studies [165, 193–197] later confirmed those findings. It is worth noting that while the phantom studies included cardiac applications showing promising results, the patient studies focused mainly on respiratory motion correction for thoracic and abdominal ^{18}F-FDG PET-MR imaging in oncology.

Most of the current approaches for MR-based PET motion compensation estimate the motion-induced deformation of the organs within the field of view by using one of the following techniques: 1) pre-calibrated motion modelling, where MR images are acquired before or during the first few minutes of the PET acquisition to form a motion model that is then used to correct for motion during the whole PET acquisition, or 2) simultaneous motion modelling techniques, where motion is estimated by applying image-based registration algorithms to MR images acquired throughout the whole PET data acquisition (Figure 3.21). Both of these approaches have been used to estimate cardiac, respiratory, or cardiac and respiratory motion for motion-compensation in PET-MR, using a variety of MR acquisition sequences, as described hereafter.

The most widely used acquisition techniques in MR imaging to estimate cardiac motion are cine MR and tagged MR imaging [198]. As described in Section 3.1, for cine MR imaging, data are continuously acquired throughout several cardiac cycles and retrospectively binned into several motion-free cardiac phases using a simulta-

neously acquired ECG signal. In terms of motion estimation for PET-MR, cine MR has been used as a simultaneous motion model technique. For instance, stacks of 2D cine MR images have been used to estimate cardiac motion in a phantom PET-MR study, using B-spline non-rigid registration of 25 cardiac phases with respect to an arbitrary reference phase [191]. An important drawback of this approach is that no information about 3D motion is available, so errors due to misalignment between slices can be produced. In order to measure 3D motion accurately, in [185] simulated 3D T_1-weighted images were used to estimate motion between eight cardiac phases and the end-diastolic phase using an optical flow framework. Although such an approach could potentially be extended to *in vivo* studies, cardiac motion can be difficult to track in regions with uniform contrast such as the myocardium.

In tagged MR, radiofrequency prepulses are used to generate a pattern of alternating bright and dark stripes over the image being acquired, allowing for tracking deformation even in areas of uniform contrast. The most commonly used tagged MR techniques are based on SPAMM (SPAtial Modulation of Magnetisation), proposed by Axel and Dougherty in [199], where the deformation of a sinusoidal pattern superimposed on 2D images can be used to visualise and estimate motion. The pattern fades after the tagging preparation pulse due to spin relaxation, so multiple acquisitions are required in order to characterise the entire cardiac cycle. Furthermore, in order to track the 3D motion of the heart, multiple orthogonal image planes (i.e. coronal, sagittal, transverse) or orthogonally motion-encoded volumes need to be acquired [200]. For this reason, tagged MR images are simultaneously acquired with an external ECG signal that allows for the triggering of the tagging preparation pulse and gating of the data in different cardiac phases. Once the tagged MR images have been reconstructed for each cardiac phase, different approaches can be used to estimate motion. B-spline non-rigid registration of SPAMM-tagged images has successfully been applied to track myocardial motion in PET-MR phantom studies [163, 192], and more recently in a proof-of-concept clinical study [193] dividing the cardiac cycle into 9 phases.

One of the main disadvantages of tagged MR is the extended time required to obtain a complete description of the motion during the cardiac cycle, so it is typically used as a simultaneous motion model technique. As reported in [193], the acquisition

time of fully sampled tagged MR images for motion estimation in a patient experiment was more than 8 min, preventing the application of other clinically relevant sequences to assess cardiac anatomy and function. Half k-space acquisition [192], and compressed sensing and parallel imaging reconstruction techniques [193] have been employed to accelerate the acquisition of tagged MR images and move towards a pre-calibrated motion model approach. For instance, in [193] it was demonstrated that by combining tagged MR with conventional compressed sensing techniques, it was possible to accelerate the acquisition 8 times, and still provide accurate cardiac motion estimation, yielding motion-corrected PET images of a similar quality to those corrected with motion estimated from fully sampled tagged MRI. This was demonstrated both in phantom studies and in one patient, using myocardial defect contrast as measurement of image quality.

Unlike the case of cardiac motion, pre-calibrated motion model techniques have been widely used for estimating respiratory motion. These techniques aim to create a patient-specific motion model from the MR imaging data, usually by acquiring a surrogate signal simultaneously with the imaging data, so that the created model approximates the relationship between the surrogate and the motion [201].

In the context of PET-MR imaging, pre-calibrated motion models are based on near real-time MR images acquired prior to, or during a fraction of the simultaneous PET-MR acquisition. The first approach has been applied in MR-based PET simulation studies [169,186,188,202–205] using MR data acquired from healthy subjects. 3D T_1-weighted turbo field echo (TFE) MR images were acquired using parallel imaging (SENSE) with an acceleration factor of 8, so that each whole-thorax volume was acquired in 0.7 s. Motion displacements estimated from hierarchical local affine registration of these fast acquired 3D MR volumes are modelled as functions of a 1D surrogate signal, so that during the subsequent simultaneous PET-MR acquisition only information from the position of a 1D navigator echo is required for motion estimation. In [187], 2D images were used as surrogate for a statistical motion model, and more robust results were obtained compared with 1D surrogates.

A different pre-calibrated model-based approach was proposed in [197], and tested in thoracic images of four patients. Here, a motion model is generated during a one-minute PET-MR acquisition by acquiring multiple high-resolution 2D sagittal

spoiled gradient echo MR images, with a temporal resolution of 0.3 s. During the remainder of the acquisition, a respiratory surrogate extracted from the list-mode PET data itself is used to perform MR-based motion correction, so no additional 1D surrogate is required. One of the limitations of this approach is that given the 2D nature of the MR acquisition, the left-right component of the motion is neglected. A similar approach that addresses this issue is proposed in [194], where high-resolution 2D sagittal acquired during a 3 minute scan are retrospectively reordered to form four 3D volumes representing different respiratory positions. These 3D volumes are then used for estimating non-rigid motion fields via image registration, using end-expiration as reference position. While in both studies the authors stated that reducing the time required for motion estimation was desirable in order to provide time for diagnostic MR sequences to be acquired simultaneously with PET, there is no discussion about the impact of changing the time allocated for generating the motion model.

Simultaneous motion model approaches have also been used for estimating respiratory motion, typically by applying non-rigid registration to images reconstructed at different respiratory bins (so called bin-to-bin respiratory motion estimation). Thanks to the capability that MR offers for monitoring respiratory motion, most of these techniques rely on 1D navigator echoes or self-gating approaches instead of external devices for binning the acquired MR data. The 1D navigator approach has been used in two PET-MR patient studies. In [206], data acquired using a golden-angle radial spoiled gradient echo pulse sequence is retrospectively binned into eight respiratory bins for thoracic imaging, while in [195] data acquired using a navigated steady-state free-precession MR acquisition protocol was binned into seven bins for abdominal imaging.

A self-gating approach for respiratory motion estimation in PET-MR was proposed in [165, 207] and evaluated in abdominal and thoracic images of 15 patients. MR data was acquired using a 3D T_1-weighted golden-radial stack-of-stars spoiled gradient echo with fat suppression sequence. The stack-of-stars trajectory allows the estimation of a respiratory surrogate from the centre of the k-space ($k_x = k_y = 0$) for each line acquired in the central slice of the volume ($k_z = 0$). Based on this signal, the MR data was retrospectively binned into 2 to 15 uniform respiratory

bins. The authors concluded that up to 10 bins are required to recover the full respiratory amplitude depending on the respiratory pattern of the patient. However, when analysing the average binning error, with only 5 bins the 95th percentile fell below 2 mm, suggesting that increasing the number of bins over 5 does not have a significant impact in the accuracy of the estimated motion.

A study comparing the performance of a simultaneous motion model using five different 1D respiratory surrogates for retrospective binning of MR data was presented in [196], including respiratory bellows, an MR-based self-gated signal, and three PET-based navigators, finding high correlation between the different respiratory signals. This study was performed in 20 patients, who were referred for diagnosis of malignant diseases in the abdomen (11 patients), heart (1 patient) and thorax (8 patients).

A different bin-to-bin-based simultaneous motion model approach involves the acquisition of near real-time MR images that are subsequently classified in different respiratory phases. In [191], an image-based navigator is used to select 6 respiratory phases from a set of 35 acquired 3D TFE images of a phantom capable of both cardiac and respiratory motion.

Tagged MR imaging has also been used to estimate respiratory motion to improve accuracy in regions with uniform contrast such as the liver. B-spline non-rigid registration of tagged MR images using two different similarity measures (i.e. sum of squared differences and negative mutual information) has been applied to PET-MR abdominal imaging of rabbits and non-human primates [208]. The authors found no statistically significant difference in the detectability of lesions in motion-corrected PET images using either similarity measure. In [190], respiratory motion is estimated through regularised phase-tracking of multi-slice tagged MR images. The proposed approach was demonstrated to be robust against noise in a numerical simulation study, but its applicability to *in vivo* data has not been tested. As discussed by the authors, a severe limitation of tagged MR approaches for respiratory motion estimation is the lack of signal in the lungs.

Finally, in order to address both cardiac and respiratory motion simultaneously, dual-gating approaches have been proposed in the literature for both pre-calibrated and simultaneous model techniques. In [185], respiratory motion was assumed to be

rigid within each cardiac phase, so rotation and translation parameters that characterise motion between respiratory phases were estimated using least squares minimisation. Using these parameters, respiratory corrected MR images were reconstructed for each cardiac phase and afterwards, non-rigid cardiac motion was estimated using optical flow. A more general framework, where non-rigid registration of dual gated images into a reference cardiac and respiratory phase is performed assuming the existence of 1D surrogates for both the cardiac-induced and respiratory-induced motion of the heart, has been shown in simulation studies [167, 209] and more recently in preliminary patient studies [210, 211].

While pre-calibrated motion model approaches allow for real-time motion estimation, they do not measure motion directly during PET data acquisition, so they are susceptible to changes in the cardiac and respiratory pattern of the patient during long examinations. This limitation is alleviated when using simultaneous motion modelling approaches, which capture the motion throughout the whole data acquisition process. However, the main drawback of these approaches is that the MR images acquired simultaneously with PET are in general designed only for motion estimation purposes, so they have limited or no diagnostic value.

Furthermore, in the context of cardiac PET-MR applications, both pre-calibrated and simultaneous motion modelling techniques have focused on improving only PET image quality using motion information estimated from MR. Clinically useful MR images are in general acquired after the simultaneous PET-MR examination, leading to long acquisition times and misaligned diagnostic PET and MR images.

More recently, a novel approach where the motion estimated from MR is used to simultaneously correct both PET and MR images has been proposed [212]; however, MR images showed reduced contrast between blood and myocardium due to the absence of preparation pulses and limited spatial resolution for visualisation of the coronary arteries, impairing the diagnostic use of such MR images.

In the following chapters, the novel approach for motion-corrected cardiac PET-MR imaging developed in this thesis will be described, where respiratory and cardiac motion information estimated from MR is used to correct for non-rigid motion in simultaneously acquired CMRA and ^{18}F-FDG PET data, allowing for the visualisation of the coronary arteries and myocardial integrity in a single efficient examination.

Chapter 4:
Respiratory Motion-Corrected CMRA-PET

Respiratory motion is a major source of image degradation in both PET and MR imaging. In particular, within the context of cardiac PET-MR imaging, respiratory motion can result in image blurring and ghosting artefacts in MR, and image blurring and artefacts due to mismatches between attenuation maps and emission maps in PET. As described in Chapter 3, the development of simultaneous hybrid PET-MR scanners has stimulated the development of novel approaches to address the problem of respiratory motion in cardiac PET-MR imaging. Most of such approaches rely on acquiring MR images with sufficient contrast, spatial and temporal resolution to produce motion estimates for improving PET image quality. In other words, such MR images are designed to provide motion information only, hindering their use for diagnostic purposes.

In this Chapter a novel framework for efficient free-breathing simultaneous whole-heart CMRA-PET is introduced. An acquisition that enables non-rigid respiratory motion correction of simultaneously acquired CMRA and cardiac PET data was developed, allowing for the visualisation of the coronary arteries and assessment of myocardial integrity from a single examination. This was achieved by including a 2D image navigator (iNAV) in the MR acquisition sequence, which allows estimation of the position of the heart within the respiratory cycle at each heartbeat. Then, by combining a beat-to-beat 2D translational motion correction with a bin-to-bin 3D non-rigid motion correction approach for CMRA, the MR-derived non-rigid motion fields can be used to correct for both the CMRA and the simultaneously acquired

PET data to the same respiratory position.

The beat-to-beat 2D translational motion correction compensates for the main components of intra-bin motion, while 3D non-rigid deformations of the heart during the breathing cycle are captured by the bin-to-bin motion correction. This approach is highly efficient since nearly all acquired MR data is used for reconstruction (∼100% scan efficiency after respiratory outlier rejection), resulting in a shorter scan time than conventional 1D diaphragmatic gated MR acquisitions, as has recently been demonstrated for coronary and vessel wall balanced steady-state free precession (bSSFP) MR imaging at 1.5 T [159]. Additionally, it enables the acquisition of diagnostic MR and PET images simultaneously, significantly reducing the total exam time compared to techniques that perform diagnostic MR acquisitions after the simultaneous PET-MR scan. The framework for motion-corrected CMRA reconstruction was tested in ten healthy subjects and compared to a reference scan with 1D diaphragmatic navigator gating and tracking. The motion-corrected PET-CMRA approach was then tested in five oncology patients (without known or suspected cardiac disease) that exhibited ^{18}F-FDG uptake in the myocardium. Some of the results presented in this chapter have been published as a journal article [27].

4.1 Methods

4.1.1 Image Acquisition

The proposed PET-MR acquisition protocol consists of an ECG-triggered free-breathing CMRA acquisition simultaneously acquired with list-mode PET data on a 3 T hybrid PET-MR system. Before the simultaneous PET-MR acquisition, a 2D cine acquisition is performed to determine a subject-dependent trigger delay and acquisition window for CMRA, with both estimated visually targeting the mid-diastolic quiescent period of the cardiac cycle. Following this, a Dixon-based attenuation map (called μ-map hereafter) is acquired during a breath-hold at end-expiration [117]. This approach uses a conventional two-point Dixon acquisition in combination with a water/fat separation algorithm, so that each voxel within the image is classified as belonging to one of four categories: background, lung,

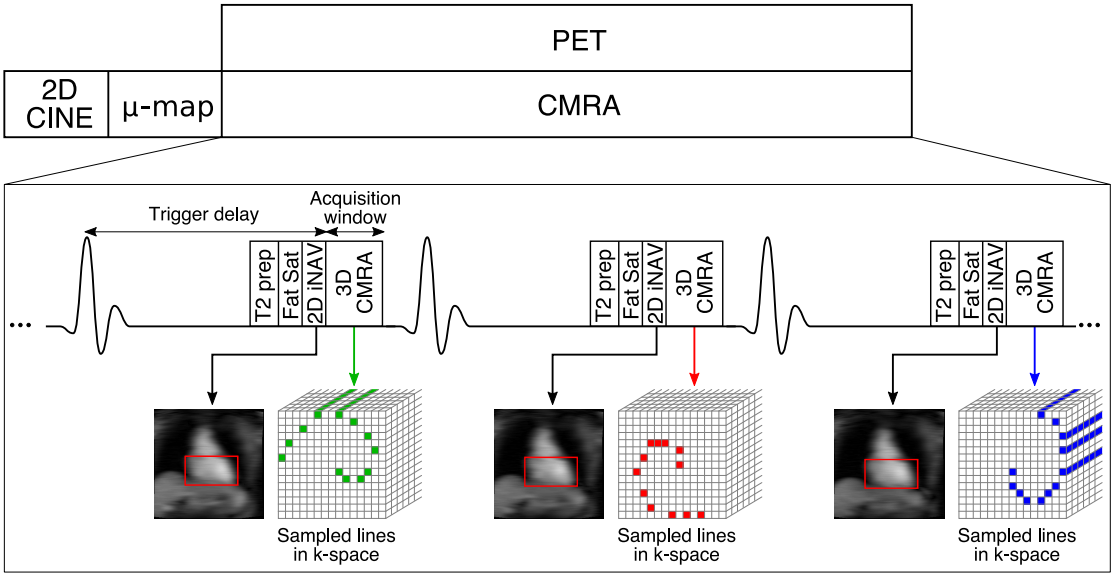

Figure 4.1: Cardiac PET-MR acquisition scheme. Before the simultaneous CMRA-PET acquisition a μ-map is acquired for attenuation correction of the PET data, and a 2D CINE image is acquired to define a subject-dependent trigger delay and acquisition window for the CMRA acquisition. 3D CMRA data is acquired using a golden-step Cartesian spiral profile order sampling trajectory (one spiral interleaf per heartbeat) and a low-resolution 2D iNAV is acquired at each cardiac cycle using spatially-encoded low flip angle echoes at the beginning of the CMRA acquisition. T_2 preparation (T2 prep) and fat saturation (Fat Sat) prepulses are applied before the 3D CMRA acquisition to improve contrast between the coronary arteries and the surrounding tissues. List-mode PET data is acquired during the whole CMRA acquisition.

fat, or soft-tissue. Each tissue class is then assigned a known attenuation value, background: $0\,\mathrm{cm}^{-1}$, lung: $0.018\,\mathrm{cm}^{-1}$, fat: $0.086\,\mathrm{cm}^{-1}$, and soft-tissue: $0.1\,\mathrm{cm}^{-1}$. Finally, the patient-specific μ-map is added to a previously acquired μ-map of the bed and scanner hardware to produce a complete μ-map for attenuation correction during PET image reconstruction. The whole image acquisition scheme is shown in Figure 4.1.

The CMRA data is acquired using a 3D spoiled gradient echo sequence with a fully sampled golden-step Cartesian spiral profile order sampling trajectory [155]. This trajectory samples the phase-encoding plane in k-space following approximate spiral interleaves on a Cartesian grid. In each cardiac cycle a predefined number of profiles following a spiral-like shape is acquired. At the following heartbeat, a new spiral rotated by the golden angle ($\theta_{\mathrm{GR}} = 111.24°$) is acquired, as shown in the schematic k-space sampling in Figure 4.1. This acquisition trajectory leads to

a homogeneous filling of k-space over time, and allows retrospective binning of the acquired data according to a respiratory signal, ensuring a quasi-uniform distribution of k-space samples in each of the respiratory bins.

A low-resolution 2D iNAV is acquired at each cardiac cycle by adding spatially-encoded low flip-angle lines at the beginning of each interleaf of the spoiled gradient echo 3D CMRA acquisition, in contrast to previously published approaches where the start-up echoes of a bSSFP acquisition were spatially-encoded to obtain the iNAVs [78]. An adiabatic T_2 preparation pulse is performed before data acquisition at each heartbeat to improve contrast between blood and myocardium without the use of exogenous contrast agents [91], and a conventional spectrally selective fat saturation preparation pulse is performed to minimise the signal arising from the epicardial, visceral and subcutaneous fat.

4.1.2 Motion Estimation and Motion-Corrected CMRA Image Reconstruction

MR motion estimation and correction is performed in a beat-to-beat and bin-to-bin fashion for gradient echo acquisition at 3 T PET-MR scanner, similarly to what has previously been introduced for bSSFP CMRA at 1.5 T [159]. First, beat-to-beat 2D translational motion in the foot-head (FH) and right-left (RL) directions is estimated from the iNAVs using normalised cross correlation of a template covering the apex of the heart, using the first acquired 2D iNAV as a reference frame. In order to produce an accurate estimation of FH and RL motion, the iNAVs are interpolated to a 10× resolution, and a search window around the template used for tracking the heart is defined. Thus, normalised cross correlation is calculated between the reference template and the subsequent iNAVs by shifting the template over the search area, so that the 2D translation for a given heartbeat corresponds to the shift that resulted in the highest cross correlation.

The estimated FH motion is then used to assign the acquired 3D CMRA data to N_{bins} different respiratory bins according to their position in the breathing cycle, as shown in Figure 4.2. Outlier data due to deep breaths are removed, so that only data acquired within two standard deviations from the mean FH translation is used

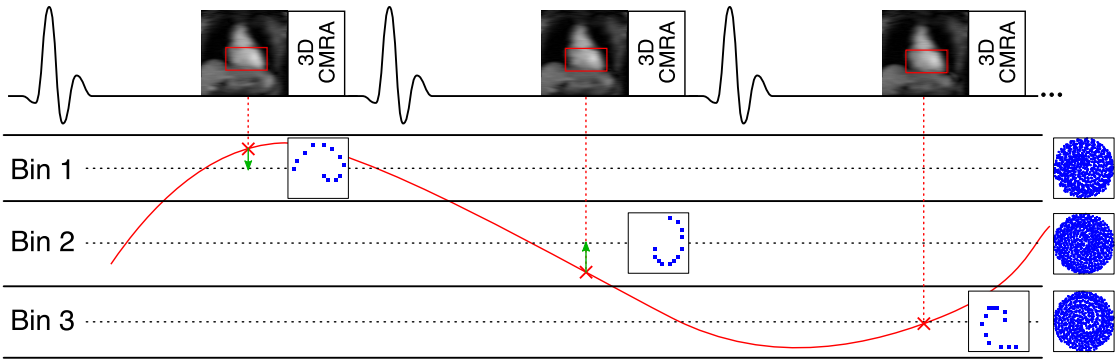

Figure 4.2: Respiratory binning for CMRA. Foot-head motion estimated from the 2D iNAVs (in red) is used to define a number of respiratory bins, three in this example. 3D CMRA data acquired at each heartbeat are translationally corrected to the centre of the corresponding bin (green arrows). At the end of the binning process, an undersampled k-space is obtained for each respiratory bin.

for image reconstruction. MR data assigned to each respiratory bin is corrected for 2D translational motion to the centre of the bin by applying a phase shift in k-space according to the estimated FH and RL motion, as described in Equation 3.48.

It is worth noting that although the CMRA acquisition is fully sampled, the binning process results in undersampled respiratory bins. In order to reduce the artefacts introduced by the undersampling, the image reconstruction problem is modified to allow the partial inclusion of data acquired outside each bin. This approach, usually known as soft-binning, introduces a set of weights for the acquired data that varies according to the FH distance to the centre of each bin. The degree of undersampling is then reduced, and each soft-bin can be then reconstructed independently by using, for instance, the iterative SENSE approach introduced in Section 3.3.1 [150].

The image reconstruction problem for each bin can be formulated as

$$\hat{\mathbf{x}}_b = \arg\min_{\mathbf{x}_b} \|\mathbf{W}_b \left(\mathbf{E}\mathbf{x}_b - \mathbf{k}_b\right)\|_2^2 \tag{4.1}$$

where $\hat{\mathbf{x}}_b$ are the reconstructed bin images, $\mathbf{W}_b$ is a diagonal matrix containing the data weights for respiratory bin b, $\mathbf{E}$ is the encoding matrix, including the discrete Fourier transform operator and coil sensitivities, and $\mathbf{k}_b$ is the k-space data acquired at each respiratory bin after 2D translational motion correction.

The diagonal elements of $\mathbf{W}_b$ are defined as a function of the respiratory position

where the data was acquired, so that samples acquired within the bin have a unitary weight, and samples acquired outside have a weight that decreases linearly to zero as the distance to the bin increases. The soft-binning weights can be written as

$$w_k^b = \begin{cases} 1, & \text{if } \Big(d_{\mathrm{FH}}(b) - t_{\mathrm{FH}}^b(k) + \delta\Big)/\delta > 1 \\ 0, & \text{if } \Big(d_{\mathrm{FH}}(b) - t_{\mathrm{FH}}^b(k) + \delta\Big)/\delta < 0 \\ \Big(d_{\mathrm{FH}}(b) - t_{\mathrm{FH}}^b(k) + \delta\Big)/\delta, & \text{otherwise} \end{cases} \tag{4.2}$$

where w_k^b are the diagonal weights for data k at bin b, $d_{\mathrm{FH}}(b)$ is the FH distance from the bin centre to the edge of the bin, $t_{\mathrm{FH}}^b(k)$ is the FH distance between the centre of bin b and the respiratory position when the k-space sample k was acquired and δ is a parameter defining the amplitude of the soft-bin.

After each bin has been reconstructed, bin-to-bin 3D non-rigid motion can be estimated via image registration based on free-form deformations with normalised mutual information as the similarity metric [213], using one of the respiratory bins (typically end-expiration) as the reference, as shown in Figure 4.3. The free-form deformations algorithm outputs direct and inverse deformation fields that transform an image at the reference position to any given respiratory position and vice versa, respectively. These deformation fields represent the movement in each dimension for each voxel in the images, and can be re-written as sparse matrix operators using trilinear interpolation.

Then, the estimated 3D non-rigid motion operators can be incorporated directly into a GMD motion-corrected reconstruction framework [155, 158, 159], as described in Equation 3.51. Considering $\mathbf{x}_{\mathrm{MF}}$ as the motion-free image, the motion-corrupted acquired k-space data $\mathbf{k}_c$ is given by

$$\mathbf{k}_c = \sum_{b=1}^{N_{\mathrm{bins}}} \mathbf{S}_b \mathbf{E} \mathbf{U}_b \mathbf{x}_{\mathrm{MF}} \tag{4.3}$$

where $\mathbf{S}_b$ is the sampling matrix that selects the k-space points acquired at bin b, $\mathbf{E}$ is the encoding matrix and $\mathbf{U}_b$ are the non-rigid motion operators that transform the object in the reference position to a respiratory state b. The motion-free image $\mathbf{x}_{\mathrm{MF}}$ can be then reconstructed by solving Equation 4.3 using the conjugate gradient method [145].

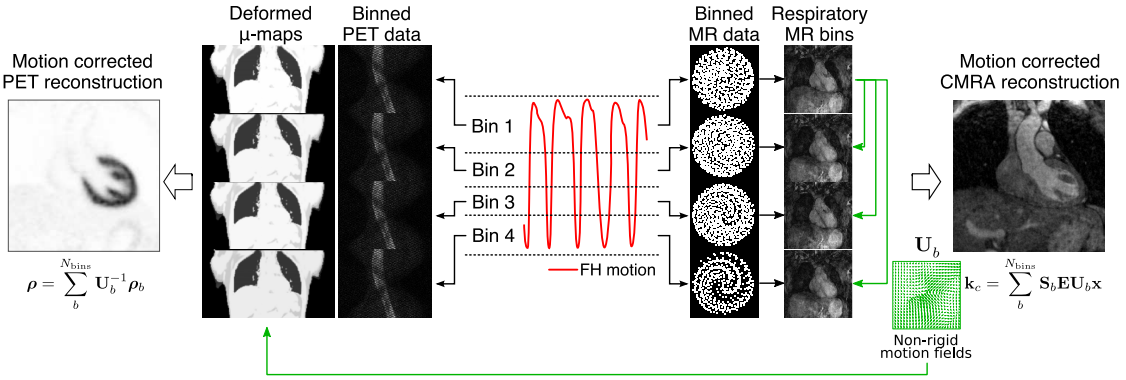

Figure 4.3: Motion-corrected PET-MR reconstruction scheme. The foot-head motion estimated from iNAVs acquired at each cardiac cycle is used to bin both the MR and PET data into a number of respiratory windows. Reconstructed MR images at each respiratory position are used to estimate 3D non-rigid respiratory deformation fields that are then used to correct both PET (emission and attenuation) and CMRA data to the same respiratory position.

4.1.3 Motion-Corrected PET Image Reconstruction

List-mode PET data are assigned to different respiratory bins according to their position in the breathing cycle, in the same manner as previously described for the CMRA data. The same bins are used for both PET and MR, as shown in Figure 4.3, using the ECG signal to accurately synchronise the PET and MR data acquisition.

Using the motion information estimated from the MR respiratory bins, motion-corrected PET reconstruction can be performed using the reconstruct-transform-average (RTA) approach [164]. Each respiratory bin can be reconstructed independently using any conventional statistical iterative reconstruction algorithm, such as OSEM [161], including random and scatter as well as attenuation and normalisation effects. As described in Section 3.4.1, OSEM is a widely used iterative PET reconstruction algorithm that divides the acquired data into a number of subsets, and calculates image updates for each subset in turn. One full iteration of the algorithm comprises one loop over all the subsets. The 3D non-rigid motion operators provided by the simultaneously acquired CMRA data are used to compute one μ-map for each respiratory bin position by transforming the static attenuation map acquired at end-expiration to each respiratory motion state. Therefore, each bin is reconstructed according to Equation 3.60, repeated here for completeness.

$$\boldsymbol{\rho}_b^{(\mathrm{it}+1)} = \frac{\boldsymbol{\rho}_b^{(\mathrm{it})}}{(\mathbf{N}\mathbf{A}_b\mathbf{P})^{\mathrm{T}}\mathbf{1}_I}(\mathbf{N}\mathbf{A}_b\mathbf{P})^{\mathrm{T}}\frac{\mathbf{m}_b}{\mathbf{N}\mathbf{A}_b\mathbf{P}\boldsymbol{\rho}_b^{(\mathrm{it})} + \mathbf{r} + \mathbf{s}} \tag{4.4}$$

where $\boldsymbol{\rho}_b^{(\mathrm{it})}$ is a vector that contains the PET image for respiratory bin b after (it) full iterations of the OSEM algorithm, $\mathbf{P}$ is a matrix that models the geometric aspect of the system forward-projection, $\mathbf{N}$ and $\mathbf{A}_b$ are diagonal matrices with entries down the diagonal equal to the reciprocal of the normalisation and attenuation correction factors for respiratory bin b, respectively, $\mathbf{m}_b$ is a vector that contains the fraction of the data acquired in respiratory bin b and $\mathbf{r}$ and $\mathbf{s}$ represent estimations of random and scattered coincidences, respectively. Once again, the subsets division was omitted in Equation 4.4 for simplicity. It is worth noting that in general, random and scatter coincidences are assumed to vary slowly compared to the activity distribution, so the effect of motion on them is neglected.

Once all respiratory bin PET images have been reconstructed, they are transformed back to the reference end-expiration bin using inverse deformation fields and ultimately added so that one motion compensated image is obtained using all measured data as follows

$$\boldsymbol{\rho} = \sum_{b=1}^{N_{\mathrm{bins}}} \mathbf{U}_b^{-1}\boldsymbol{\rho}_b \tag{4.5}$$

As can be observed in Equation 4.5, the motion operators are applied to the data in PET image space. As the MR motion fields are estimated at a higher spatial resolution, they are resampled prior to PET reconstruction.

4.2 Experiments

For this study two *in vivo* experiments were performed. The first experiment aimed to validate the non-rigid motion correction CMRA framework at 3 T, and was performed in a cohort of ten healthy subjects, using only the MR capabilities of a hybrid PET-MR scanner (Biograph mMR, Siemens Healthcare, Erlangen, Germany). Then, the whole motion-corrected PET-CMRA framework was tested in a small cohort of five oncology patients without known or suspected CAD. Written informed consent was obtained from all subjects according to institutional guidelines and the institutional ethics committee approved the study.

4.2.1 Healthy Subject Data Acquisition

Ten healthy subjects (age 30.0±3.7 years, 4 males) were scanned during free breathing using a prototype implementation of the proposed 3D CMRA sequence. The following MR image acquisition parameters were used: coronal slices, RL phase encoding, $1 \times 1\,\text{mm}^2$ in-plane resolution, 304×304 in-plane matrix size, 2 mm slice thickness, subject-specific number of slices covering the whole heart, ranging from 40 to 48 slices, TR/TE = 3.7/1.7 ms, flip angle = 15°, readout bandwidth = 685 Hz/px.

A subject-specific trigger delay was set targeting the mid-diastolic rest period and an acquisition window ranging from 89 to 119 ms (corresponding to 24-32 k-space lines forming the spiral interleaves acquired at each heartbeat) was used depending on the length of the quiescent diastolic period of the subject. In order to improve the contrast between the coronary arteries and the surrounding tissue, an adiabatic T2 preparation pulse of 50 ms was implemented in the scanner software (not available in the standard vendor product), and a vendor-provided spectrally selective fat saturation preparation pulse was used.

For the 2D iNAV data acquisition, the following parameters were used: high-low linear Cartesian trajectory, coronal orientation, RL phase encoding, flip angle = 3°, 14 lines [78] with the same field of view of CMRA acquisition (304 mm × 304 mm), obtaining a 1 mm × 21.7 mm acquired in-plane resolution, interpolated to $1 \times 1\,\text{mm}^2$ reconstructed resolution, with a slice thickness ranging from 80 to 96 mm, depending on the coverage of the CMRA acquisition.

An additional conventional Cartesian ECG-triggered CMRA scan with a 1D diaphragmatic respiratory gating and tracking with the same image acquisition parameters was performed for comparison purposes, using a 6 mm gating window and a tracking factor of 0.6, in line with the population-based factor proposed in [41]. As discussed in Chapter 3, 1D gating approaches lead to prolonged and unpredictable scan times. In order to avoid long scan times, the 1D-gated acquisition was performed using GRAPPA parallel imaging [148] with an undersampling factor of 2 and 24 calibration lines. It is worth noting that such differences in the acquisition protocol result in slight differences in image SNR and contrast compared to the proposed iNAV-based CMRA.

4.2.2 Patient Data Acquisition

Five oncology patients (ages 53.4±10.4 years, 3 males) that had received an ^{18}F-FDG injection of 334.82 ± 24.35 MBq were scanned 2.3 ± 0.5 hours after injection using the proposed PET-CMRA approach. Before the CMRA acquisition, a μ-map was acquired during a ∼19 s breath-hold at end-expiration using the vendor's standard 2-point Dixon acquisition. By default, these data are acquired with the following imaging parameters: coronal orientation, FH phase encoding, $328 \times 500 \times 399\,\text{mm}^3$ field of view, $2.6 \times 2.6 \times 3.12\,\text{mm}^3$ voxel size, TR/TE1/TE2 = 3.60/1.23/2.46 ms. The segmentation of the water/fat images into four tissue classes and generation of the μ-map for PET reconstruction was performed automatically by the vendor-provided software. Following this, the subjects were scanned during free-breathing using the proposed CMRA sequence with the same MR imaging parameters described for the healthy subjects. List-mode PET data was acquired during the whole CMRA acquisition, resulting in a subject-specific PET acquisition duration of 10.8 ± 0.7 minutes on average.

4.2.3 PET-CMRA Image Reconstruction

CMRA image reconstruction was performed inline in the scanner software for 2D translational motion correction only (i.e. using only the FH and RL motion estimated to produce one translationally motion-corrected image). The proposed combined 2D translational and 3D non-rigid motion correction approach was implemented offline in MATLAB (Mathworks, Natick, Massachusetts, USA).

The CMRA data acquired with the proposed approach was reconstructed with (a) the proposed non-rigid motion-corrected approach (TC+GMD), (b) 2D translational motion correction only (TC) and (c) without motion correction (NMC) for comparison purposes. The TC+GMD method used between three and six respiratory bins, automatically defined such that the maximum bin size was set to 4.5 mm and each bin contained approximately the same amount of data [155]. This ensures that the respiratory bin images have a similar quality, improving the robustness of the free form deformations image registration algorithm. The soft-gate amplitude (δ) was empirically determined and set to 1 mm.

The TC+GMD CMRA image reconstruction required 2D translational motion-corrected soft-binned iterative SENSE reconstructions (reconstruction time of ∼250 s per bin), followed by 3D bin-to-bin non-rigid registration (registration time of ∼50 s per bin) and finally the GMD reconstruction (reconstruction time of ∼2200s), for a total reconstruction time of ∼3700 s. The CMRA data acquired with 1D diaphragmatic respiratory gating and tracking (called Gated hereafter) was also reconstructed inline in the scanner software for comparison purposes.

List-mode PET data was binned using the MR-derived respiratory signal and bins, so that one 3D set of span 11 sinograms was created per each respiratory bin. Non-rigid motion operators estimated from the MR bins were used to deform the μ-map acquired at end-expiration to each respiratory bin position. PET image reconstruction was performed separately for each respiratory bin in Siemens e7 Tools (Siemens Healthcare, Knoxville, USA) using the OSEM algorithm with 3 iterations and 21 subsets, including point spread function modelling. Images were reconstructed with a voxel size of $2.08 \times 2.08 \times 2.03\,\text{mm}^3$ and a matrix size of $344 \times 344 \times 127$. Once all PET bins were reconstructed, they were transformed to the reference respiratory position and aggregated in MATLAB to produce one motion-corrected (MC) image.

The MC PET image reconstruction required a set of OSEM reconstructions (∼240 s per bin), followed by 3D non-rigid deformation (∼10 s per bin) and finally summation, for a total reconstruction time of ∼1250 s. Additionally, a) an uncorrected reconstruction including all the acquired PET data (NMC) and b) a gated reconstruction at end-expiration (Gated) were performed with Siemens e7 Tools for comparison purposes.

4.2.4 Image Analysis

In order to evaluate the quality of the non-rigid motion correction, each reconstructed CMRA image was reformatted onto a 2D plane containing both the right coronary artery (RCA) and left anterior descending (LAD) artery using the 'Soap Bubble' software described in Section 2.3.1 [49]. Image quality metrics were obtained separately for each coronary artery, including visible vessel length and vessel sharpness for the first 4 cm and for the whole visible length of the vessel. Vessel

sharpness values were normalised to the signal intensity of the centre line of each vessel, so that 100% sharpness refers to a maximum signal intensity change at the vessel edge. For the healthy subjects, the difference between the image quality metrics (vessel length and sharpness) for each reconstructed image was evaluated with a paired t-test with a p-value of 0.01 considered statistically significant, including corrections for multiple comparisons.

Reconstructed PET images were visually assessed with line profiles across the left ventricle. Additionally the mean and coefficient of variation (CV) of the reconstructed image intensity (a.u.) in a region of interest (ROI) within the myocardium were analysed for all reconstructed PET images. The ROI was defined as a 10 mm diameter sphere inside the myocardium. As the ROI is close to the edge of the myocardium, the mean value reflects the sharpness of images, as blurring will induce a decrease in image intensity. On the other hand, the CV (standard deviation/mean) is conventionally used to measure noise levels in PET imaging [214]. When high levels of noise are present in reconstructed PET images, a post-processing Gaussian filter is typically applied to reduce the noise level at the expense of introducing some blurring. In order to evaluate the improvement achieved by the motion correction, analysis was performed here in the original unsmoothed images and in the post-processed images smoothed with a 4 mm Gaussian filter.

4.3 Results

4.3.1 Healthy Subjects

Scans were completed successfully in all subjects. The average acquisition time for the proposed CMRA acquisition was 12.3 ± 1.7 minutes compared to 17.0 ± 3.2 minutes for the 2× accelerated acquisition with 1D navigator gating and tracking. The minimum, maximum and average (and standard deviation) efficiency of the latter was 39%, 65% and 52.3 ± 8.9% respectively for a 6 mm gating window. For the proposed non-rigid motion correction approach, 3 to 5 (4.3 ± 0.9 bins on average) respiratory bins were used with bin sizes of 2.84 ± 1.20 mm on average.

Figure 4.4 shows a slice of five reconstructed respiratory bins for two represen-

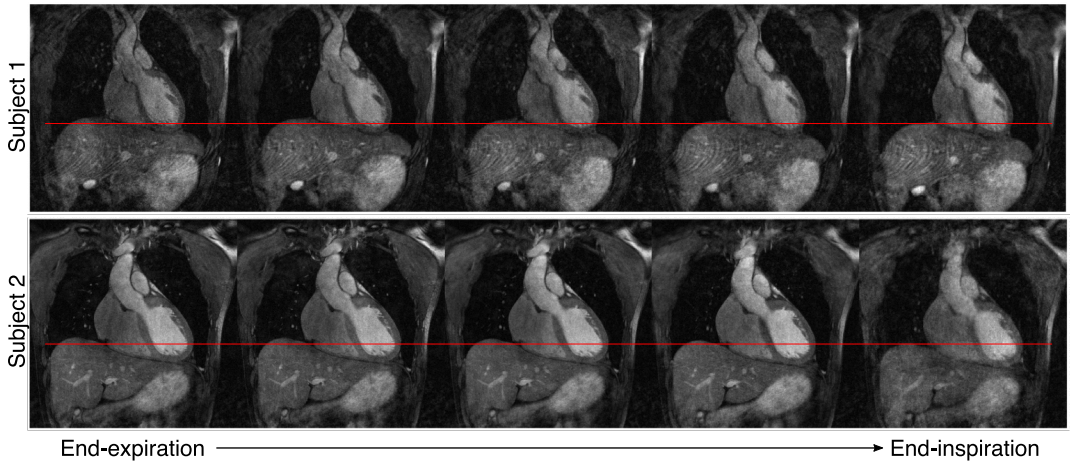

Figure 4.4: Reconstructed MR images at five respiratory positions (bins) for two representative healthy subjects. A red line drawn at the level of the diaphragm in end-inspiration is included for reference purposes. Despite residual undersampling artefacts, the respiratory bins allow for estimation of non-rigid motion fields.

tative subjects. A red line placed at the level of the diaphragm in end-inspiration shows the magnitude of respiratory motion in free breathing. Although each respiratory bin is undersampled, the soft binning approach allows the reconstruction of images with sufficient image quality for non-rigid motion estimation.

Figure 4.5 shows the reformatted images for the non-motion-corrected (NMC), translational motion-corrected (TC), and non-rigid motion-corrected (TC+GMD) reconstructions for five representative subjects. Gated images are displayed next to the TC+GMD images for comparison purposes. Improvements in the visualisation of the distal part of the LAD and RCA can be observed for all subjects when applying TC in comparison with NMC, and further improvements can be observed with TC+GMD in the visualisation of the vessels. Similar image quality can be seen for TC+GMD and Gated approaches for both LAD and RCA coronary arteries. Loss in vessel definition and sharpness can be observed in the proximal LAD for subject 3 with TC. This is because TC correction depends on the position of the template for motion tracking (as the motion of the heart is not purely translational), which in this work was located near the apex of the heart (Figure 4.1, in red over iNAV). The TC+GMD approach overcomes this limitation by correcting for the complex non-rigid motion of the heart.

Image quality metrics for the RCA and LAD are displayed in Figure 4.6. It can be observed in Figures 4.6(a,d) that measured vessel lengths were similar for TC+GMD

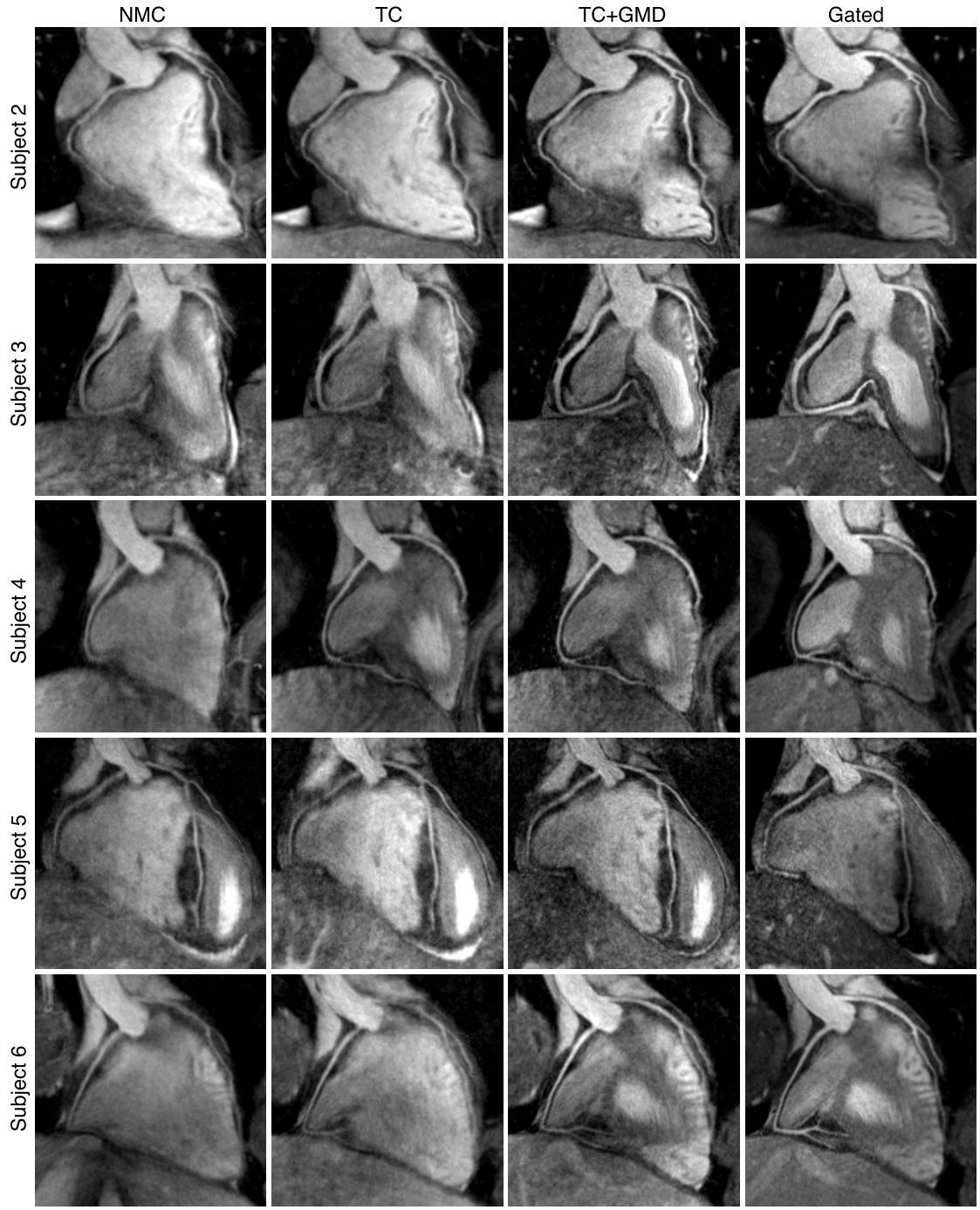

Figure 4.5: Reformatted CMRA images for five representative healthy subjects (rows) showing non-motion-corrected (NMC), translational motion-corrected (TC), translational plus non-rigid motion-corrected (TC+GMD) and gated and tracked (Gated) images. Improvements in the visualisation of the distal part of the RCA and LAD can be observed when applying TC and TC+GMD in comparison to NMC. As the motion is tracked near the apex of the heart (Figure 4.1, in red over iNAV), TC produces a loss in definition of the proximal LAD for subject 3. The TC+GMD approach produces images of quality comparable to the Gated images.

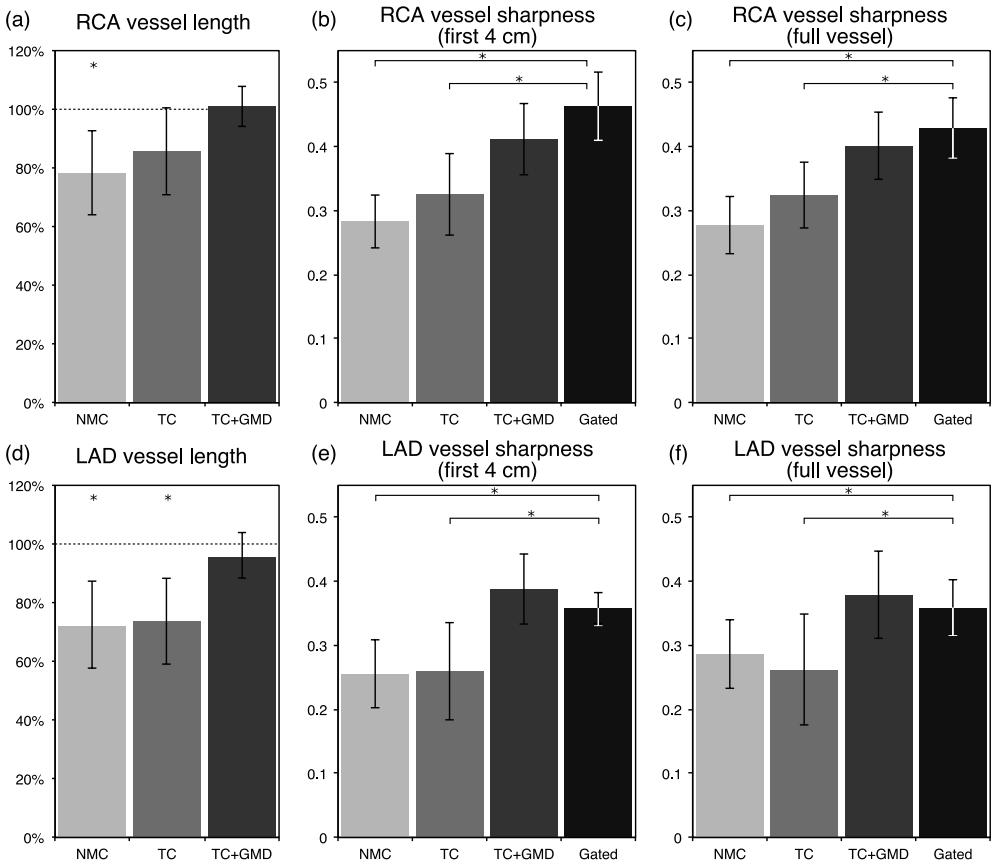

Figure 4.6: Image quality metrics for the RCA and LAD arteries for ten healthy subjects, for NMC, TC, TC+GMD and Gated images. The metrics included: visible vessel length along the (a) RCA and (d) LAD, where each measure is normalised to the length observed in the corresponding Gated image; vessel sharpness for the (b,c) RCA and (e,f) LAD, for both the first 4 cm and full length of each vessel. *denotes a statistically significant difference with $p < 0.01$ compared to the Gated images.

and Gated, reaching $101.0 \pm 6.9\%$ and $95.4 \pm 8.7\%$ of the visible length of the Gated images for the RCA and LAD respectively on average. Lower values were obtained for TC and NMC, with an average of 85.7 ± 14.9 and $78.3 \pm 14.2\%$ for the RCA and 73.7 ± 14.7 and $72.0 \pm 15.6\%$ for the LAD, respectively. Significant differences were found between Gated and NMC for both coronaries, and between Gated and TC for the LAD. Similar results were obtained for vessel sharpness, as can be observed in Figure 4.6(b,c) for the RCA and Figure 4.6(e,f) for the LAD. Significant differences between Gated and NMC and between Gated and TC were obtained for both the LAD and RCA coronaries, when analysing either the proximal segment (first 4 cm) or the full length of each vessel. No statistically significant differences were observed between the Gated and the TC+GMD approach for any of the measurements.

4.3.2 Patients

Scans were completed successfully in all subjects. The average acquisition time for the proposed PET-CMRA acquisition was 10.8 ± 0.7 minutes. For the TC+GMD reconstruction, and subsequently for the motion-compensated PET image reconstruction, 3 to 6 respiratory bins (4.4 ± 1.5 bins on average) were used, with bin sizes of 2.77 ± 1.06 mm on average. This binning scheme resulted in PET respiratory bins with 47.28 ± 24.92 million counts on average.

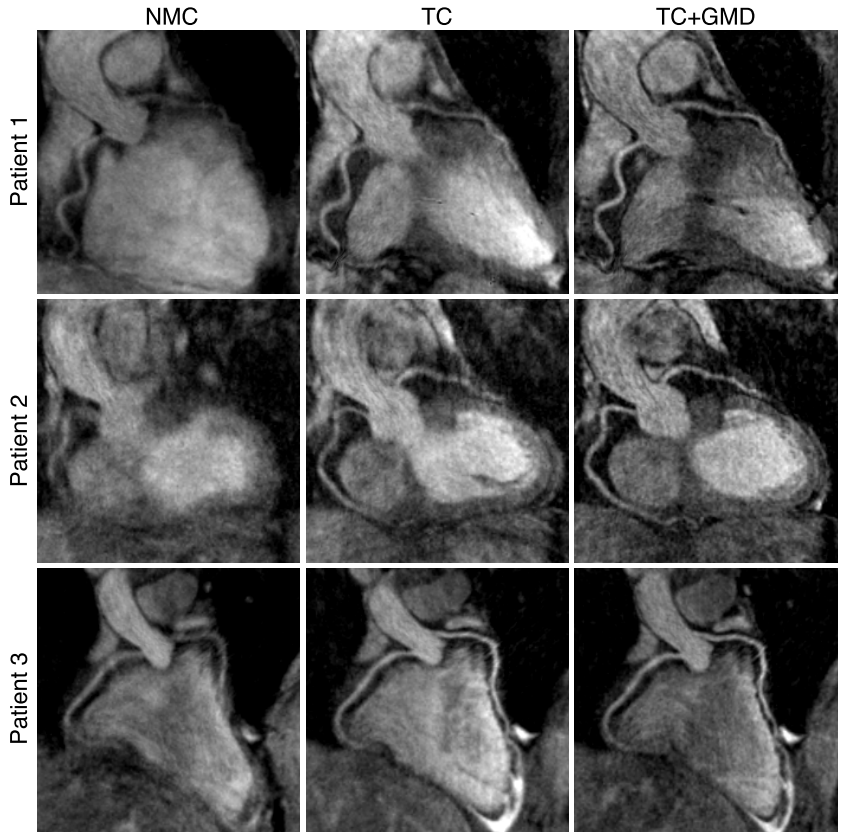

Figure 4.7: Reformatted CMRA images for three representative oncology patients (rows) showing NMC, TC and TC+GMD images. Extreme respiratory motion prevents visualisation of the left anterior descending artery in patient 2. Improvements in the visualisation of the vessels are observed when applying TC and further improvements are observed with TC+GMD.

Figure 4.7 shows the reformatted CMRA images along the RCA and LAD for the NMC, TC and TC+GMD reconstructions three representative oncology patients. Pronounced blurring is observed in all cases when no motion correction is applied, and extreme blurring prevents the visualisation of the proximal LAD artery for patient 2. TC reconstructed images allow visualisation of the proximal segments

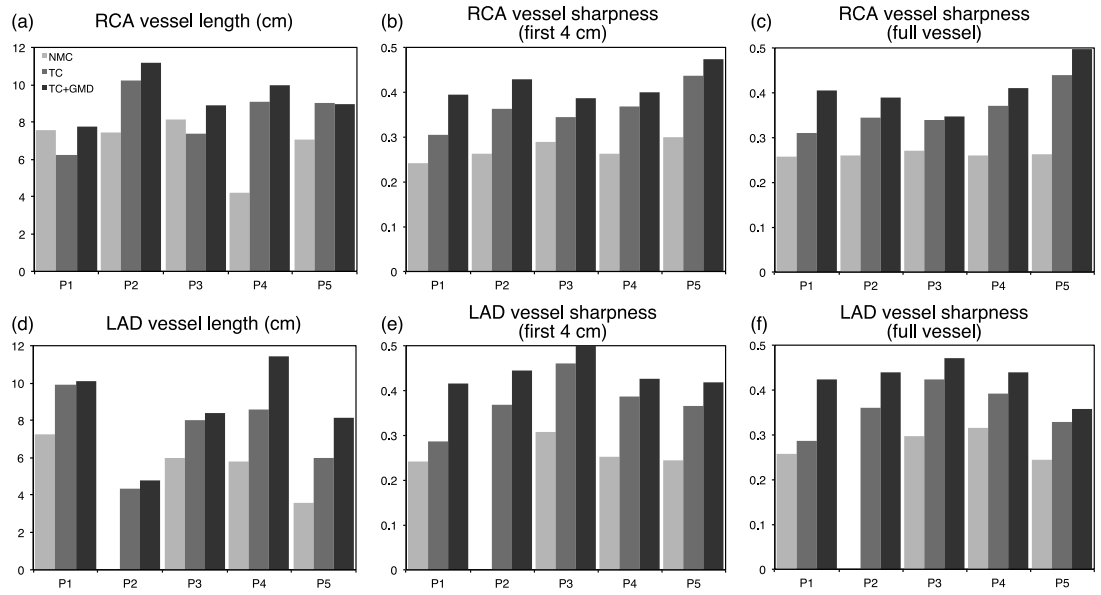

Figure 4.8: Image quality metrics for the RCA and LAD arteries for five oncology patients for NMC, TC, and TC+GMD. (a,d) Vessel length along the RCA (a) and LAD (d). (b,c) Vessel sharpness for the first 4 cm (b), and full length (c) of the RCA. (e,f) Vessel sharpness for the first 4 cm (e), and full length (f) of the LAD.

of the vessel in all the cases, however important residual aliasing due to non-rigid motion can still be observed. A consistent improvement in the visualisation of the distal segment of the coronary arteries can be observed for all subjects when applying TC+GMD.

Image quality metrics confirm the observed improvements in vessel sharpness for both the RCA and the LAD for all the patients (P1-P5), as shown in Figure 4.8(b-c, e-f). The visible length of both coronaries also increases when applying TC+GMD compared to TC and NMC, as can be observed in Figure 4.8(a,d). On average, visible length of the RCA and LAD increased by 45.53% and 75.45%, respectively, when applying TC+GMD compared to uncorrected images. Similarly, vessel sharpness for the full visible length of the vessels increased by 56.44% and 51.11% on average for the RCA and LAD, respectively.

Reconstructed PET images with no motion correction (NMC), Gated (only considering the end-expiration respiratory bin, containing $27.6 \pm 8.4\%$ of the acquired data) and MR-based motion correction (MC) for patients 1–5 are shown in Figure 4.9. Profiles across the myocardium for each patient are displayed alongside the images. It can be observed that MC improves sharpness of the left ventricle

myocardium compared to NMC while reducing noise levels compared to the Gated reconstruction. From the shown profiles it can be observed that small features, such as the papillary muscles, cannot be identified in the NMC images in all cases. In the Gated images, sharpness is improved at the expense of an increased noise, and small features become apparent. On the other hand, profiles across MC images show the same sharpness as the Gated images while keeping signal to noise levels comparable to NMC.

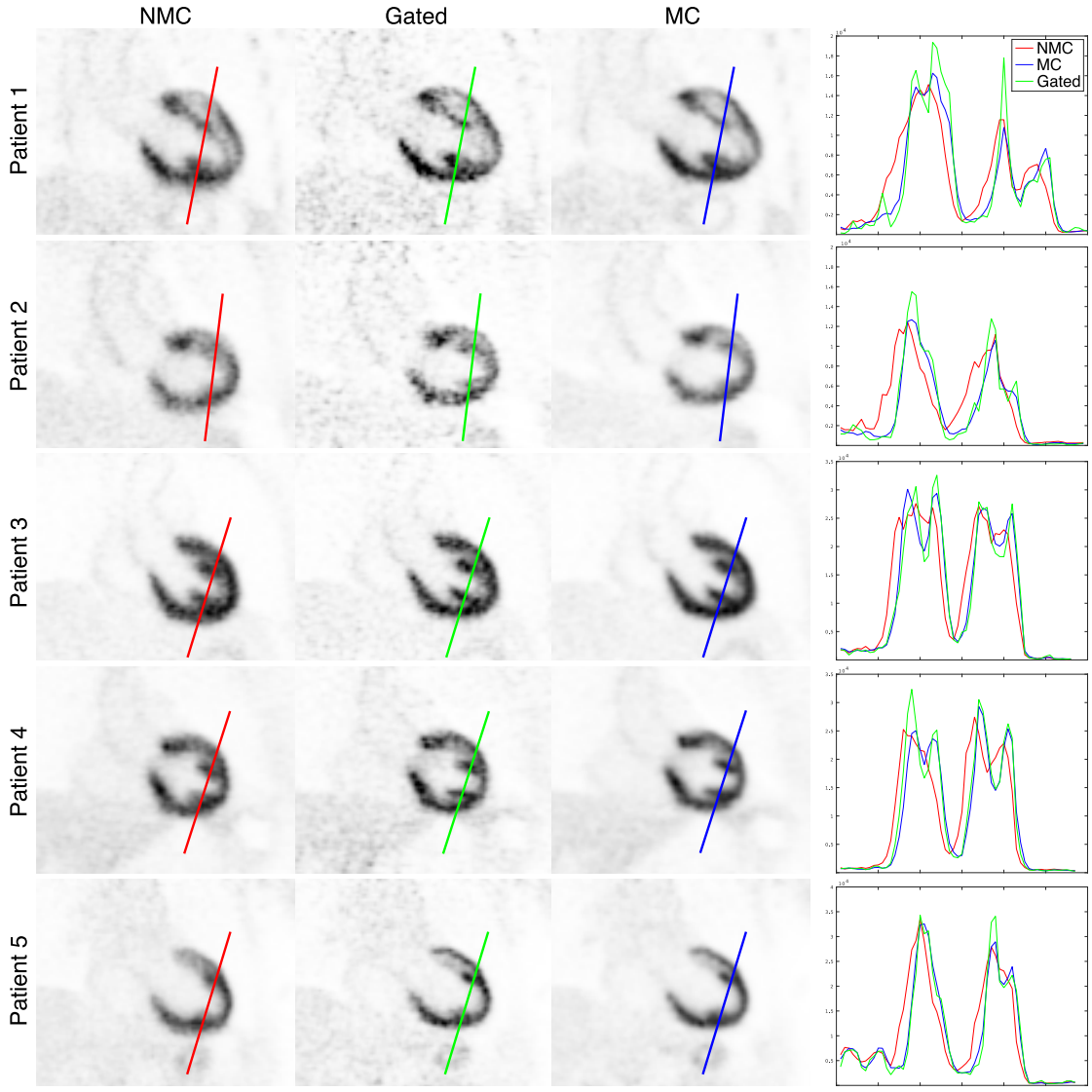

Figure 4.9: Coronal slice for the five acquired oncology patients (rows) showing NMC, Gated and MC PET images, alongside with profiles across the left ventricle myocardium. MC improves the sharpness of the myocardium and papillary muscles compared to NMC and reduces noise levels compared to Gated.

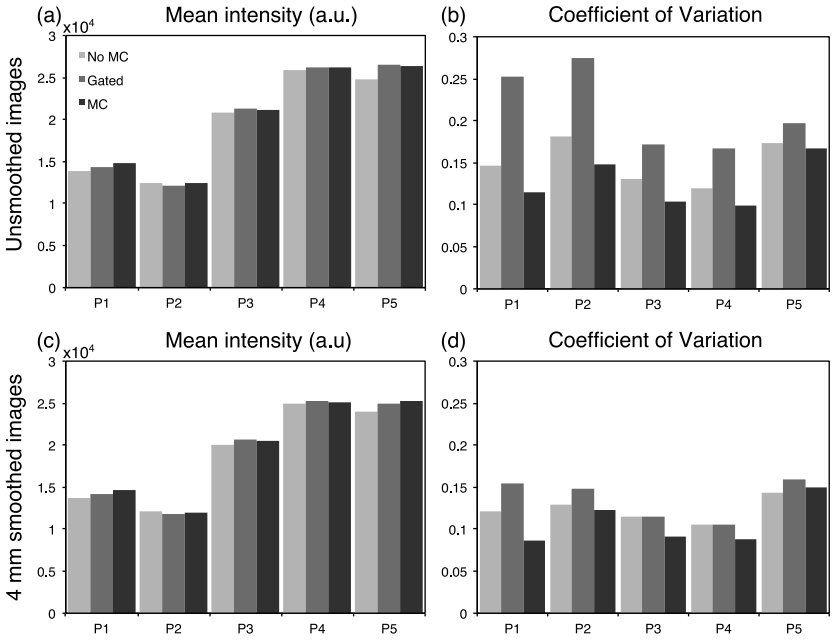

Figure 4.10: Mean and coefficient of variation of the image intensity for NMC, Gated and MC PET images in a spherical ROI within the myocardium of 10 mm diameter. Each reconstructed image was smoothed after reconstruction with a 4 mm Gaussian filter, and both the unsmoothed and smoothed images were analysed. For all patients, MC outperforms Gated and NMC in terms of noise (i.e. lower coefficient of variation), and outperforms NMC in terms of mean image intensity, suggesting an increased sharpness.

Figure 4.10 shows the mean image intensity and the CV for a ROI within the myocardium in each patient, for unsmoothed and smoothed images. It can be observed than when no smoothing is applied, the mean intensity in the ROI for NMC is lower than in the Gated images, suggesting that NMC is underestimating the real uptake value due to blurring. When MC is used, the mean increases for three of the patients, and it remains nearly constant for the other two patients. MC images also have a lower CV compared to Gated images for all the subjects. When images are smoothed with a 4 mm Gaussian filter, it can be observed that the CV is significantly reduced for Gated images, but the minimum CV is still achieved by the MC images.

Finally, Figure 4.11 shows example slices for two representative patients of the fused motion compensated PET-CMRA image. It can be observed that the motion compensation scheme produces co-registered images at the same respiratory position, and the left ventricle myocardium matches in both modalities.

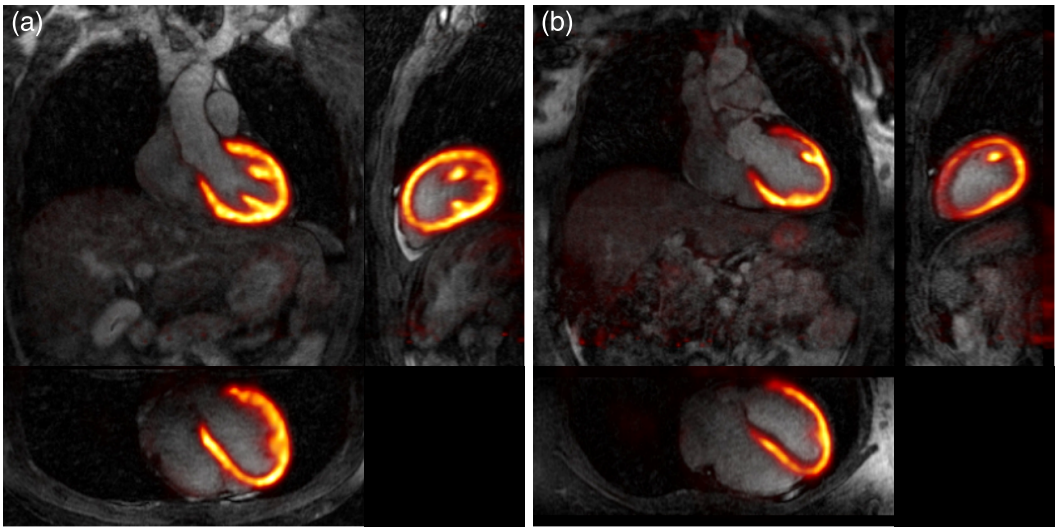

Figure 4.11: Example coronal, sagittal and transverse views of fused motion-compensated cardiac PET-CMRA images for (a) patient 3 and (b) patient 5.

4.4 Discussion

In this Chapter, a respiratory motion-corrected approach for simultaneous whole-heart coronary MR angiography and cardiac PET imaging has been proposed and implemented for visualisation of the coronary lumen and myocardial viability imaging. The proposed method estimates FH and RL translational motion with a high temporal resolution in a beat-to-beat fashion, and uses the FH motion to bin both the acquired CMRA and PET data in several respiratory bins and to correct the CMRA data for intra-bin motion. MR images reconstructed for each bin are used to estimate 3D non-rigid bin-to-bin respiratory motion, which is then used to correct both the CMRA and PET data. The motion-corrected MR reconstruction approach has been previously introduced for coronary and vessel wall imaging at 1.5 T for a balanced steady state free precession sequence with a radial-like Cartesian trajectory [159], and here it is extended to a 3 T hybrid PET-MR system using a 3D spoiled gradient echo sequence with a golden-step Cartesian trajectory with spiral profile order sampling without the use of exogenous contrast agents.

The CMRA acquisition and reconstruction approach was tested in a cohort of 10 healthy subjects and compared against a 6 mm gated and tracked acquisition. An intermediate TC approach was implemented on the scanner, showing improvements in image quality compared to NMC reconstruction, especially in the visualisation of

the distal RCA and LAD. However, as the motion of the heart during the breathing cycle is not purely translational, the TC might produce a loss of definition in the proximal segment (or distal segment, depending on the location of the template to estimate the translational motion) of the vessels for subjects with a more complex non-rigid motion of the heart. The TC+GMD approach overcomes this limitation, showing further improvements compared to TC and recovering both the proximal and distal segments of the coronary arteries.

When quantifying vessel length and sharpness for both the RCA and the LAD, no statistically significant differences were observed between the Gated and the TC+GMD approach. The proposed approach had a shorter and predictable scan time of ∼12 minutes (fully sampled acquisition) compared to ∼17 minutes for the 2× undersampled 1D gated and tracked, while simultaneously providing non-rigid motion fields for correcting PET data. It is worth noting that the fully sampled CASPR trajectory produces an elliptical sampling mask in the phase encoding plane [155, 215], further reducing scan time compared to traditional fully sampled Cartesian acquisitions.

The full PET-CMRA acquisition and reconstruction approach was then tested in a small cohort of five oncology patients that exhibited radiotracer (^{18}F-FDG) uptake in the myocardium. For the CMRA data, extreme blurring was observed when no motion correction was applied, in some cases completely obscuring the visualisation of the vessels. TC images allowed visualisation of the arteries in all cases, and a further improvement in visible length and sharpness of the coronary arteries was observed when using TC+GMD approach.

Non-rigid motion fields obtained from CMRA data were also used to correct PET data for respiratory motion. Increased sharpness of the myocardium and improved visualisation of small features such as the papillary muscles can be observed for all the subjects compared to non-motion-corrected PET images. In addition, reduced noise levels compared to gated PET reconstruction were observed, as a greater number of counts are used to produce the motion compensated images.

For reconstructed images without smoothing, an increased mean image intensity in a ROI within the myocardium was observed for three of the subjects when applying motion correction compared to non-motion-corrected images, due to a significant

reduction in blurring. For the other two subjects, the value remained approximately constant, because the ROI was located in a region with less motion. When images are smoothed, it can be observed that noise levels are significantly reduced for all the images, however, minimum noise is achieved by the motion-corrected images for all patients. Motion-corrected images also present a larger mean image intensity in the ROI compared to non-motion-corrected, suggesting an increased sharpness in the image.

In this work, each PET respiratory bin was reconstructed independently, and motion fields were then used to warp all the images to a common reference position. This motion compensation approach has been shown to produce an increased bias in the standardised uptake values due the reduced number of counts in each respiratory bin in simulation studies [169]. Including the motion directly in the system model of the PET reconstruction algorithm can alleviate this problem, so that a motion compensated image reconstruction can be performed instead, however this approach requires a longer reconstruction time.

The validation and proof-of-concept study presented in this Chapter included only healthy subjects and oncology patients without a history of cardiac disease. However, respiratory breathing patterns in patients with cardiac disease are more irregular. A first validation of the proposed method in patients with coronary artery disease is presented in Chapter 5.

Furthermore, the method introduced in this Chapter only allows respiratory motion correction to be performed for PET data. An extension of this approach for acquiring an additional cardiac phase so that both respiratory and cardiac motion correction can be performed is presented in Chapter 6, which further reduces blurring of the myocardium in the PET images.

Finally, in this Chapter, the attenuation correction map is acquired using a $\sim$19 s breath-hold 2-point Dixon protocol. While this breath-hold time is feasible for most healthy subjects, it becomes challenging for patients with respiratory or cardiac disease. Incomplete breath-holds might produce tissue misclassification, resulting in errors in the attenuation map. Chapter 7 investigates a potential solution for the acquisition of free-breathing 2-point Dixon based attenuation maps, while simultaneously acquiring diagnostic CMRA images.

4.5 Summary

A framework for simultaneous coronary MR angiography and cardiac PET has been introduced. This approach allows the correction of both the CMRA and PET data for respiratory motion, producing potentially diagnostic images that allow simultaneous visualisation of the coronary arteries, myocardial viability and potentially myocardial perfusion. The motion-corrected CMRA reconstruction framework was validated in healthy subjects. No statistically significant differences were found when comparing the proposed approach with a standard 1D diaphragmatic 2× undersampled gated and tracked acquisition. However, the proposed approach has a predictable scan time, was 30% faster on average, and provides non-rigid respiratory deformation fields for PET motion correction. The PET-CMRA framework was tested in oncology patients, and results show improvements in sharpness and reductions in image noise compared to standard uncorrected and gated reconstructions respectively.

Chapter 5: Respiratory Motion-Corrected CMRA-PET: Initial Clinical Validation

The promising results obtained in initial patient studies have promoted an increasing role of PET-MR imaging as a non-invasive technique for the comprehensive assessment of several cardiac conditions [24, 177, 181, 216–218]. For instance, an increased accuracy for the diagnosis of active cardiac sarcoidosis was observed by combining ^{18}F-FDG PET and cardiovascular MR in [184], while promising results of increased sensitivity for the detection of borderline myocarditis using hybrid ^{18}F-FDG PET and cardiovascular MR scans are shown in [131]. A significant PET-MR intermodality agreement was observed in acute myocardial infarction [180] and more recently cardiovascular MR in combination with ^{18}F-FDG and ^{18}F-NaF was successfully used for imaging of inflammation and calcification in the coronary arteries [174].

Most of the currently used cardiac PET-MR imaging clinical workflows consist of the acquisition of several MR images with differing contrasts and geometry, while simultaneously acquiring list-mode PET data throughout the whole or most of the scanning session. Cardiac MR images acquired in these protocols typically include a stack of 2D cine images, 2D LGE images, CMRA and T_1 and T_2 mapping, leading to scanning sessions that range between 30 to 90 minutes in duration [174, 180, 184]. During this prolonged examination time, physiological motion occurs due to breathing and cardiac motion, thus requiring motion compensation techniques to minimise ghosting, blurring and associated image artefacts in both modalities.

As described in Chapter 3, the effect of cardiac motion in MR images is conventionally minimised in the clinical routine by synchronising the acquisition with an ECG device, and the effect of respiratory motion by using diaphragmatic navigation techniques for 3D imaging or a series of breath-hold for 2D imaging. In both the cardiac and respiratory cases, these techniques result in a significant reduction in the effective data acquisition time, limiting the usability of similar techniques in PET, as this reduction of available data would produce images with increased noise. Therefore, in practice, most of cardiac PET-MR clinical studies still aggregate all the PET data acquired throughout the cardiac and respiratory cycle into a single static time frame blurred by both respiratory and cardiac motion [180, 184].

Several approaches for MR-based motion correction of cardiac PET data have been recently proposed in the literature, as reviewed in Chapter 3, where the MR images acquired simultaneously with PET are usually designed for motion estimation purposes only [197, 211, 212]. The lack of appropriate tissue contrast and/or sufficient spatial resolution of these MR images might prevent their use for diagnostic purposes. Therefore, such approaches generally lead to prolonged examination times, as the diagnostic MR images are acquired afterwards, hindering their integration in the clinical practice.

In Chapter 4, a novel approach for respiratory motion-corrected cardiac PET-MR imaging was introduced. With this approach motion estimated from MR images is used to correct both ^{18}F-FDG PET and CMRA datasets, enabling visualisation of myocardial viability and coronary anatomy in a single efficient examination. The feasibility of this PET-CMRA framework was initially shown in a small cohort of oncology patients without known or suspected heart disease, however its feasibility in patients with cardiovascular disease presents unique challenges in terms of robustness and reliability of the technique in cases of more irregular breathing patterns.

This Chapter presents an initial clinical validation of the proposed method for the simultaneous visualisation of myocardial integrity by ^{18}F-FDG PET and coronary lumen integrity by CMRA. The study was performed in a cohort of patients with known coronary artery disease, in particular, patients with chronic total occlusion of at least one of the coronary arteries. Some of the results presented in this chapter have been published as a journal article [29].

5.1 Methods

5.1.1 PET-CMRA Image Acquisition

The whole-heart PET-CMRA acquisition consists of a free-breathing ECG-triggered CMRA sequence simultaneously acquired with list-mode cardiac PET data, as described in Chapter 4 [27]. The main characteristics of such acquisition are briefly summarised here for completeness. CMRA data is acquired using a 3D spoiled gradient echo sequence following a fully sampled golden-step Cartesian trajectory with spiral profile ordering, so that one spiral interleaf is acquired at each heartbeat [155]. A 2D iNAV [78] is acquired at the beginning of each interleaf by spatially encoding low flip angle k-space lines, and fat saturation and T_2 preparation [91] pulses are performed immediately prior to CMRA data acquisition to improve the contrast between arterial blood and the surrounding myocardium and epicardial fat.

As part of the cardiac PET-CMRA acquisition protocol, a standard Dixon-based attenuation map (μ-map hereafter) is acquired in breath-hold at end-expiration for MR-based attenuation correction of the PET data, with missing tissue due to the limited field of view of the MR (as compared to PET) estimated using the MLAA (maximum likelihood reconstruction of attenuation and activity) approach [219]. Following the same approach presented in Chapter 4, a conventional 2D cine image is acquired for defining the trigger delay and length of the acquisition window of the 3D CMRA.

5.1.2 PET-CMRA Image Reconstruction

Motion compensated PET-CMRA image reconstruction is performed as in Chapter 4, following a method that can be briefly summarised in four steps. In the first step, foot-head (FH) and right-left (RL) translational respiratory motion is estimated from the 2D iNAVs by using rigid image registration of a template covering the apex of the heart. In the second step, FH motion is used to bin the acquired PET and CMRA data in a number of respiratory windows ranging from end-expiration to end-inspiration, each containing approximately the same amount of data. Outlier rejection is performed in this step, by excluding CMRA data acquired in deep breaths.

In a third step, 3D MR images are reconstructed at each respiratory position using iterative SENSE with a soft-binning approach, and bin-to-bin respiratory deformation fields are estimated by non-rigid image registration, using the end-expiration bin as reference. Finally, the non-rigid deformation fields are used in a generalised matrix description formulation for motion-compensated CMRA reconstruction. Moreover, the non-rigid motion fields are also used to move the attenuation maps to each respiratory position and perform a motion-compensated PET reconstruction. Therefore, at the end of the reconstruction process, co-registered respiratory motion-corrected CMRA and cardiac PET images are obtained.

5.2 Experiments

Fourteen patients with symptomatic CAD (angina or angina equivalent, excluding acute ST-elevation myocardial infarction patients), chronic total occlusion (CTO) of a relevant coronary artery (segment 1, 2, 6, 7, 11 or 13, diameter >2.5 mm), and echocardiographic or angiographic evidence of a wall motion abnormality in the corresponding area were recruited for this study between 12.10.2016 and 26.06.2017 (Figure 5.1). In order to improve risk stratification before elective percutaneous coronary intervention (PCI) of the CTO, all patients underwent a hybrid ^{18}F-FDG PET-MR examination in a Biograph mMR scanner (Siemens Healthcare, Erlangen, Germany). Relevant patient characteristics include: age 66.1 ± 9.5 years, 9 males, left-ventricle ejection fraction (LVEF) $49 \pm 12\%$, and previous PCI stenting of at least one of the coronary arteries. Written informed consent with respect to participation was obtained from all subjects, and the study was performed in concordance with the Declaration of Helsinki and approved by the institutional ethics committee.

5.2.1 Data Acquisition

The clinical PET-MR examination protocol included a scan of 40 to 50 minutes with a list-mode PET acquisition for the assessment of myocardial viability under insulin-clamped conditions 60 minutes after injection of 326 ± 29 MBq of ^{18}F-FDG, and a multi-slice 2D phase-sensitive inversion recovery (PSIR) LGE acquisition (1.4–2.2 mm in-plane resolution, 8 mm slice thickness). During the 10–15 minutes

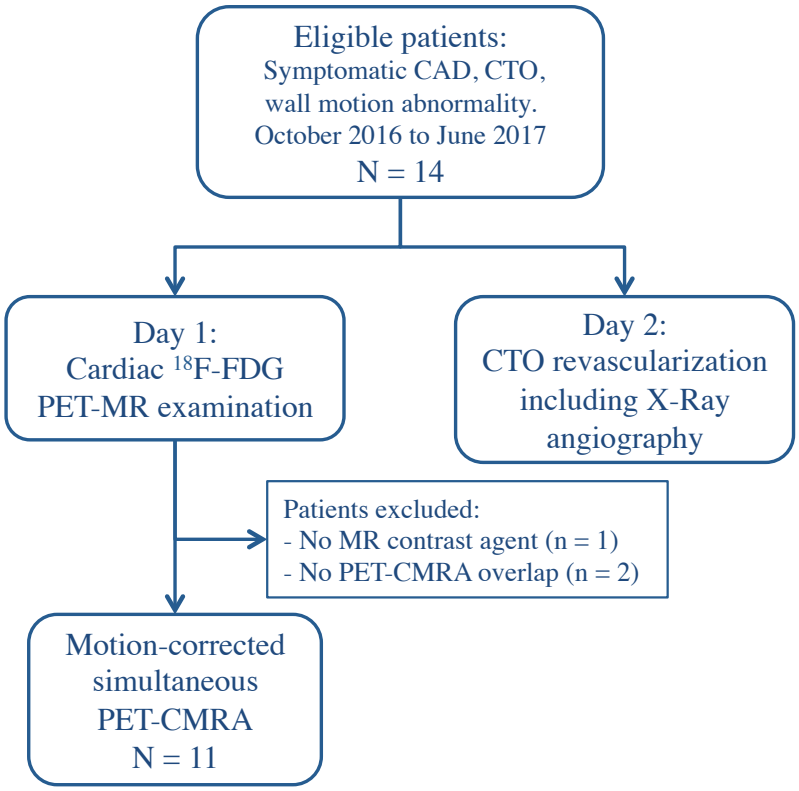

Figure 5.1: Flow chart of patients included in the study. 14 patients with symptomatic coronary artery disease (CAD), chronic total occlusion (CTO) of a coronary artery and evidence of wall motion abnormality were recruited for this study.

waiting time required for optimal contrast in LGE images, an acquisition with the proposed PET-CMRA sequence was performed.

For the CMRA acquisition, relevant imaging parameters included: coronal orientation, resolution = $1 \times 1 \times 2\,\mathrm{mm}^3$ (interpolated to $1\,\mathrm{mm}^3$ isotropic resolution during MR image reconstruction), field of view = $304 \times 304 \times 88$–$112\,\mathrm{mm}^3$ covering the whole heart, TR/TE = 3.72/1.70 ms, flip angle = 15°. A subject-specific trigger delay was defined targeting the mid-diastolic quiescent period of the cardiac cycle, and an acquisition window of 89 to 119 ms (corresponding to 24 to 32 lines per spiral interleaf) was selected depending on the length of the mid-diastolic period. The 2D iNAVs were acquired using the following imaging parameters: same field of view as the 3D CMRA acquisition, flip-angle = 3°, 14 acquired lines with a centric-in Cartesian trajectory, corresponding to a $1 \times 21.7\,\mathrm{mm}^2$ acquired resolution interpolated to $1\,\mathrm{mm}^2$ before FH and RL motion estimation. The vendor-provided fat saturation preparation pulse was used, and an adiabatic T2-prep (50 ms duration) was implemented to improve tissue contrast. μ-maps were acquired for each patient during a

19 s breath-hold at end-expiration using the vendor's standard 2-point Dixon protocol (acquisition parameters: coronal orientation, resolution = $2.6 \times 2.6 \times 3.1\,\text{mm}^3$, field of view = $328 \times 500 \times 399\,\text{mm}^3$, TR/TE1/TE2 = 3.60/1.23/2.46 ms). All patients underwent interventional X-ray angiography the day after the PET-MR examination, for elective CTO revascularisation.

CMRA and PET datasets were reconstructed with the described motion correction scheme (MC) and without motion correction (NMC) for comparison purposes. For each patient, the fraction of list-mode PET data acquired simultaneously with the CMRA sequence was selected for PET image reconstruction. Due to variations in planning time, the overlap between CMRA and list-mode PET acquisition varied between patients, with an average overlap of $80.3 \pm 20.9\%$ of the duration of the CMRA acquisition.

MR image reconstruction was performed offline in MATLAB (Mathworks, Natick, Massachusetts, USA) using custom developed software. PET image reconstruction was performed offline using RTA motion correction. For this, the μ-map acquired at end-expiration was moved to each respiratory position in MATLAB using the deformation fields estimated from MR images. Each respiratory bin was independently reconstructed offline with e7 Tools (Siemens Healthcare, Knoxville, USA) using the OSEM algorithm, with 3 iterations and 21 subsets, point spread function modelling, voxel size = $2.03 \times 2.08 \times 2.08\,\text{mm}^3$, matrix size = $127 \times 344 \times 344$. Finally, images reconstructed at each respiratory position were combined in MATLAB to produce a motion-corrected PET image.

5.2.2 Image Analysis

Reconstructed CMRA images were reformatted to simultaneously visualise the left anterior descending (LAD) artery and right coronary artery (RCA) using the 'Soap Bubble' software [49]. Metrics of visible vessel length and sharpness were obtained for vessels without stents in the proximal artery. Vessel sharpness values were normalised to the signal intensity of the centre line of each vessel, so that 100% sharpness refers to a maximum signal intensity change at the vessel edge. Additionally, motion-corrected CMRA images were reformatted following the anatomy observed in the X-ray angiography in order to compare both of them visually.

Reconstructed ^{18}F-FDG PET images were analysed by automatically applying the 17-segment model according to the American Heart Association [50] (see Section 2.3.2) to the left ventricular myocardium using dedicated software (MunichHeart [220]). The relative increase in ^{18}F-FDG signal of motion-corrected images over uncorrected images was computed for each of the 17 segments for each patient. Additionally, NMC and MC PET images were reoriented in short axis to visually compare them with the LGE images acquired in the same scan session.

5.3 Results

Scans were successfully completed in all subjects. The average acquisition time for the proposed PET-CMRA framework was 11.2 ± 2.4 minutes. Due to differences in planning time, in two of the patients there was no overlap between the PET and the CMRA acquisition, so that motion correction of the PET data could not be performed. Additionally, one of the patients was not able to receive the gadolinium-based contrast agent. These three patients were excluded from the following analysis. For the rest of the patients (N = 11), the average overlap between PET and CMRA acquisition was 8.8 ± 1.2 minutes, corresponding to list-mode PET data being acquired during $80.3 \pm 20.9\%$ of the duration of the CMRA acquisition. For the motion-compensated PET-CMRA image reconstruction, 3 to 5 respiratory bins (4.1 ± 0.9 bins on average) were used, resulting in PET bins with 62.93 ± 30.40 million counts.

Reformatted CMRA images showing non-stented RCA and LAD for three of the patients are shown in Figure 5.2. Improvements in the delineation of the RCA and LAD were observed in the CMRA images after applying MC, allowing depiction of non-stented vessels, even in cases where severe respiratory motion prevented the visualisation of both the left and right proximal coronary arteries in the NMC image, as observed for Patient 1. Figure 5.3 shows example coronal slices of the ^{18}F-FDG PET images reconstructed for three representative patients. MC increased the sharpness of the left ventricle myocardium and improved visualisation of small features such as the papillary muscles (blue arrows) and delineation of viability defects (red arrow) compared to NMC.

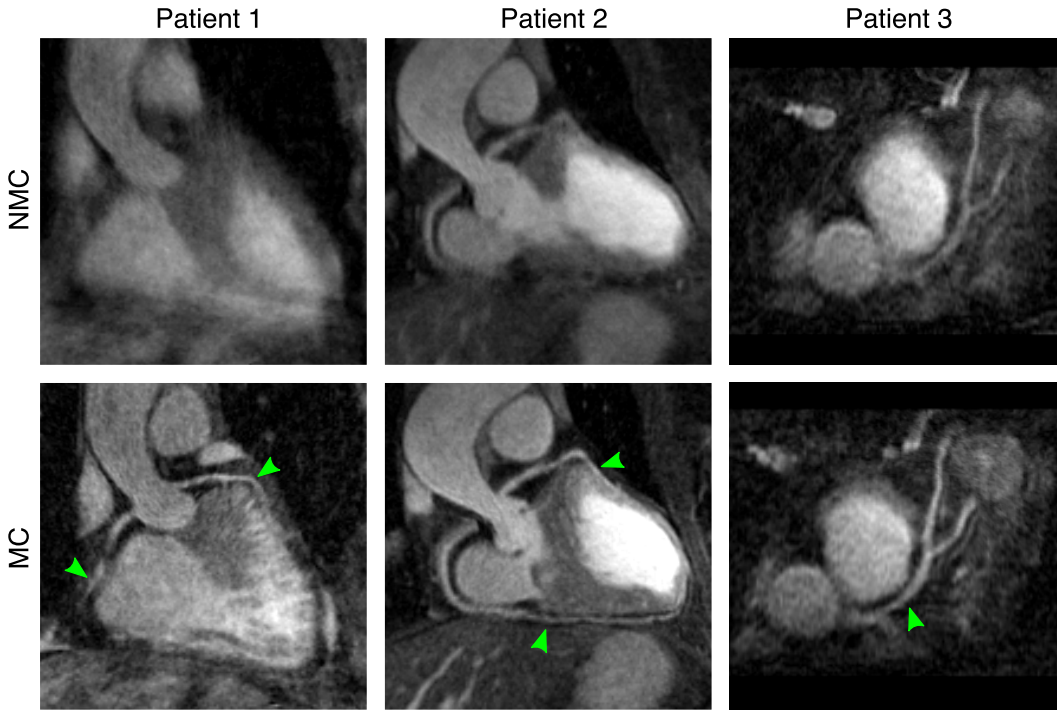

Figure 5.2: Reformatted images for 3 representative patients (columns) showing uncorrected (NMC) and motion-corrected (MC) CMRA images. Improvements in the visualisation of the vessels are observed when applying MC (green arrows) for all cases, particularly in the distal segments of the arteries.

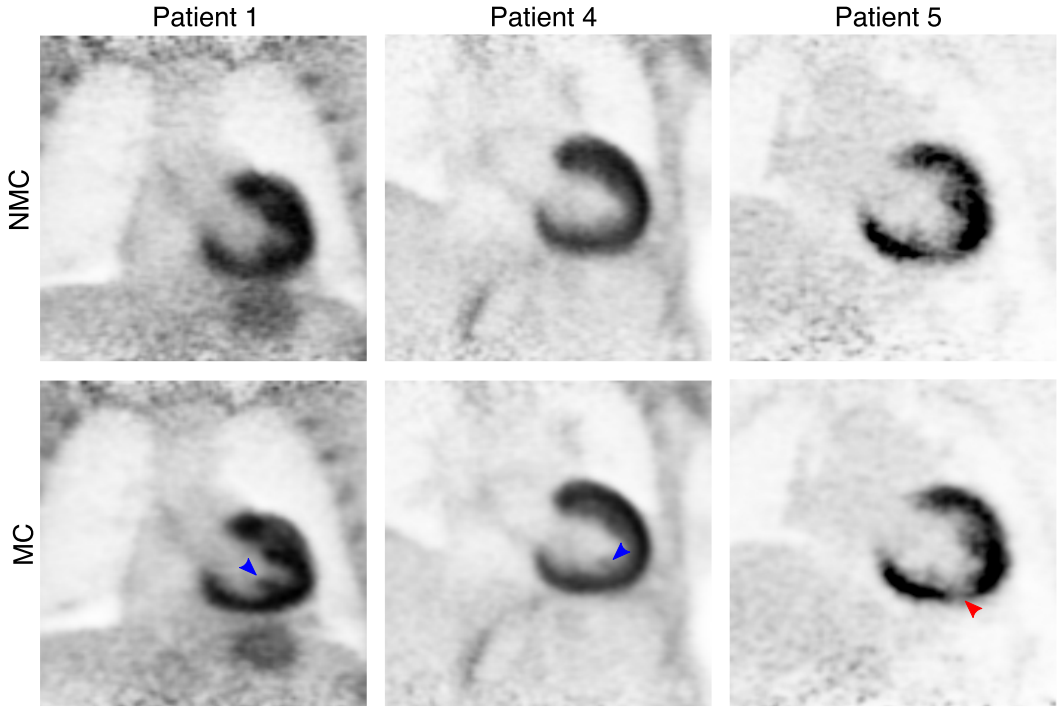

Figure 5.3: Coronal slice for 3 representative patients (columns) showing uncorrected (NMC) and motion-corrected (MC) viability ^{18}F-FDG PET images. Improvements in image quality can be observed when applying MC, particularly in small structures (blue and red arrows), compared to NMC.

A visual comparison between the reformatted MC CMRA and the corresponding invasive X-ray angiogram is shown in Figure 5.4 for two patients. Adequate spatial resolution and contrast in CMRA images allowed for a depiction of the proximal arteries comparable to the X-ray angiogram for both cases. In Patient 6, a stenosis observed in the mid segment of the RCA in CMRA was confirmed in the angiogram (Figure 5.4, red arrows), while in Patient 7 an aneurysm in the proximal RCA was seen in both modalities (Figure 5.4, green arrows).

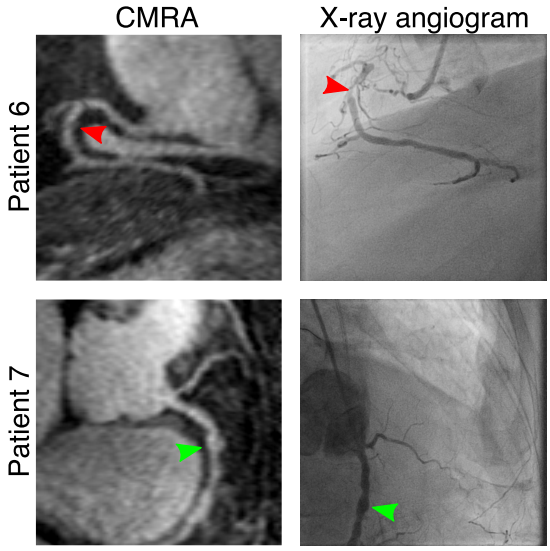

Figure 5.4: Reformatted CMRA and corresponding X-ray angiogram for two representative patients. In Patient 6, a stenosis in the mid segment of the right coronary artery (RCA) can be observed in both modalities (red arrows), while in Patient 7 an aneurysm can be observed in the proximal segment of the RCA (green arrows).

Figure 5.5 shows a short axis view of the ^{18}F-FDG PET both for NMC and MC reconstructions and corresponding slice of the 2D LGE scan for two patients. It can be observed that MC PET images have an improved correspondence to the anatomy as observed in the LGE images and reduced noise compared to NMC images. In particular, improvements in delineation of viability defects are apparent: for Patient 6, the transmural viability defect observed in the infero-lateral wall was better depicted after motion correction (Figure 5.5, blue arrows), while in Patient 8, motion correction allowed for the identification of viable myocardium in a defect that appeared misleadingly as transmural in the NMC image (Figure 5.5, green arrows). MC also enabled the depiction of thinner structures, such as the right ventricular myocardium (Figure 5.5, pink arrow).

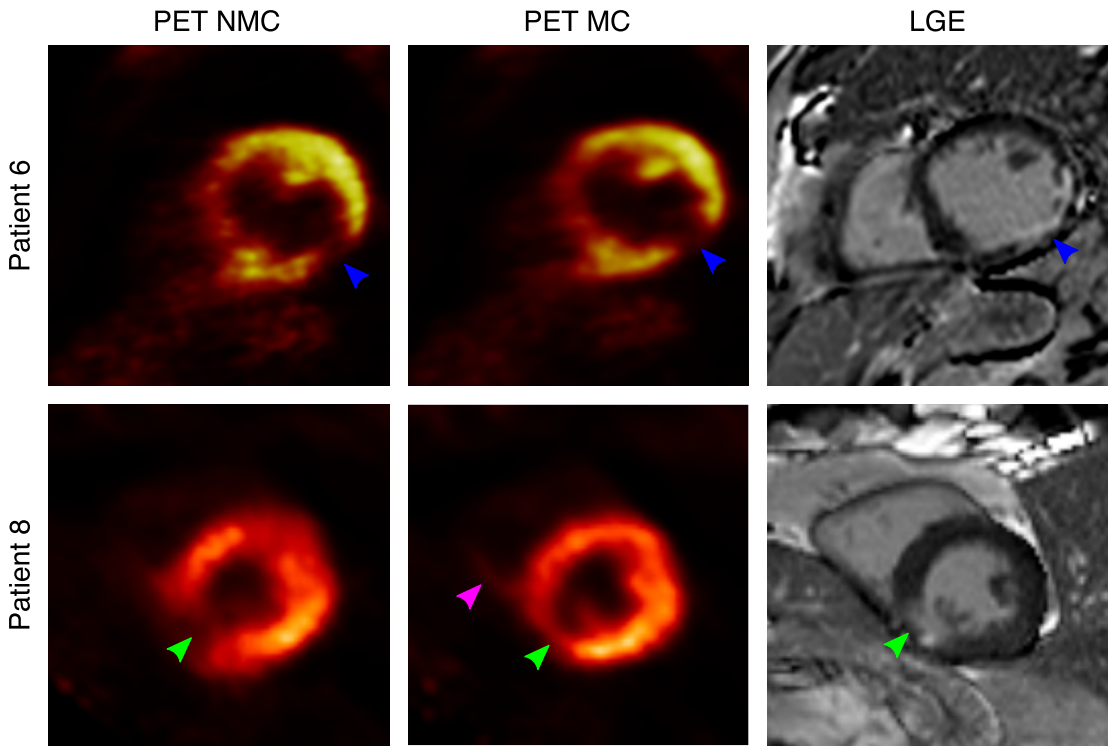

Figure 5.5: Short axis view for 2 representative patients (rows) showing uncorrected (NMC) and motion-corrected (MC) viability ^{18}F-FDG PET images, and corresponding conventional 2D LGE-MR scans. MC improves the correspondence of the PET images to the anatomy as observed in the LGE images, particularly in the delineation of viability defects (green and blue arrows) and right ventricle myocardium (pink arrow).

Image quality metrics for uncorrected and motion-corrected CMRA images are shown in Figure 5.6. Tracking of the vessels was possible in 14 out of 15 non-stented vessels (8 RCA, 6 LAD). In one of the patients, significant cardiac motion prevented the visualisation of the coronary arteries. For the rest of the vessels, increased visible length of the vessels were observed after motion correction for both the RCA (49.9% increase on average) and the LAD (32.6% increase on average), as shown in Figure 5.6(a,c). Similarly, vessel sharpness increased by 12.3% and 18.9% on average for the proximal RCA and LAD respectively when using motion correction, as shown in Figure 5.6(b,d).

Polar maps showing the relative increase in ^{18}F-FDG PET signal in the left ventricular myocardium after motion correction are displayed in Figure 5.7, for two patients with distinct respiratory patterns alongside the average across the whole cohort. For the patient with significant respiratory motion, the average signal increased across all segments was 33%, with a maximum of $\sim$ 50% increase in the

anterior wall. For the patient with moderate respiratory motion, an average of 3% signal increase was observed across all segments. When considering the cohort average for each myocardial segment, signal increased most towards the inferior and inferolateral regions, i.e. by an average of 8% across the six corresponding sectors of the myocardium.

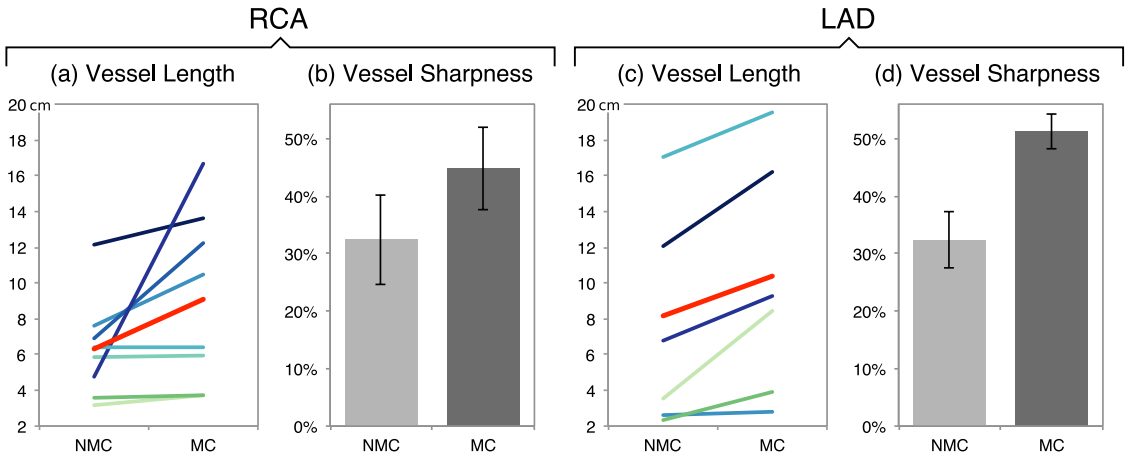

Figure 5.6: Image quality analysis for uncorrected (NMC) and motion-corrected (MC) CMRA images in eleven patients, including: visible vessel length for (a) RCA and (c) LAD, for each of the patients (green/blue lines) and average (red line); and vessel sharpness for (b) RCA and (d) LAD. Visible vessel length and sharpness improve after motion correction for all cases. Note that image analysis was performed only in vessels without stents in the proximal segment of the coronary arteries.

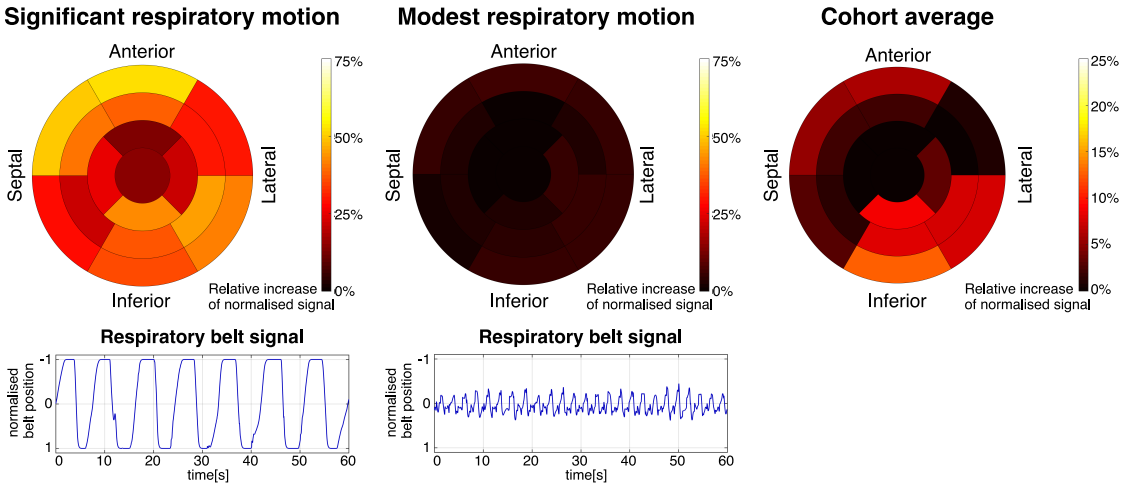

Figure 5.7: 17-segment polar maps of the relative increase in ^{18}F-FDG PET signal after motion correction for the left ventricular myocardium. Two representative patients with high amplitude respiratory motion and moderate respiratory motion are shown, alongside the average across the cohort.

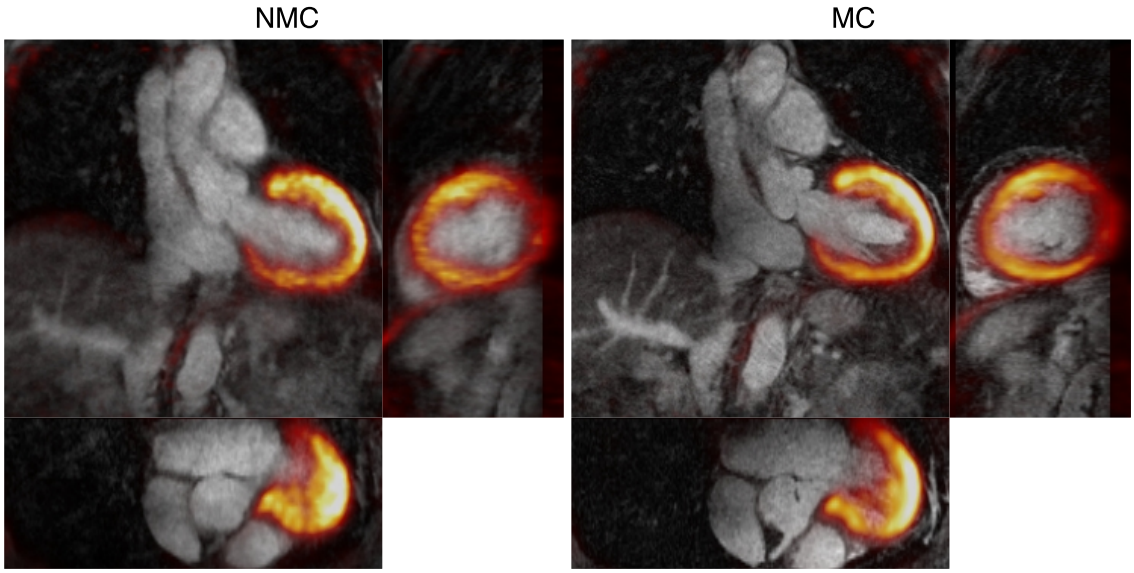

Figure 5.8: Example fused PET-CMRA image (Patient 4) showing uncorrected (NMC) and motion-corrected (MC) images. The motion correction framework produces co-registered diagnostic PET and MR images where an improved correspondence between both modalities can be observed.

Finally, Figure 5.8 shows an example fused PET-CMRA dataset before and after motion correction. The framework produces co-registered diagnostic PET and CMRA images, improving the correspondence between modalities compared to uncorrected images.

5.4 Discussion

In this Chapter the proposed approach for respiratory motion-corrected cardiac PET-MR for the simultaneous visualisation of coronary anatomy by CMRA and myocardial viability by ^{18}F-FDG PET was tested in a cohort of patients with coronary artery disease. In contrast to most proposed MR-based motion correction approaches for cardiac PET data that utilise MR images mainly for improving PET image quality [197, 211, 212], this approach produces diagnostic images in both modalities, potentially reducing total PET-MR examination time. Furthermore, the proposed PET-CMRA acquisition and reconstruction scheme has a short and predictable scan time of approximately 11 minutes, which makes it suitable for clinical practice. Indeed, for this study the proposed PET-CMRA acquisition was included into a standard clinical PET-MR protocol during the waiting time required for con-

ventional LGE MR imaging.

Although the motion correction framework for CMRA data had been previously shown and validated for healthy subjects [27, 159], this study focused on demonstrating the feasibility of applying such framework to patients with documented cardiovascular disease. For the cohort of patients in this study, improvement in image quality after motion correction is apparent, allowing the visualisation of 14 out of 15 non-stented vessels and increasing visible length and sharpness of the coronary arteries. Furthermore, visual comparison showed good agreement between the motion-corrected CMRA and gold standard invasive X-ray angiograms, including visualisation of stenosis and aneurysm in the proximal segment of the arteries (Figure 5.4).

For the ^{18}F-FDG myocardial viability PET images, the proposed motion correction approach improved the depiction of small structures such as the right ventricle myocardium and papillary muscles, and enhanced the visualisation of transmural and non-transmural viability defects in the left ventricle myocardium. In general, motion correction produced an increased PET signal in each of the myocardial segments, with an average of 8% relative increase for the inferolateral wall. When analysing the relative signal increase for each dataset, it was observed that improvements were strongly related to the respiratory pattern of each subject: modest increase in signal was obtained in patients with shallow breathing, while regional increases of up to 33% were observed in patients with significant respiratory motion. Such increases come both from a reduction in the blurring and from appropriate alignment between attenuation maps and emission data in the motion-corrected reconstruction framework. This is particularly significant in the anterior wall (Figure 5.7), located closer to the heart-lung interface. The results obtained are consistent with findings in recent studies [221], where respiratory-induced mismatches between emission and attenuation maps resulted in an average $6 \pm 7\%$ relative change in ^{18}F-FDG uptake in the myocardium, compared to the ^{18}F-FDG uptake obtained with corrected attenuation maps, in a cohort of 20 patients.

The results obtained in this study suggest that respiratory motion compensation is fundamental for avoiding misinterpretation of non-viable segments in the myocardium by ^{18}F-FDG PET. An improved correspondence to the anatomy and

delineation of transmural and non-transmural myocardial viability defects was observed when comparing LGE-MRI with the motion-corrected PET images. Recent studies have compared conventional LGE-MRI and ^{18}F-FDG PET for the assessment of myocardial viability [179, 180], finding good agreement between the two imaging modalities. However, both studies report some mismatches between ^{18}F-FDG PET and LGE. It is worth noting that in these studies LGE-MR images were acquired during breath-hold using 2D ECG-triggered sequences, as conventionally done in clinical practice, to minimise cardiac and respiratory motion. On the contrary, in both studies, PET images did not include any motion compensation technique, which could partially explain the mismatches between the two modalities. Further simultaneous ^{18}F-FDG PET and LGE-MRI studies with 3D MR acquisition sequences that allow for motion compensation in both modalities, such as the recently proposed MR BOOST sequence [222], could allow for a fairer comparison.

The study presented in this Chapter had a number of limitations. First, the presence of stents in at least one of the coronary arteries for each of the patients limited the number of MR visible vessels available for analysis. A larger cohort would be required to provide a sufficient number of vessels for a more robust statistical analysis of improvements in image quality after motion correction. Second, variations in the overlap between the CMRA and PET acquisitions resulted in high variability in the fraction of PET data that could be motion-corrected and therefore in the quality of the PET images. An acquisition protocol with an extended PET list-mode acquisition that guarantees full overlap between the two acquisitions would allow the use of the full capabilities of the motion correction approach. Third, patients with known chronic total occlusion were recruited for this study. In order to assess the diagnostic performance of the proposed simultaneous visualisation of myocardial viability and coronary anatomy a similar study would need to be performed in subjects with suspected coronary artery disease.

The proposed PET-CMRA protocol includes the acquisition of a Dixon-based attenuation correction map, which segments the image into four tissue classes and assigns a fixed attenuation value to each of them, as proposed in [117]. Studies have shown that assigning a fixed attenuation value to the lung tissue can affect accuracy of the PET images in the thoracic region, inducing bias in quantification

of lung lesions [120] and volumes of interest within the lungs [121]. However, this effect was shown to be less significant in cardiac structures. Moreover, a recent study focused on cardiac imaging showed no statistically significant differences in average myocardial uptake when comparing PET-CT and PET-MR using Dixon-based attenuation correction [122].

While the presence of stents in the coronary arteries has been shown to produce additional artefacts in MR-based attenuation correction due to misclassification of voxels in stented arteries as air [221], such artefacts were not observed in this study. Indeed, in this cohort of patients, voxels belonging to stented vessels were classified as soft-tissue. It is worth noting that the impact of the stents themselves in the accuracy of MR-based attenuation correction is challenging to assess, as such devices usually produce artefacts in CT images [223], making gold-standard measurements difficult to obtain.

As discussed in Chapter 4, the proposed motion compensation technique only addresses the problem of respiratory motion. In CMRA, the problem of cardiac motion was addressed by acquiring data only during the quiescent mid-diastolic period of the cardiac cycle. A similar approach could be used for the PET data by rejecting the fraction of data that falls outside the diastolic period, however, this would impact image quality by increasing the noise in the PET images. Chapter 6 describes a novel approach for compensating for the effect of both cardiac and respiratory motion on the PET images.

Finally, the proposed approach does not include a mechanism for compensating for unpredictable bulk motion of the patient during the PET-CMRA examination. Although this problem is alleviated when reducing total acquisition time, techniques such as the one proposed in [224] for detection and correction of whole-body motion in both PET and MR could be adapted to be used with the proposed framework for improved robustness.

PET radiotracer	Clinical Indication	Patient	Gender	Age (y)
^{13}N-ammonia	Healthy subject	P1	M	51
		P2	M	59
^{18}F-FDG	Suspected sarcoidosis	P3	M	37
		P4	M	47
		P5	M	53
		P6	M	40
^{18}F-choline†	Coronary inflammation	P7	M	67
		P8	M	62
^{18}F-NaF‡	Coronary plaque calcification	P9	$*$	$*$
		P10	$*$	$*$

Table 5.1: Summary of patient characteristics, including gender, age, cardiac PET protocol and clinical indication. $*$ according to Institutional Ethics, this information can not be disclosed. †Data acquired in collaboration with Rob Holtackers, Rik Moonen and Eline Kooi (Maastricht UMC+). ‡Data acquired in collaboration with Bas Bekkers, Bas Streukens and Eline Kooi (Maastricht UMC+).

5.5 Additional Clinical Experience

In order to demonstrate the benefits of the proposed respiratory motion correction framework for simultaneous coronary MR angiography and cardiac PET in different clinical contexts and with different PET radiotracers, preliminary tests have been performed in 10 patients. Table 5.1 summarises the patient characteristics, clinical indication and cardiac PET radiotracer used in each case.

All subjects were scanned in a 3 T Biograph mMR scanner (Siemens Healthcare, Erlangen, Germany). The CMRA-PET data was acquired after injection of a Gadolinium-based MR contrast agent with the following CMRA parameters: voxel size = $1 \times 1 \times 2$ mm, field of view = $304 \times 304 \times 96{-}104$ mm, TR/TE= 3.7/1.7 ms, flip angle = 15°, T2-prep = 50 ms and spectrally selective fat saturation.

A variety of PET radiotracers was used, depending on the clinical indication, including ^{18}F-FDG for myocardial inflammation, ^{13}N-ammonia for myocardial perfusion, ^{18}F-choline for vascular inflammation, and ^{18}F-NaF for plaque calcification PET imaging. Motion-corrected (MC) and uncorrected (NMC) images were reconstructed in each case, for comparison purposes.

Scans were successfully completed in all subjects. The average acquisition time for the PET-CMRA scan was 12.85 ± 2.50 minutes. Improvements in the delineation of the left anterior descending and right coronary arteries were observed after

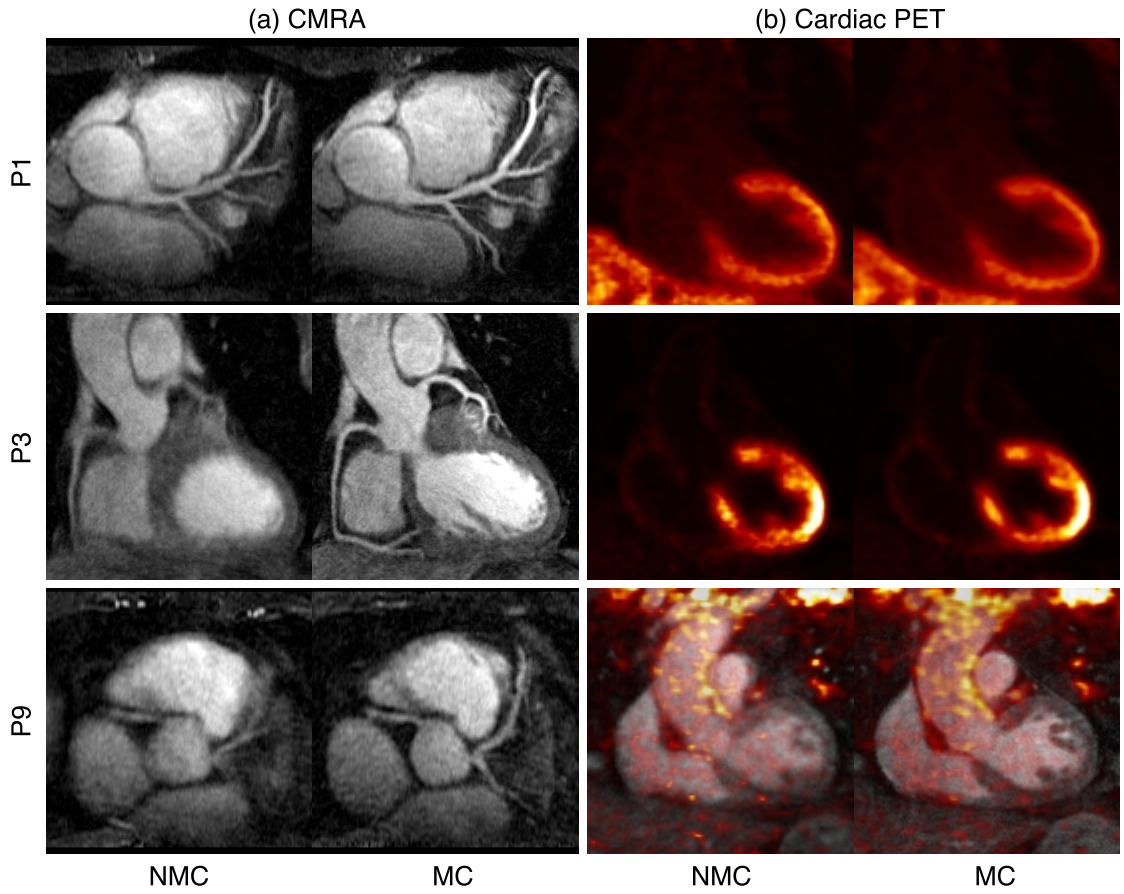

Figure 5.9: Uncorrected (NMC) and motion-corrected (MC) (a) reformatted CMRA images and (b) cardiac PET images for 3 representative patients. Fused PET-CMRA is displayed for P9, due to the nature of the ^{18}F-NaF uptake.

applying motion correction to the CMRA images in all cases, as can be observed in Figure 5.9. In P3, an inadequate suppression of physiological myocardial uptake can be observed, so myocardial inflammation could not be assessed. In P9, fused cardiac PET-CMRA images are displayed, as the focal nature of the ^{18}F-NaF uptake requires an anatomical reference for localisation purposes. Overall, motion-corrected CMRA shows sufficient image quality for depicting the proximal coronary anatomy, while in the cardiac PET images, motion correction increases the sharpness of large structures such as the liver or the myocardium, and enhances depiction of small structures such as the papillary muscles.

5.6 Summary

A first clinical validation of the introduced respiratory motion-corrected whole-heart PET-CMRA framework for simultaneous visualisation of coronary anatomy and myocardial integrity in 11 patients with coronary artery disease has been described. The reported results have shown that motion correction consistently improves image quality compared to the uncorrected images for both imaging modalities. A good agreement between coronary anatomy depicted by motion-corrected CMRA and X-ray angiography was observed. In addition, motion-corrected ^{18}F-FDG PET images were in good agreement with LGE-MRI, showing more accurate depiction of both transmural and non-transmural viability defects.

Results obtained from the cohort of patients with coronary artery disease and from additional preliminary tests in patients with a variety of cardiac conditions have shown that the PET-CMRA framework approach is robust and can be applied in combination with different PET radiotracers. Furthermore, the results suggest that the PET-CMRA framework allows the acquisition of diagnostic images with both modalities in a short and time-efficient examination, showing promise for its integration in clinical practice.

Chapter 6:
Respiratory and Cardiac Motion-Corrected Simultaneous Dual-Phase CMRA-PET

The approach for simultaneous CMRA-PET introduced in Chapters 4 and 5 only enables correction of the effect of the respiratory-induced motion of the heart in both imaging modalities. Whereas in the proposed approach for CMRA the effect of cardiac motion is minimised by acquiring data only during the mid-diastolic quiescent period of the cardiac cycle, no cardiac motion compensation was considered for the PET data, which was simply aggregated over each heartbeat.

In order to assess the effect of cardiac motion correction in myocardial integrity PET imaging, a preliminary simulation study was performed. In this study, the impact of varying the spatial resolution and temporal resolution (i.e. number of cardiac phases) of the cardiac motion fields was analysed, and results suggested that using two cardiac phases, representing systole and diastole, and a spatial resolution of 2 mm allows for an accurate estimation of the extent and degree of transmurality of simulated viability defects. The methods and results of this study are briefly summarised in this Chapter.

Following the simulation study results, the method proposed in Chapters 4 and 5 is extended in this Chapter to correct for both cardiac and respiratory induced non-rigid motion of the heart. This is achieved through the implementation of a simultaneous dual-phase CMRA and cardiac PET data acquisition that provides: (1) coronary anatomy visualisation from CMRA acquisition, (2) left ventricular function

from a dual-phase anatomic whole-heart MR acquisition, and (3) assessment of myocardial integrity from cardiac and respiratory motion-corrected ^{18}F-FDG PET data, in a single efficient examination.

Using the same framework described in Chapters 4 and 5, respiratory motion is estimated from 2D iNAVs, acquired now at each heartbeat before both the systolic and diastolic CMRA phases, and from high-resolution 3D CMRA images reconstructed at different respiratory positions for each cardiac phase. Furthermore, estimation of non-rigid cardiac motion fields is performed by image registration of the systolic and diastolic 3D images obtained from the proposed dual-phase CMRA acquisition. The MR-derived deformation fields are used to correct both the dual-phase CMRA (respiratory motion correction for each cardiac phase) and the simultaneously acquired cardiac PET data (respiratory and cardiac motion correction). This approach is highly efficient, because it uses all the acquired PET and dual-phase CMRA data for image reconstruction, and it produces good quality images with both modalities within a short and predictable acquisition time.

The motion-corrected dual-phase CMRA image reconstruction was tested in eight healthy subjects. CMRA images were reformatted to visualise the coronary and cardiac anatomy, and left ventricular function (systolic and diastolic volumes, ejection fraction and stroke volume) derived from the proposed dual-phase 3D CMRA sequence was compared against reference values obtained from a conventional stack of 2D cine images. The whole respiratory and cardiac PET-CMRA motion correction framework was then tested in six cardiac patients with coronary artery disease, using ^{18}F-FDG for assessing either myocardial viability or inflammation. Some of the results presented in this Chapter have been published as a journal article [28].

6.1 Impact of Spatio-Temporal Resolution of Motion Fields on Cardiac Motion-Corrected PET

As described above, a simulation study was performed to evaluate the impact of cardiac motion correction on myocardial PET imaging. The effect of varying the spatial and temporal resolution of cardiac motion information on image quality and quantitative standardised uptake values (SUV) was analysed. This study was

performed using the commercially available XCAT digital phantom [225], which provides a numerical representation of a human torso and parameterised models of motion for each organ in the thorax. The software can be used for simulation of cardiac motion only, respiratory motion only or both cardiac and respiratory motion simultaneously. Detailed information about the motion can be obtained from the XCAT software as a set of vectors that describe the 3D position of each voxel relative to the first generated frame. For the purposes of this study, only cardiac motion was used. The XCAT software generates emission maps, in which user-defined activity values are assigned to each tissue class, and attenuation maps created using realistic energy-dependent attenuation coefficients. These emission and attenuation maps are produced for each motion state of the simulation.

6.1.1 Methods

Using the XCAT phantom, four myocardial viability lesions with different degrees of transmurality (100%, 50% and 25%), and varying extension and location (anterior and lateral wall) were simulated using realistic ^{18}F-FDG uptake values [226]. A short axis view of the resulting emission maps for each case can be observed in Figure 6.1.

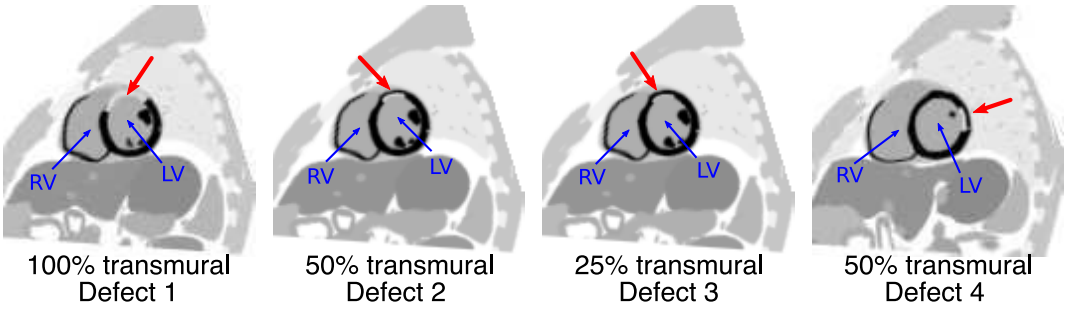

Figure 6.1: Example short-axis slice of the simulated myocardial viability defects. Left (LV) and right (RV) ventricles are indicated in the images, as well as the simulated defects (red arrow).

Cardiac motion was simulated based on a normal cardiac cycle with an RR interval of 1 s and 20 cardiac phases. Analytical PET simulations were performed using the STIR software [227], with the geometry of the Siemens Biograph mMR scanner, i.e. 60 cm bore size, 8 rings of $4 \times 4 \times 20\,\text{mm}^3$ LSO crystal detectors, resulting in an axial field of view of 258 mm. The simulation of PET data acquisition comprised the 3D forward-projections of emission maps at each motion state and

the application of corresponding attenuation factors. Background coincidences from scattered and random coincidences were not included in these simulations. Emission maps were scaled to produce a total of 35×10^6 counts over the entire cardiac cycle, which is representative of the number of true counts acquired in a 5-minutes ^{18}F-FDG cardiac scan. Poisson noise was introduced to each cardiac phase to simulate coincidence counting.

Motion information was obtained from the XCAT software with five temporal resolutions, i.e. 20, 10, 5, 2 and 2* cardiac phases, and four spatial resolutions, i.e. 2, 4, 5.68 and 9.84 mm^3 isotropic voxel size, resulting in twenty sets motion operators of varying spatial and temporal resolution. The 2* non-uniform division of the cardiac cycle groups two thirds of the cardiac cycle around maximum relaxation in one cardiac phase, approximately corresponding to diastole, and the remaining third as the second phase, representing systole.

The motion fields were interpolated to PET image resolution and used as input in an ordered-subsets motion compensated PET image reconstruction algorithm, also provided by the STIR software [171]. The reconstruction used 21 subsets and 3 iterations, a voxel size of $2.03 \times 2.08 \times 2.08$ mm^3, a matrix size of $127 \times 285 \times 285$ and a 4 mm full-width at half-maximum (FWHM) isotropic Gaussian post-reconstruction filter. Additionally, a motion-free image was simulated and reconstructed for reference purposes, and an uncorrected reconstruction was performed for further comparison.

Reconstructed PET images were assessed based on clinical metrics, including detectability of damaged segments in high-resolution AHA polar plots computed from the left ventricular myocardium [50], and extent and degree of transmurality (i.e. fraction of the wall affected) of the myocardial lesion. Detectability of the lesion was defined such that segments with an SUV 2.5 standard deviations below the mean myocardial SUV were labelled as non-viable [228], and the number of segments labelled as non-viable was used for approximating the lesion extent. For assessing degree of transmurality, three image profiles were placed across the damaged and healthy myocardium in a short-axis slice. For improved robustness, the background signal was thresholded and a Gaussian curve was fitted to each profile. An example of healthy and damaged myocardium profiles, with their corresponding Gaussian

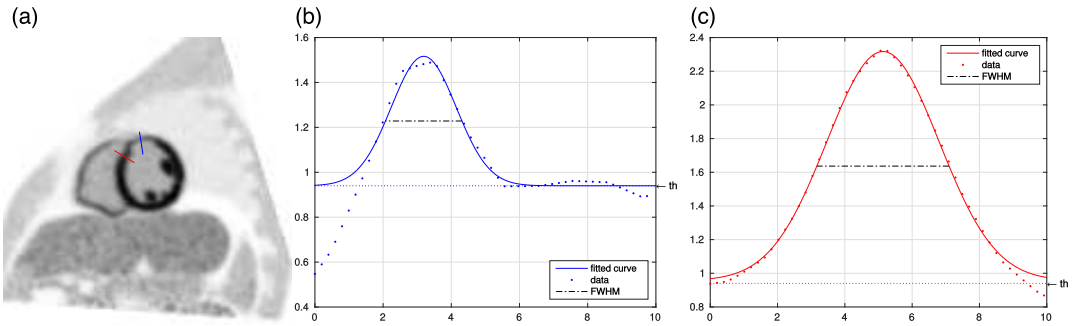

Figure 6.2: (a) Example of profiles used for transmurality analysis in the damaged (blue) and healthy (red) myocardium. Background signal is removed prior to the gaussian fit for the (b) damaged and (c) healthy myocardium using a threshold indicated as 'th'. The standard deviation of the fitted curve is used to estimate the full-width at half-maximum (FWHM) thickness of the myocardium.

fits are shown in Figure 6.2. The average standard deviation of the Gaussian curve was used to estimate the FWHM thickness of the myocardium. Then, the degree of transmurality was defined as one minus the ratio between the FWHM of the affected and healthy myocardium, so that 100% represents a transmural defect and 0% implies a non-damaged myocardium, following Equation 6.1.

$$\%\ \text{Trans} = 100 \times \left(1 - \frac{\text{FWHM}_{\text{damaged}}}{\text{FWHM}_{\text{healthy}}}\right) \tag{6.1}$$

6.1.2 Results

For both transmural and non-transmural defects, results showed that although image quality degrades when reducing temporal and spatial resolution of the motion fields, non-viable myocardium can be detected even without motion correction, as shown in Figure 6.3. For defects 1 (transmural) and 2 (50% transmural), a resolution of 10 mm and 2* phases allowed the detection of more of 90% of the non-viable segments. For defects 3 (25% transmural) and 4 (50% transmural), a minimum resolution of 2 mm and 2* cardiac phases was required to detect more than 90% of the non-viable segments correctly.

For the transmurality analysis both the 2 mm-20 phases resolution and the 2 mm-2* phases resolution lead to accurate results; considering only the non-transmural defects, an average error of $7.17 \pm 3.44\%$ and $5.58 \pm 1.53\%$ compared to the motion-free reference was obtained, respectively. A summary of the transmurality analysis

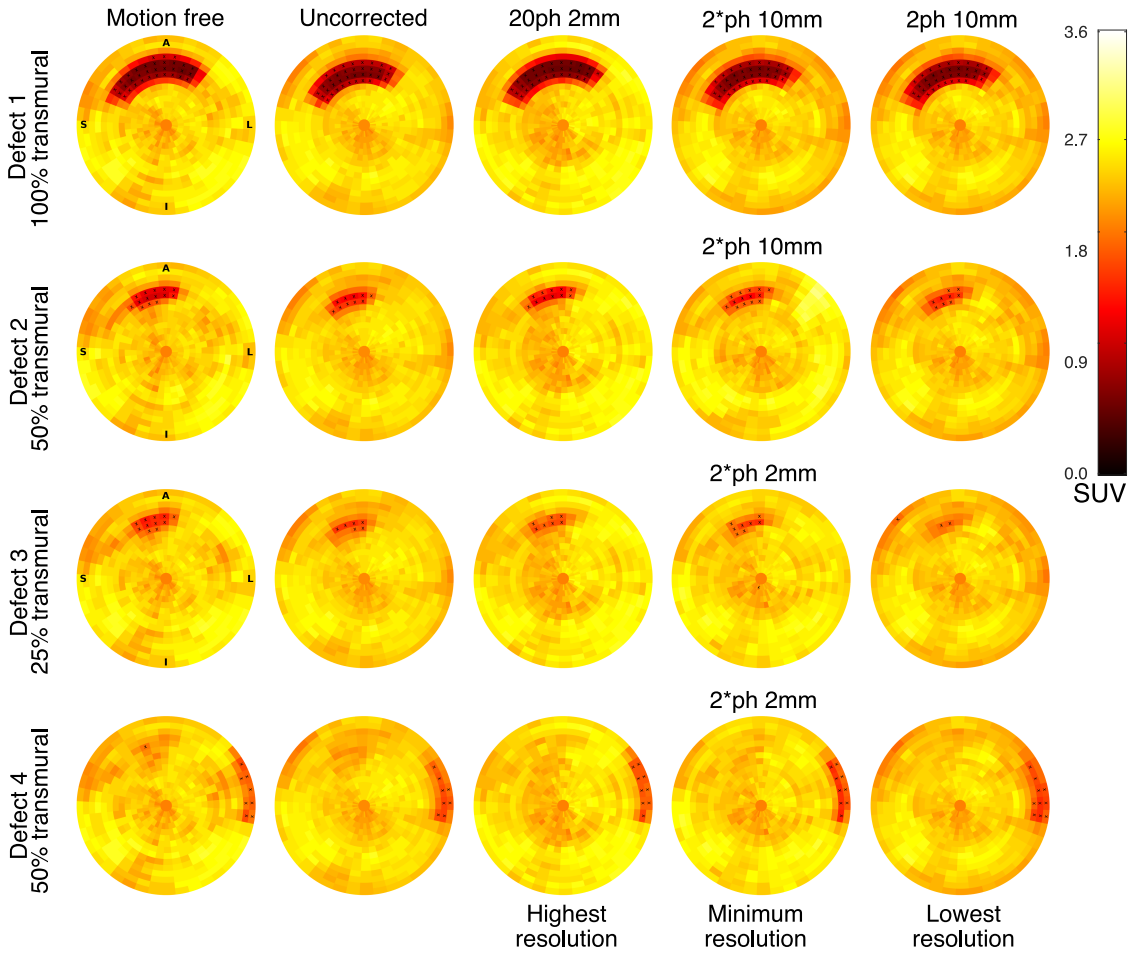

Figure 6.3: Polar plots for all simulated defects, showing reference motion-free, uncorrected, and motion-corrected images with highest, minimum and lowest spatio-temporal resolutions. Damaged segments are indicated in each plot with a black X. When using 2* phases and an appropriate spatial resolution, more of 90% of the non-viable segments can be detected. (A: anterior, S: septal, L: lateral, I: inferior)

for these defects is shown in Figure 6.4. For defects 2 and 3, using 2 cardiac phases leads to an underestimation of the degree of transmurality of the defect, independently of the spatial resolution used. For defect 4, located in an area of large cardiac motion amplitude, when no motion correction is performed, the lesion is erroneously detected as transmural, as depicted in Figure 6.5.

6.1.3 Conclusion

This preliminary simulation study assessed the impact of spatial and temporal resolution of motion fields for cardiac motion-corrected myocardial integrity PET imaging. Results showed that non-viable myocardium can be detected even without

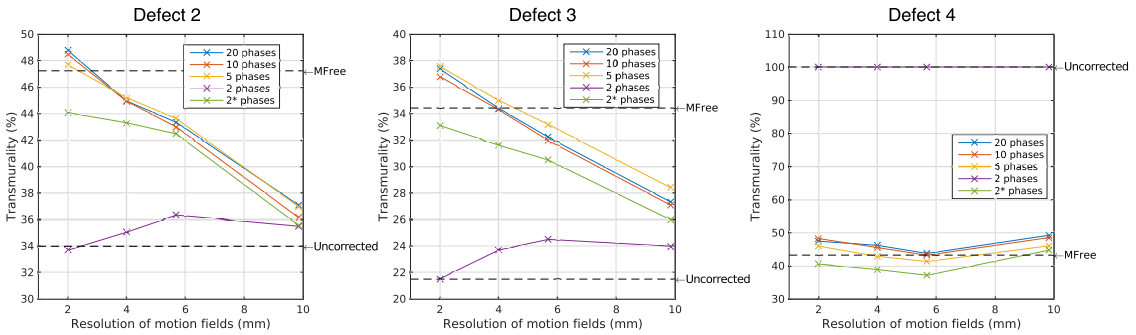

Figure 6.4: Transmurality estimation for 50% transmural viability defects located in areas of small (defect 2) and large (defect 4) cardiac motion amplitude, and for a small transmural defect (defect 3). For all defects resolution can be reduced to 2 mm-2*phases without losing accuracy. For defect 4, the lesion appears erroneously as 100% transmural in the uncorrected and 2-phases motion-corrected reconstructions.

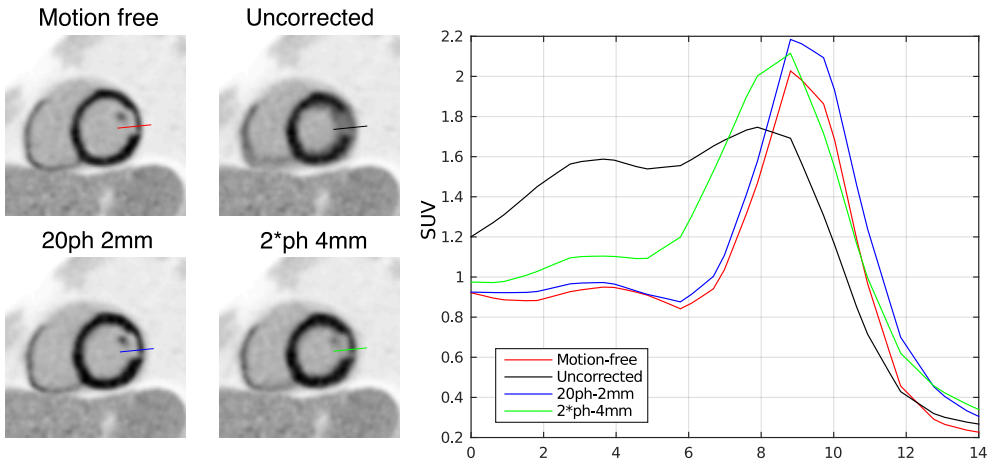

Figure 6.5: Short axis slices for motion free, uncorrected and two motion compensated reconstructions for defect 4 alongside profiles through the lesion. For the uncorrected reconstruction, the remaining healthy myocardium cannot be identified so the lesion appears erroneously as transmural.

motion correction, however, motion correction is essential for accurate estimation of the size and degree of transmurality of defects.

The non-uniform two-phase division of the cardiac cycle achieved less than 10% error in the estimation of extent and transmurality of all simulated defects using a spatial resolution of 2 mm. Thus, temporal resolution of the motion fields can be significantly reduced without losing diagnostic accuracy. In the context of simultaneous CMRA-PET imaging, these results suggest that including one additional cardiac phase in the CMRA acquisition sequence would enable accurate motion estimation for cardiac motion correction in PET, provided that such acquisition is performed during systole.

6.2 Methods

6.2.1 Image Acquisition

The proposed PET-CMRA acquisition protocol consists of an ECG triggered free-breathing dual-phase CMRA sequence simultaneously acquired with list-mode PET data on a 3 T hybrid PET-MR system as shown in Figure 6.6. Similarly to the framework introduced in Chapter 4, a standard 2-point Dixon-based attenuation map (μ-map) is acquired during breath-hold at end-expiration before the simultaneous PET-MR acquisition [117]. A 2D cine acquisition is performed to determine two subject specific trigger delays, which coincide with the mid-systolic and mid-diastolic quiescent periods of the cardiac cycle, and the length of the acquisition window for 3D CMRA. As the acquisition window is the same in both cardiac phases, its length is defined by the shortest quiescent period, usually mid-systole.

The dual-phase CMRA data is acquired using a 3D spoiled gradient echo sequence with a fully sampled golden-step Cartesian spiral profile order sampling trajectory [155], with one spiral interleaf acquired both in mid-systole and mid-diastole at each cardiac cycle as shown in Figure 6.6a. A low-resolution 2D iNAV [78] is acquired before each 3D CMRA acquisition by adding spatially encoded low flip-angle lines. Finally, the same preparatory pulses used for the single-phase CMRA method are performed before data acquisition, to enhance the contrast between the coronary arteries and surrounding tissues: an adiabatic T2 preparation pulse is used to improve contrast between blood and myocardium without the use of exogenous contrast agents [91], and fat saturation is used to reduce the signal from subcutaneous and epicardial fat.

6.2.2 Respiratory and Cardiac Motion Estimation and Motion-Corrected Dual-phase CMRA Reconstruction

Before PET and CMRA image reconstruction, the acquired 2D iNAVs are used to estimate the translational respiratory motion of the heart in the foot-head (FH) and right-left (RL) directions by tracking a rectangular template positioned around

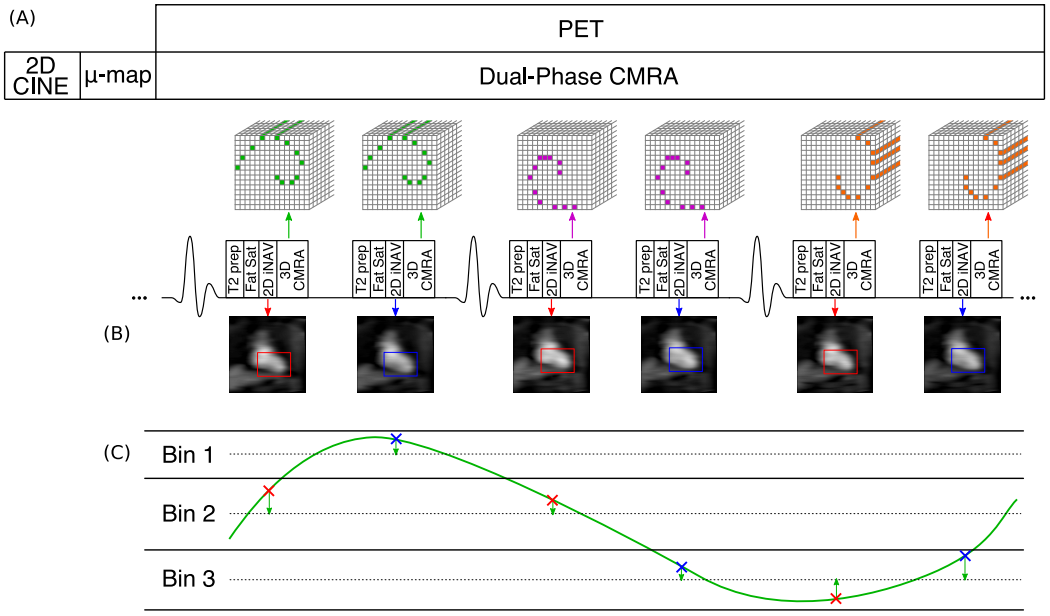

Figure 6.6: Simultaneous dual-phase CMRA and cardiac PET acquisition scheme. (a) A 2D CINE image, used for defining the mid-systolic and mid-diastolic delays, and a MR-based μ-map, used for attenuation correction of PET data, are obtained before the PET-CMRA acquisition. Dual-phase CMRA data is acquired following a golden-step spiral ordering in a Cartesian grid, so that at each heartbeat, a spiral interleaf is acquired both in systole and diastole. Fat saturation (Fat Sat) and T2 preparation (T2 prep) pulses are used to enhance the contrast between the coronary arteries and surrounding tissues. (b) A low-resolution coronal 2D iNAV is acquired before the 3D CMRA for foot-head (FH) and right-left (RL) respiratory motion estimation in both cardiac phases. (c) FH motion is used to define a number of respiratory bins, each containing the same amount of CMRA data, and FH and RL motion are used to correct the CMRA data (2D translational correction) to the centre of each respiratory bin (green arrows).

the apex of the heart using rigid image registration (Figure 6.6b). The FH motion is then used to define N_{bins} respiratory bins, ranging from end-expiration to end-inspiration, each containing approximately the same amount of dual-phase CMRA data.

CMRA data acquired during deep breaths are excluded from image reconstruction at this point, by rejecting k-space data acquired outside two standard deviations from the mean FH translation [27, 159]. Additionally, FH and RL translational motion estimates are used to correct the dual-phase CMRA data to the centre of each respiratory bin by applying a linear phase to the k-space data according to Equation 3.48, as represented in Figure 6.6c (green arrows).

The motion estimation and respiratory motion-corrected dual-phase CMRA im-

age reconstruction approach is shown in Figure 6.7. The translationally corrected dual-phase CMRA data is divided into the two cardiac phases (Figure 6.7a), and the following steps of the image reconstruction process are performed in each one of them separately.

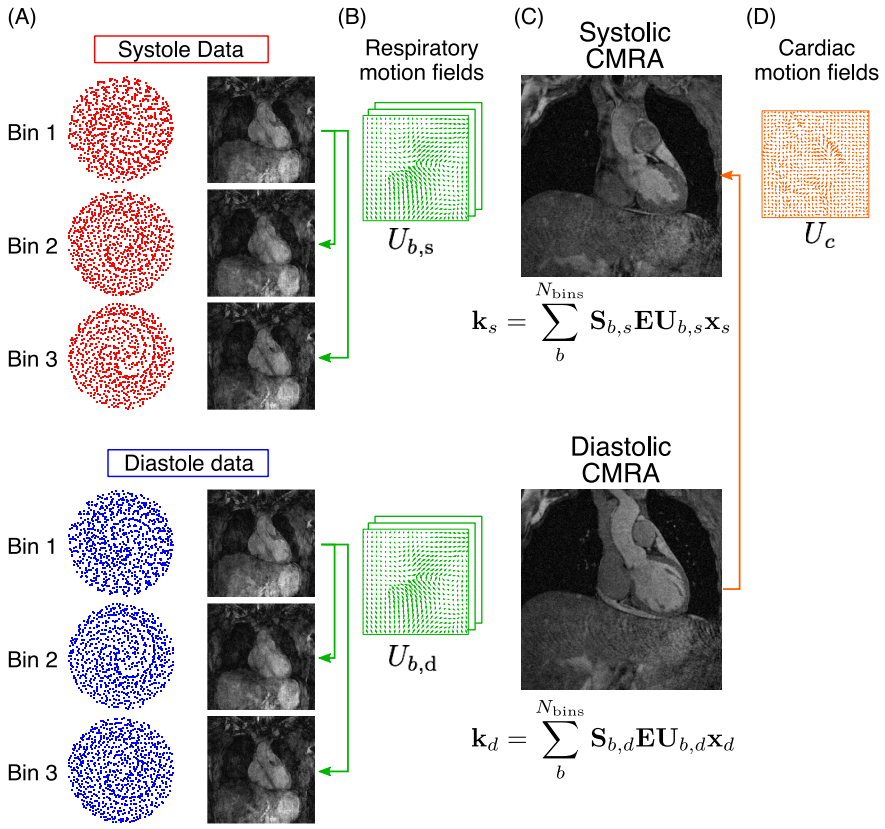

Figure 6.7: Motion-corrected dual-phase CMRA reconstruction scheme. (a) Respiratory bins (Figure 6.6c) are used to bin the dual-phase CMRA. (b) MR images reconstructed at each cardiac and respiratory phase are used for estimation of non-rigid respiratory motion fields (in green). (c) Respiratory motion-corrected CMRA images for systole and diastole are reconstructed by including the respiratory motion fields in a generalised matrix description framework, and (d) used to estimate cardiac motion (in orange).

In the first step, the N_{bins} undersampled bins are reconstructed with a soft-binning iterative SENSE [150] approach with exponential decay weighting by solving Equation 6.2 for each of them:

$$\hat{\mathbf{x}}_b = \arg\min_{\mathbf{x}_b} \|\mathbf{W}_b \left(\mathbf{E}\mathbf{x}_b - \mathbf{k}_b\right)\|_2^2 \tag{6.2}$$

where $\hat{\mathbf{x}}_b$ are the reconstructed bin images, $\mathbf{W}_b$ is a diagonal matrix containing data weights for bin b, $\mathbf{E}$ is the encoding operator, including the discrete Fourier

transform and coil sensitivities, and $\mathbf{k}_b$ is the data acquired at each respiratory bin after 2D translational motion correction to the centre of the bin. In this Chapter, the diagonal elements of $\mathbf{W}_b$ are defined as an exponential decay function of the respiratory position where the k-space data was acquired, so that points that belong to the respiratory bin being reconstructed will have a unitary weight, and points acquired outside the bin have a weight that decreases exponentially to zero as the distance to the centre of the bin increases. This ensures that each bin contains information from the centre of k-space, allowing for an increased homogeneity in the image contrast in all the respiratory bins.

After the N_{bins} respiratory bins have been reconstructed, 3D non-rigid deformation fields that represent the respiratory motion are estimated in the second step of the reconstruction scheme (Figure 6.7b) via free-form image registration using the end expiratory bin as reference, with normalised mutual information as similarity metric [213]. Finally, the motion compensated CMRA image reconstruction problem is formulated using the generalised matrix description approach described before [158], so that if $\mathbf{x}_c$ is the motion-free image to be reconstructed for cardiac phase c ($c = \text{systole}, \text{diastole}$), then the motion-corrupted measured k-space acquired at each phase can be expressed as

$$\mathbf{k}_c = \sum_{b=1}^{N_{\text{bins}}} \mathbf{S}_{b,c}\mathbf{E}\mathbf{U}_{b,c}\mathbf{x}_c \tag{6.3}$$

where $\mathbf{U}_{b,c}$ are the motion operators which transform the cardiac phase c at the reference position to any respiratory position b, and $\mathbf{S}_b$ corresponds to the sampling matrix containing the k-space points acquired at respiratory bin b and cardiac phase c. Each motion free image can then be reconstructed by solving Equation 6.3 for $\mathbf{x}_c$ using the linear CG algorithm [145].

At the end of the dual-phase CMRA reconstruction process, one systolic and one diastolic respiratory motion-corrected CMRA image is obtained, as shown in Figure 6.7c. These images can be used both for visualisation of the coronary anatomy in systole and diastole and estimation of ventricular function. Furthermore, these images can be used to estimate the non-rigid motion of the heart $\mathbf{U}_c$ between systole and diastole, as shown in Figure 6.7d.

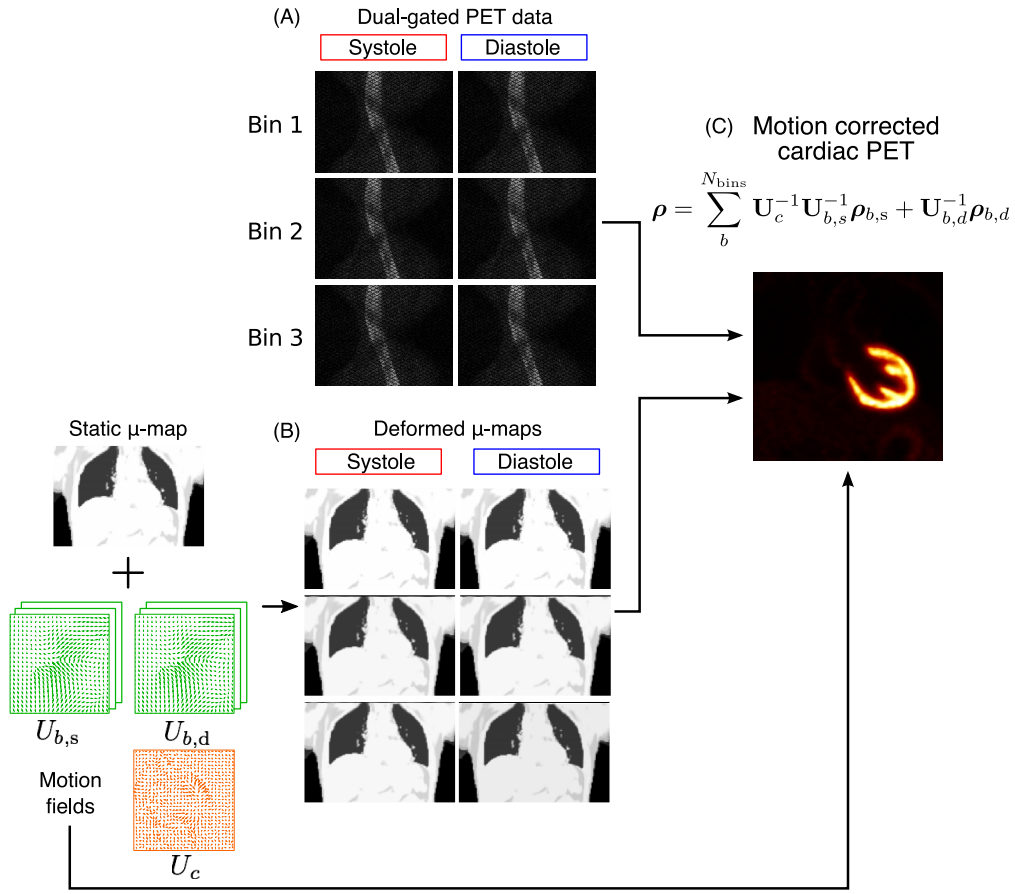

Figure 6.8: Cardiac and respiratory motion-corrected PET reconstruction scheme. (a) Respiratory bins (Figure 6.6c) and ECG signal are used to dual-gate the PET data. (b) Respiratory and cardiac motion fields estimated from MR are used for transforming the static μ-map to each cardiac and respiratory position, and (c) to produce a motion-corrected PET image.

6.2.3 Motion-Corrected PET Reconstruction

List-mode PET acquisition is synchronised with the dual-phase CMRA acquisition using the ECG signal time stamps, so that only PET data acquired simultaneously with MR is selected for image reconstruction. For each heartbeat, one third of the data acquired around maximum contraction of the left ventricle is assigned to the systolic phase, and the remaining two thirds are assigned to the diastolic phase, as indicated by the preliminary simulation study (Section 6.1). The cardiac binned PET data is then assigned to the corresponding respiratory bin, using the same respiratory windows defined in the dual-phase CMRA reconstruction. Thus, list-mode PET data is dual-gated into respiratory and cardiac phases as shown in Figure 6.8a.

The static attenuation map acquired at end-expiration is transformed to each cardiac and respiratory phase using the corresponding cardiac and respiratory deformation fields estimated during CMRA image reconstruction, as represented in Figure 6.8b. Using a RTA approach [164], each gate is independently reconstructed with an ordered-subsets expectation-maximisation (OSEM) algorithm [161], including normalisation, attenuation, random and scatter corrections.

Omitting the subsets division for simplicity, the iterative PET reconstruction algorithm for each gate can be written as

$$\boldsymbol{\rho}_{b,c}^{(\mathrm{it}+1)} = \frac{\boldsymbol{\rho}_{b,c}^{(\mathrm{it})}}{(\mathbf{N}\mathbf{A}_{b,c}\mathbf{P})^{\mathrm{T}}\mathbf{1}_I}(\mathbf{N}\mathbf{A}_{b,c}\mathbf{P})^{\mathrm{T}}\frac{\mathbf{m}_{b,c}}{\mathbf{N}\mathbf{A}_{b,c}\mathbf{P}\boldsymbol{\rho}_{b,c}^{(\mathrm{it})} + \mathbf{r} + \mathbf{s}} \tag{6.4}$$

where $\boldsymbol{\rho}_{b,c}^{(\mathrm{it})}$ is a vector that contains the PET image for respiratory bin b and cardiac phase c ($b = 1...N_{\mathrm{bins}}$,$c = \mathrm{s}, \mathrm{d}$) after (it) iterations of the algorithm, $\mathbf{P}$ is the matrix that models the system forward projection considering the scanner geometry, $\mathbf{N}$ and $\mathbf{A}_{b,c}$ are diagonal matrices with entries down the diagonal equal to the reciprocal of the normalisation and attenuation correction factors for respiratory bin b and cardiac phase c, respectively, $\mathbf{m}_{b,c}$ is a vector that contains the dual-gated data corresponding to respiratory bin b and cardiac phase c, and $\mathbf{r}$ and $\mathbf{s}$ represent estimations of random and scattered coincidences, respectively.

Finally, the images reconstructed at each respiratory and cardiac phase are transformed back to the diastolic and end-expiratory phase (Figure 6.8c), and aggregated to produce a motion-compensated PET image $\boldsymbol{\rho}$, according to Equation 6.5. It is worth noting that only systolic images require transformation in the cardiac dimension, as the reference cardiac phase is diastole.

$$\boldsymbol{\rho} = \sum_{b=1}^{N_{\mathrm{bins}}} \mathbf{U}_c^{-1}\mathbf{U}_{b,\mathrm{s}}^{-1}\boldsymbol{\rho}_{b,\mathrm{s}} + \mathbf{U}_{b,\mathrm{d}}^{-1}\boldsymbol{\rho}_{b,\mathrm{d}} \tag{6.5}$$

6.3 Experiments

For this study two *in vivo* experiments were performed. The aim of the first experiment was to validate the motion-corrected dual-phase CMRA framework for estimating left ventricular function, and was performed in a cohort of eight healthy

subjects, using only the MR capabilities of a 3 T hybrid PET-MR scanner (Biograph mMR, Siemens Healthcare, Erlangen, Germany). Then, the whole motion-corrected dual-phase CMRA-PET framework was tested in a cohort of six patients with known coronary artery disease. Written informed consent was obtained from all subjects according to institutional guidelines and the institutional ethics committee approved the study.

6.3.1 Healthy Subjects Data Acquisition

Eight healthy subjects (age 29.9±3.4 years, 4 male) were scanned during free breathing using a prototype implementation of the proposed dual-phase CMRA sequence. The following acquisition parameters were used: coronal slices, RL phase encoding, $1 \times 1 \times 2\,\text{mm}^3$ resolution, field of view $304 \times 304 \times 80{-}96\,\text{mm}^3$ with a subject-specific number of slices covering the whole heart, TR/TE = 3.7/1.7 ms, flip angle = 12°, readout bandwidth = 685 Hz/px. Two subject-specific trigger delays were set targeting the mid-systolic and mid-diastolic rest period and an acquisition window ranging from 82 to 104 ms (corresponding to 22 to 28 k-space lines acquired per heartbeat) was used depending on the minimal length of the quiescent periods of the subject. Contrast between the arteries and surrounding tissues was enhanced using an adiabatic T2 preparation pulse of 50 ms and a conventional fat saturation pulse. For the 2D iNAV acquisition, the following parameters were used: high-low Cartesian trajectory, coronal orientation, RL phase encoding, flip angle = 3°, 14 readouts with the same field of view of the CMRA acquisition, resulting in a $1 \times 21.7\,\text{mm}^2$ acquired in-plane resolution (reconstructed to $1 \times 1\,\text{mm}^2$).

Additionally, a conventional multi-breath-hold of 2D short-axis CINE acquisition was performed and used as reference standard for left ventricular function estimation. The stack of 2D CINE images was acquired with an in-plane resolution of $1.5 \times 1.5\,\text{mm}^2$, using GRAPPA parallel imaging [148] with an undersampling factor of 2 and 24 calibration lines, slice thickness of 8 mm, 8 to 10 slices covering the whole left-ventricle and 25 cardiac phases.

6.3.2 Patient Data Acquisition

Six patients with symptomatic CAD (angina or angina equivalent, excluding acute ST-elevation myocardial infarction patients) and known chronic total occlusion of at least one of the coronary arteries (ages 66.3 ± 8.6 years, 5 male) received an ^{18}F-FDG injection of 330.7 ± 30.3 MBq and were scanned 1.73 ± 0.77 hours after injection. The simultaneous PET-CMRA acquisition was performed ∼1–2 minutes after injection of a Gadolinium-based contrast agent, during the 10–15 minutes waiting time required for optimal contrast in conventional LGE imaging. Before the dual-phase CMRA acquisition, a μ-map was acquired during a 19 s breath-hold at end-expiration using the vendor's standard 2-point Dixon acquisition (coronal orientation, FH phase encoding, TR/TE1/TE2 = 3.60/1.23/2.46 ms, $2.604 \times 2.604 \times 3.12$ mm^3 resolution, field of view $328 \times 500 \times 399$ mm^3, no ECG triggering). Following this, the subjects were scanned during free-breathing using the proposed dual-phase CMRA sequence with the same acquisition parameters described for the healthy subjects. List-mode PET data was acquired during the whole dual-phase CMRA scan, resulting in a patient-specific PET acquisition duration.

6.3.3 PET-CMRA Image Reconstruction

For all datasets, dual-phase CMRA image reconstruction was performed offline in MATLAB (Mathworks, Natick, Massachusetts, USA) using custom developed software. CMRA data were reconstructed offline with the proposed motion correction approach (MC) and without motion correction (NMC) for comparison purposes. Image registration for estimating respiratory and cardiac motion operators was performed using a free-form deformation algorithm [213], that provides both forward and inverse motion fields. The MC dual-phase CMRA reconstruction required 2D translational motion-corrected soft-binning iterative SENSE reconstructions to produce 3D images at each cardiac and respiratory phase (reconstruction time of ∼3.6 min per bin), followed by 3D respiratory bin-to-bin non-rigid registration at each cardiac phase (registration time of ∼40 s per bin) and finally, the motion-corrected CMRA reconstruction (reconstruction time of ∼30 min per cardiac phase), with a total reconstruction time of ∼103 min. Reconstruction of the stack

of 2D CINE images was performed directly on the scanner.

PET image reconstruction was performed offline using MATLAB and e7 Tools (Siemens Healthcare, Knoxville, USA) using the OSEM algorithm, with 3 iterations and 21 subsets, point spread function modelling, voxel size = $2.03 \times 2.08 \times 2.08\,\text{mm}^3$, matrix size = $127 \times 344 \times 344$. PET images were reconstructed using both cardiac and respiratory motion correction (MC), using only respiratory motion correction (RespMC) and without motion correction (NMC) for comparison purposes. The MC PET image reconstruction required OSEM reconstructions at each cardiac and respiratory phase ($\sim$4 min per bin), followed by 3D non-rigid deformation ($\sim$10 s per bin) and finally adding, with a total reconstruction time of $\sim$42 min.

6.3.4 Image Analysis

For assessment of image quality, reconstructed systolic and diastolic CMRA images were reformatted to visualise the left anterior descending (LAD) and right coronary artery (RCA) simultaneously using dedicated software [49]. For the healthy subjects, left ventricular function was estimated using dedicated commercially available software (OsiriX, Geneva, Switzerland). For the diastolic and systolic CMRA images, end-diastolic (EDV) and end-systolic (ESV) volumes were obtained from semi-automatic segmentations of the left ventricular blood pool. For the 2D CINE images, EDV and ESV were obtained by semi-automatically contouring the left ventricle. In both cases, stroke volume (SV) and ejection fraction (EF) were then derived by subtracting the ESV from the EDV and by taking the ratio between SV and EDV, respectively, as described in Chapter 2. A Bland-Altman analysis [229] was performed for each of the indices in order to assess the agreement between both measurements.

Reconstructed ^{18}F-FDG PET images were analysed using the AHA 17-segment model for the left ventricular myocardium [50] using dedicated software (Munich-Heart, [220]). The relative increase in ^{18}F-FDG signal of RespMC and MC images over uncorrected images was computed for each of the 17 segments for each patient.

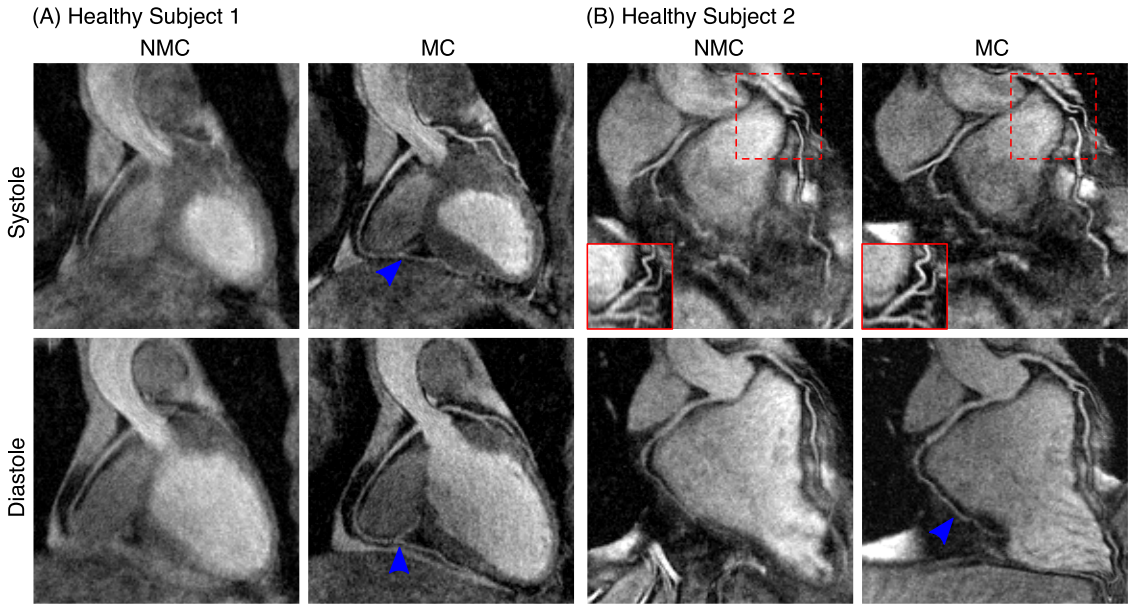

Figure 6.9: Reformatted dual-phase CMRA images showing uncorrected (NMC) and motion-corrected (MC) images for both systole and diastole in two representative healthy subjects. MC improves the visualisation of both the left (LAD) and right coronary arteries (RCA), allowing for the depiction of both proximal and distal segments (blue arrows). In (B), the tortuous anatomy of the LAD in systole prevents the visualisation of the artery in the reformatted coronal plane (dashed red box) but this is solved when reformatting in the transverse plane (solid red box).

6.4 Results

Scans were successfully completed in all subjects, with an average acquisition time of 12.72 ± 2.29 minutes for the proposed PET-CMRA framework. For all subjects, 3 to 5 respiratory bins (4.5 ± 0.8 bins on average) and 2 cardiac phases were used for both PET and MR data. For the patients with cardiovascular disease, this binning process resulted in 30.09 ± 14.50 million counts for the PET systolic bins, and 52.97 ± 25.67 million counts for the PET diastolic bins on average.

Figures 6.9 and 6.10 show reformatted uncorrected (NMC) and motion-corrected (MC) systolic and diastolic CMRA images for representative healthy subjects and patients, respectively. It can be observed that MC improved the delineation of the vessels, allowing for visualisation of both the RCA and LAD in all cases. For the healthy subjects, it can be observed that MC increased the visible length of the vessels, allowing for visualisation of the distal segment of the arteries in both systole and diastole (Figure 6.9a, blue arrows). For the second healthy subject, the

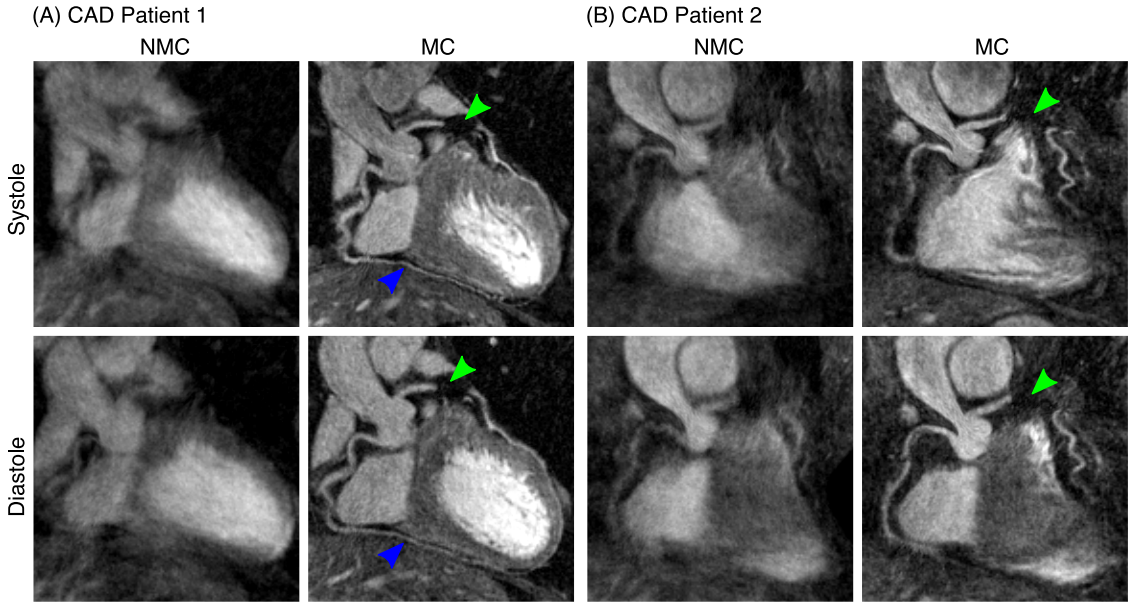

Figure 6.10: Reformatted dual-phase CMRA images showing uncorrected (NMC) and motion-corrected (MC) images for both systole and diastole in two representative patients with coronary artery disease. MC improves the visualisation of the proximal left (LAD) and right coronary arteries (RCA), and in (a) allows for the depiction of non-stented distal segments of the RCA (blue arrows). In both cases, the LAD can be clearly depicted despite the presence of a stent (green arrows) in the mid segment of the vessel.

tortuous anatomy of the LAD in systole prevented an appropriate reformatting in the coronal plane, as shown in Figure 6.9b (dashed red box). However, changing the reformatting plane solved this issue, and the vessel is clearly depicted in the transverse plane (Figure 6.9b, solid red box).

In the CAD patients, who have more irregular breathing patterns and larger respiratory amplitude as shown in previous Chapters, improvements in the delineation of the vessels after MC become even more apparent (Figure 6.10). In both cases, the proximal RCA and LAD were well depicted in the MC images, and the presence of a stent in the mid segment of the LAD did not prevent visualisation of the distal segment of the vessel, as shown in Figure 6.10a,b (green arrow). For the second CAD patient (Figure 6.10b), residual cardiac motion was observed in the MC systolic CMRA, affecting the sharpness of the mid and distal RCA.

Conventional orthogonal planes obtained from MC systolic and diastolic CMRA images of a representative subject are shown in Figure 6.11a, in addition to the corresponding volumetric rendering of the left ventricular blood pool. It can be

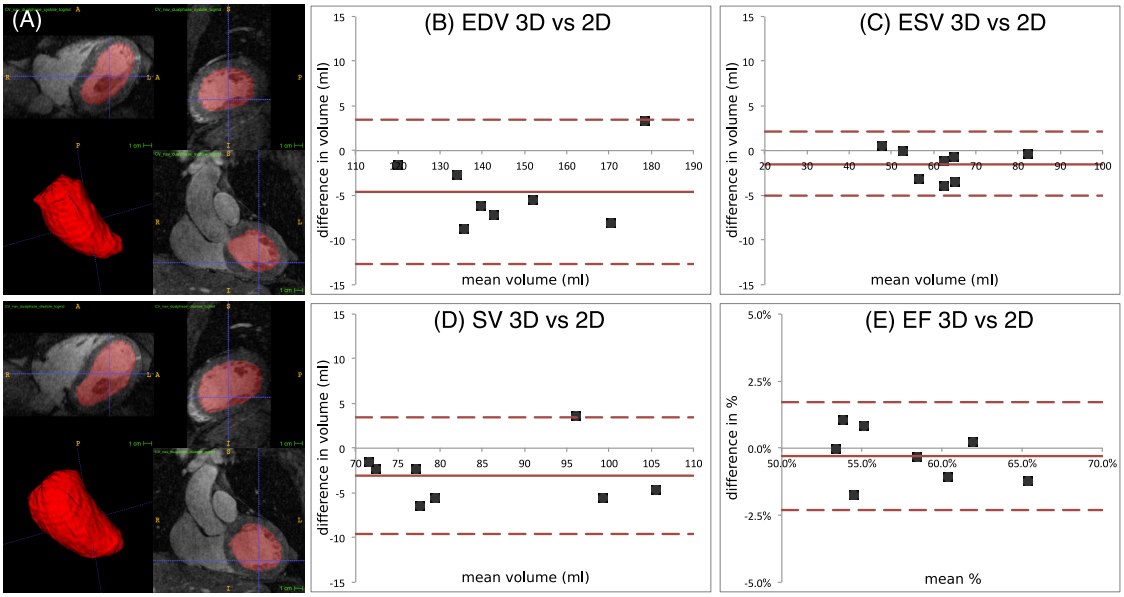

Figure 6.11: Dual-phase CMRA approach for estimation of left ventricular function. (a) Semi-automatic segmentation for a representative subject, showing three orthogonal planes for systole and diastole and corresponding rendering of the left ventricular cavity. Bland-Altman plots of (b) end diastolic volume (EDV), (c) end systolic volume (ESV), (d) stroke volume (SV) and (e) ejection fraction (EF) comparing dual-phase 3D CMRA images and conventional multi-slice 2D CINE acquisition. Middle red line: mean difference; upper and lower dashed red lines: 95% limits of agreement.

observed that the contrast between blood pool and myocardium was sufficient, and allowed for semi-automatic segmentation of the left ventricular cavity in both cardiac phases. Figure 6.11b-e shows Bland-Altman plots for left ventricular volumes and indices obtained for the cohort of healthy subjects, indicating in each case the average bias (solid red line) and 95% limits of agreement (dashed red lines). EDV and ESV estimated from dual-phase 3D CMRA images are comparable to the estimation from multi-slice multi-breath-hold 2D cine images, with an average underestimation of 4.61 ± 4.03 mL and 1.54 ± 1.75 mL respectively (Figure 6.11b,c). Functional indices obtained from dual-phase CMRA therefore resulted in good agreement with the standard 2D CINE approach, with an average bias of -3.07 ± 3.26 mL and $-0.30 \pm 1.01\%$ for the SV and EF respectively (Figure 6.11d,e).

Respiratory motion-corrected systolic and diastolic CMRA and PET images for a representative patient are shown in Figure 6.12, alongside the respiratory motion-corrected (RespMC) PET image. Differences in the anatomy of the heart between the two cardiac phases are apparent in both imaging modalities, including thick-

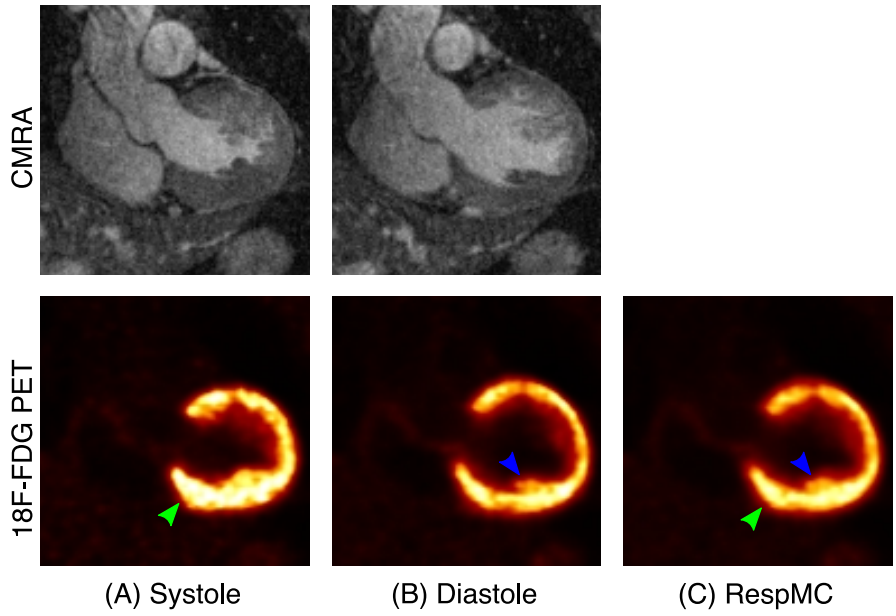

Figure 6.12: Coronal views from a cardiac patient, showing respiratory motion-corrected (a) systolic and (b) diastolic CMRA and ^{18}F-FDG PET images, alongside (c) respiratory motion-corrected (RespMC) PET image. RespMC aggregates data acquired at different cardiac phases, resulting in cardiac-induced blurring of small structures (blue arrow) and apparent thickening of the myocardium (green arrow).

ening of the left ventricle myocardium in the systolic phase as compared to the diastolic phase. RespMC aggregates data acquired at both cardiac phases, resulting in cardiac-induced blurring of small structures, such as the papillary muscles, compared to diastolic PET images (Figure 6.12b-c, blue arrow). Furthermore, the RespMC image depicts a thicker myocardium than the diastolic PET image, due to signal arising from the systolic phase (Figure 6.12a-c, green arrow). It is worth noting that the myocardium depicted by the RespMC image is dominated by the diastolic image, since diastole comprises a longer fraction of the cardiac cycle.

Cardiac PET images reconstructed without motion correction (NMC), with respiratory motion correction only (RespMC) and with both cardiac and respiratory motion correction (MC) from three representative patients together with profiles across the left ventricle myocardium obtained from transverse slices are shown in Figure 6.13. RespMC improved image quality by increasing the sharpness of the myocardium in all cases, as can be observed in the narrowing of the peak in the profiles. MC further increased myocardial sharpness and improved delineation of features such as the papillary muscles (as can be observed for cardiac patients 2 and 4) and the right ventricle myocardium (cardiac patient 4, white arrow).

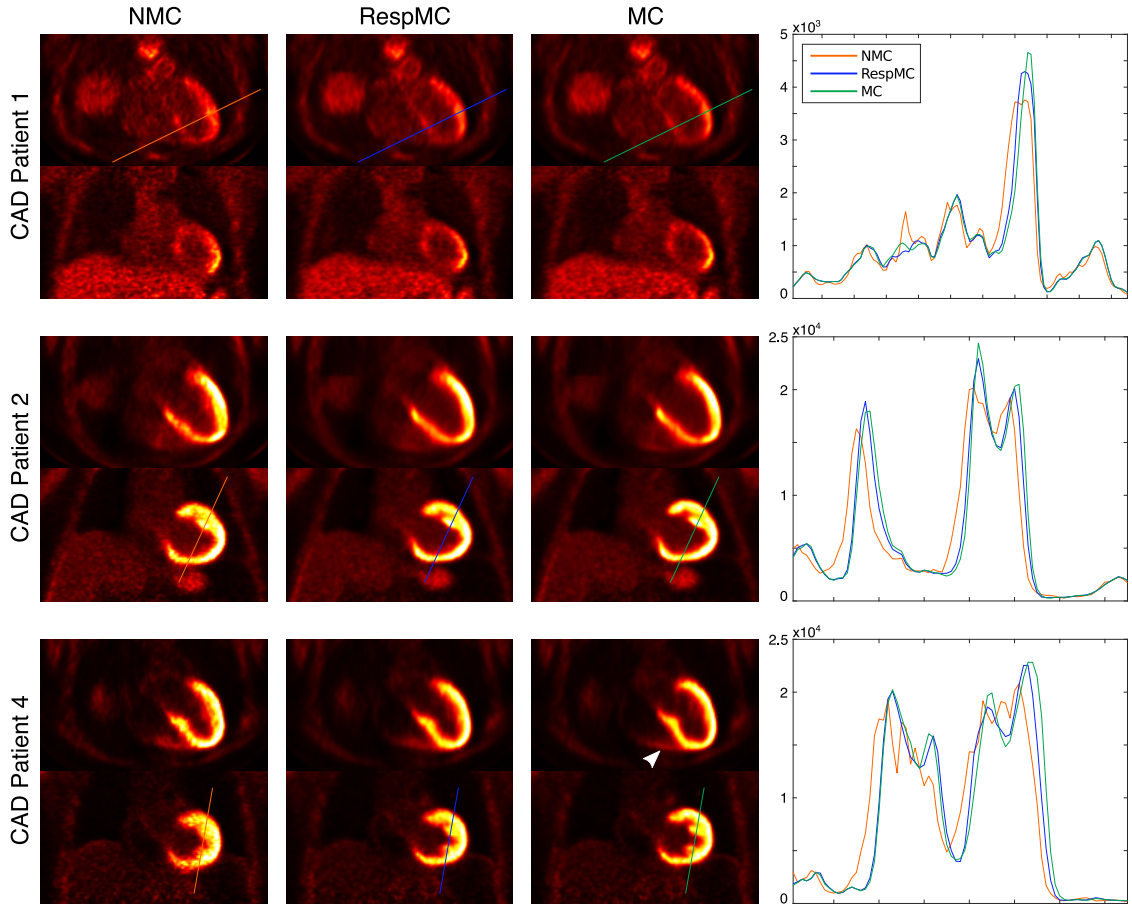

Figure 6.13: Uncorrected (NMC), respiratory motion-corrected (RespMC) and cardiac and respiratory motion-corrected (MC) cardiac PET images for three cardiac patients, including transverse and coronal views alongside profiles across the myocardium (intensity in arbitrary units). RespMC increases sharpness of the myocardium, and MC further improves sharpness, illustrating the impact of cardiac motion correction in both the left and right ventricle myocardium (white arrow).

Figure 6.14 shows standard 17-segment plots for three representative patients, displaying the relative increase of the ^{18}F-FDG signal in each myocardial segment after RespMC and MC compared to uncorrected images. In all cases, an increased signal in the basal segments of the myocardial wall was observed after RespMC, with a maximum relative increase ranging from 6.8 to 11.2% compared to uncorrected images. Further increase was observed in MC images, ranging from 13.1 to 28.7%, the latter observed in the anteroseptal segments in cardiac patient 5.

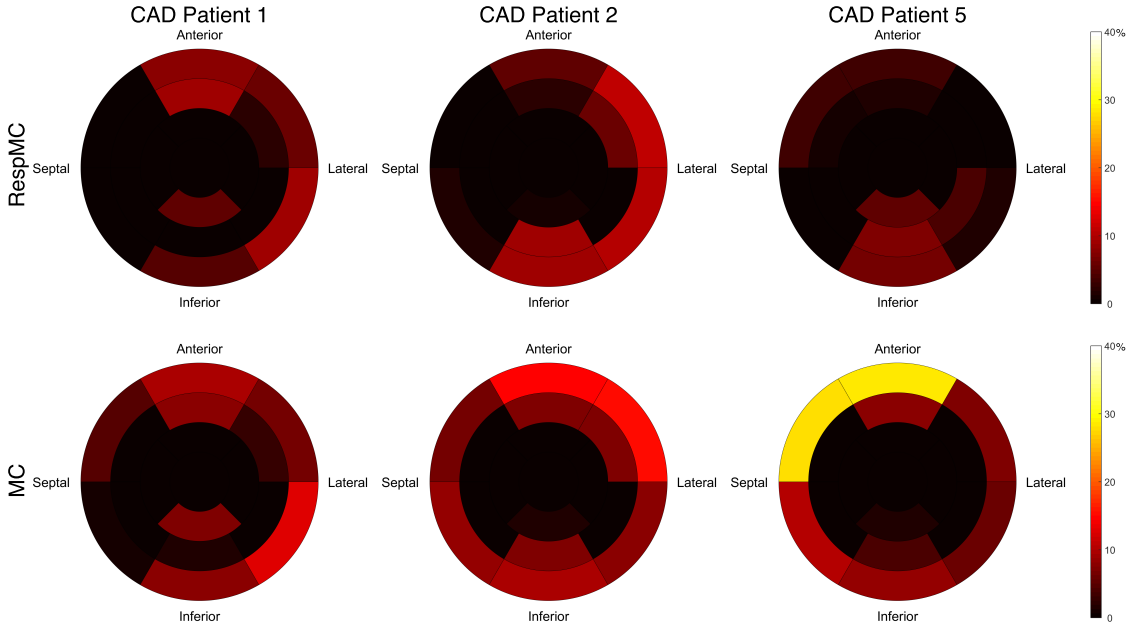

Figure 6.14: 17-segment polar maps of the relative increase (%) in ^{18}F-FDG PET signal after respiratory motion correction only (RespMC) and after cardiac and respiratory motion correction (MC) for the left ventricular myocardium in three representative patients.

6.5 Discussion

In this Chapter, a novel approach for the simultaneous acquisition of coronary MR angiography, left ventricular function and motion-corrected cardiac PET has been introduced. This approach extends the framework described in Chapter 4 to a dual-phase acquisition, so that a systolic and a diastolic CMRA image are acquired in a single examination, allowing quantification of left ventricular volumes and functional indices, in addition to providing cardiac motion deformation fields for motion correction of PET images. This approach is highly efficient, as it uses all the acquired data for image reconstruction (100% scan efficiency after outlier rejection) and produces co-registered high quality images in both modalities from a single examination of ∼12.7 minutes.

The proposed approach was tested in eight healthy subjects (MR-only acquisitions) and six patients with coronary artery disease (PET-MR acquisition), and an improved delineation and increased visible length of both the RCA and LAD arteries after motion correction was observed for all subjects. For the healthy subjects, proximal and distal segments of the coronary arteries are clearly depicted in

both systole and diastole. It is worth noting the significant change in the coronary anatomy between the two cardiac phases: for one of the subjects (Figure 6.9b), a tortuous anatomy of the proximal LAD in systole prevented its visualisation in the coronal view, requiring an additional view in the transverse plane for appropriate depiction of the vessel. For the CAD patients, improved delineation of the coronary arteries after motion correction was observed even for stented vessels, as shown in Figure 6.10a,b. In one of the patients, a short systolic quiescent period resulted in residual cardiac motion, as can be observed in Figure 6.10b. However, the coronary anatomy could be assessed in the diastolic CMRA, while the systolic CMRA still provided sufficient information for estimating cardiac motion.

Left ventricular function estimation was validated in the cohort of eight healthy subjects, by comparing volume quantification and functional indices obtained from systolic and diastolic CMRA images to a conventional stack of 2D CINE images. Results suggest that quantification of left ventricular function from dual-phase CMRA data is in agreement with the reference method, with an average underestimation in stroke volume of 3.07 ± 3.26 mL and a $0.30 \pm 1.01\%$ underestimation of ejection fraction. These results are comparable to the study presented in [230], where left ventricular volumes obtained from a prospectively ECG-triggered dual-phase whole-heart cardiac MR with a balanced steady-state free-precession acquisition performed on a 1.5 T system were compared to conventional retrospectively gated 2D CINE images, finding an underestimation of 0.95 mL and 0.67% in stroke volume and ejection fraction, respectively. In this study, systolic and diastolic CMRA datasets were acquired during mid-systole and mid-diastole to minimise the effect of cardiac motion in the coronary arteries, however, this might produce an underestimation of the ventricular volumes compared with conventional CINE imaging. This bias could be reduced by acquiring data towards the end of systole and diastole.

Reconstructed cardiac PET images showed that motion correction improves image quality compared to uncorrected images. For all subjects, it was observed that respiratory motion correction increased the sharpness of the myocardium and definition of small features, and incremental improvements were obtained when both respiratory and cardiac motion correction was performed. This is consistent with findings in [211], where minor visual improvements were observed after cardiac mo-

tion correction in patients with suspected liver or lung metastasis that exhibited myocardial uptake during the PET examination.

Quantitative analysis of 17-segment polar plots obtained from the reconstructed PET images showed that motion correction increased ^{18}F-FDG signal in the basal segments of the myocardial wall compared to uncorrected images. Across the whole cohort, maximum increase in the signal was observed when both cardiac and respiratory motion correction was applied, in the anterior and septal basal segments, corresponding to the regions of larger cardiac motion. As described in previous Chapters, this increase of signal corresponds to the combined effect of reduced image blurring and improved alignment between attenuation maps and emission data.

In this work, the vendor provided acquisition protocol for MR-based attenuation correction was used. This protocol has a higher voxel size than PET images, potentially affecting the accuracy of PET attenuation correction due to partial volume effects. Furthermore, the protocol does not include ECG-triggering, in practice averaging data over the entire cardiac cycle. Since the diastolic phase comprises the majority of the cardiac cycle, the produced μ-map is an approximation of the diastolic μ-map, and in this study it was used as such. In order to acquire a true diastolic μ-map, ECG-triggering would be required, resulting in a clinically unfeasible breath-hold time. In Chapter 7, a novel method that could enable the acquisition of high-resolution free-breathing ECG-triggered diastolic μ-maps is presented, which could potentially improve attenuation correction of cardiac PET data.

Conventionally, 3D CMRA imaging at 3 T uses spoiled gradient-echo sequences in order to minimise artefacts due to field inhomogeneity, relying on relatively long times between acquisitions ($\sim$800 ms for a heart rate of 60 bpm) to produce sufficient longitudinal magnetisation recovery. For the dual-phase CMRA approach the time between acquisitions is reduced by 50% approximately compared to conventional mid-diastolic single-phase CMRA, producing a penalty in SNR, especially in acquisitions without contrast agent injection. Acceleration techniques that reduce the length of the acquisition window without increasing total acquisition time would allow for increased longitudinal magnetisation recovery between systolic and diastolic acquisition, thereby improving SNR of the CMRA images. Furthermore, these acceleration techniques could potentially alleviate the problem of residual cardiac

motion during systolic CMRA acquisition.

The framework introduced here provides visualisation of the coronary anatomy in systole and diastole and ventricular function by dual-phase CMRA and motion-corrected myocardial viability by ^{18}F-FDG PET in a single examination. However, a comprehensive assessment of cardiac disease may require the acquisition of additional contrasts, for example LGE imaging for assessment of scar or T_2 mapping for quantification of oedema. In both cases similar motion-corrected approaches could be used, for example, by extending the approach proposed in [222] to a 3 T PET-MR system, allowing for simultaneous visualisation of the coronary anatomy and scar by MR and myocardial viability by ^{18}F-FDG PET. Similarly, simultaneous whole-heart T_2 mapping and myocardial viability by ^{18}F-FDG PET could be achieved by extending the approach proposed in [231].

Recently published approaches for cardiac and respiratory motion correction of PET data have proposed the use of 8 to 12 [211, 212] cardiac phases, while the approach described here considers motion correction only between the two extreme cardiac phases to ensure good coronary MR depiction in at least one of the cardiac phases. Preliminary results obtained from the described simulation study suggest that accurate quantification of size and degree of transmurality of myocardial viability defects by PET can be obtained when correcting for cardiac motion using only the systolic and diastolic cardiac phases. However, for radiotracers targeted at different cardiac applications, such as ^{18}F-NaF for imaging of inflammation and calcification of coronary plaques, additional cardiac phases might be required for accurate motion correction of PET data and therefore, further investigation is needed.

Finally, the feasibility of the proposed framework was demonstrated in a small cohort of patients and further studies are now warranted to validate the whole-heart PET-dual-phase CMRA method in larger cohorts of patients with heart disease.

6.6 Summary

A novel framework for the simultaneous acquisition of coronary MR angiography, left ventricular function and motion-corrected cardiac PET for hybrid whole-heart PET-MR imaging has been presented in this Chapter. This approach produces co-

registered high quality images in both imaging modalities in short and predictable scan time of ∼12.7 minutes, and thus is suitable for integration into clinical routine. Left ventricular function quantification has been validated in a cohort of healthy subjects, finding a good agreement between left ventricular volumes and functional indices from the dual-phase CMRA and conventional multi-slice 2D CINE images. Additionally, the feasibility of the proposed method was tested in patients with known coronary artery disease. Using the proposed respiratory and cardiac motion correction in both PET and MRI allowed visualisation of the coronary anatomy by CMRA as well as an improved delineation of the left ventricular myocardium and other cardiac structures by ^{18}F-FDG PET.

Chapter 7:
Respiratory Motion-Corrected Water/Fat CMRA

As described in previous Chapters, conventional whole-heart CMRA requires the use of fat suppression techniques to produce a good quality depiction of the vessels, because the coronary arteries are embedded in a thick layer of epicardial fat for most of their course. The most common approach for fat suppression in CMRA and other cardiac MR sequences is based on using a spectral pre-saturation with inversion recovery (SPIR) preparation pulse, so that signal arising from the fat is minimal during data acquisition. This is the method that has been used previously in this thesis.

As described in Chapter 3, SPIR relies on the chemical shift and relaxation times differences of water and fat to null or minimise the fat signal, but its intrinsic sensitivity to field inhomogeneities impairs its performance at higher magnetic fields. In fact, when observing the whole acquired field of view in some of the images obtained with the methods proposed in previous Chapters, a non-homogeneous suppression of the fat signal can be seen. Particularly, the subcutaneous fat tends to be poorly suppressed around the edges of the field of view (Figure 7.1a). In some subjects, this unsuppressed fat signal can introduce ghosting artefacts after translational motion correction, which can negatively impact the image quality of the coronary MR angiography (Figure 7.1b).

An alternative approach is to exploit the chemical shift between water and fat to produce images where the two species are fully separated, by acquiring images at multiple echo times and then processing them using so-called water/fat or Dixon

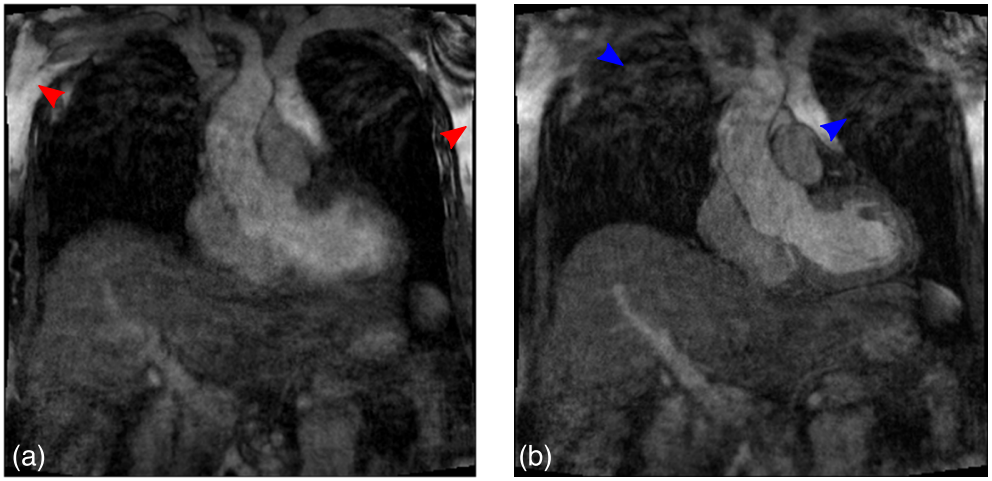

Figure 7.1: Example of (a) incomplete fat suppression in subcutaneous fat (red arrows) in a non-motion-corrected image and (b) ghosting (blue arrows) due to translational motion correction of unsuppressed static fat tissue.

separation methods [99]. As briefly discussed in Chapter 3, Dixon-based CMRA imaging has been shown to improve image quality at 1.5 T [105] and 3 T [106] compared to conventional SPIR fat suppression, increasing the SNR of the blood and improving the blood-to-fat CNR in the water images. So far, these methods have performed respiratory motion compensation using 1D diaphragmatic navigators only, resulting in prolonged and unpredictable scan times.

The water/fat separation approach for CMRA also has the benefit of providing a fat image that carries additional diagnostic value: studies have suggested that increased epicardial and pericardial fat volumes are associated with increased cardiovascular risk, including increased vascular calcification, luminal stenosis and plaque burden, and increased likelihood of adverse cardiovascular events [232–235]. Furthermore, water/fat cardiac MR imaging has shown promising results for the assessment of fibro-fatty infiltration in the myocardium and cardiac masses [236, 237].

Finally, as discussed in previous Chapters, motion-compensated attenuation correction is fundamental for accurate quantification in cardiac PET. In the context of thoracic PET-MR imaging, the conventional approach for attenuation correction is to estimate an attenuation map (μ-map) from a segmented water/fat MR image acquired during a $\sim$20 s breath hold before the clinical PET-MR protocol. However, changes in the breathing pattern of the subjects during the rest of the examination and/or incomplete breath holds can lead to errors in the μ-map, impacting severely

PET image quality.

More recently, respiratory resolved attenuation maps have been proposed to alleviate this problem. In these approaches, a multi-echo MR dataset is acquired throughout [238] or during the first minutes [239] of the PET acquisition, and μ-maps estimated at different respiratory positions are used for motion-resolved attenuation correction. However, such multi-echo sequences do not include preparatory pulses for appropriate tissue contrast and have insufficient spatial resolution, preventing the use of these MR images for diagnostic purposes and leading to long examination times since diagnostic MR images are acquired subsequently.

In this Chapter a novel framework based on a dual-echo water/fat coronary MR angiography acquisition is introduced, which is then combined with a respiratory motion-corrected reconstruction scheme that extends the approach introduced in Chapter 4. This framework allows for the simultaneous visualisation of the coronary anatomy and cardiac fat, and enables the calculation of respiratory-resolved high-resolution μ-maps for accurate attenuation correction in cardiac PET imaging. The proposed scheme can potentially be used for accurate and highly efficient whole-heart motion-corrected cardiac PET-MR imaging, ensuring alignment between emission PET data, attenuation maps and diagnostic MR images, exploiting the improved contrast of Dixon-based MR methods.

A first study to demonstrate the feasibility of the dual-echo water/fat CMRA acquisition and accuracy of the respiratory motion-corrected reconstruction for water/fat CMRA imaging was performed in a cohort of ten healthy subjects. This study included an investigation about the accuracy of the 2D translational motion estimated from the different iNAVs that can be obtained from the dual-echo acquisition. After identifying the iNAV that produced the optimum motion estimates, the non-rigid respiratory motion-corrected approach introduced in Chapter 4 was extended to dual-echo acquisitions, and the resulting water/fat CMRA images were compared to a reference scan with diaphragmatic navigator gating and tracking with matching imaging parameters. As a proof of concept, motion-resolved μ-maps were obtained for two subjects in order to test the feasibility of motion correction approach to produce good quality tissue segmentation. Some of the results presented in this Chapter have been presented as an abstract at an international conference [240].

7.1 Methods

7.1.1 Image Acquisition

The proposed acquisition sequence consists of an ECG-triggered free-breathing dual-echo CMRA sequence as shown in Figure 7.2a. Similarly to the acquisition protocol introduced in Chapter 4, a 2D cine image is acquired before the CMRA acquisition to determine a subject-specific trigger delay and acquisition window so that the dual-echo 3D CMRA acquisition window coincides with the mid-diastolic period of the cardiac cycle.

The dual-echo 3D CMRA data is acquired using a spoiled gradient echo sequence, with a bipolar readout gradient, following a fully sampled golden-step Cartesian spiral profile order sampling trajectory [155], so that one spiral interleaf is acquired at each cardiac cycle for both in-phase and out-of-phase echo times. Using the 2D iNAV framework already introduced, spatially encoded dual-echo low flip-angle lines are acquired at each heartbeat before the 3D CMRA acquisition, and an adiabatic T_2 preparation pulse is used to improve contrast between blood and myocardium. Contrary to the previously introduced scheme, the dual-echo approach does not require the use of a fat suppression module, as the water/fat separation scheme provides the blood/fat contrast required for coronary MR angiography.

7.1.2 Image Reconstruction

The image reconstruction scheme extends the non-rigid motion-corrected reconstruction method proposed in [27, 159] to a dual-echo acquisition as follows: in the first step, the foot-head (FH) motion estimated from the 2D iNAVs is used to define a number of respiratory bins, each containing approximately the same amount of data, and the 3D k-space data are corrected to the centre of the corresponding bin by applying a linear phase in the FH and right-left (RL) directions (Figure 7.2b). In the second step, the acquired data are binned and echo images are reconstructed for each respiratory bin using the soft-gated iterative SENSE approach with exponential decay weights introduced in Chapter 6, as shown in Figure 7.2c. These images are used to estimate 3D non-rigid deformation fields via free-form image reg-

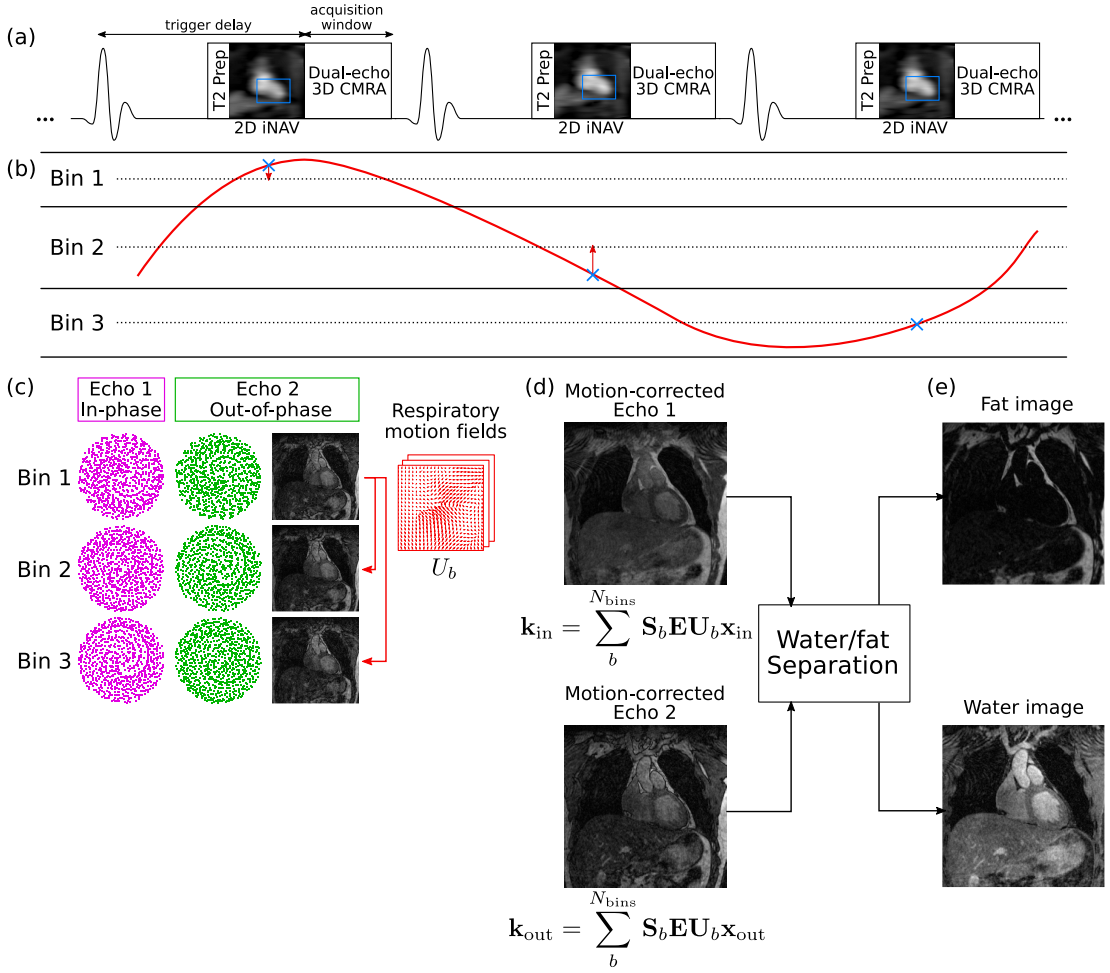

Figure 7.2: Water/fat CMRA acquisition and reconstruction scheme. (a) Dual-echo CMRA data is acquired following a golden-step spiral ordering in a Cartesian grid. A low-resolution coronal 2D iNAV is acquired before CMRA acquisition, respiratory motion estimation; and a T_2 preparation (T2-prep) pulse is used to enhance the contrast between the coronary arteries and myocardium (b) Foot-head motion is used to define a number of respiratory windows, and correct the data to the centre of the corresponding bin (red arrows). (c) Dual-echo CMRA data are binned, and echo images reconstructed at different respiratory positions are used to estimate non-rigid motion fields. (d) This non-rigid motion is used to reconstruct motion-corrected echoes, which are finally used as an input in (e) the water/fat separation algorithm to obtain motion-corrected water and fat CMRA images.

istration [213] using the end-expiratory bin as the reference position. In the third step, motion-corrected images are reconstructed separately for each echo using the generalized matrix description (GMD) approach, by solving Equation 7.1 (Figure 7.2d).

$$\mathbf{k}_e = \sum_{b=1}^{N_{\text{bins}}} \mathbf{S}_b\mathbf{E}\mathbf{U}_b\mathbf{x}_e \tag{7.1}$$

where $\mathbf{x}_e$ are the images for each echo (e = in-phase, out-of-phase), $\mathbf{k}_e$ is the translationally corrected k-space for echo e, $\mathbf{E}$ is the forward encoding operator, including the discrete Fourier transform and coil sensitivities, $\mathbf{U}_b$ are the motion operators which transform an image from the reference position to any respiratory position b, and $\mathbf{S}_b$ corresponds to the sampling matrix containing the k-space points acquired at respiratory bin b.

In the fourth and final step of the reconstruction (Figure 7.2e), water and fat images are obtained with the B0-NICEbd method proposed in [103] for water/fat separation of dual-echo acquisitions performed with bipolar gradients. This method assumes that the total difference in phase between the in-phase and out-of-phase images, $\boldsymbol{\varphi}_{\text{io}}$, arises from three sources: first, the gain in phase between echoes due to the water/fat chemical shift as described by Equation 3.24; second, a phase due to field inhomogeneities, $\boldsymbol{\varphi}_{B0}$, and third, a linear phase in the frequency encoding direction due to the bipolar readout gradient, $\boldsymbol{\varphi}_{\text{bi}}$. The method estimates each of these components separately, and then uses Equation 7.2 to obtain the water and fat images $\mathbf{x}_w$ and $\mathbf{x}_f$ respectively, with $\Delta\boldsymbol{\varphi} = \boldsymbol{\varphi}_{\text{io}} - \boldsymbol{\varphi}_{B0} - \boldsymbol{\varphi}_{\text{bi}}$ representing the phase induced by the chemical shift between fat and water.

$$\begin{aligned} \mathbf{x}_w &= \frac{||\mathbf{x}_{\text{in}}| + |\mathbf{x}_{\text{out}}|e^{-i\Delta\boldsymbol{\varphi}}|}{2} \\ \mathbf{x}_f &= \frac{||\mathbf{x}_{\text{in}}| - |\mathbf{x}_{\text{out}}|e^{-i\Delta\boldsymbol{\varphi}}|}{2} \end{aligned} \tag{7.2}$$

The B0-NICEbd method estimates $\boldsymbol{\varphi}_{\text{io}}$, $\boldsymbol{\varphi}_{B0}$ and $\boldsymbol{\varphi}_{\text{bi}}$ following a 5-step algorithm, depicted in Figure 7.3. In the first step, the element-wise Hermitian product between the echo images is computed as $\mathbf{x}_{\text{io}} = \mathbf{x}_{\text{in}}\mathbf{x}^*_{\text{out}}$, to obtain the phase $\boldsymbol{\varphi}_{\text{io}} = \arg\{\mathbf{x}_{\text{io}}\}$.

In the second step, $\boldsymbol{\varphi}_{\text{bi}}$ is obtained following the method proposed in [241], which uses the image $\mathbf{x}_{\text{io}}(l, m, n)$ to estimate an average linear phase correction factor assuming that $\boldsymbol{\varphi}_{\text{bi}} = \phi l$, where l is the readout direction. This method estimates ϕ by computing the product between $\mathbf{x}_{\text{io}}$ and a shifted and complex conjugated version of $\mathbf{x}_{\text{io}}$ (Equation 7.3), which minimises the effect of any constant phase present in $\mathbf{x}_{\text{io}}$. This factor ϕ is then used to produce a bipolar-gradient corrected

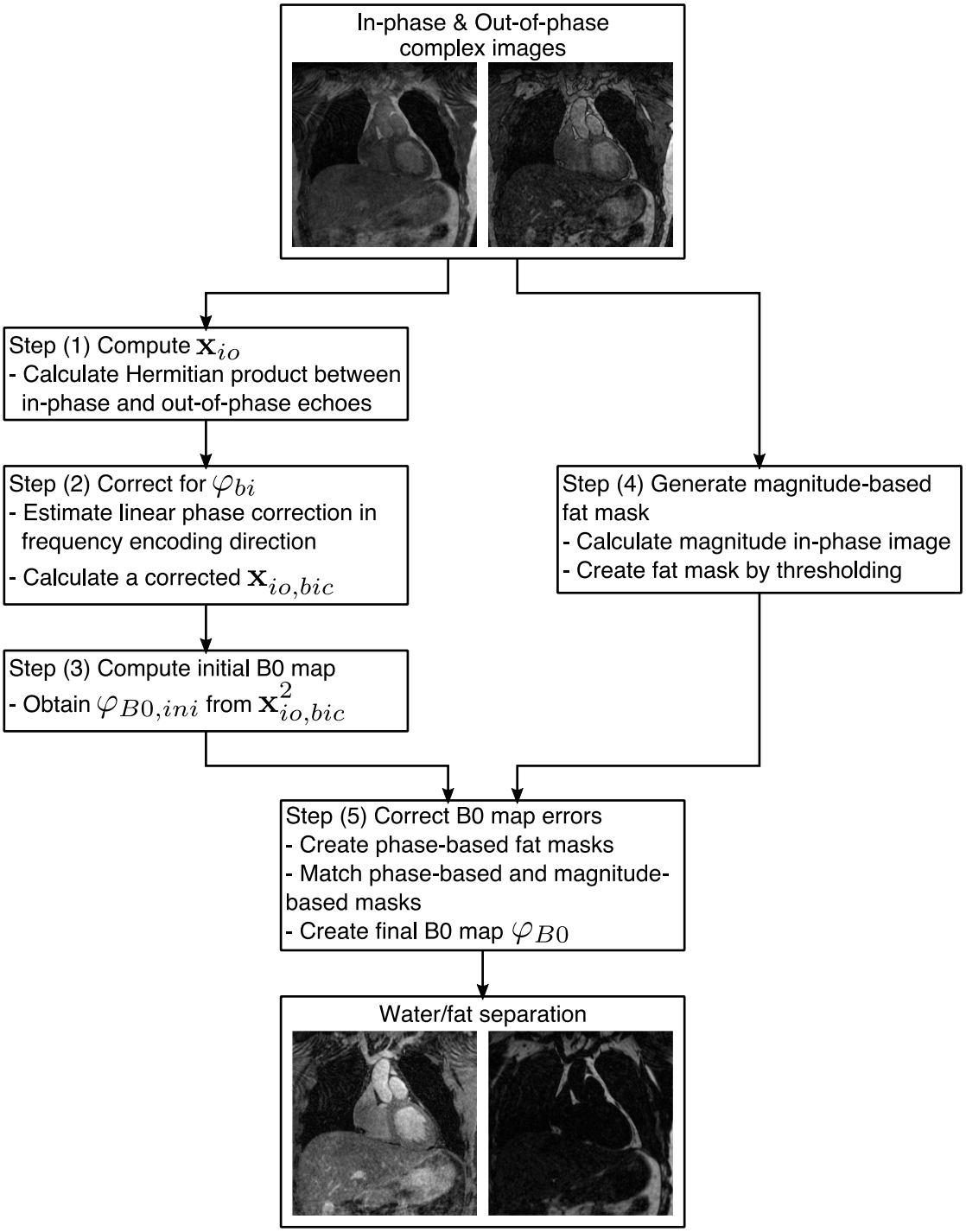

Figure 7.3: Flowchart of the B0-NICEbd [103] water/fat separation method for dual-echo MR acquisitions with bipolar readout gradients. See text for a full description.

image $\mathbf{x}_{\mathrm{io,bic}} = \mathbf{x}_{\mathrm{io}} e^{i\varphi_{\mathrm{bi}}}$.

$$2\phi = \arg\left\{ \sum_{l,m,n} \mathbf{x}^2_{\mathrm{io}}(l,m,n)\mathbf{x}^{*2}_{\mathrm{io}}(l+1,m,n) \right\} \tag{7.3}$$

In the third step, an initial estimate for $\boldsymbol{\varphi}_{B0}$ is obtained using the method proposed in [242], so that $2\boldsymbol{\varphi}_{B0,\text{ini}} = \arg\left\{\mathbf{x}^2_{\text{io,bic}}\right\}$. Theoretically, if there are no errors in $\boldsymbol{\varphi}_{B0,\text{ini}}$, it would be possible to obtain water and fat images using Equation 7.2, and the estimates obtained so far. However, as discussed by the authors in [103], regional phase errors can occur, for example due to flow and low SNR, and as the computed phase map is relative (i.e. it was obtained from $\mathbf{x}_{\text{io}}$ instead of using the absolute phase of each echo image), the B_0 phase map might be shifted by $\pm\pi$, resulting in global phase errors. Therefore, the fourth and fifth steps of the method aim to improve the estimation of $\boldsymbol{\varphi}_{B0}$, in order to produce an accurate water/fat separation.

In the fourth step, a binary mask of voxels belonging to fat tissue is created by applying a threshold to $|\mathbf{x}_{\text{in}}|$. This step assumes that the acquired MR images have some T_1 weighting, so that the fat appears bright on the in-phase images. In the fifth step, the global and regional errors in $\boldsymbol{\varphi}_{B0,\text{ini}}$ are corrected. First, three possible $\boldsymbol{\varphi}_{B0}$ phase maps are created by using the original $\boldsymbol{\varphi}_{B0,\text{ini}}$ and by shifting $\boldsymbol{\varphi}_{B0,\text{ini}}$ by $+\pi$ and $-\pi$. An estimate of $\Delta\boldsymbol{\varphi}$ is computed using each of these phase maps, and assuming that voxels with a total phase close to zero are most likely water, while the ones with a total phase close to π are most likely fat, a phase-based fat mask is obtained for each of the $\boldsymbol{\varphi}_{B0}$ estimates. Then, the final $\boldsymbol{\varphi}_{B0}$ estimate is obtained by choosing on a regional basis which of the three possible maps produces the best match between the phase-based and the magnitude-based fat masks. Finally, Equation 7.2 is used to compute the water and fat CMRA images.

7.2 Experiments

Ten healthy subjects (age 30.2 ± 2.8 years, 4 male) were scanned under free breathing using a prototype implementation of the proposed dual-echo 3D CMRA sequence, with the following imaging parameters: coronal orientation, RL phase encoding, bipolar readout acquisition, resolution = 1.3 mm isotropic, field of view = $312 \times 312 \times 78$–104 mm covering the whole heart, flip angle = 20°, TR/TE1/TE2 = 5.26/2.46/3.69 ms, bandwidth = 1302 Hz/px, and a T2-prep duration of 50 ms. The 2D dual-echo iNAVs were acquired with the following parameters: high-low Carte-

sian trajectory, coronal orientation, RL phase encoding, 14 low flip-angle lines (flip angle = 3°), same TR/TE1/TE2 and field of view as the 3D CMRA acquisition, resulting in an acquired resolution of 1.3×22.8 mm, interpolated to 1.3×1.3 mm during reconstruction. A subject-specific trigger delay and acquisition window (95–115 ms, corresponding to 18–22 lines in k-space) was set coinciding with the mid-diastolic quiescent period of the cardiac cycle, resulting in a total acquisition time of approximately 15 min.

In order to evaluate the performance of the motion correction approach, an additional Cartesian ECG-triggered dual-echo 3D CMRA scan with a 1D diaphragmatic navigator was implemented in the scanner software. This acquisition was performed in all subjects for comparison purposes, with respiratory gating (6 mm gating window) and tracking (tracking factor of 0.6 [41]) and matching imaging parameters. In order to reduce scan time, this acquisition was performed using GRAPPA parallel imaging [148] with 24 calibration lines and an undersampling factor of 2.

All the *in vivo* experiments were performed on a 3 T hybrid PET-MR scanner (Biograph mMR, Siemens Healthcare, Erlangen, Germany). Written informed consent was obtained from all subjects according to institutional guidelines and the institutional ethics committee approved the study.

7.2.1 Preliminary Study: Comparison of Image Navigators

As the 2D iNAVs are acquired with a dual-echo bipolar readout, it is possible to reconstruct image navigators with different contrasts from the data acquired. The objective of this preliminary study was to compare the performance of water, fat, in-phase and out-of phase iNAVs for 2D translational motion estimation. For this purpose, FH and RL motion were estimated from each iNAV using the same template. Then, 3D CMRA in-phase and out-of-phase images were reconstructed with translational motion correction only, and were then used to obtain translationally-corrected water and fat CMRA images using the B0-NICEbd method described above.

Three representative subjects were selected for this preliminary study, covering a range of motion amplitude and volume of epicardial and pericardial fat. Reconstructed images were assessed in terms of presence of blurring and artefacts due

to residual water/fat swaps, and visually compared to the reference 1D gated and tracked reference water/fat images.

7.2.2 Main Study: Validation of the Respiratory Motion Correction Approach

After finding the best iNAV for FH and RL estimation, three reconstructions were performed for each acquired dataset: (a) the proposed non-rigid respiratory motion-corrected reconstruction approach described in Section 7.1.2 (TC+GMD), (b) 2D translational motion correction only (TC) and (c) without motion correction (NMC) for comparison purposes. All of these reconstructions were performed offline in MATLAB (Mathworks, Natick, Massachusetts, USA). For these datasets, the B0-NICEbd water/fat separation was performed using available MATLAB code, provided by the authors of the paper[1].

The water/fat CMRA data acquired with 1D diaphragmatic respiratory gating and tracking (called Gated hereafter) was reconstructed in the scanner software, including water/fat separation, for comparison purposes.

Water CMRA images were reformatted to simultaneously visualise the right coronary artery (RCA) and the left anterior descending (LAD) artery, and the same reformatting was applied to the corresponding fat images. Image quality metrics of visible vessel length and sharpness were obtained for the water images only, with sharpness computed for both the first 4 cm and the whole visible length of each coronary artery. Vessel sharpness values were normalised to the signal intensity of the centre line of each vessel, so that 100% sharpness refers to a maximum signal intensity change at the vessel edge. The difference between the image quality metrics (vessel length and sharpness) for each reconstructed image was evaluated with a paired t-test with a p value of 0.01 considered statistically significant, including corrections for multiple comparisons.

[1]Available at https://uk.mathworks.com/matlabcentral/fileexchange/60660-b0-mapping-for-bipolar-two-point-dixon-mri

7.3 Results

Scans were successfully completed in all subjects. The average acquisition time for the proposed motion-corrected water/fat CMRA sequence was 15.28 ± 1.13 min, while the average acquisition time for the $2\times$ accelerated water/fat Gated acquisition was 27.03 ± 6.16 min. The minimum, maximum and average (and standard deviation) efficiency of the latter was 32%, 63% and 47.3 ± 11.5% respectively, for a 6 mm gating window.

7.3.1 Preliminary Study: Comparison of Image Navigators

Figure 7.4 shows example water, fat, in-phase and out-of-phase iNAVs for two subjects. It can be observed that subcutaneous fat is accurately separated in the water/fat iNAVs for both subjects. However, as the iNAVs are a projection of the excited volume in the anterior-posterior (AP) direction, and were acquired with a low spatial resolution in the RL direction, smaller fat structures, such as the epicardial and pericardial fat are not clearly depicted in the fat iNAV.

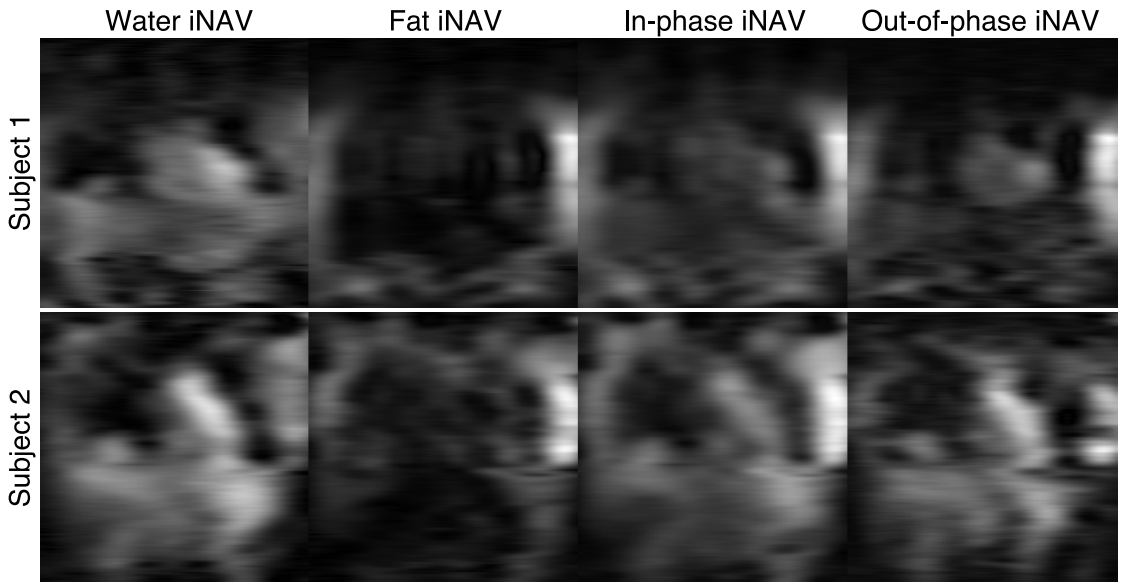

Figure 7.4: Example iNAVs for two subjects, showing water, fat, in-phase and out-of-phase navigators. In both cases, water/fat separation results in a clear depiction of subcutaneous fat in the fat iNAVs. Reduced spatial resolution prevents the visualisation of smaller fatty structures.

The presence and distribution of cardiac fat significantly affects the estimation

of translational motion, as can be observed in Figure 7.5, that shows the FH and RL motion estimated from each of the reconstructed iNAVs for the same two subjects. It can be observed that for both subjects, the estimation of FH motion is consistent across the different navigators, while differences are apparent in the RL estimation. In Subject 1, water and in-phase iNAVs result in larger RL estimates compared to fat and out-of-phase iNAVs. A more extreme case can be observed for Subject 2, where the lack of defined structures in the fat iNAVs resulted in unrealistic RL motion estimation, impacting the accuracy of FH motion estimation.

Figure 7.6a shows reformatted water images obtained after translational motion correction, with FH and RL motion estimated from each of the iNAVs for three subjects, alongside the corresponding Gated images. Corresponding reformatted fat images are shown in Figure 7.6b for the same subjects. From both the water and fat reformatted images it can be observed that for Subject 1, water and in-phase iNAVs result in blurring in the mid and distal segments of the LAD (red arrows), preventing the visualisation of the vessel, while additional artefacts can be seen in the RCA when using the water iNAVs (light blue arrow). On the contrary, when using the fat or the out-of-phase iNAVs, the resulting image quality improves, with no apparent artefacts and a depiction of the coronary arteries similar to the one observed in the Gated images. On the contrary, for Subjects 2 and 3, water and in-phase iNAVs result in similar image quality, with no presence of localised artefacts and enough sharpness to visualise the vessels in the resulting water images. When using fat iNAVs, however, the RCA appears blurred (green arrows), due to errors in motion estimation. Finally, for these two subjects, using out-of-phase iNAVs results in a slight improvement in vessel sharpness, particularly in the LAD, compared to water or in-phase iNAVs.

Overall in this cohort of subjects, using out-of-phase iNAVs for translational motion estimation resulted in consistently good image quality, for subjects with varying respiratory motion amplitude and amount of visceral and cardiac fat. These iNAVs were therefore used for estimating motion for the remainder of this Chapter.

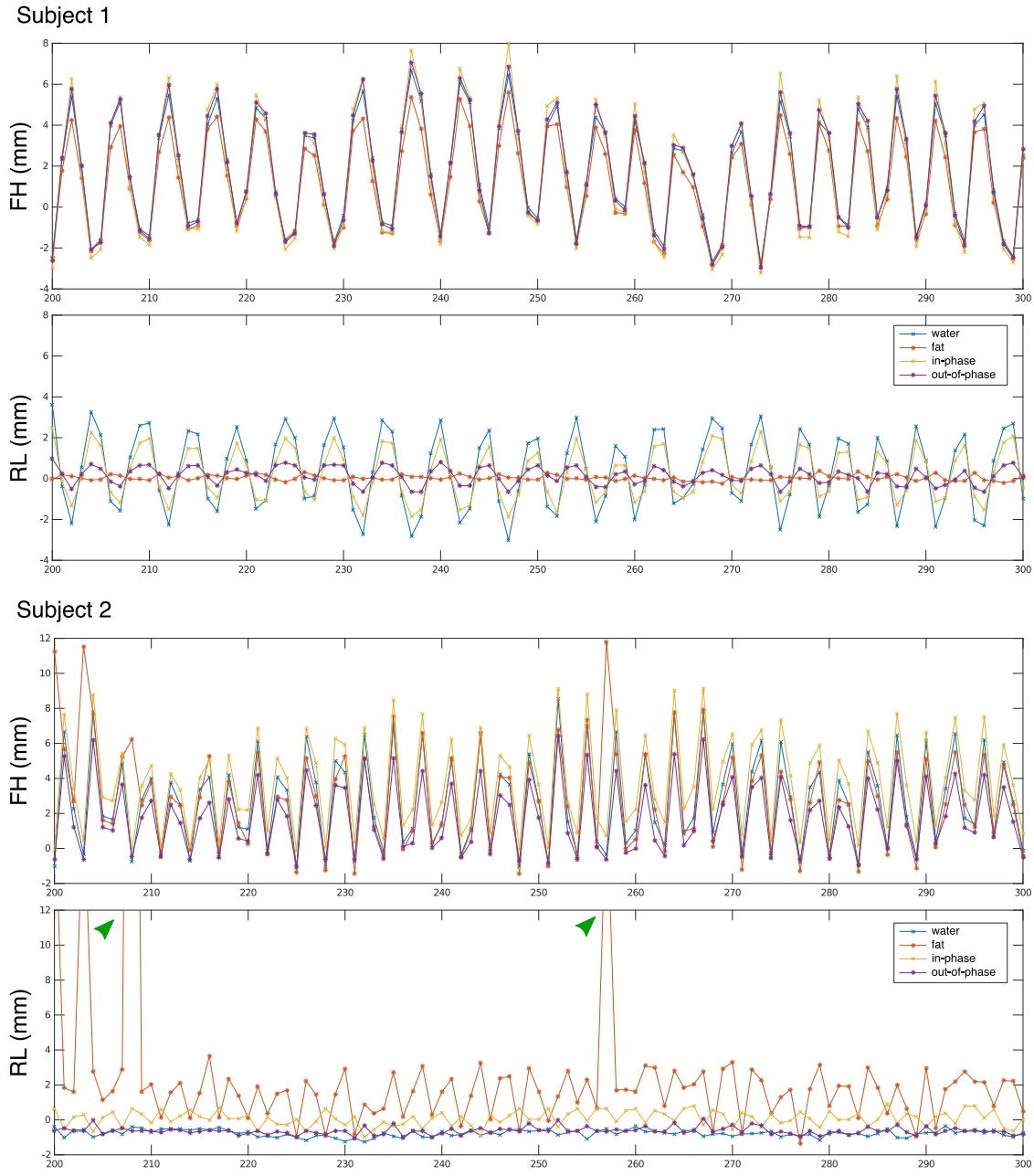

Figure 7.5: Foot-head (FH) and right-left (RL) motion estimation from water, fat, in-phase and out-of-phase iNAVs for two subjects. In both subjects, FH estimation is consistent across different iNAVs, while differences are apparent in RL estimation. In particular for subject 2, fat iNAVs result in unrealistic RL motion estimation ($> 12\,\text{mm}$, green arrows).

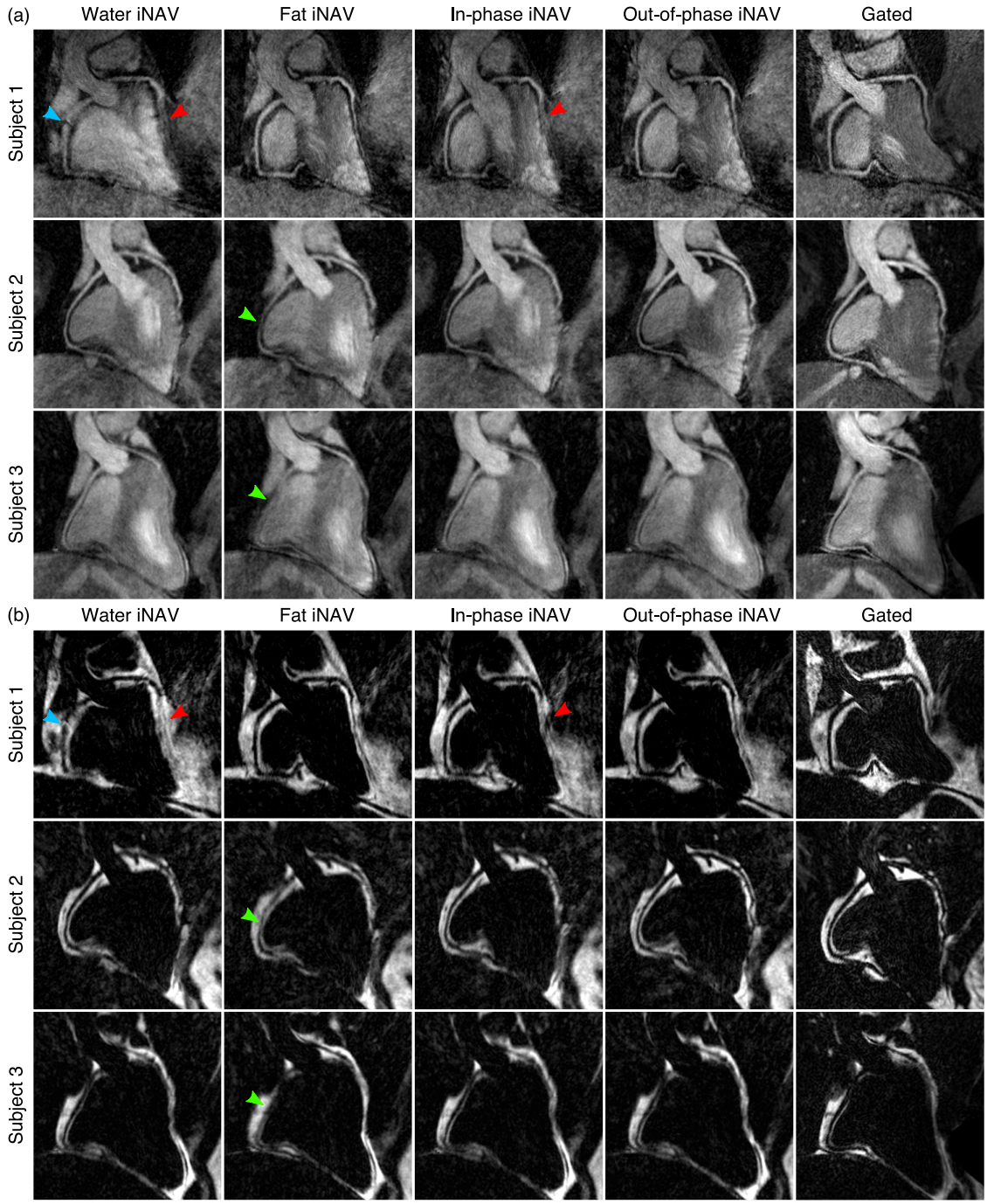

Figure 7.6: Reformatted translationally motion-corrected (a) water and (b) fat images for 3 subjects, with motion estimated from water, fat, in-phase and out-of-phase iNAVs, alongside corresponding Gated water and fat images. Water and in-phase iNAVs resulted in blurring and artefacts for Subject 1 (red and blue arrows), while fat iNAVs resulted in blurring in Subjects 2 and 3 (green arrows). Out-of-phase iNAVs resulted in good image quality across subjects, with a delineation of the coronary arteries comparable to the Gated water images and a depiction of the fat tissue comparable to the Gated fat images.

7.3.2 Main Study: Validation of the Motion Correction

Figure 7.7 shows reformatted water CMRA images for four representative subjects for the NMC, TC and TC+GMD reconstructions, alongside Gated images for comparison purposes. Corresponding reformatted fat images for the same cases are shown in Figure 7.8. For all subjects, an improved delineation of the RCA and LAD can be observed in the water CMRA images after applying TC, in terms of visible length and delineation of the vessels. Further improvements are observed when the TC+GMD approach is used, particularly in the depiction of the distal segments of the arteries, resulting in images that are visually comparable to the Gated images. Similarly, in the corresponding cardiac fat images, it can be observed that TC and TC+GMD improve depiction of the epicardial fat compared to NMC images, and delineation of the vessels is also significantly improved.

The observed improvement in image quality was quantified by measuring visible vessel length and vessel sharpness of the first 4 cm and the full length of each of the arteries in the water CMRA images. These results are summarised in Figure 7.9, which shows that measured vessel lengths for TC+GMD images was similar to the one obtained from Gated images. In particular, visible length of RCA and LAD in the TC+GMD images was on average $102.0 \pm 5.8\%$ and $104.9 \pm 12.0\%$ of the length measured in Gated images, respectively. Lower values were obtained for TC and NMC, with an average of $92.6 \pm 14.1\%$ and $67.6 \pm 16.6\%$ for the RCA and $77.5 \pm 28.2\%$ and $88.5 \pm 20.5\%$ for the LAD, respectively. Statistically significant differences were found in the visible vessel length between NMC and gated images for both coronaries.

A similar trend was observed when analysing the sharpness of the coronaries. Statistically significant differences between Gated and NMC were obtained when analysing either the proximal segment (first 4 cm) or the full length of both the RCA and LAD. Furthermore, significant differences were also observed in vessel sharpness between Gated and TC for the RCA only. No statistically significant differences were observed between the Gated and the TC+GMD approach for any of the image quality metrics.

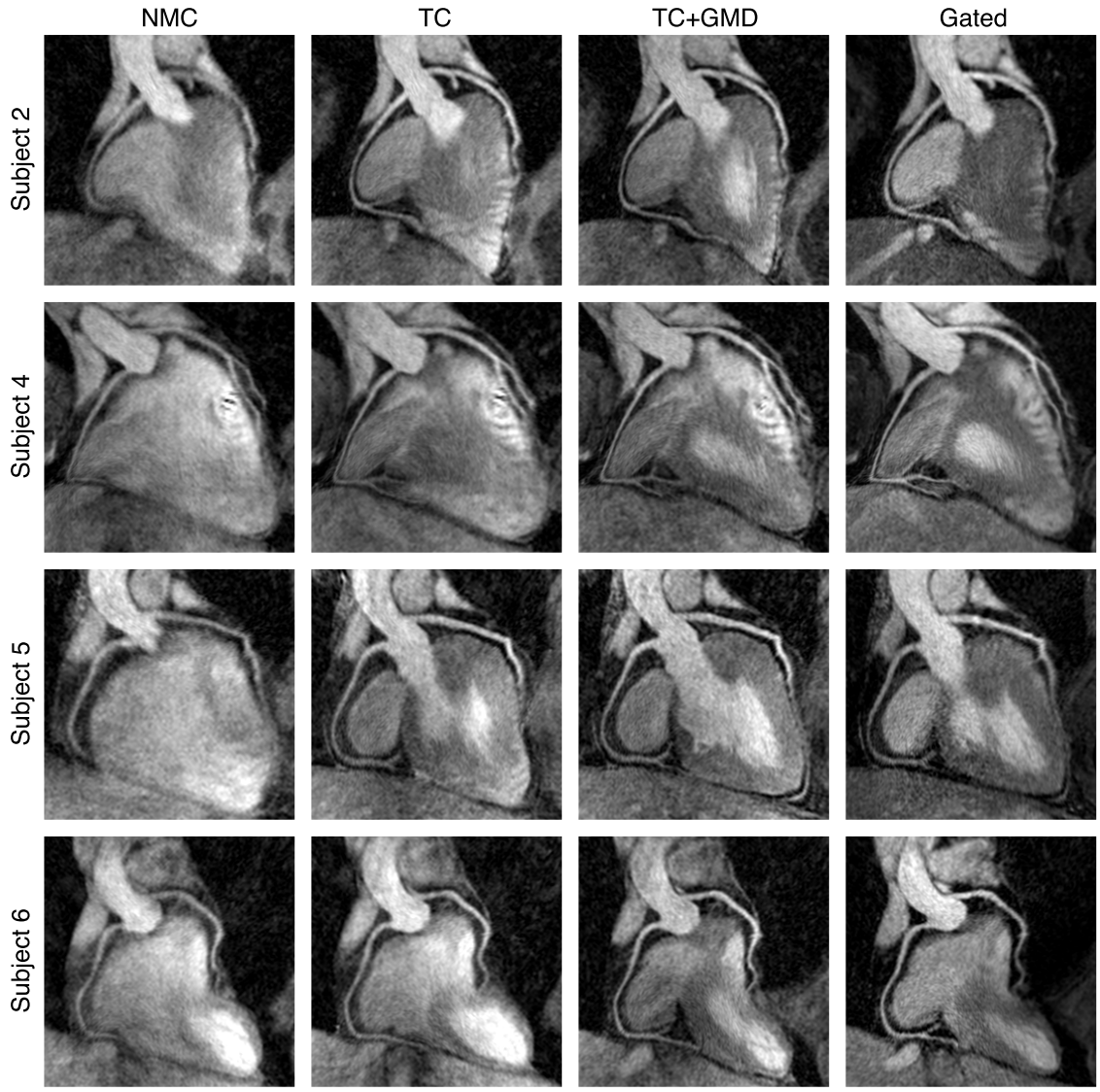

Figure 7.7: Reformatted CMRA water images for four representative subjects (rows) showing uncorrected (NMC), translational motion-corrected (TC), translational plus non-rigid motion-corrected (TC+GMD) and Gated images. TC improves depiction of both the RCA and LAD in all cases. Further improvements are obtained with the TC+GMD approach, which results in images comparable to the Gated images.

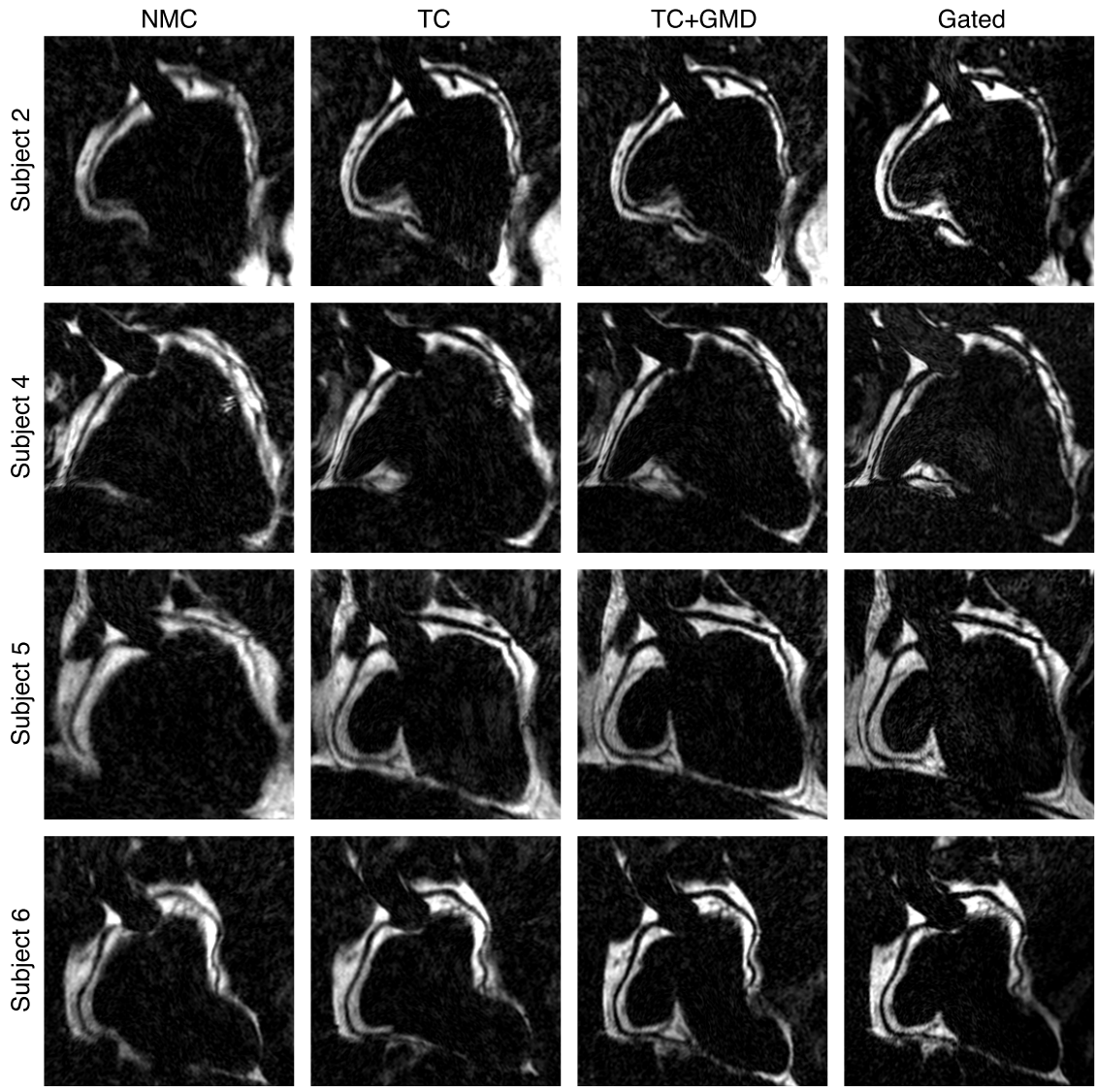

Figure 7.8: Reformatted cardiac fat images corresponding to the four representative subjects (rows) in Figure 7.7; showing NMC, TC, TC+GMD and Gated images. Similarly to the water CMRA images, depiction of the vessels improves in both TC and TC+GMD images, compared to NMC images.

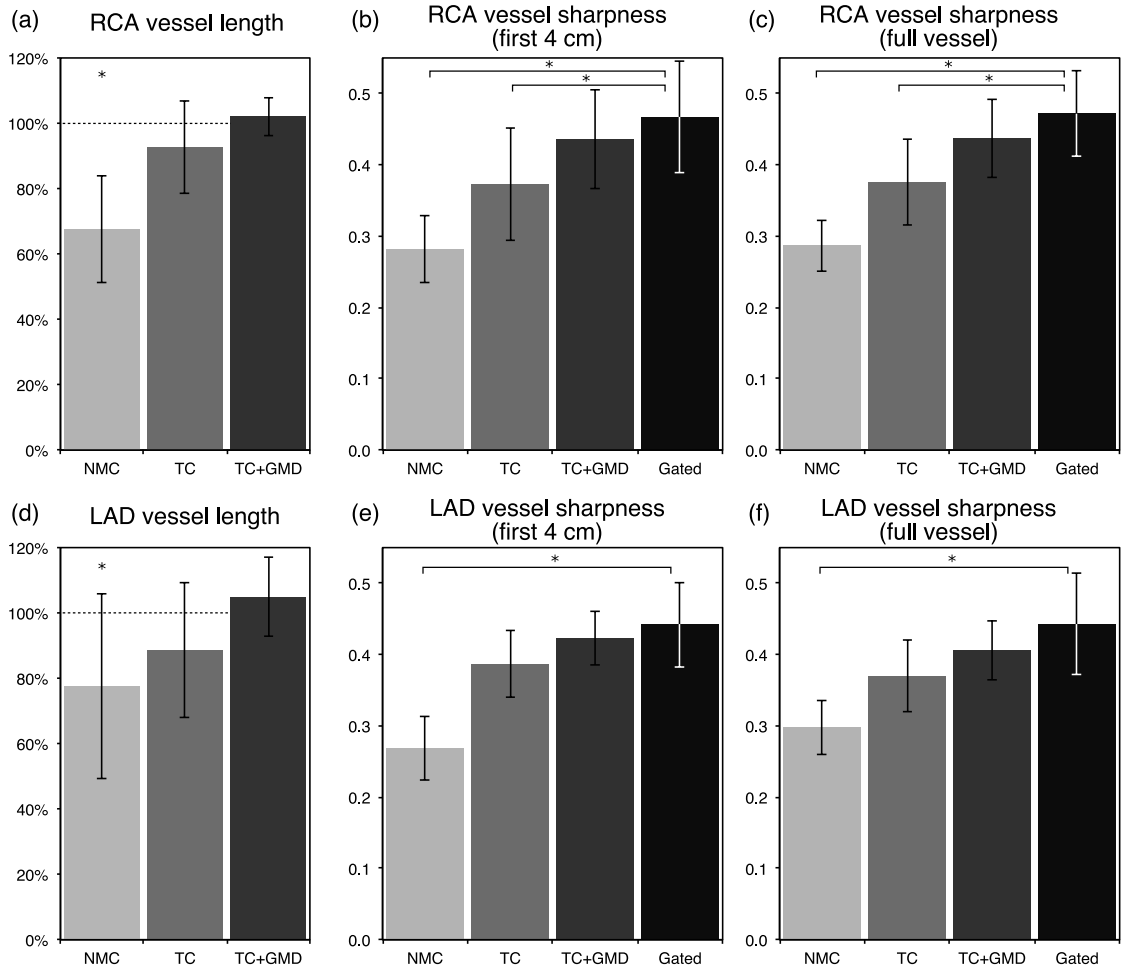

Figure 7.9: Image quality metrics for the RCA and LAD arteries for ten healthy subjects, for NMC, TC, TC+GMD and Gated images. The metrics included: visible vessel length along the (a) RCA and (d) LAD, where each measure is normalised to the length observed in the corresponding Gated image; vessel sharpness for the (b,c) RCA and (e,f) LAD, for both the first 4 cm and full length of each vessel. *denotes a statistically significant difference with $p < 0.01$ compared to the Gated images.

Finally, Figure 7.10 shows example Dixon-based μ-maps for two subjects, showing three different respiratory positions in each case. It can be observed that the water/fat CMRA approach allows the segmentation of the images into the three tissue classes (soft-tissue, fat, lungs), potentially allowing for accurate motion-compensated attenuation correction for cardiac PET-MR imaging.

7.4 Discussion

In this Chapter a novel approach for respiratory motion-corrected water/fat CMRA imaging was introduced. This approach enables the simultaneous visualisation of

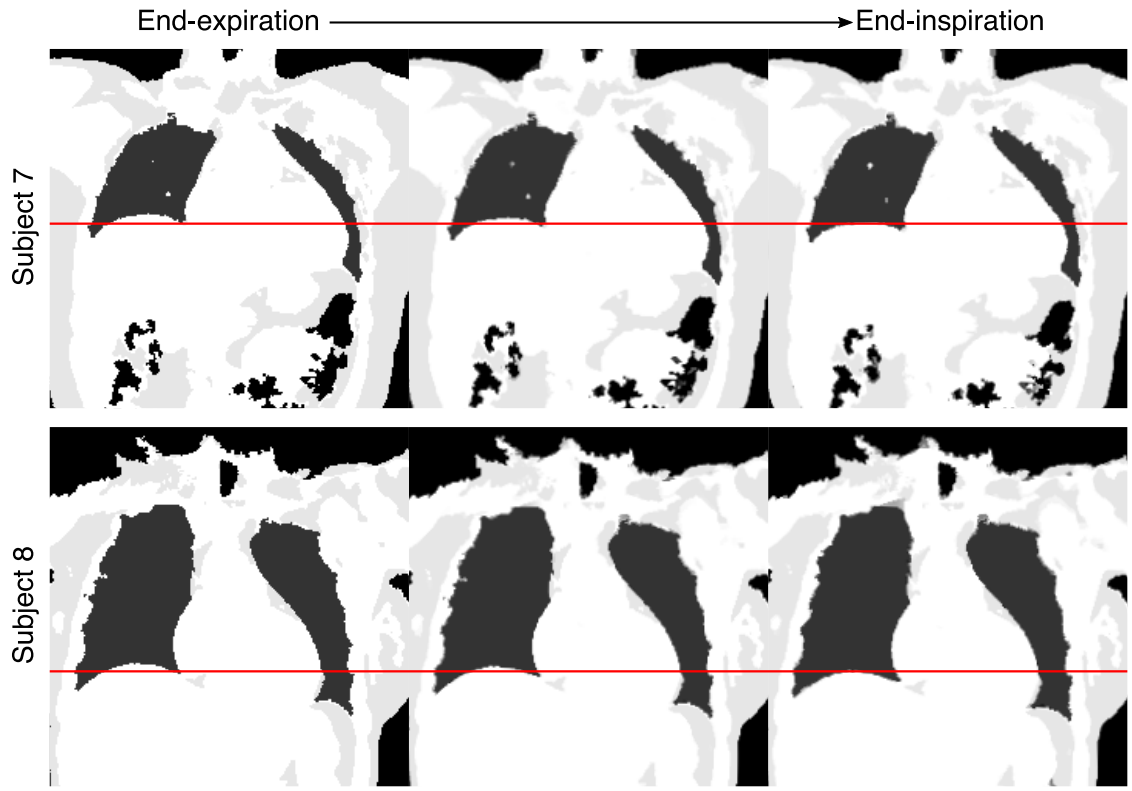

Figure 7.10: Attenuation maps for two subjects (rows), for three different respiratory positions and three tissue classes (soft-tissue, fat, lungs). A reference red line indicates the position of the liver in end-inspiration. Respiratory motion can be observed in both subjects, particularly in the dome of the liver.

coronary arteries in the water CMRA images and the cardiac fat, while potentially producing motion-resolved attenuation maps for accurate attenuation correction of simultaneously acquired PET data. This approach extends the respiratory motion-corrected acquisition and reconstruction presented in Chapter 4 to a dual-echo sequence, allowing the acquisition of two datasets: a first one acquired when water and fat signals in-phase and a second one when such signals are out-of-phase. The framework performs translational plus non-rigid motion correction separately for each of the echoes. Then, the motion-corrected echoes are used to obtain water and fat cardiac CMRA images by using a water/fat separation algorithm available in the literature [103] specifically designed for dual-echo acquisitions with bipolar readout gradients.

A first preliminary study to compare the performance of the different iNAVs that can be obtained from dual-echo acquisitions (water, fat, in-phase, out-of-phase) for estimating 2D translational motion was performed in three healthy subjects.

Results showed that FH motion estimation was similar when using different image navigators, whereas apparent differences were observed in RL motion estimation.

The iNAVs are designed to provide accurate information in the main direction of the respiratory-induced motion of the heart. Therefore, they are acquired with high-resolution in the FH direction, resulting in stable and consistent motion estimation across navigators. On the other hand, the iNAVs are heavily interpolated in the RL direction, so that changes in tissue contrast in that direction have a significant impact in the motion estimation. For subjects with larger amount of adipose tissue around the heart, such as Subject 1, fat iNAVs were shown to provide accurate RL motion, outperforming water and in-phase iNAVs, which in turn resulted in blurring and artefacts due to erroneous motion estimation. However, for subjects with less visceral and/or cardiac fat, such as Subjects 2 and 3, these fat iNAVs resulted in erroneous RL motion estimation, impacting the quality of translationally motion-corrected images. Furthermore, water and in-phase iNAVs were shown to perform better in the latter cases. Interestingly, out-of-phase iNAVs was observed to perform consistently well in all studied cases. This is likely due to the high-contrast edge between myocardium and epicardial fat produced by the chemical shift between water and fat, which can be accurately tracked by the image registration algorithm.

In the main study, performance of the translational correction only (TC) and the translational plus non-rigid motion correction (TC+GMD) was compared to uncorrected (NMC) images and to a reference diaphragmatic 6 mm gated and tracked acquisition for the whole cohort of ten subjects. In all cases, improvements are apparent in the delineation of the coronary arteries when using TC compared to NMC, and additional improvements are observed when using the TC+GMD approach. Metrics of image quality showed no statistically significant difference between TC+GMD and gated water CMRA images for the visible vessel length and vessel sharpness for both the right and left coronary arteries.

These results are consistent with previous findings in this thesis (Chapter 4), and other studies using the TC+GMD approach in conventional fat-suppressed CMRA imaging at 1.5T [159]. This indicates that the 2D iNAV-based TC+GMD approach is robust and reliable for coronary imaging, and can be used with different image contrasts and in different sequence configurations.

This study had some limitations. First, the introduced approach used conventional in-phase and out-of-phase echo times to produce the water/fat CMRA images. This restriction in the echo times resulted in an increased TR compared to conventional fat-suppressed CMRA approaches. Indeed, while in Chapters 4 to 6, a TR of ∼3.7 ms was used, allowing for ∼26 lines of k-space to be acquired in the mid-diastolic quiescent period for an average subject, the dual-echo approach introduced in this Chapter required a minimum TR of ∼5.3 ms, reducing the number of k-space lines that can be acquired at each heartbeat to ∼19, producing a significant increase in total acquisition time. In future studies, this problem can be alleviated by using flexible echo time approaches [104, 243]. These flexible echo-times approaches allow the echo images not to be acquired at exact in-phase and out-phase times, enabling the use of reduced TEs and therefore, for reduced TRs.

Although a proof of concept segmentation of the water/fat CMRA images for generating motion-resolved μ-maps was shown, the anterior-posterior coverage of the images acquired for this study is insufficient for performing full thoracic attenuation correction. Indeed, 3D images were acquired with whole-heart coverage, excluding the chest and back of the subjects. If the introduced approach is to be used as the only source for creating attenuation maps, a significant increase in the anterior-posterior coverage is fundamental. Alternatively, the water/fat CMRA-based μ-maps could be integrated in approaches that aggregate information from multiple scans, such as [244], so that attenuation of static tissues are obtained from a separate sequence, while the water/fat CMRA can provide information about the attenuation of moving organs through the respiratory cycle.

Future work includes accelerating the introduced approach using variable density trajectories that allow undersampled acquisitions, such as the ones described in [245, 246], in order to increase spatial resolution and anterior-posterior coverage without increasing acquisition time. Furthermore, future studies are required for a clinical validation of the introduced water/fat PET-CMRA approach in patients with cardiovascular disease, including an assessment of the impact of motion-resolved attenuation correction in PET image quality.

7.5 Summary

A framework for respiratory motion-corrected water/fat coronary MR angiography has been introduced. The framework allows the simultaneous visualisation of the coronary anatomy, cardiac fat and generation of motion-resolved attenuation maps throughout the respiratory cycle. This approach provides 100% scan efficiency, as all the acquired data is used for image reconstruction, and has a predictable scan time that only depends on the heart rate of the subject being scanned. The motion-corrected reconstruction framework was tested in a cohort of ten healthy subjects and compared to a reference 1D diaphragmatic gated and tracked acquisition. No statistically significant differences were found between them when quantifying image quality in the water CMRA images, in terms of visible length and sharpness of the vessels. However, the motion-corrected approach was faster and enables the creation of motion-resolved attenuation maps for accurate attenuation correction in cardiac PET-MR imaging. Future work includes accelerating the acquisition for improved spatial resolution and coverage, and validating the whole water/fat PET-CMRA framework in patients with cardiovascular disease.

Chapter 8:

Discussion and Final Remarks

This thesis introduced a novel approach for motion-corrected simultaneous cardiac PET-MR imaging. Instead of using MR images for motion estimation purposes only, as most of the current approaches for MR-based motion correction in cardiac PET-MR do, a novel MR acquisition scheme was designed in this work, in order to simultaneously provide diagnostic-quality images and motion information. This was achieved by integrating a 2D image navigator (iNAV [78]) to a CMRA acquisition sequence, so that the position of the heart could be tracked at each heartbeat. Furthermore, by using a golden-step Cartesian spiral profile order sampling trajectory for the 3D CMRA acquisition [155], the acquired data could be retrospectively sorted into a number of respiratory windows. Due to the properties of this trajectory, 3D images could be reconstructed at different respiratory positions from undersampled data, enabling the measurement of the complex non-rigid motion of the heart throughout the respiratory cycle. A general PET-CMRA motion-corrected reconstruction framework was then developed, so that the motion information estimated from MR was used to correct both the PET and CMRA datasets to the same position, resulting in intrinsically aligned, good quality images in both modalities from a single efficient examination with short and predictable scan time.

In Chapter 4, a framework for respiratory motion-corrected PET-CMRA was introduced. Although the non-rigid motion correction scheme for CMRA had been previously validated against a diaphragmatic gated and tracked CMRA acquisition for visualisation of the coronary anatomy at 1.5 T, using a balanced SSFP readout and a golden radial phase-encoding trajectory [159], such acquisition approach is not directly applicable to a 3 T PET-MR system. Magnetic field inhomogeneities

prevent the use of balanced SSFP readouts, so a spoiled gradient echo acquisition was used in this thesis instead. Furthermore, the acquisition trajectory was modified to a Cartesian spiral-like trajectory, simplifying the MR reconstruction problem and reducing image reconstruction time. In order to enhance contrast between the coronary arteries and surrounding myocardium without using exogenous contrast agents, an adiabatic T_2 preparation module was implemented in the scanner software. Finally, a framework for motion compensation of the simultaneously acquired PET data was developed, based on a reconstruct-transform-average approach [164], where motion information was used both to create attenuation maps at each respiratory position, and to transform PET images reconstructed at different respiratory positions to the end-expiration position.

In order to study the performance of the proposed respiratory motion correction framework for PET-CMRA, three studies were performed. First, an MR-only validation study was performed in a cohort of healthy subjects; comparing the motion-corrected CMRA images to reference diaphragmatic gated and tracked images. Results showed no statistically significant difference in metrics of image quality between both approaches, but the motion-corrected CMRA resulted in significantly reduced scan time (30% faster than a 2× accelerated gated acquisition on average) and importantly provides motion information for MR-based motion correction of PET images. A second study was performed in a small cohort of oncology patients that had received an injection of ^{18}F-FDG for a conventional PET-CT examination. This study served as proof-of-concept for the whole motion-corrected PET-CMRA framework. In these patients, significant improvements in the depiction of the coronary arteries was observed in the CMRA images after motion correction, while motion-corrected PET images showed improvements in the delineation of small structures such as the papillary muscles, and increased the sharpness of the left ventricular myocardial wall compared to uncorrected images.

In Chapter 5 a third study was presented, describing the performance of the approach introduced in Chapter 4 in a cohort of patients with known cardiovascular disease. In particular, patients with chronic total occlusion of at least one of the coronary arteries were scanned with the proposed PET-CMRA sequence, allowing simultaneous visualisation of the coronary anatomy by CMRA and my-

ocardial viability by ^{18}F-FDG PET. Results obtained in this cohort were consistent with previous findings, with an improved delineation of relevant cardiac structures in both PET and MR after motion correction, suggesting that the framework is robust in cases of more irregular breathing patterns. Furthermore, when visually comparing the coronary anatomy as depicted by motion-corrected CMRA and the invasive gold-standard (X-ray angiography), a good agreement between modalities was found. Similarly, a visual comparison between motion-corrected ^{18}F-FDG PET images and LGE-MRI showed a good correspondence between modalities in the depiction of both transmural and non-transmural myocardial viability defects. Additional tests in patients with different cardiovascular conditions and using novel PET radiotracers were also presented in this Chapter, demonstrating the versatility and robustness of the motion correction approach and its potential for enabling the simultaneous acquisition of diagnostic images with both modalities.

In order to address the effect of cardiac motion in PET image quality, Chapter 6 extended the framework introduced in Chapter 4 to a dual-phase CMRA-PET acquisition. By acquiring CMRA data in systole and diastole, cardiac motion could also be estimated and used to correct the simultaneously acquired PET data. Furthermore, these two 3D CMRA images can be used to estimate left ventricular function, including relevant functional indices such as ejection fraction and stroke volume. Therefore, this approach potentially allows for a comprehensive assessment of coronary artery disease from a single examination, including visualisation of the coronary anatomy and estimation of ventricular function from the systolic and diastolic CMRA images, and assessment of myocardial integrity by cardiac and respiratory motion-corrected PET imaging. A first MR-only study in healthy subjects was performed to study the accuracy of the dual-phase CMRA for estimating left ventricular function, and good agreement with conventional 2D cine MR imaging was found. A preliminary study using the whole dual-phase CMRA-PET approach in patients with cardiovascular disease was also performed. Results suggest that the respiratory motion correction has a stronger impact than cardiac motion correction in terms of increased SUV in PET images and improvements in image quality, but nonetheless, incremental improvements were observed. Although this is consistent with findings in the motion-corrected cardiac PET-MR literature [211] which has

focused on ^{18}F-FDG or ^{13}N-ammonia for myocardial PET imaging, this may not be the case for PET radiotracers that target smaller structures, such as ^{18}F-NaF for plaque imaging. Further studies are required to ascertain the impact of cardiac motion correction in these cases.

Finally, Chapter 7 explored an alternative method for enhancing the contrast between coronary arteries and epicardial fat. Instead of using a conventional fat suppression preparation pulse to minimise the fat signal, a dual-echo acquisition approach was introduced, so that separate water and fat CMRA images could be produced. In this Chapter, the performance of iNAVs with different contrast for estimation of respiratory motion was studied. Results from three healthy subjects suggest that out-of-phase iNAVs produce accurate estimates of foot-head and right-left motion of the heart, for subjects with varying amount of visceral and cardiac fat. The non-rigid respiratory motion-corrected reconstruction scheme introduced in Chapter 4 was extended to dual-echo imaging, and tested in a cohort of healthy subjects. A validation study comparing motion-corrected and gated water/fat CMRA images was performed, and similarly to Chapter 4, findings suggest that image quality obtained with the motion-correction approach is not significantly different to the gated images, but scan time is significantly reduced (45% faster than a 2× accelerated gated acquisition) and motion information is available for motion correction of simultaneously acquired cardiac PET data. Furthermore, as water/fat images can be reconstructed at different respiratory positions throughout the breathing cycle, the proposed water/fat CMRA approach allows the computation of respiratory motion-resolved attenuation maps, which can be used for attenuation correction of the PET data. Due to its intrinsic robustness to field inhomogeneities, the water/fat scheme could potentially improve the robustness of the iNAV-based CMRA in larger patients, where conventional fat suppression is challenging. Moreover, it can provide additional diagnostic information from the fat image, and potentially improve the accuracy of the attenuation correction of PET images.

Although the respiratory motion-corrected CMRA images were compared to a reference diaphragmatic gated and tracked acquisition for healthy subjects in Chapters 4 and 7, such validation was not performed in patients with cardiovascular disease, where respiratory motion can be more variable. Furthermore, comparison

between motion-corrected CMRA and invasive X-ray angiography in terms of depiction of the coronary anatomy was performed only visually in Chapter 5. Further validation of the introduced approach for respiratory motion-corrected CMRA in larger cohorts of patients with known or suspected coronary artery disease is required, including a comparison between clinical findings from the motion-corrected CMRA approach and a gold standard method, such as invasive X-ray angiography or coronary CT angiography.

For all the proposed methods, 2D translational correction for the CMRA acquisition was implemented in the scanner software, so that a first correction could be immediately visualised after scanning. However, PET-MR data synchronisation, and both the non-rigid motion-corrected CMRA and the motion-compensated PET reconstruction were performed offline. Indeed, PET-MR synchronisation was performed offline using the ECG R-wave detection tags in the raw data of each modality, ensuring less than 2.5 ms uncertainty in synchronisation between PET and MR, which was sufficient for motion-compensated static PET imaging. Future work includes implementing the whole motion compensation framework on the scanner software, including improved PET-MR synchronisation, as well as non-rigid motion estimation from MR and motion-corrected reconstruction for both PET and CMRA. This would enable a smoother integration of the proposed methods into clinical routine.

Throughout this thesis, attenuation correction of PET data was performed using attenuation maps produced by a 4-tissue class segmentation of MR images. While investigating novel MR-based attenuation correction approaches was out of the scope of this thesis, and thus the conventional method provided by the vendor was used, such an approach has several limitations. First, MR data is acquired during a $\sim$19 s breath-hold, which can be challenging for some patients. Although not observed in this thesis, incomplete breath-holds can result in segmentation errors and tissue misclassification, producing erroneous attenuation maps. Second, the 4-tissue class model only considers homogeneous attenuation values for air, lung tissue, soft-tissue and adipose tissue. Therefore, inaccuracies arise from the presence of other tissues and materials, such as bone tissue, coronary stents, or mixtures of any of these tissues. Furthermore, the MR-based attenuation maps assign a unique attenuation

value to the lung tissue. However, studies have shown wide intra an inter-patient variability in lung tissue density, including variations throughout the respiratory cycle. While these inaccuracies in MR-based attenuation correction might impact absolute PET quantification, this is rarely the task of clinical cardiac PET imaging. Moreover, if more accurate MR-based attenuation maps become clinically available, they can be readily incorporated into the motion-compensated PET framework proposed in this thesis.

A conventional spatially-invariant resolution model was considered in this work, neglecting the spatially-variant effect of the scanner geometry. This approach also ignores the effects of non-isotropic and tissue-dependent positron range on PET image resolution. Although in whole-body PET-MR scanners for ^{18}F-based radiotracers these effects are typically smaller than the component arising from detector width, they might become significant for other radionuclides. In the future, spatially-variant resolution modelling, including the effects of tissue-dependency and anisotropy of positron range, could be incorporated into the PET reconstruction method. This might be particularly important for absolute PET quantification in regions where there is a sharp transition in tissue density, such as the lung/soft-tissue interface.

In this thesis, a reconstruct-transform-average (RTA) approach was used for motion compensation of PET data. Studies have shown that this approach might result in image degradation due to interpolation, and that including motion directly in the image reconstruction algorithm can address this issue, however at the expense of longer reconstruction times. Moreover, including the motion directly in the reconstruction might reduce the bias associated to low counts in each bin when using the RTA approach. In this thesis, such bias was not observed, probably due to the high count levels associated to ^{18}F-FGD. However, a larger impact could potentially be observed when using radiotracers that target smaller structures, such as ^{18}F-NaF, in low-dose imaging, or in dynamic PET imaging. Implementing an iterative motion-corrected PET image reconstruction framework and comparing it to the approach used in this thesis remains for future work. Furthermore, the proposed scheme only enables motion correction of the PET data acquired simultaneously with the CMRA data, preventing motion correction of PET data acquired before or after this window. In future, a motion model could be generated during the simultaneous PET-CMRA

acquisition, and used to correct for motion in subsequent PET acquisitions using appropriate surrogate signals.

The reconstruction framework proposed in this thesis used MR-based motion information to correct both the PET and CMRA datasets. However, ^{18}F-FDG myocardial PET images can also provide information about the physiological motion of the heart. Joint motion estimation techniques such as the one proposed in [209] could improve the robustness of the proposed method. Furthermore, in this thesis, PET and MR images were reconstructed separately. Recent advances in the joint PET-MR image reconstruction literature have shown potential for improvements in image quality in both PET and MR for brain imaging [247–249]. The impact and applicability of such techniques to cardiac PET-MR imaging remains an open question.

Although the image resolution used for CMRA in this thesis was enough to depict the proximal coronary anatomy (i.e. $1\times1\times2\,\text{mm}^3$ in Chapters 4, 5 and 6 and 1.3 mm isotropic in Chapter 7), an accurate depiction of distal segments and stenosis might require higher spatial resolution. In order to increase image resolution without increasing total acquisition time, novel acquisition trajectories and more advanced undersampled reconstruction techniques can be incorporated to the proposed PET-CMRA framework. Indeed, a variable-density version of the golden-step Cartesian spiral profile order sampling trajectory has recently been introduced for CMRA with sub-millimetre resolution in a 1.5 T MR system [246], which could be adapted for PET-CMRA at 3 T.

Furthermore, novel undersampled reconstruction techniques for CMRA imaging such as [250] could enable the extension of the proposed MR acquisition framework to multiple contrasts without increasing total scan time. For instance, the recently introduced multi-contrast BOOST sequence [176,222], that allows simultaneous bright and black-blood imaging at 1.5 T could be extended to a 3 T PET-MR system for use with a range of PET radiotracers. For example, a motion-corrected ^{18}F-NaF PET-BOOST CMRA scan could provide simultaneous co-registered images for the visualisation of coronary anatomy and intra-plaque haemorrhage by MR and plaque calcification by PET. Alternatively, used after injection of a Gadolinium-based contrast agent, a ^{18}F-FDG PET-BOOST CMRA scan could provide visualisation of the

coronary lumen from CMRA and fibrosis visualisation from black-blood LGE-MRI, in addition to quantification of myocardial inflammation from ^{18}F-FDG PET, which could be beneficial in the differential diagnosis of cardiac sarcoidosis.

The research developed throughout this dissertation focused on the use of simultaneous PET-MR imaging for a comprehensive assessment of coronary artery disease, including visualisation of the coronary anatomy by CMRA and myocardial integrity by ^{18}F-FDG PET. However, the flexibility and robustness of the motion-corrected simultaneous PET-CMRA framework introduced in this thesis could enable a whole range of exciting new research opportunities for whole-heart PET-MR imaging for a range of cardiac conditions. For instance, as mentioned above, the proposed PET-CMRA approach could have a significant role in atherosclerotic plaque imaging, by providing detection of plaque micro-calcification by ^{18}F-NaF and precise localisation within the coronary tree from the simultaneously acquired CMRA. Moreover, in inflammatory diseases such as cardiac sarcoidosis or myocarditis, the proposed motion-corrected approach could improve the confidence in interpreting the findings observed in both modalities (i.e. myocardial inflammation by ^{18}F-FDG and fibrosis or oedema from MR), by ensuring accurate alignment between both PET and MR images. Furthermore, in such diseases, PET-CMRA imaging could potentially be used to guide the biopsy of areas with active inflammation detected by PET through anatomical localisation provided by the whole-heart CMRA image [251]. The ability of the proposed framework for producing co-registered diagnostic PET and MR images that provide complementary information about different disease processes would be beneficial for encouraging the adoption of PET-MR for cardiac imaging in routine clinical practice.

Publications

The work presented in this thesis resulted in the following publications:

- Munoz, C., Cruz, G., Neji, R., Botnar, R.M., Prieto, C. Motion Corrected Water/Fat Whole-Heart Coronary MR Angiography with 100% Respiratory Efficiency. *Magnetic Resonance in Medicine* (in press)

- Munoz, C., Neji, R., Kunze, K.P., Nekolla, S.G., Botnar, R.M., Prieto, C. Respiratory and Cardiac Motion Corrected Simultaneous Whole-heart PET and Dual Phase Coronary MR Angiography. *Magnetic Resonance in Medicine*, 2019. 81:1671–1684.

- Munoz, C., Kunze, K.P., Neji, R., Vitadello, T., Rischpler, C., Botnar, R.M., Nekolla, S.G., Prieto, C. Motion-corrected whole-heart PET-MR for the simultaneous visualisation of coronary artery integrity and myocardial viability: an initial clinical validation. *European Journal of Nuclear Medicine and Molecular Imaging*, 2018, 45(11):1975–1986.

- Munoz, C., Neji, R., Cruz, G., Mallia, A., Jeljeli, S., Reader, A.J., Botnar, R.M. and Prieto, C. Motion-corrected simultaneous cardiac positron emission tomography and coronary MR angiography with high acquisition efficiency. *Magnetic Resonance in Medicine*, 2017, 79:339–350.

- Munoz, C., Kolbitsch, C., Reader, A.J., Marsden, P., Schaeffter, T. and Prieto, C. MR-Based Cardiac and Respiratory Motion-Compensation Techniques for PET-MR Imaging. *PET Clinics*, 2016, 11(2):179-191.

And the following presentations at international conferences:

- Munoz, C., Neji, R., Kunze, K.P., Nekolla, S.G., Botnar, R.M., Prieto, C. Cardiac and Respiratory Motion-Compensated Simultaneous Whole-heart PET-MR Imaging. In *Proceedings of the 2018 IEEE NSS/MIC*, Sydney, Australia, November 2018

- Munoz, C., Neji, R., Kunze, K.P., Rashid, I., Nazir, M.S., Nekolla, S.G., Botnar, R.M., Prieto, C. Motion-corrected coronary MR angiography and myocardial PET: initial clinical experience. In *Proceedings of the 2018 SMRA Annual Meeting*, Glasgow, Scotland, August 2018

- Munoz, C., Kunze, K.P., Neji, R., Rischpler, C., Botnar, R.M., Nekolla, S.G., Prieto, C. Respiratory motion-corrected simultaneous myocardial viability PET and coronary MR angiography: initial clinical validation. In *Proceedings of the 26th Annual Meeting of ISMRM*, Paris, France, June 2018

- Munoz, C., Neji, R., Kunze, K.P., Rashid, I., Rischpler, C., Nekolla, S.G., Botnar, R.M., Prieto, C. Cardiac and respiratory motion-corrected whole-heart PET-MR imaging for simultaneous assessment of coronary anatomy, cardiac function and myocardial integrity. In *Proceedings of the 26th Annual Meeting of ISMRM*, Paris, France, June 2018

- Munoz, C., Neji, R., Cruz, G., Botnar, R.M., Prieto, C. Simultaneous acquisition of motion-corrected coronary MRA and respiratory-resolved attenuation maps for whole-heart PET-MR imaging. In *Proceedings of the 26th Annual Meeting of ISMRM*, Paris, France, June 2018

- Munoz, C., Kunze, K.P., Neji, R., Botnar R.M., Prieto, C., Nekolla, S.G. Initial clinical validation of respiratory motion-corrected myocardial viability PET and simultaneous coronary MR angiography. In *Proceedings of the 2018 SNMMI Annual Meeting*, Philadelphia, Pennsylvania, USA, June 2018

- Munoz, C., Neji, R., Botnar, R.M. and Prieto, C. Highly efficient respiratory motion corrected dual-phase coronary MR angiography in a 3T PET-MR system. In *Proceedings of the 25th Annual Meeting of ISMRM*, Honolulu, USA, Apr, 2017

- Munoz, C., Neji, R., Lima da Cruz, G.J., Botnar, R.M. and Prieto, C. Respiratory motion-corrected simultaneous cardiac PET and coronary MR angiography using a hybrid 3T PET-MR. In *Proceedings of the 25th Annual Meeting of ISMRM*, Honolulu, USA. Apr, 2017

- Munoz, C., Neji, R., Marsden, P.K., Reader, A.J., Botnar, R.M. and Prieto, C. Highly Efficient Motion-Corrected Simultaneous Cardiac PET-MR Imaging. In *Proceedings of the 2016 IEEE Nuclear Science Symposium and Medical Imaging Conference (NSS/MIC)*, Strasbourg, France. Nov, 2016.

- Munoz, C., Neji, R., Weale, P., Botnar, R.M. and Prieto, C. 100% efficient motion corrected coronary MR angiography using a gradient echo sequence in a 3T PET-MR system. In *Proceedings of the 24th Annual Meeting of ISMRM*, Singapore. May, 2016.

- Munoz, C., Kolbitsch, C.P. and Prieto, C. Impact of spatio-temporal resolution on MR-based cardiac motion correction PET-MR. In *Proceedings of the 24th Annual Meeting of ISMRM*, Singapore. May, 2016.

Awards

The following awards were obtained as a result of the research presented in this thesis:

- Potchen Award, 1st Runner up - for the work "Motion-corrected coronary magnetic resonance angiography and myocardial positron emission tomography: initial clinical experience" (SMRA 2018)

- Best Presentation Award ISMRM PET-MR study group - for the work "Respiratory motion-corrected simultaneous myocardial viability PET and coronary MR angiography: initial clinical validation" (ISMRM 2018)

- Magna Cum Laude Merit Award - for the work "Cardiac and respiratory motion-corrected whole-heart PET-MR imaging for simultaneous assessment of coronary anatomy, cardiac function and myocardial integrity" (ISMRM 2018)

- Magna Cum Laude Merit Award - for the work "Highly efficient respiratory motion corrected dual-phase coronary MR angiography in a 3 T PET-MR system" (ISMRM 2017)
- Summa Cum Laude Merit Award - for the work "Respiratory Motion-Corrected Simultaneous Cardiac PET and Coronary MR Angiography using a Hybrid 3 T PET-MR" (ISMRM 2017)

Bibliography

[1] Global Burden Diseases (GBD) 2013 Mortality and Causes of Death Collaborators, "Global, regional, and national age–sex specific all-cause and cause-specific mortality for 240 causes of death, 1990–2013: a systematic analysis for the Global Burden of Disease Study 2013," *Lancet*, vol. 385, no. 9963, pp. 117–71, 2014.

[2] S. Yusuf, D. Wood, J. Ralston, and K. S. Reddy, "The World Heart Federation's vision for worldwide cardiovascular disease prevention," *Lancet*, vol. 386, no. 9991, pp. 399–402, 2015.

[3] World Health Organization, "Global Action Plan for the Prevention and Control of NCDS, 2013-2020," Tech. Rep., 2013.

[4] D. Mehta, J. Curwin, J. A. Gomes, and V. Fuster, "Sudden Death in Coronary Artery Disease: Acute Ischemia Versus Myocardial Substrate," *Circulation*, vol. 96, no. 9, pp. 3215–3223, 1997.

[5] R. W. Nesto and G. J. Kowalchuk, "The ischemic cascade: Temporal sequence of hemodynamic, electrocardiographic and symptomatic expressions of ischemia," *Am J Cardiol*, vol. 59, no. 7, pp. C23–C30, 1987.

[6] G. Ginami, I. Rashid, R. M. Botnar, and C. Prieto, "Technical Advances and Clinical Perspectives in Coronary MR Imaging," in *Cardiovascular Imaging and Image Analysis*, A. El-Baz and J. Suri, Eds. Taylor & Francis, 2018, pp. 321–343.

[7] J. Sanz and Z. A. Fayad, "Imaging of atherosclerotic cardiovascular disease," *Nature*, vol. 451, no. 7181, pp. 953–957, 2008.

[8] N. V. Joshi, A. T. Vesey, M. C. Williams, A. S. V. Shah, P. A. Calvert, F. H. M. Craighead, S. E. Yeoh, W. Wallace, D. Salter, A. M. Fletcher, E. J. R. van Beek, A. D. Flapan, N. G. Uren, M. W. H. Behan, N. L. M. Cruden, N. L. Mills, K. A. A. Fox, J. H. F. Rudd, M. R. Dweck, and D. E. Newby, "18F-fluoride positron emission tomography for identification of ruptured and high-risk coronary atherosclerotic plaques: a prospective clinical trial." *Lancet*, vol. 383, no. 9918, pp. 705–13, 2014.

[9] J. M. Tarkin, F. R. Joshi, N. R. Evans, M. M. Chowdhury, N. L. Figg, A. V. Shah, L. T. Starks, A. Martin-Garrido, R. Manavaki, E. Yu, R. E. Kuc, L. Grassi, R. Kreuzhuber, M. A. Kostadima, M. Frontini, P. J. Kirkpatrick, P. A. Coughlin, D. Gopalan, T. D. Fryer, J. R. Buscombe, A. M. Groves, W. H. Ouwehand, M. R. Bennett, E. A. Warburton, A. P. Davenport, and J. H. Rudd, "Detection of Atherosclerotic Inflammation by 68Ga-DOTATATE PET Compared to [18F]FDG PET Imaging," *J Am Coll Cardiol*, vol. 69, no. 14, pp. 1774–1791, 2017.

[10] M. Hamon, R. Morello, J. W. Riddell, and M. Hamon, "Coronary arteries: diagnostic performance of 16- versus 64-section spiral CT compared with invasive coronary angiography–meta-analysis," *Radiology*, vol. 245, no. 3, pp. 720–731, 2007.

[11] F. A. Mettler, W. Huda, T. T. Yoshizumi, and M. Mahesh, "Effective Doses in Radiology and Diagnostic Nuclear Medicine: A Catalog," *Radiology*, vol. 248, no. 1, pp. 254–263, 2008.

[12] P. G. Danias, A. Roussakis, and J. P. A. Ioannidis, "Diagnostic performance of coronary magnetic resonance angiography as compared against conventional x-ray angiography: A meta-analysis," *J Am Coll Cardiol*, vol. 44, no. 9, pp. 1867–1876, 2004.

[13] G. Di Leo, E. Fisci, F. Secchi, M. Alì, F. Ambrogi, L. M. Sconfienza, and F. Sardanelli, "Diagnostic accuracy of magnetic resonance angiography for detection of coronary artery disease: a systematic review and meta-analysis," *Eur Radiol*, vol. 26, no. 10, pp. 3706–3718, 2016.

[14] P. Garg, S. R. Underwood, R. Senior, J. P. Greenwood, and S. Plein, "Noninvasive cardiac imaging in suspected acute coronary syndrome," *Nat Rev Cardiol*, vol. 13, no. 5, pp. 266–275, 2016.

[15] M. F. Di Carli, S. Dorbala, J. Meserve, G. El Fakhri, A. Sitek, and S. C. Moore, "Clinical myocardial perfusion PET/CT." *J Nucl Med*, vol. 48, no. 5, pp. 783–793, 2007.

[16] K. C. Allman, L. J. Shaw, R. Hachamovitch, and J. E. Udelson, "Myocardial viability testing and impact of revascularization on prognosis in patients with coronary artery disease and left ventricular dysfunction: A meta-analysis," *J Am Coll Cardiol*, vol. 39, no. 7, pp. 1151–1158, 2002.

[17] S. S. Gambhir, D. S. Berman, J. Ziffer, M. Nagler, M. Sandler, J. Patton, B. Hutton, T. Sharir, S. B. Haim, and S. B. Haim, "A Novel High-Sensitivity Rapid-Acquisition Single-Photon Cardiac Imaging Camera," *J Nucl Med*, vol. 50, no. 4, pp. 635–643, 2009.

[18] F. P. Esteves, P. Raggi, R. D. Folks, Z. Keidar, J. Wells Askew, S. Rispler, M. K. O'Connor, L. Verdes, and E. V. Garcia, "Novel solid-state-detector dedicated cardiac camera for fast myocardial perfusion imaging: Multicenter comparison with standard dual detector cameras," *J Nucl Cardiol*, vol. 16, no. 6, pp. 927–934, 2009.

[19] E. V. Garcia, T. L. Faber, and F. P. Esteves, "Cardiac Dedicated Ultrafast SPECT Cameras: New Designs and Clinical Implications," *J Nucl Med*, vol. 52, no. 2, pp. 210–217, 2011.

[20] P. J. Slomka, D. S. Berman, and G. Germano, "New Cardiac Cameras: Single-Photon Emission CT and PET," *Semin Nucl Med*, vol. 44, no. 4, pp. 232–251, 2014.

[21] M. F. Di Carli and R. Hachamovitch, "New technology for noninvasive evaluation of coronary artery disease," *Circulation*, vol. 115, no. 11, pp. 1464–1480, 2007.

[22] J. Machac, "Cardiac positron emission tomography imaging," *Semin Nucl Med*, vol. 35, no. 1, pp. 17–36, 2005.

[23] L. Le Meunier, R. Maass-Moreno, J. a. Carrasquillo, W. Dieckmann, and S. L. Bacharach, "PET/CT imaging: Effect of respiratory motion on apparent myocardial uptake," *J Nucl Cardiol*, vol. 13, no. 6, pp. 821–830, 2006.

[24] F. Nensa, F. Bamberg, C. Rischpler, L. Menezes, T. D. Poeppel, C. la Fougère, D. Beitzke, S. Rasul, C. Loewe, K. Nikolaou, J. Bucerius, A. Kjaer, M. Gutberlet, N. H. Prakken, R. Vliegenthart, R. H. J. A. Slart, S. G. Nekolla, M. L. Lassen, B. J. Pichler, T. Schlosser, A. Jacquier, H. H. Quick, M. Schäfers, M. Hacker, European Society of Cardiovascular Radiology (ESCR), and European Association of Nuclear Medicine (EANM) Cardiovascular Committee, "Hybrid cardiac imaging using PET/MRI: a joint position statement by the European Society of Cardiovascular Radiology (ESCR) and the European Association of Nuclear Medicine (EANM)," *Eur Radiol*, vol. 2, no. 1, p. 14, 2018.

[25] C. Catana, "Motion Correction Options in PET/MRI," *Semin Nucl Med*, vol. 45, no. 3, pp. 212–223, 2015.

[26] C. Munoz, C. Kolbitsch, A. J. Reader, P. Marsden, T. Schaeffter, and C. Prieto, "MR-Based Cardiac and Respiratory Motion-Compensation Techniques for PET-MR Imaging," *PET Clin*, vol. 11, no. 2, pp. 179–191, 2016.

[27] C. Munoz, R. Neji, G. Cruz, A. Mallia, S. Jeljeli, A. J. Reader, R. M. Botnar, and C. Prieto, "Motion-corrected simultaneous cardiac positron emission tomography and coronary MR angiography with high acquisition efficiency," *Magn Reson Med*, vol. 79, no. 1, pp. 339–350, 2017.

[28] C. Munoz, R. Neji, K. P. Kunze, S. G. Nekolla, R. M. Botnar, and C. Prieto, "Respiratory and Cardiac Motion Corrected Simultaneous Whole-heart PET and Dual Phase Coronary MR Angiography," *Magn Reson Med*, vol. 81, no. 3, pp. 1671–1684, 2019.

[29] C. Munoz, K. P. Kunze, R. Neji, T. Vitadello, C. Rischpler, R. M. Botnar, S. G. Nekolla, and C. Prieto, "Motion-corrected whole-heart PET-MR for

the simultaneous visualisation of coronary artery integrity and myocardial viability : an initial clinical validation," *Eur J Nucl Med Mol Imaging*, pp. 1–12, 2018.

[30] E. Pierce, "Diagram of the human heart," 2006. [Online]. Available: https://commons.wikimedia.org/wiki/File:Diagram_of_the_human_heart.svg

[31] M. Häggström, "Coronary Arteries," 2010. [Online]. Available: https://commons.wikimedia.org/wiki/File:Coronary_arteries.svg

[32] A. M. Weissler, W. S. Harris, and C. D. Schoenfeld, "Systolic time intervals in man," *Circulation*, vol. 37, no. 2, pp. 149–159, 1968.

[33] H. Boudoulas, P. Geleris, R. P. Lewis, and S. E. Rittgers, "Linear relationship between electrical systole, mechanical systole, and heart rate." *Chest*, vol. 80, no. 5, pp. 613–617, 1981.

[34] K. Wanderman, Z. Hayek, I. Ovsyshcher, G. Loutaty, A. Cantor, Y. Gussarsky, and M. Gueron, "Systolic time intervals in adolescents. Normal standards for clinical use and comparison with children and adults." *Circulation*, vol. 63, no. 1, pp. 204–209, 1981.

[35] S. Spitaels, R. Arbogast, J. C. Fouron, and A. Davignon, "The Influence of Heart Rate and Age on the Systolic and Diastolic Time Intervals in Children," *Circulation*, vol. 49, no. 6, pp. 1107–1115, 1974.

[36] A. D. Scott, J. Keegan, and D. N. Firmin, "Motion in Cardiovascular MR Imaging," *Radiology*, vol. 250, no. 2, pp. 331–351, 2009.

[37] C. Petitjean, N. Rougon, and P. Cluzel, "Assessment of myocardial function: A review of quantification methods and results using tagged MRI," *J Cardiovasc Magn Reson*, vol. 7, no. 2, pp. 501–516, 2005.

[38] W. K. Yong, M. Stuber, K. V. Kissinger, N. T. Andersen, W. J. Manning, and R. M. Botnar, "Impact of bulk cardiac motion on right coronary MR angiography and vessel wall imaging," *J Magn Reson Imaging*, vol. 14, no. 4, pp. 383–390, 2001.

[39] B. Lu, S. S. Mao, N. Zhuang, H. Bakhsheshi, H. Yamamoto, J. Takasu, S. C. Liu, and M. J. Budoff, "Coronary artery motion during the cardiac cycle and optimal ECG triggering for coronary artery imaging," *Invest Radiol*, vol. 36, no. 5, pp. 250–256, 2001.

[40] O. Al-Kwifi, J. Stainsby, W. D. Foltz, M. S. Sussman, Y. Huang, and G. A. Wright, "Characterizing coronary motion and its effect on MR coronary angiography - Initial experience," *J Magn Reson Imaging*, vol. 24, no. 4, pp. 842–850, 2006.

[41] Y. Wang, S. J. Riederer, and R. L. Ehman, "Respiratory Motion of the Heart: Kinematics and the Implications for the Spatial Resolution in Coronary Imaging," *Magn Reson Med*, vol. 33, no. 5, pp. 713–719, 1995.

[42] K. Nehrke, P. Börnert, D. Manke, and J. C. Böck, "Free-breathing cardiac MR imaging: study of implications of respiratory motion-initial results." *Radiology*, vol. 220, no. 3, pp. 810–815, 2001.

[43] K. McLeish, D. L. Hill, D. Atkinson, J. M. Blackall, and R. Razavi, "A study of the motion and deformation of the heart due to respiration," *IEEE Trans Med Imaging*, vol. 21, no. 9, pp. 1142–1150, 2002.

[44] P. G. Danias, M. Stuber, R. M. Botnar, K. V. Kissinger, R. R. Edelman, and W. J. Manning, "Relationship between motion of coronary arteries and diaphragm during free breathing: Lessons from real-time MR imaging," *Am J Roentgenol*, vol. 172, no. 4, pp. 1061–1065, 1999.

[45] D. Manke, K. Nehrke, P. Börnert, P. Rösch, and O. Dössel, "Respiratory motion in coronary magnetic resonance angiography: A comparison of different motion models," *J Magn Reson Imaging*, vol. 15, no. 6, pp. 661–671, 2002.

[46] G. Shechter, C. Ozturk, J. R. Resar, and E. R. McVeigh, "Respiratory motion of the heart from free breathing coronary angiograms," *IEEE Trans Med Imaging*, vol. 23, no. 8, pp. 1046–1056, 2004.

[47] A. M. Taylor, P. Jhooti, F. Wiesmann, J. Keegan, D. N. Firmin, and D. J. Pennell, "MR navigator-echo monitoring of temporal changes in diaphragm

position: Implications for MR coronary angiography," *J Magn Reson Imaging*, vol. 7, no. 4, pp. 629–636, 1997.

[48] G. L. Raff, Chair, A. Abidov, S. Achenbach, D. S. Berman, L. M. Boxt, M. J. Budoff, V. Cheng, T. DeFrance, J. C. Hellinger, and R. P. Karlsberg, "SCCT guidelines for the interpretation and reporting of coronary computed tomographic angiography," *J Cardiovasc Comput Tomogr*, vol. 3, no. 2, pp. 122–136, 2009.

[49] A. Etienne, R. M. Botnar, A. M. C. Van Muiswinkel, P. Boesiger, W. J. Manning, and M. Stuber, ""Soap-Bubble" visualization and quantitative analysis of 3D coronary magnetic resonance angiograms." *Magn Reson Med*, vol. 48, no. 4, pp. 658–66, 2002.

[50] M. D. Cerqueira, N. J. Weissman, V. Dilsizian, A. K. Jacobs, S. Kaul, W. K. Laskey, D. J. Pennell, J. a. Rumberger, T. J. Ryan, and M. S. Verani, "Standardized Myocardial Segmentation and Nomenclature for Tomographic Imaging of the Heart," *Circulation*, vol. 105, no. 4, pp. 539–542, 2002.

[51] V. Dilsizian, S. L. Bacharach, R. S. Beanlands, S. R. Bergmann, D. Delbeke, S. Dorbala, R. J. Gropler, J. Knuuti, H. R. Schelbert, and M. I. Travin, "ASNC imaging guidelines/SNMMI procedure standard for positron emission tomography (PET) nuclear cardiology procedures," *J Nucl Cardiol*, vol. 23, no. 5, pp. 1187–1226, 2016.

[52] Z. P. Liang and P. C. Lauterbur, *Principles of Magnetic Resonance Imaging: A Signal Processing Perspective*, ser. IEEE Press Series in Biomedical Engineering. SPIE Optical Engineering Press, 1999.

[53] M. Lustig, S. J. Kim, and J. M. Pauly, "A fast method for designing time-optimal gradient waveforms for arbitrary k-space trajectories," *IEEE Trans Med Imaging*, vol. 27, no. 6, pp. 866–873, 2008.

[54] F. von Knobelsdorff-Brenkenhoff and J. Schulz-Menger, "Role of cardiovascular magnetic resonance in the guidelines of the European Society of Cardiology," *J Cardiovasc Magn Reson*, vol. 18, no. 1, p. 6, 2016.

[55] F. von Knobelsdorff-Brenkenhoff, G. Pilz, and J. Schulz-Menger, "Representation of cardiovascular magnetic resonance in the AHA/ACC guidelines," *J Cardiovasc Magn Reson*, vol. 19, no. 1, p. 70, 2017.

[56] D. J. Pennell, "Cardiovascular magnetic resonance," *Circulation*, vol. 121, no. 5, pp. 692–705, 2010.

[57] W. G. Hundley, D. A. Bluemke, J. P. Finn, S. D. Flamm, M. A. Fogel, M. G. Friedrich, V. B. Ho, M. Jerosch-Herold, C. M. Kramer, W. J. Manning, M. Patel, G. M. Pohost, A. E. Stillman, R. D. White, and P. K. Woodard, "ACCF/ACR/AHA/NASCI/SCMR 2010 Expert Consensus Document on Cardiovascular Magnetic Resonance," *J Am Coll Cardiol*, vol. 55, no. 23, pp. 2614–2662, 2010.

[58] J. T. Dodge, B. G. Brown, E. L. Bolson, and H. T. Dodge, "Lumen diameter of normal human coronary arteries. Influence of age, sex, anatomic variation, and left ventricular hypertrophy or dilation." *Circulation*, vol. 86, no. 1, pp. 232–246, 1992.

[59] C. M. Kramer, J. Barkhausen, S. D. Flamm, R. J. Kim, and E. Nagel, "Standardized cardiovascular magnetic resonance (CMR) protocols 2013 update," *J Cardiovasc Magn Reson*, vol. 15, no. 1, p. 91, 2013.

[60] M. Stuber and R. G. Weiss, "Coronary magnetic resonance angiography." *J Magn Reson Imaging*, vol. 26, no. 2, pp. 219–34, 2007.

[61] C. Jahnke, I. Paetsch, S. Achenbach, B. Schnackenburg, R. Gebker, E. Fleck, and E. Nagel, "Coronary MR Imaging: Breath-hold Capability and Patterns, Coronary Artery Rest Periods, and β-Blocker Use," *Radiology*, vol. 239, no. 1, pp. 71–78, 2006.

[62] A. M. Gharib, D. A. Herzka, A. O. Ustun, M. Y. Desai, J. Locklin, R. I. Pettigrew, and M. Stuber, "Coronary MR angiography at 3T during diastole and systole," *J Magn Reson Imaging*, vol. 26, no. 4, pp. 921–926, 2007.

[63] G. F. Greil, A. Seeger, S. Miller, C. D. Claussen, M. Hofbeck, R. M. Botnar, and L. Sieverding, "Coronary magnetic resonance angiography and vessel wall

imaging in children with Kawasaki disease," *Pediatr Radiol*, vol. 37, no. 7, pp. 666–673, 2007.

[64] T. Tangcharoen, A. Bell, S. Hegde, T. Hussain, P. Beerbaum, T. Schaeffter, R. Razavi, R. M. Botnar, and G. F. Greil, "Detection of coronary artery anomalies in infants and young children with congenital heart disease by using MR imaging," *Radiology*, vol. 259, no. 1, pp. 240–247, 2011.

[65] C. Prieto, M. R. Makowski, W. Y. Kim, W. J. Manning, and R. M. Botnar, "Cardiac MR Angiography," in *Protocols and Methodologies in Basic Science and Clinical Cardiac MRI*. Cham: Springer International Publishing, 2018, pp. 399–432.

[66] S. Coppo, D. Piccini, G. Bonanno, J. Chaptinel, G. Vincenti, H. Feliciano, R. B. Van Heeswijk, J. Schwitter, and M. Stuber, "Free-running 4D whole-heart self-navigated golden angle MRI: Initial results," *Magn Reson Med*, vol. 74, no. 5, pp. 1306–1316, 2015.

[67] J. Pang, Y. Chen, Z. Fan, C. Nguyen, Q. Yang, Y. Xie, and D. Li, "High efficiency coronary MR angiography with nonrigid cardiac motion correction," *Magn Reson Med*, vol. 76, no. 5, pp. 1345–1353, 2016.

[68] D. Firmin and J. Keegan, "Navigator echoes in cardiac magnetic resonance," *J Cardiovasc Magn Reson*, vol. 3, no. 3, pp. 183–193, 2001.

[69] R. L. Ehman and J. P. Felmlee, "Adaptive technique for high-definition MR imaging of moving structures." *Radiology*, vol. 173, no. 1, pp. 255–263, 1989.

[70] P. G. Danias, M. V. McConnell, V. C. Khasgiwala, M. L. Chuang, R. R. Edelman, and W. J. Manning, "Prospective navigator correction of image position for coronary MR angiography." *Radiology*, vol. 203, no. 3, pp. 733–736, 1997.

[71] K. Nehrke, P. Bornert, J. Groen, J. Smink, and J. C. Bock, "On the performance and accuracy of 2D navigator pulses," *Magn Reson Imaging*, vol. 17, no. 8, pp. 1173–1181, 1999.

[72] A. M. Taylor, J. Keegan, P. Jhooti, D. N. Firmin, and D. J. Pennell, "Calculation of a Subject-Specific Adaptive Motion-Correction Factor for Improved Real-Time Navigator Echo-Gated Magnetic Resonance Coronary Angiography," *J Cardiovasc Magn Reson*, vol. 1, no. 2, pp. 131–138, 1999.

[73] M. H. Moghari, P. Hu, K. V. Kissinger, B. Goddu, L. Goepfert, L. Ngo, W. J. Manning, and R. Nezafat, "Subject-specific estimation of respiratory navigator tracking factor for free-breathing cardiovascular MR," *Magn Reson Med*, vol. 67, no. 6, pp. 1665–1672, 2012.

[74] M. Buehrer, J. Curcic, P. Boesiger, and S. Kozerke, "Prospective self-gating for simultaneous compensation of cardiac and respiratory motion," *Magn Reson Med*, vol. 60, no. 3, pp. 683–690, 2008.

[75] P. Lai, X. Bi, R. Jerecic, and D. Li, "A respiratory self-gating technique with 3D-translation compensation for free-breathing whole-heart coronary MRA," *Magn Reson Med*, vol. 62, no. 3, pp. 731–738, 2009.

[76] D. Piccini, A. Littmann, S. Nielles-Vallespin, and M. O. Zenge, "Respiratory self-navigation for whole-heart bright-blood coronary MRI: Methods for robust isolation and automatic segmentation of the blood pool," *Magn Reson Med*, vol. 68, no. 2, pp. 571–579, 2012.

[77] C. Stehning, P. Börnert, K. Nehrke, H. Eggers, and M. Stuber, "Free-breathing whole-heart coronary MRA with 3D radial SSFP and self-navigated image reconstruction," *Magn Reson Med*, vol. 54, no. 2, pp. 476–480, 2005.

[78] M. Henningsson, P. Koken, C. Stehning, R. Razavi, C. Prieto, and R. M. Botnar, "Whole-heart coronary MR angiography with 2D self-navigated image reconstruction." *Magn Reson Med*, vol. 67, no. 2w, pp. 437–45, 2012.

[79] M. Henningsson, J. Smink, R. Razavi, and R. M. Botnar, "Prospective respiratory motion correction for coronary MR angiography using a 2D image navigator," *Magn Reson Med*, vol. 69, no. 2, pp. 486–494, 2013.

[80] H. H. Wu, P. T. Gurney, B. S. Hu, D. G. Nishimura, and M. V. McConnell, "Free-breathing multiphase whole-heart coronary MR angiography

using image-based navigators and three-dimensional cones imaging," *Magn Reson Med*, vol. 69, no. 4, pp. 1083–1093, 2013.

[81] K. Kawaji, P. Spincemaille, T. D. Nguyen, N. Thimmappa, M. A. Cooper, M. R. Prince, and Y. Wang, "Direct coronary motion extraction from a 2D fat image navigator for prospectively gated coronary MR angiography," *Magn Reson Med*, vol. 71, no. 2, pp. 599–607, 2014.

[82] J. Keegan, P. D. Gatehouse, G. Z. Yang, and D. N. Firmin, "Non-model-based correction of respiratory motion using beat-to-beat 3D spiral fat-selective imaging," *J Magn Reson Imaging*, vol. 26, no. 3, pp. 624–629, 2007.

[83] A. D. Scott, J. Keegan, and D. N. Firmin, "Beat-to-beat respiratory motion correction with near 100% efficiency: A quantitative assessment using high-resolution coronary artery imaging," *Magn Reson Imaging*, vol. 29, no. 4, pp. 568–578, 2011.

[84] M. H. Moghari, S. Roujol, M. Henningsson, K. V. Kissinger, D. Annese, R. Nezafat, W. J. Manning, T. Geva, and A. J. Powell, "Three-dimensional heart locator for whole-heart coronary magnetic resonance angiography," *Magn Reson Med*, vol. 71, no. 6, pp. 2118–2126, 2014.

[85] M. H. Moghari, D. Annese, T. Geva, and A. J. Powell, "Three-dimensional heart locator and compressed sensing for whole-heart MR angiography," *Magn Reson Med*, vol. 75, no. 5, pp. 2086–2093, 2016.

[86] N. O. Addy, R. R. Ingle, J. Luo, C. A. Baron, P. C. Yang, B. S. Hu, and D. G. Nishimura, "3D Image-Based Navigators for Coronary MR Angiography," *Magn Reson Med*, vol. 77, no. 5, pp. 1874–1883, 2017.

[87] J. Luo, N. O. Addy, R. R. Ingle, C. A. Baron, J. Y. Cheng, B. S. Hu, and D. G. Nishimura, "Nonrigid Motion Correction With 3D Image-Based Navigators for Coronary MR Angiography," *Magn Reson Med*, vol. 77, no. 5, pp. 1884–1893, 2017.

[88] D. Li, R. P. Dolan, R. C. Walovitch, and R. B. Lauffer, "Three-dimensional MRI of coronary arteries using an intravascular contrast agent," *Magn Reson Med*, vol. 39, no. 6, pp. 1014–1018, 1998.

[89] M. Stuber, R. M. Botnar, P. G. Danias, M. V. McConnell, K. V. Kissinger, E. K. Yucel, and W. J. Manning, "Contrast agent-enhanced, free-breathing, three-dimensional coronary magnetic resonance angiography," *J Magn Reson Imaging*, vol. 10, no. 5, pp. 790–799, 1999.

[90] J. H. Brittain, B. S. Hu, G. A. Wright, C. H. Meyer, A. Macovski, and D. G. Nishimura, "Coronary Angiography with Magnetization-Prepared T2 Contrast," *Magn Reson Med*, vol. 33, no. 5, pp. 689–696, 1995.

[91] R. M. Botnar, M. Stuber, P. G. Danias, K. V. Kissinger, and W. J. Manning, "Improved coronary artery definition with T2-weighted, free-breathing, three-dimensional coronary MRA," *Circulation*, vol. 99, no. 24, pp. 3139–3148, 1999.

[92] R. Nezafat, M. Stuber, R. Ouwerkerk, A. M. Gharib, M. Y. Desai, and R. I. Pettigrew, "B1-Insensitive T2 preparation for improved coronary magnetic resonance angiography at 3 T," *Magn Reson Med*, vol. 55, no. 4, pp. 858–864, 2006.

[93] A. J. Coristine, R. B. van Heeswijk, and M. Stuber, "Fat signal suppression for coronary MRA at 3T using a water-selective adiabatic T2 -preparation technique," *Magn Reson Med*, vol. 72, no. 3, pp. 763–769, 2014.

[94] D. Li, C. Paschal, M. E. Haacke, and L. P. Adler, "Coronary Arteries: Three-dimensional MR Imaging with Fat Saturation and Magnetization Transfer Contrast," *Radiology*, vol. 187, no. 2, pp. 401–406, 1993.

[95] P. Börnert, M. Stuber, R. M. Botnar, K. V. Kissinger, and W. J. Manning, "Comparison of fat suppression strategies in 3D spiral coronary magnetic resonance angiography," *J Magn Reson Imaging*, vol. 15, no. 4, pp. 462–466, 2002.

[96] O. Dietrich, M. F. Reiser, and S. O. Schoenberg, "Artifacts in 3-T MRI: Physical background and reduction strategies," *Eur J Radiol*, vol. 65, no. 1, pp. 29–35, 2008.

[97] M. Stuber, R. M. Botnar, S. E. Fischer, R. Lamerichs, J. Smink, P. Harvey, and W. J. Manning, "Preliminary report on in vivo coronary MRA at 3 Tesla in humans," *Magn Reson Med*, vol. 48, no. 3, pp. 425–429, 2002.

[98] T. Sommer, M. Hackenbroch, U. Hofer, A. Schmiedel, W. A. Willinek, S. Flacke, J. Gieseke, F. Träber, R. Fimmers, H. Litt, and H. Schild, "Coronary MR angiography at 3.0 T versus that at 1.5 T: initial results in patients suspected of having coronary artery disease," *Radiology*, vol. 234, no. 3, pp. 718–25, 2005.

[99] W. T. Dixon, "Simple proton spectroscopic imaging." *Radiology*, vol. 153, no. 1, pp. 189–194, 1984.

[100] G. H. Glover and E. Schneider, "Three-point dixon technique for true water/fat decomposition with B0 inhomogeneity correction," *Magn Reson Med*, vol. 18, no. 2, pp. 371–383, 1991.

[101] G. H. Glover, "Multipoint dixon technique for water and fat proton and susceptibility imaging," *J Magn Reson Imaging*, vol. 1, no. 5, pp. 521–530, 1991.

[102] J. Ma, "Breath-hold water and fat imaging using a dual-echo two-point dixon technique with an efficient and robust phase-correction algorithm," *Magn Reson Med*, vol. 52, no. 2, pp. 415–419, 2004.

[103] J. Liu, D. C. Peters, and M. Drangova, "Method of B0 mapping with magnitude-based correction for bipolar two-point Dixon cardiac MRI," *Magn Reson Med*, vol. 78, no. 5, pp. 1862–1869, 2017.

[104] H. Eggers, B. Brendel, A. Duijndam, and G. Herigault, "Dual-echo Dixon imaging with flexible choice of echo times," *Magn Reson Med*, vol. 65, no. 1, pp. 96–107, 2011.

[105] P. Börnert, P. Koken, K. Nehrke, H. Eggers, and P. Ostendorf, "Water/fat-resolved whole-heart Dixon coronary MRA: An initial comparison," *Magn Reson Med*, vol. 71, no. 1, pp. 156–163, 2014.

[106] M. Nezafat, M. Henningsson, D. P. Ripley, N. Dedieu, G. Greil, J. P. Greenwood, P. Börnert, S. Plein, and R. M. Botnar, "Coronary MR angiography at 3T: fat suppression versus water-fat separation," *Magn Reson Mater Physics, Biol Med*, vol. 29, no. 5, pp. 733–738, 2016.

[107] S. R. Cherry, J. A. Sorenson, and M. E. Phelps, *Physics in Nuclear Medicine*. Elsevier Health Sciences, 2012.

[108] O. Bertolli, A. Eleftheriou, M. Cecchetti, N. Camarlinghi, N. Belcari, and C. Tsoumpas, "PET iterative reconstruction incorporating an efficient positron range correction method," *Phys Medica*, vol. 32, no. 2, pp. 323–330, 2016.

[109] I. Polycarpou, G. Soultanidis, and C. Tsoumpas, "Synthesis of Realistic Simultaneous Positron Emission Tomography and Magnetic Resonance Imaging Data," *IEEE Trans Med Imaging*, vol. 37, no. 3, pp. 703–711, 2018.

[110] S. E. Derenzo, "Mathematical removal of positron range blurring in high resolution tomography," *IEEE Trans Nucl Sci*, vol. 33, no. 1, pp. 565–569, 1986.

[111] C. S. Levin and E. J. Hoffman, "Calculation of positron range and its effect on the fundamental limit of positron emission tomography system spatial resolution," *Phys Med Biol*, vol. 44, no. 3, pp. 781–799, 1999.

[112] H. Zaidi and K. F. Koral, "Scatter modelling and compensation in emission tomography," *Eur J Nucl Med Mol Imaging*, vol. 31, no. 5, pp. 761–782, 2004.

[113] H. Zaidi and M. L. Montandon, "Scatter Compensation Techniques in PET," *PET Clin*, vol. 2, no. 2, pp. 219–234, 2007.

[114] P. E. Kinahan, D. W. Townsend, T. Beyer, and D. Sashin, "Attenuation correction for a combined 3D PET/CT scanner," *Med Phys*, vol. 25, no. 10, p. 2046, 1998.

[115] J. P. J. Carney, D. W. Townsend, V. Rappoport, and B. Bendriem, "Method for transforming CT images for attenuation correction in PET/CT imaging," *Med Phys*, vol. 33, no. 4, pp. 976 – 983, 2006.

[116] D. Izquierdo-Garcia and C. Catana, "MR Imaging-Guided Attenuation Correction of PET Data in PET/MR Imaging," pp. 129–149, 2016.

[117] A. Martinez-Möller, M. Souvatzoglou, G. Delso, R. A. Bundschuh, C. Chefd'hotel, S. I. Ziegler, N. Navab, M. Schwaiger, and S. G. Nekolla, "Tissue classification as a potential approach for attenuation correction in whole-body PET/MRI: evaluation with PET/CT data." *J Nucl Med*, vol. 50, no. 4, pp. 520–6, 2009.

[118] J. A. Zach, J. D. Newell, J. Schroeder, J. R. Murphy, D. Curran-Everett, E. A. Hoffman, P. M. Westgate, M. K. Han, E. K. Silverman, J. D. Crapo, and D. A. Lynch, "Quantitative computed tomography of the lungs and airways in healthy nonsmoking adults," *Invest Radiol*, vol. 47, no. 10, pp. 596–602, 2012.

[119] B. F. Holman, V. Cuplov, B. F. Hutton, A. M. Groves, and K. Thielemans, "The effect of respiratory induced density variations on non-TOF PET quantitation in the lung," *Phys Med Biol*, vol. 61, no. 8, pp. 3148–3163, 2016.

[120] I. Rauscher, M. Eiber, S. Furst, M. Souvatzoglou, S. G. Nekolla, S. I. Ziegler, E. J. Rummeny, M. Schwaiger, and A. J. Beer, "PET/MR Imaging in the Detection and Characterization of Pulmonary Lesions: Technical and Diagnostic Evaluation in Comparison to PET/CT," *J Nucl Med*, vol. 55, no. 5, pp. 724–729, 2014.

[121] H. R. Marshall, F. S. Prato, L. Deans, J. Theberge, R. T. Thompson, and R. Z. Stodilka, "Variable Lung Density Consideration in Attenuation Correction of Whole-Body PET/MRI," *J Nucl Med*, vol. 53, no. 6, pp. 977–984, 2012.

[122] J. M. Lau, R. Laforest, H. Sotoudeh, X. Nie, S. Sharma, J. McConathy, E. Novak, A. Priatna, R. J. Gropler, and P. K. Woodard, "Evaluation of attenuation correction in cardiac PET using PET/MR," *J Nucl Cardiol*, vol. 24, no. 3, pp. 839–846, 2017.

[123] J. O'Doherty and P. Schleyer, "Effect of MR contrast agent on quantitative PET during simultaneous PET-MR imaging in cardiology," *Phys Medica*, vol. 32, no. 7, p. 949, 2016.

[124] V. Ruhlmann, P. Heusch, H. Kühl, K. Beiderwellen, G. Antoch, M. Forsting, A. Bockisch, C. Buchbender, and H. H. Quick, "Potential influence of Gadolinium contrast on image segmentation in MR-based attenuation correction with Dixon sequences in whole-body 18F-FDG PET/MR," *Magn Reson Mater Physics, Biol Med*, vol. 29, no. 2, pp. 301–308, 2016.

[125] D. Le Guludec, R. Lautamäki, J. Knuuti, J. J. Bax, and F. M. Bengel, "Present and future of clinical cardiovascular PET imaging in Europe - A position statement by the European Council of Nuclear Cardiology (ECNC)," *Eur J Nucl Med Mol Imaging*, vol. 35, no. 9, pp. 1709–1724, 2008.

[126] A. F. L. Schinkel, D. Poldermans, A. Elhendy, and J. J. Bax, "Assessment of myocardial viability in patients with heart failure." *J Nucl Med*, vol. 48, no. 7, pp. 1135–46, 2007.

[127] R. J. Bing, "Cardiac metabolism," *Physiol Rev*, vol. 45, no. 2, pp. 171–213, 1965.

[128] J. Knuuti, H. R. Schelbert, and J. J. Bax, "The need for standardisation of cardiac FDG PET imaging in the evaluation of myocardial viability in patients with chronic ischaemic left ventricular dysfunction," *Eur J Nucl Med Mol Imaging*, vol. 29, no. 9, pp. 1257–1266, 2002.

[129] S. L. Bacharach, J. J. Bax, J. Case, D. Delbeke, K. A. Kurdziel, W. H. Martin, and R. E. Patterson, "PET myocardial glucose metabolism and perfusion imaging: Part 1-Guidelines for data acquisition and patient preparation." *J Nucl Cardiol*, vol. 10, no. 5, pp. 543–556, 2003.

[130] G. Youssef, E. Leung, I. Mylonas, P. Nery, K. Williams, G. Wisenberg, K. Y. Gulenchyn, R. A. DeKemp, J. DaSilva, D. Birnie, G. A. Wells, and R. S. B. Beanlands, "The Use of 18F-FDG PET in the Diagnosis of Cardiac Sarcoidosis: A Systematic Review and Metaanalysis Including the Ontario Experience," *J Nucl Med*, vol. 53, no. 2, pp. 241–248, 2012.

[131] F. Nensa, J. Kloth, E. Tezgah, T. D. Poeppel, P. Heusch, J. Goebel, K. Nassenstein, and T. Schlosser, "Feasibility of FDG-PET in myocarditis: Comparison to CMR using integrated PET/MRI," *J Nucl Cardiol*, pp. 1–10, 2016.

[132] P. M. Robson, D. Dey, D. E. Newby, D. Berman, D. Li, Z. A. Fayad, and M. R. Dweck, "MR/PET Imaging of the Cardiovascular System," *JACC Cardiovasc Imaging*, vol. 10, no. 10, pp. 1165–1179, 2017.

[133] M. C. Huisman, T. Higuchi, S. Reder, S. G. Nekolla, T. Poethko, H.-J. Wester, S. I. Ziegler, D. S. Casebier, S. P. Robinson, and M. Schwaiger, "Initial Characterization of an 18F-Labeled Myocardial Perfusion Tracer," *J Nucl Med*, vol. 49, no. 4, pp. 630–636, 2008.

[134] Y. Fujibayashi, C. S. Cutler, C. J. Anderson, D. W. McCarthy, L. A. Jones, T. Sharp, Y. Yonekura, and M. J. Welch, "Comparative studies of Cu-64-ATSM and C-11-acetate in an acute myocardial infarction model: Ex vivo imaging of hypoxia in rats," *Nucl Med Biol*, vol. 26, no. 1, pp. 117–121, 1999.

[135] M. R. Dweck, M. W. Chow, N. V. Joshi, M. C. Williams, C. Jones, A. M. Fletcher, H. Richardson, A. White, G. McKillop, E. J. Van Beek, N. A. Boon, J. H. Rudd, and D. E. Newby, "Coronary arterial 18F-sodium fluoride uptake: A novel marker of plaque biology," *J Am Coll Cardiol*, vol. 59, no. 17, pp. 1539–1548, 2012.

[136] A. Irkle, A. T. Vesey, D. Y. Lewis, J. N. Skepper, J. L. Bird, M. R. Dweck, F. R. Joshi, F. A. Gallagher, E. A. Warburton, M. R. Bennett, K. M. Brindle, D. E. Newby, J. H. Rudd, and A. P. Davenport, "Identifying active vascular microcalcification by 18F-sodium fluoride positron emission tomography," *Nat Commun*, vol. 6, no. 1, p. 7495, 2015.

[137] M. F. Di Carli, F. Asgarzadie, H. R. Schelbert, R. C. Brunken, H. Laks, M. E. Phelps, and J. Maddahi, "Quantitative Relation Between Myocardial Viability and Improvement in Heart Failure Symptoms After Revascularization in Patients With Ischemic Cardiomyopathy," *Circulation*, vol. 92, no. 12, pp. 3436–3444, 1995.

[138] A. Rahmim, O. Rousset, and H. Zaidi, "Strategies for Motion Tracking and Correction in PET," *PET Clin*, vol. 2, no. 2, pp. 251–266, 2007.

[139] J. Hadamard, "Sur les problèmes aux dérivées partielles et leur signification physique," *Princeton university bulletin*, pp. 49–52, 1902.

[140] H. Jung, K. Sung, K. S. Nayak, E. Y. Kim, and J. C. Ye, "K-t FOCUSS: A general compressed sensing framework for high resolution dynamic MRI," *Magn Reson Med*, vol. 61, no. 1, pp. 103–116, 2009.

[141] R. Otazo, D. Kim, L. Axel, and D. K. Sodickson, "Combination of compressed sensing and parallel imaging for highly accelerated first-pass cardiac perfusion MRI," *Magn Reson Med*, vol. 64, no. 3, pp. 767–776, 2010.

[142] M. Akçakaya, H. Rayatzadeh, T. A. Basha, S. N. Hong, R. H. Chan, K. V. Kissinger, T. H. Hauser, M. E. Josephson, W. J. Manning, and R. Nezafat, "Accelerated Late Gadolinium Enhancement Cardiac MR Imaging with Isotropic Spatial Resolution Using Compressed Sensing: Initial Experience," *Radiology*, vol. 264, no. 3, pp. 691–699, 2012.

[143] M. Usman, D. Atkinson, F. Odille, C. Kolbitsch, G. Vaillant, T. Schaeffter, P. G. Batchelor, and C. Prieto, "Motion corrected compressed sensing for free-breathing dynamic cardiac MRI," *Magn Reson Med*, vol. 70, no. 2, pp. 504–516, 2013.

[144] L. Feng, L. Axel, H. Chandarana, K. T. Block, D. K. Sodickson, and R. Otazo, "XD-GRASP: Golden-angle radial MRI with reconstruction of extra motion-state dimensions using compressed sensing," *Magn Reson Med*, vol. 75, no. 2, pp. 775–788, 2016.

[145] M. R. Hestenes and E. Stiefel, *Methods of conjugate gradients for solving linear systems*. NBS, 1952, vol. 49.

[146] D. K. Sodickson and W. J. Manning, "Simultaneous acquisition of spatial harmonics (SMASH): Fast imaging with radiofrequency coil arrays," *Magn Reson Med*, vol. 38, no. 4, pp. 591–603, 1997.

[147] K. P. Pruessmann, M. Weiger, M. B. Scheidegger, and P. Boesiger, "SENSE: Sensitivity encoding for fast MRI," *Magn Reson Med*, vol. 42, no. 5, pp. 952–962, 1999.

[148] M. A. Griswold, P. M. Jakob, R. M. Heidemann, M. Nittka, V. Jellus, J. Wang, B. Kiefer, and A. Haase, "Generalized Autocalibrating Partially Parallel Acquisitions (GRAPPA)," *Magn Reson Med*, vol. 47, no. 6, pp. 1202–1210, 2002.

[149] M. A. Griswold, "Basic Reconstruction Algorithms for Parallel Imaging," in *Parallel Imaging Clin MR Appl*, S. O. Schoenberg, O. Dietrich, and M. F. Reiser, Eds. Springer Berlin Heidelberg, 2007, pp. 19–36.

[150] K. P. Pruessmann, M. Weiger, P. Börnert, and P. Boesiger, "Advances in sensitivity encoding with arbitrary k-space trajectories," *Magn Reson Med*, vol. 46, no. 4, pp. 638–651, 2001.

[151] D. O. Walsh, A. F. Gmitro, and M. W. Marcellin, "Adaptive reconstruction of phased array MR imagery," *Magn Reson Med*, vol. 43, no. 5, pp. 682–690, 2000.

[152] M. Uecker, P. Lai, M. J. Murphy, P. Virtue, M. Elad, J. M. Pauly, S. S. Vasanawala, and M. Lustig, "ESPIRiT - An eigenvalue approach to autocalibrating parallel MRI: Where SENSE meets GRAPPA," *Magn Reson Med*, vol. 71, no. 3, pp. 990–1001, 2014.

[153] P. B. Roemer, W. A. Edelstein, C. E. Hayes, S. P. Souza, and O. M. Mueller, "The NMR phased array," *Magn Reson Med*, vol. 16, no. 2, pp. 192–225, 1990.

[154] M. Henningsson, C. Prieto, A. Chiribiri, G. Vaillant, R. Razavi, and R. M. Botnar, "Whole-heart coronary MRA with 3D affine motion correction using 3D image-based navigation," *Magn Reson Med*, vol. 71, no. 1, pp. 173–181, 2014.

[155] C. Prieto, M. Doneva, M. Usman, M. Henningsson, G. Greil, T. Schaeffter, and R. M. Botnar, "Highly efficient respiratory motion compensated free-breathing coronary MRA using golden-step Cartesian acquisition." *J Magn Reson Imaging*, vol. 41, no. 3, pp. 738–46, 2015.

[156] J. Pang, H. Bhat, B. Sharif, Z. Fan, L. E. Thomson, T. Labounty, J. D. Friedman, J. Min, D. S. Berman, and D. Li, "Whole-heart coronary MRA with 100% respiratory gating efficiency: Self-navigated three-dimensional retrospective image-based motion correction (TRIM)," *Magn Reson Med*, vol. 71, no. 1, pp. 67–74, 2014.

[157] A. P. Aitken, M. Henningsson, R. M. Botnar, T. Schaeffter, and C. Prieto, "100% Efficient three-dimensional coronary MR angiography with two-dimensional beat-to-beat translational and bin-to-bin affine motion correction," *Magn Reson Med*, vol. 74, no. 3, pp. 756–64, 2015.

[158] P. G. Batchelor, D. Atkinson, P. Irarrazaval, D. L. G. Hill, J. Hajnal, and D. Larkman, "Matrix description of general motion correction applied to multishot images," *Magn Reson Med*, vol. 54, no. 5, pp. 1273–1280, 2005.

[159] G. Cruz, D. Atkinson, M. Henningsson, R. M. Botnar, and C. Prieto, "Highly efficient nonrigid motion-corrected 3D whole-heart coronary vessel wall imaging," *Magn Reson Med*, vol. 77, no. 5, pp. 1894–1908, 2017.

[160] L. A. Shepp and Y. Vardi, "Maximum Likelihood Reconstruction for Emission Tomography," *IEEE Trans Med Imaging*, vol. 1, no. 2, pp. 113–122, 1982.

[161] H. M. Hudson and R. S. Larkin, "Accelerated image reconstruction using ordered subsets of projection data." *IEEE Trans Med Imaging*, vol. 13, no. 4, pp. 601–9, 1994.

[162] G. Tarantola, F. Zito, and P. Gerundini, "PET Instrumentation and Reconstruction Algorithms in Whole-Body Applications," *J Nucl Med*, vol. 44, no. 5, pp. 756–769, 2003.

[163] J. Ouyang, Q. Li, and G. El Fakhri, "Magnetic resonance-based motion correction for positron emission tomography imaging," *Semin Nucl Med*, vol. 43, no. 1, pp. 60–67, 2013.

[164] Y. Picard and C. J. Thompson, "Motion correction of PET images using multiple acquisition frames." *IEEE Trans Med Imaging*, vol. 16, no. 2, pp. 137–44, 1997.

[165] R. Grimm, S. Fürst, M. Souvatzoglou, C. Forman, J. M. Hutter, I. Dregely, S. I. Ziegler, B. Kiefer, J. Hornegger, T. Block, and S. G. Nekolla, "Self-gated MRI motion modeling for respiratory motion compensation in integrated PET/MRI." *Med Image Anal*, vol. 19, no. 1, pp. 110–120, 2014.

[166] F. Qiao, T. Pan, J. W. Clark, and O. R. Mawlawi, "A motion-incorporated reconstruction method for gated PET studies." *Phys Med Biol*, vol. 51, no. 15, pp. 3769–83, 2006.

[167] Y. Petibon, G. El Fakhri, R. Nezafat, N. Johnson, T. J. Brady, and J. Ouyang, "Towards coronary plaque imaging using simultaneous PET-MR: a simulation study." *Phys Med Biol*, vol. 59, no. 5, pp. 1203–22, 2014.

[168] N. Dikaios, D. Izquierdo-Garcia, M. J. Graves, V. Mani, Z. A. Fayad, and T. D. Fryer, "MRI-based motion correction of thoracic PET: initial comparison of acquisition protocols and correction strategies suitable for simultaneous PET/MRI systems." *Eur Radiol*, vol. 22, no. 2, pp. 439–46, 2012.

[169] I. Polycarpou, C. Tsoumpas, and P. K. Marsden, "Analysis and comparison of two methods for motion correction in PET imaging," *Med Phys*, vol. 39, no. 10, pp. 6474–6483, 2012.

[170] C. Tsoumpas, S. Agarwal, P. K. Marsden, and A. P. King, "Evaluation of two PET motion correction techniques for simultaneous real-time PET-MR acquisitions using an MR-derived motion model," in *IEEE Nucl Sci Symp Conf Rec*. IEEE, 2012, pp. 2519–2522.

[171] C. Tsoumpas, I. Polycarpou, K. Thielemans, C. Buerger, A. P. King, T. Schaeffter, and P. K. Marsden, "The effect of regularization in motion compensated PET image reconstruction: a realistic numerical 4D simulation study." *Phys Med Biol*, vol. 58, no. 6, pp. 1759–73, 2013.

[172] K. P. Kunze, S. G. Nekolla, C. Rischpler, S. H. Zhang, C. Hayes, N. Langwieser, T. Ibrahim, K.-L. Laugwitz, and M. Schwaiger, "Myocardial perfusion quantification using simultaneously acquired 13NH3-ammonia PET and dynamic contrast-enhanced MRI in patients at rest and stress," *Magn Reson Med*, 2018.

[173] Y. Petibon, N. J. Guehl, T. G. Reese, B. Ebrahimi, M. D. Normandin, T. M. Shoup, N. M. Alpert, G. El Fakhri, and J. Ouyang, "Impact of motion and partial volume effects correction on PET myocardial perfusion imaging using simultaneous PET-MR," *Phys Med Biol*, vol. 62, no. 2, pp. 326–343, 2017.

[174] P. M. Robson, M. R. Dweck, M. G. Trivieri, R. Abgral, N. A. Karakatsanis, J. Contreras, U. Gidwani, J. P. Narula, V. Fuster, J. C. Kovacic, and Z. A. Fayad, "Coronary Artery PET/MR Imaging: Feasibility, Limitations, and Solutions," *JACC Cardiovasc Imaging*, vol. 10, no. 10, pp. 1103–1112, 2017.

[175] Y. Xie, Y. J. Kim, J. Pang, J. S. Kim, Q. Yang, J. Wei, C. T. Nguyen, Z. Deng, B. W. Choi, Z. Fan, C. N. Bairey Merz, P. K. Shah, D. S. Berman, H. J. Chang, and D. Li, "Coronary Atherosclerosis T1-Weighed Characterization With Integrated Anatomical Reference: Comparison With High-Risk Plaque Features Detected by Invasive Coronary Imaging," *JACC Cardiovasc Imaging*, vol. 10, no. 6, pp. 637–648, 2017.

[176] G. Ginami, R. Neji, A. Phinikaridou, J. Whitaker, R. M. Botnar, and C. Prieto, "Simultaneous bright- and black-blood whole-heart MRI for noncontrast enhanced coronary lumen and thrombus visualization," *Magn Reson Med*, vol. 79, no. 3, pp. 1460–1472, 2018.

[177] O. Ratib and R. Nkoulou, "Potential Applications of PET/MR Imaging in Cardiology." *J Nucl Med*, vol. 55, no. Supplement 2, pp. 40S–46S, 2014.

[178] F. Nensa, T. Poeppel, E. Tezgah, P. Heusch, K. Nassenstein, A. A. Mahabadi, M. Forsting, A. Bockisch, R. Erbel, G. Heusch, and T. Schlosser, "Integrated FDG PET/MR Imaging for the Assessment of Myocardial Salvage in Reperfused Acute Myocardial Infarction," *Radiology*, vol. 276, no. 2, pp. 400–407, 2015.

[179] H. Bulluck, S. K. White, G. M. Fröhlich, S. G. Casson, C. O'Meara, A. Newton, J. Nicholas, P. Weale, S. M. Wan, A. Sirker, J. C. Moon, D. M. Yellon, A. Groves, L. Menezes, and D. J. Hausenloy, "Quantifying the Area at Risk in Reperfused ST-Segment-Elevation Myocardial Infarction Patients Using Hy-

brid Cardiac Positron Emission Tomography-Magnetic Resonance Imaging," *Circ Cardiovasc Imaging*, vol. 9, no. 3, p. e003900, 2016.

[180] C. Rischpler, N. Langwieser, M. Souvatzoglou, A. Batrice, S. van Marwick, J. Snajberk, T. Ibrahim, K.-L. Laugwitz, S. G. Nekolla, and M. Schwaiger, "PET/MRI early after myocardial infarction: evaluation of viability with late gadolinium enhancement transmurality vs. 18F-FDG uptake," *Eur Hear J - Cardiovasc Imaging*, vol. 16, no. 6, pp. 661–669, 2015.

[181] R. Abgral, M. R. Dweck, M. G. Trivieri, P. M. Robson, N. Karakatsanis, V. Mani, M. Padilla, M. Miller, A. Lala, J. Sanz, J. Narula, V. Fuster, J. Contreras, J. C. Kovacic, and Z. A. Fayad, "Clinical Utility of Combined FDG-PET/MR to Assess Myocardial Disease," *JACC Cardiovasc Imaging*, vol. 10, no. 5, pp. 594–597, 2017.

[182] S. Schneider, A. Batrice, C. Rischpler, M. Eiber, T. Ibrahim, and S. G. Nekolla, "Utility of multimodal cardiac imaging with PET/MRI in cardiac sarcoidosis: Implications for diagnosis, monitoring and treatment," *Eur Heart J*, vol. 35, no. 5, p. 312, 2014.

[183] K. Wada, T. Niitsuma, T. Yamaki, A. Masuda, H. Ito, H. Kubo, T. Hara, S. Takenoshita, and Y. Takeishi, "Simultaneous cardiac imaging to detect inflammation and scar tissue with 18F-fluorodeoxyglucose PET/MRI in cardiac sarcoidosis," *J Nucl Cardiol*, vol. 23, no. 5, pp. 1180–1182, 2016.

[184] M. R. Dweck, R. Abgral, M. G. Trivieri, P. M. Robson, N. Karakatsanis, V. Mani, A. Palmisano, M. A. Miller, A. Lala, H. L. Chang, J. Sanz, J. Contreras, J. Narula, V. Fuster, M. Padilla, Z. A. Fayad, and J. C. Kovacic, "Hybrid Magnetic Resonance Imaging and Positron Emission Tomography With Fluorodeoxyglucose to Diagnose Active Cardiac Sarcoidosis," *JACC Cardiovasc Imaging*, vol. 11, no. 1, pp. 94–107, 2017.

[185] J. Tang, N. Hall, and A. Rahmim, "MRI assisted motion correction in dual-gated 5D myocardial perfusion PET imaging," in *2012 IEEE Nucl Sci Symp Med Imaging Conf Rec.* IEEE, 2012, pp. 4054–4057.

[186] C. Buerger, C. Tsoumpas, A. P. Aitken, A. P. King, P. J. Schleyer, V. Schulz, P. K. Marsden, and T. Schaeffter, "Investigation of MR-Based Attenuation Correction and Motion Compensation for Hybrid PET/MR," *IEEE Trans Nucl Sci*, vol. 59, no. 5, pp. 1967–1976, 2012.

[187] A. P. King, C. Buerger, C. Tsoumpas, P. K. Marsden, and T. Schaeffter, "Thoracic respiratory motion estimation from MRI using a statistical model and a 2-D image navigator." *Med Image Anal*, vol. 16, no. 1, pp. 252–64, 2012.

[188] I. Polycarpou, C. Tsoumpas, A. P. King, and P. K. Marsden, "Impact of respiratory motion correction and spatial resolution on lesion detection in PET: a simulation study based on real MR dynamic data." *Phys Med Biol*, vol. 59, no. 3, pp. 697–713, 2014.

[189] H. Fayad, F. Odille, H. Schmidt, C. Würslin, T. Küstner, J. Feblinger, and D. Visvikis, "The use of a generalized reconstruction by inversion of coupled systems (GRICS) approach for generic respiratory motion correction in PET/MR imaging," *Phys Med Biol*, vol. 60, no. 6, pp. 2529–2546, 2015.

[190] B. Guerin, S. Cho, S. Y. Chun, X. Zhu, N. M. Alpert, G. El Fakhri, T. G. Reese, and C. Catana, "Nonrigid PET motion compensation in the lower abdomen using simultaneous tagged-MRI and PET imaging." *Med Phys*, vol. 38, no. 6, pp. 3025–3038, 2011.

[191] M. Fieseler, H. Kugel, F. Gigengack, T. Kosters, F. Buther, H. H. Quick, C. Faber, X. Jiang, and K. P. Schafers, "A dynamic thorax phantom for the assessment of cardiac and respiratory motion correction in PET/MRI: A preliminary evaluation," *Nucl Instruments Methods Phys Res Sect A Accel Spectrometers, Detect Assoc Equip*, vol. 702, pp. 59–63, 2012.

[192] Y. Petibon, J. Ouyang, X. Zhu, C. Huang, T. G. Reese, S. Y. Chun, Q. Li, and G. El Fakhri, "Cardiac motion compensation and resolution modeling in simultaneous PET-MR: a cardiac lesion detection study." *Phys Med Biol*, vol. 58, no. 7, pp. 2085–102, 2013.

[193] C. Huang, Y. Petibon, J. Ouyang, T. G. Reese, M. A. Ahlman, D. A. Bluemke, and G. El Fakhri, "Accelerated acquisition of tagged MRI for cardiac mo-

tion correction in simultaneous PET-MR: Phantom and patient studies," *Med Phys*, vol. 42, no. 2, pp. 1087–1097, 2015.

[194] C. Würslin, H. Schmidt, P. Martirosian, C. Brendle, A. Boss, N. F. Schwenzer, and L. Stegger, "Respiratory motion correction in oncologic PET using T1-weighted MR imaging on a simultaneous whole-body PET/MR system." *J Nucl Med*, vol. 54, no. 3, pp. 464–71, 2013.

[195] Y. Petibon, C. Huang, J. Ouyang, T. G. Reese, Q. Li, A. Syrkina, Y.-L. Chen, and G. El Fakhri, "Relative role of motion and PSF compensation in whole-body oncologic PET-MR imaging." *Med Phys*, vol. 41, no. 4, p. 042503, 2014.

[196] S. Fürst, R. Grimm, I. Hong, M. Souvatzoglou, M. E. Casey, M. Schwaiger, S. G. Nekolla, and S. I. Ziegler, "Motion Correction Strategies for Integrated PET/MR," *J Nucl Med*, vol. 56, pp. 261–269, 2015.

[197] R. Manber, K. Thielemans, B. Hutton, A. Barnes, S. Ourselin, S. Arridge, C. O'Meara, M. Y. S. Wan, and D. Atkinson, "Practical PET Respiratory Motion Correction in Clinical PET/MR," *J Nucl Med*, vol. 56, no. 6, pp. 890–896, 2015.

[198] H. Wang and A. A. Amini, "Cardiac motion and deformation recovery from MRI: a review." *IEEE Trans Med Imaging*, vol. 31, no. 2, pp. 487–503, 2012.

[199] L. Axel and L. Dougherty, "MR imaging of motion with spatial modulation of magnetization." *Radiology*, vol. 171, no. 3, pp. 841–845, 1989.

[200] A. K. Rutz, S. Ryf, S. Plein, P. Boesiger, and S. Kozerke, "Accelerated whole-heart 3D CSPAMM for myocardial motion quantification." *Magn Reson Med*, vol. 59, no. 4, pp. 755–63, 2008.

[201] J. R. McClelland, D. J. Hawkes, T. Schaeffter, and A. P. King, "Respiratory motion models: a review." *Med Image Anal*, vol. 17, no. 1, pp. 19–42, 2013.

[202] A. P. King, C. Tsoumpas, C. Buerger, V. Schulz, P. K. Marsden, and T. Schaeffter, "Real-time respiratory motion correction for simultaneous PET-MR

using an MR-derived motion model," *2011 IEEE Nucl Sci Symp Conf Rec*, pp. 3589–3594, 2011.

[203] I. Polycarpou, C. Tsoumpas, and P. K. Marsden, "Statistical evaluation of PET motion correction methods using MR derived motion fields," in *IEEE Nucl Sci Symp Conf Rec*, no. 1, 2012, pp. 3579–3585.

[204] I. Polycarpou, P. K. Marsden, and C. Tsoumpas, "Evaluation of two approaches to motion-corrected PET image reconstruction," *J Phys Conf Ser*, vol. 317, no. 1, p. 012001, 2011.

[205] D. R. Balfour, P. K. Marsden, I. Polycarpou, C. Kolbitsch, and A. P. King, "Respiratory motion correction of PET using MR-constrained PET-PET registration," *Biomed Eng Online*, vol. 14, no. 1, p. 85, 2015.

[206] J. Dutta, G. El Fakhri, C. Huang, Y. Petibon, T. G. Reese, and Q. Li, "Respiratory motion compensation in simultaneous PET/MR using a maximum a posteriori approach," in *2013 IEEE 10th Int Symp Biomed Imaging*. IEEE, 2013, pp. 800–803.

[207] R. Grimm, S. Fürst, I. Dregely, C. Forman, J. M. Hutter, S. I. Ziegler, S. G. Nekolla, B. Kiefer, M. Schwaiger, J. Hornegger, and T. Block, "Self-gated Radial MRI for Respiratory Motion Compensation on Hybrid PET/MR Systems," in *Med Image Comput Comput Interv – MICCAI 2013 SE - 3*, ser. Lecture Notes in Computer Science, K. Mori, I. Sakuma, Y. Sato, C. Barillot, and N. Navab, Eds. Springer Berlin Heidelberg, 2013, vol. 8151, pp. 17–24.

[208] S. Y. Chun, T. G. Reese, J. Ouyang, B. Guerin, C. Catana, X. Zhu, N. M. Alpert, and G. El Fakhri, "MRI-Based Nonrigid Motion Correction in Simultaneous PET/MRI," *J Nucl Med*, vol. 53, no. 8, pp. 1284–1291, 2012.

[209] M. Fieseler, F. Gigengack, X. Jiang, and K. P. Schäfers, "Motion correction of whole-body PET data with a joint PET-MRI registration functional." *Biomed Eng Online*, vol. 13 Suppl 1, no. Suppl 1, p. S2, 2014.

[210] R. Guo, Y. Petibon, Y. Ma, G. El Fakhri, K. Ying, and J. Ouyang, "MR-based motion correction for cardiac PET parametric imaging: a simulation study," *EJNMMI Phys*, vol. 5, no. 1, p. 3, 2018.

[211] T. Küstner, M. Schwartz, P. Martirosian, S. Gatidis, F. Seith, C. Gilliam, T. Blu, H. Fayad, D. Visvikis, F. Schick, B. Yang, H. Schmidt, and N. F. Schwenzer, "MR-based respiratory and cardiac motion correction for PET imaging," *Med Image Anal*, vol. 42, pp. 129–144, 2017.

[212] C. Kolbitsch, M. A. Ahlman, C. Davies-Venn, R. Evers, M. Hansen, D. Peressutti, P. Marsden, P. Kellman, D. A. Bluemke, and T. Schaeffter, "Cardiac and respiratory motion correction for simultaneous cardiac PET-MR," *J Nucl Med*, vol. 58, no. 5, pp. 846–852, 2017.

[213] M. Modat, G. R. Ridgway, Z. A. Taylor, M. Lehmann, J. Barnes, D. J. Hawkes, N. C. Fox, and S. Ourselin, "Fast free-form deformation using graphics processing units," *Comput Methods Programs Biomed*, vol. 98, no. 3, pp. 278–284, 2010.

[214] S. Tong, A. M. Alessio, and P. E. Kinahan, "Noise and signal properties in PSF-based fully 3D PET image reconstruction: an experimental evaluation," *Phys Med Biol*, vol. 55, no. 5, pp. 1453–1473, 2010.

[215] M. A. Bernstein, S. B. Fain, and S. J. Riederer, "Effect of windowing and zero-filled reconstruction of MRI data on spatial resolution and acquisition strategy," *J Magn Reson Imaging*, vol. 14, no. 3, pp. 270–280, 2001.

[216] C. Rischpler, S. G. Nekolla, I. Dregely, and M. Schwaiger, "Hybrid PET/MR imaging of the heart: potential, initial experiences, and future prospects." *J Nucl Med*, vol. 54, no. 3, pp. 402–15, 2013.

[217] C. Rischpler, S. G. Nekolla, K. P. Kunze, and M. Schwaiger, "PET/MRI of the heart," *Semin Nucl Med*, vol. 45, no. 3, pp. 234–247, 2015.

[218] M. Schwaiger, K. Kunze, C. Rischpler, and S. G. Nekolla, "PET/MR: Yet another Tesla?" *J Nucl Cardiol*, vol. 24, no. 3, pp. 1019–1031, 2017.

[219] J. Nuyts, G. Bal, F. Kehren, M. Fenchel, C. Michel, and C. Watson, "Completion of a truncated attenuation image from the attenuated PET emission data," *IEEE Trans Med Imaging*, vol. 32, no. 2, pp. 237–246, 2013.

[220] S. G. Nekolla, C. Miethaner, N. Nguyen, S. I. Ziegler, and M. Schwaiger, "Reproducibility of polar map generation and assessment of defect severity and extent assessment in myocardial perfusion imaging using positron emission tomography," *Eur J Nucl Med*, vol. 25, no. 9, pp. 1313–1321, 1998.

[221] M. L. Lassen, S. Rasul, D. Beitzke, M. E. Stelzmüller, J. Cal-Gonzalez, M. Hacker, and T. Beyer, "Assessment of attenuation correction for myocardial PET imaging using combined PET/MRI," *J Nucl Cardiol*, pp. 1–12, 2017.

[222] G. Ginami, R. Neji, I. Rashid, A. Chiribiri, T. F. Ismail, R. M. Botnar, and C. Prieto, "3D whole-heart phase sensitive inversion recovery CMR for simultaneous black-blood late gadolinium enhancement and bright-blood coronary CMR angiography," *J Cardiovasc Magn Reson*, vol. 19, no. 1, p. 94, 2017.

[223] C. Rischpler, S. G. Nekolla, G. Heusch, L. Umutlu, T. Rassaf, P. Heusch, K. Herrmann, and F. Nensa, "Cardiac PET/MRI—an update," *Eur J Hybrid Imaging*, vol. 3, no. 1, pp. 1–17, 2019.

[224] C. Kolbitsch, C. Prieto, C. Tsoumpas, and T. Schaeffter, "A 3D MR-acquisition scheme for nonrigid bulk motion correction in simultaneous PET-MR," *Med Phys*, vol. 41, no. 8, p. 082304, 2014.

[225] W. P. Segars, G. Sturgeon, S. Mendonca, J. Grimes, and B. M. W. Tsui, "4D XCAT phantom for multimodality imaging research," *Med Phys*, vol. 37, no. 9, p. 4902, 2010.

[226] Y. Wang, E. Chiu, J. Rosenberg, and S. S. Gambhir, "Standardized uptake value atlas: Characterization of physiological 2-Deoxy-2-[18F]fluoro-d-glucose uptake in normal tissues," *Mol Imaging Biol*, vol. 9, no. 2, pp. 83–90, 2007.

[227] K. Thielemans, C. Tsoumpas, S. Mustafovic, T. Beisel, P. Aguiar, N. Dikaios, and M. W. Jacobson, "STIR: software for tomographic image reconstruction release 2," *Phys Med Biol*, vol. 57, no. 4, pp. 867–883, 2012.

[228] E. P. Ficaro, J. A. Fessler, P. D. Shreve, J. N. Kritzman, P. A. Rose, and J. R. Corbett, "Simultaneous Transmission/Emission Myocardial Perfusion Tomography: Diagnostic Accuracy of Attenuation-Corrected 99mTc-Sestamibi Single-Photon Emission Computed Tomography," *Circulation*, vol. 93, no. 3, pp. 463–473, 1996.

[229] J. M. Bland and D. Altman, "Statistical methods for assessing agreement between two methods of clinical measurement," *The lancet*, vol. 327, no. 8476, pp. 307–310, 1986.

[230] S. Uribe, T. Tangchaoren, V. Parish, I. Wolf, R. Razavi, G. Greil, and T. Schaeffter, "Volumetric cardiac quantification by using 3D dual-phase whole-heart MR imaging," *Radiology*, vol. 248, no. 2, pp. 606–614, 2008.

[231] H. J. Yang, B. Sharif, J. Pang, A. Kali, X. Bi, I. Cokic, D. Li, and R. Dharmakumar, "Free-breathing, motion-corrected, highly efficient whole heart T2 mapping at 3T with hybrid radial-cartesian trajectory," *Magn Reson Med*, vol. 75, no. 1, pp. 126–136, 2016.

[232] D. Dey, R. Nakazato, D. Li, and D. S. Berman, "Epicardial and thoracic fat - Noninvasive measurement and clinical implications." *Cardiovasc Diagn Ther*, vol. 2, no. 2, pp. 85–93, 2012.

[233] G. Iacobellis, D. Pistilli, M. Gucciardo, F. Leonetti, F. Miraldi, G. Brancaccio, P. Gallo, and C. R. Tiziana Di Gioia, "Adiponectin expression in human epicardial adipose tissue in vivo is lower in patients with coronary artery disease," *Cytokine*, vol. 29, no. 6, pp. 251–255, 2005.

[234] H. S. Yong, E. J. Kim, H. S. Seo, E.-Y. Kang, Y. K. Kim, O. H. Woo, and H. Han, "Pericardial fat is more abundant in patients with coronary atherosclerosis and even in the non-obese patients: evaluation with cardiac CT angiography." *Int J Cardiovasc Imaging*, vol. 26 Suppl 1, no. S1, pp. 53–62, 2010.

[235] M. Goeller, S. Achenbach, S. Cadet, A. C. Kwan, F. Commandeur, P. J. Slomka, H. Gransar, M. H. Albrecht, B. K. Tamarappoo, D. S. Berman, M. Marwan, and D. Dey, "Pericoronary Adipose Tissue Computed Tomography Attenuation and High-Risk Plaque Characteristics in Acute Coronary

Syndrome Compared With Stable Coronary Artery Disease," *JAMA Cardiol*, vol. 3, no. 9, p. 858, 2018.

[236] P. Kellman, D. Hernando, S. Shah, S. Zuehlsdorff, R. Jerecic, C. Mancini, Z. P. Liang, and A. E. Arai, "Multiecho dixon fat and water separation method for detecting fibrofatty infiltration in the myocardium," *Magn Reson Med*, vol. 61, no. 1, pp. 215–221, 2009.

[237] P. Kellman, D. Hernando, and A. E. Arai, "Myocardial Fat Imaging," *Curr Cardiovasc Imaging Rep*, vol. 3, no. 2, pp. 83–91, 2010.

[238] C. Kolbitsch, R. Neji, M. Fenchel, A. Mallia, P. Marsden, and T. Schaeffter, "Fully integrated 3D high-resolution multicontrast abdominal PET-MR with high scan efficiency," *Magn Reson Med*, 2017.

[239] ——, "Respiratory-resolved MR-based attenuation correction for motion-compensated cardiac PET-MR," *Phys Med Biol*, vol. 63, no. 13, p. 135008, 2018.

[240] C. Munoz, R. Neji, G. Cruz, R. M. Botnar, and C. Prieto, "Simultaneous acquisition of motion-corrected coronary MRA and respiratory-resolved attenuation maps for whole-heart PET-MR imaging," in *Proc ISMRM 26th Annu Meet Exhib*. ISMRM, 2018, p. 3349.

[241] J. Ma, Z. Slavens, W. Sun, E. Bayram, L. Estowski, K. P. Hwang, J. Akao, and A. T. Vu, "Linear phase-error correction for improved water and fat separation in dual-echo dixon techniques," *Magn Reson Med*, vol. 60, no. 5, pp. 1250–1255, 2008.

[242] B. D. Coombs, J. Szumowski, and W. Coshow, "Two-point Dixon technique for water-fat signal decomposition with B0inhomogeneity correction," *Magn Reson Med*, vol. 38, no. 6, pp. 884–889, 1997.

[243] J. Berglund, H. Ahlström, L. Johansson, and J. Kullberg, "Two-point dixon method with flexible echo times," *Magn Reson Med*, vol. 65, no. 4, pp. 994–1004, 2011.

[244] J. O. Blumhagen, H. Braun, R. Ladebeck, M. Fenchel, D. Faul, K. Scheffler, and H. H. Quick, "Field of view extension and truncation correction for MR-based human attenuation correction in simultaneous MR/PET imaging," *Med Phys*, vol. 41, no. 2, p. 022303, 2014.

[245] J. Y. Cheng, T. Zhang, N. Ruangwattanapaisarn, M. T. Alley, M. Uecker, J. M. Pauly, M. Lustig, and S. S. Vasanawala, "Free-breathing pediatric MRI with nonrigid motion correction and acceleration." *J Magn Reson Imaging*, vol. 42, no. 2, pp. 407–20, 2015.

[246] A. Bustin, G. Ginami, G. Cruz, T. Correia, T. F. Ismail, I. Rashid, R. Neji, R. M. Botnar, and C. Prieto, "Five-minute whole-heart coronary MRA with sub-millimeter isotropic resolution, 100% respiratory scan efficiency, and 3D-PROST reconstruction," *Magn Reson Med*, 2018.

[247] M. J. Ehrhardt, K. Thielemans, L. Pizarro, D. Atkinson, S. Ourselin, B. F. Hutton, and S. R. Arridge, "Joint reconstruction of PET-MRI by exploiting structural similarity," *Inverse Probl*, vol. 31, no. 1, p. 015001, 2015.

[248] F. Knoll, M. Holler, T. Koesters, R. Otazo, K. Bredies, and D. K. Sodickson, "Joint MR-PET Reconstruction Using a Multi-Channel Image Regularizer," *IEEE Trans Med Imaging*, vol. 36, no. 1, pp. 1–16, 2017.

[249] A. Mehranian, M. A. Belzunce, C. Prieto, A. Hammers, and A. J. Reader, "Synergistic PET and SENSE MR Image Reconstruction Using Joint Sparsity Regularization," *IEEE Trans Med Imaging*, vol. 37, no. 1, pp. 20–34, 2018.

[250] T. Correia, G. Cruz, T. Schneider, R. M. Botnar, and C. Prieto, "Technical note: Accelerated nonrigid motion-compensated isotropic 3D coronary MR angiography," *Med Phys*, vol. 45, no. 1, pp. 214–222, 2018.

[251] M. S. Nazir, T. F. Ismail, E. Reyes, A. Chiribiri, P. A. Kaufmann, and S. Plein, "Hybrid positron emission tomography–magnetic resonance of the heart: current state of the art and future applications," *Eur Hear J - Cardiovasc Imaging*, vol. 19, no. 9, pp. 962–974, 2018.